Power Electronics Meet Piezoelectrics: Converters, Components, and Miniaturization

by

Jessica Danielle Boles

M.S., University of Tennessee, Knoxville (2017)
B.S., University of Tennessee, Knoxville (2015)

Submitted to the Department of Electrical Engineering and Computer Science
in partial fulfillment of the requirements for the degree of

Doctor of Philosophy

at the

MASSACHUSETTS INSTITUTE OF TECHNOLOGY

September 2022

Author .....
Department of Electrical Engineering and Computer Science
August 25, 2022

Certified by .....
David J. Perreault
Ford Professor of Engineering
Thesis Supervisor

Accepted by .....
Leslie A. Kolodziejski
Professor of Electrical Engineering and Computer Science
Chair, Department Committee on Graduate Students

Power Electronics Meet Piezoelectrics:

Converters, Components, and Miniaturization

by

Jessica Danielle Boles

Submitted to the Department of Electrical Engineering and Computer Science
on August 25, 2022, in partial fulfillment of the requirements for the degree of
Doctor of Philosophy

Abstract

As converters and controllers of electrical energy, power electronics are the lifeblood of many exciting emerging technologies in transportation, manufacturing, information technology, and more. However, while integrated circuits have seen miniaturization and expanded performance characterized by Moore's Law, power electronics often remain the bulkiest, lossiest, and costliest components in the systems they serve. Miniaturization of power electronics is fundamentally bottlenecked by passive components, particularly magnetics (i.e., inductors and transformers), which pose inherent size and performance challenges at small scales.

This thesis explores how we can leverage an alternative passive component technology – piezoelectric components – to eliminate magnetics and unlock a new era of miniaturization for power electronics. Piezoelectrics offer several potential size, performance, and manufacturability advantages to power electronics, but harnessing these advantages requires fundamental re-evaluation of both power electronic circuits and piezoelectric components themselves. Accordingly, this thesis presents the following recent advances: (1) Dc-dc converter circuit topologies and operating sequences capable of efficiently utilizing piezoelectrics as sole passive components; these converter implementations demonstrate the efficiency viability of piezoelectric-based power electronics and provide their highest experimental efficiencies to date. (2) Piezoelectric component design tools for efficiency and power handling density; this framework enables maximal utilization of piezoelectric components and reveals them to have favorable scaling characteristics to small sizes. (3) An experimental demonstration of dramatic miniaturization offered by piezoelectrics; this prototype piezoelectric component has nearly an order of magnitude lower volume than a competing magnetic component design.

These are important steps in realizing the theoretical advantages of piezoelectrics in power electronics, positioning them to revolutionize what is possible for computing, wireless communication, robotics, biomedical devices, renewable energy, and beyond.

Thesis Supervisor: David J. Perreault
Title: Ford Professor of Engineering

Acknowledgments

This thesis has been supported with funds from Texas Instruments, Enphase Energy, the NSF Graduate Research Fellowship Program (1122374), the MIT Collamore-Rogers Fellowship, and the MIT Undergraduate Research Opportunities Program. Many thanks to these entities for believing in our work.

I would like to express my deepest gratitude to my research advisor, Prof. David Perreault, for his investment in me, my team, and the vision of this thesis. My investigation into piezoelectric-based power conversion began at his suggestion, and countless ideas and solutions sprinkled throughout this thesis originated with him or in our discussions. Beyond his intellectual influence, I am grateful for Prof. Perreault's mentorship, generosity, and the degree to which he truly champions each of his students. His passion, positivity, and support radiate throughout our research group and energize us all.

Over the past four years, I have had the privilege of building and leading our 'Piezo Team', comprised of five S.B. and M.Eng. students: Joshua Piel, Elaine Ng, Joseph Bonavia, Babuabel Wanyeki, and Pedro Acosta. Multiple chapters of this thesis are the fruits of their hard work, dedication, and creativity. It has been a joy and an honor to work with each of these students, to learn from them, and to watch them grow as researchers. I look forward to what each of their futures hold.

I am likewise thankful for the input of multiple collaborators throughout this thesis. As a core member of our Piezo Team, Prof. Jeffrey Lang provided significant expertise on piezoelectric components, modeling, and fabrication, and I am grateful for his wholehearted mentorship. The perspective of Dr. Yogesh Ramadass inspired the areal power density figure of merit for piezoelectric materials and vibration modes. The controller utilized in all open-loop experiments of this thesis was previously developed and customized as needed by Mr. David Otten. I would also like to acknowledge my committee members Prof. Charles Sullivan, Prof. John Kassakian, and Prof. Steven Leeb for their thoughtful suggestions and engaging discussions.

Special thanks to my labmates in the MIT LEES/GEM community for their friendship,

mentorship, and support over the past five years. This community has passed along tremendous technical and non-technical know-how and has fostered a healthy, collaborative work environment for me since the beginning. Their curiosity and enthusiasm for ideation is contagious, and their impact is felt throughout this thesis.

I would also like to acknowledge my friends and family who kept me grounded through every peak and every valley of my Ph.D. journey – figuratively and literally. Many of them believed I could do this before I did, and I am indebted to their encouragement and support. I treasure the countless memories and adventures with my friends here in Boston, and for the beauty they have added to my graduate school experience.

Last but not least, this endeavor would not have been possible without my partner, Alex Klibisz. I am grateful for his endless love and support, even through the behind-the-scenes sacrifices that nobody else sees, and for how he challenges me to strive for the best version of myself. He is the greatest teammate, partner, and best friend I can imagine, and I look forward to our next adventure together.

Contents

List of Figures

List of Tables

Chapter 1

Introduction

1.1 Background and Motivation

From power grids to motor drives to portable electronic devices, power electronics stimulate innovation in nearly every major industry. Next-generation technologies in renewable energy, electrified transportation, wireless communication, manufacturing, computing, robotics, and healthcare demand power electronics with ever-increasing capabilities, positioning the advancement of power electronics as critical to both technological progress and energy sustainability. Nevertheless, while integrated circuits for processing information have seen miniaturization and expanded performance characterized by Moore's Law, power electronics often remain the bulkiest, lossiest, and costliest components in the systems they serve.

Conceptually, a power electronic converter acquires electrical energy from a source (e.g., a battery or the grid), momentarily stores it in passive components, and then delivers it to a load in a different form. This process is repeated up to millions of times per second, controlled with semiconductor switching devices. In recent years, wide-bandgap semiconductor devices and advanced control techniques have enabled substantial size and performance improvements in power electronics. However, miniaturization of power electronics remains bottlenecked by the passive components dominating their sizes, particularly magnetics (i.e.,

inductors and transformers).

While magnetics have been integral to power electronics since the field's inception, they pose fundamental power handling and efficiency challenges at small scales that amount to lower power densities at low volume [5–7]. Alternatively, switched capacitor converters have achieved record-breaking power densities and efficiencies (e.g., [8–14]), but these architectures still require supplementary magnetics for efficient voltage regulation. Several miniaturization strategies have been developed despite the limitations of magnetics (e.g., higher switching frequencies, more sophisticated circuit topologies and operating techniques, and improved magnetic designs). Although beneficial, these strategies ultimately still face the same scaling impediments.

The scaling challenges of magnetics motivate investigation into alternative passive component technologies for power conversion that can provide the same high-level functionalities but with superior scalability to small sizes. One such alternative is piezoelectric components, which store energy in the mechanical compliance and inertia of a piezoelectric material. Piezoelectrics show promise for very high power density and efficiency with improved scaling potential to small sizes compared to magnetics; an optimistic theoretical investigation in [15] suggests that piezoelectric components may be capable of handling up to kilowatt-level power within only 1 mm^3, which is unprecedented in power conversion. Piezoelectrics also offer other potential advantages to power conversion including planar form factors, galvanic isolation (with multi-port devices), batch fabrication, and amenability to integration.

Piezoelectric components can be realized as single-port piezoelectric resonators (PRs) or multi-port piezoelectric transformers (PTs). In the proximity of a resonant mode, PRs can be modeled with the Butterworth-Van Dyke model illustrated in Fig. 1-1 [1, 2, 16]. This model contains a static capacitance C_p in parallel with an LCR branch modeling the PR's mechanical inertia, compliance, and loss properties, respectively. PTs are similarly modeled with the reduced Mason model shown in Figs. 1-2 and 1-3, which contains terminal capacitances, an LCR branch, and an ideal transformer [3, 4, 17].

Although piezoelectric components have been extensively utilized for sensing, actuation, transduction, and energy harvesting, their application in power electronics has been more

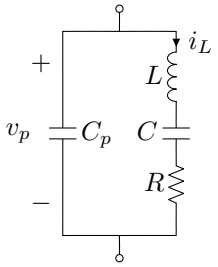

Figure 1-1: Butterworth-Van Dyke circuit model for PRs [1, 2].

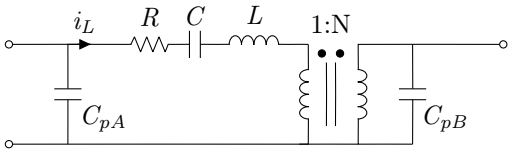

Figure 1-2: Reduced Mason circuit model for non-isolated PTs [3, 4].

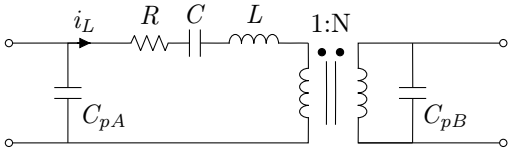

Figure 1-3: Reduced Mason circuit model for isolated PTs [3, 4].

limited. PTs have a long history that includes high-volume commercialization for CCFL backlight drivers [18], but demand for them waned with the advent of LEDs. PT-based power converter designs have often included additional magnetic components [4, 19–38], though this detracts from their potential power density advantages. Prior to this work, magnetic-less converter variations capable of zero-voltage switching (ZVS) had been realized using both PTs (e.g., [37, 39–52]) and PRs (e.g., [53–56]), but typically with limited power and/or performance capability. Notably, nearly all such designs utilize piezoelectrics in existing converter architectures, controlled for typical resonant converter behaviors.

With modern circuit design and control techniques, improved semiconductor devices and integrated circuit technologies, advanced piezoelectric materials and fabrication capabilities, and more sophisticated modeling and simulation tools, today's technological landscape is fertile for realizing the theoretical benefits of piezoelectrics in power electronics. However, manifesting the advantages of piezoelectrics will require fundamental reconsideration of both power electronic circuits and piezoelectric components themselves.

1.2 Thesis Objectives

This thesis explores the following question: **How can we leverage the theoretical advantages of piezoelectrics to substantially miniaturize power electronics?** This

investigation requires identifying the complementary roles and needs of both piezoelectrics and potential converter implementations; neither has seen significant development in context of the other, so both require fundamental re-evaluation and adaptation. This work hypothesizes that such an investigation will reveal new piezoelectric-based power conversion strategies through which major advances in converter miniaturization may be achieved. Accordingly, the objectives of this thesis are:

1. **Identify practical converter implementations that most efficiently utilize piezoelectrics.** We explore high-efficiency converter implementations based on PRs and PTs, along with their control and hybridization with switched-capacitor converters. These converter implementations are accompanied by a variety of analysis methods for periodic steady-state operation, dynamic behavior, and efficiency.

2. **Establish design criteria for piezoelectric components specifically for use in power conversion.** These tools include figures of merit for selecting piezoelectric materials and vibration modes as well as geometric dimensions for achieving maximum efficiency and power density in a component design. We apply these strategies to multiple component structures including PRs, mass-augmented PRs, and PTs.

3. **Demonstrate the miniaturization potential of piezoelectrics.** We combine the proposed high-efficiency converter implementations and piezoelectric component design techniques to experimentally demonstrate the power density promise of piezoelectrics. This effort is accompanied by a case study into the fundamental scaling characteristics of piezoelectrics.

The objectives of this thesis are addressed in three corresponding parts. Part I (comprising Chapters 2-5) explores converter implementations based on piezoelectrics, Part II (comprising Chapters 6-8) investigates piezoelectric component design, and Part III (comprising Chapter 9) demonstrates the miniaturization promise of piezoelectrics.

Part I

DC-DC Converter Implementations

Chapter 2

DC-DC Converter Implementations Based on Piezoelectric Resonators

2.1 Introduction

Over the past few decades, magnetic-less dc-dc power conversion based on piezoelectric transformers (PTs) and piezoelectric resonators (PRs) has been explored in [40–44, 48, 49, 53–56]. These converter implementations have often relied on standard resonant converter architectures and control sequences, utilizing the piezoelectric component as a resonant tank. These designs have typically yielded limited power and/or performance capabilities, and there has been little investigation beyond them towards converter implementations that more effectively utilize piezoelectrics.

In this chapter, we abandon these standard converter design approaches and conduct a systematic investigation into dc-dc converter implementations capable of efficiently utilizing PRs as their only energy storage components. We enumerate and downselect potential switching sequences and topologies based on specific high-efficiency behaviors (i.e., low-loss resonant "soft charging" of the PR's input capacitance, zero-voltage switching (ZVS), and minimal charge circulation) and the ability to maintain these behaviors across wide, continuous voltage conversion ranges. To analyze and compare implementations, we demonstrate

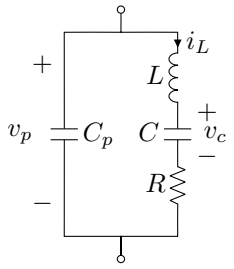

Figure 2-1: Butterworth-Van Dyke circuit model for PRs [1, 2].

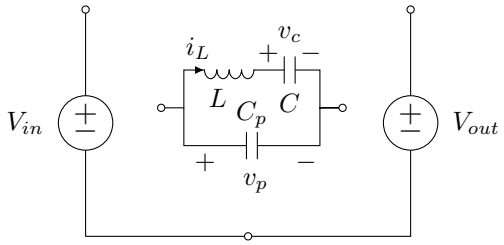

Figure 2-2: Common-negative dc-dc system considered for switching sequence enumeration, shown with an ideal PR.

methods for mapping PR state trajectories across a switching cycle and solving for their periodic steady-state solutions. We then introduce the amplitude of resonance model as a means to evaluate PR utilization and estimate efficiency with low computation. We demonstrate promising implementations and validate the proposed analysis techniques in an experimental prototype based on a commercially available PR. Through its effective utilization of the PR, this prototype achieves significantly improved efficiency compared to previous PR-based converter designs.

2.2 Switching Sequence Enumeration and Downselection

To identify dc-dc converter implementations capable of efficiently utilizing PRs, we first enumerate potential operating modes and then downselect them based on desired high-efficiency behaviors and practical characteristics.

2.2.1 Assumed System and Stages

To enumerate PR-based dc-dc converter operating modes, we assume a non-inverting common-negative system as shown in Fig. 2-2. This source-load system contains only a PR for energy storage, and its source and load are assumed to both have constant voltage (i.e., we neglect filter components). There is a finite number of ways the PR's terminals can be connected in this source/load system, and we refer to each of these connections as a possible *stage* of a switching cycle. These stages can be categorized as:

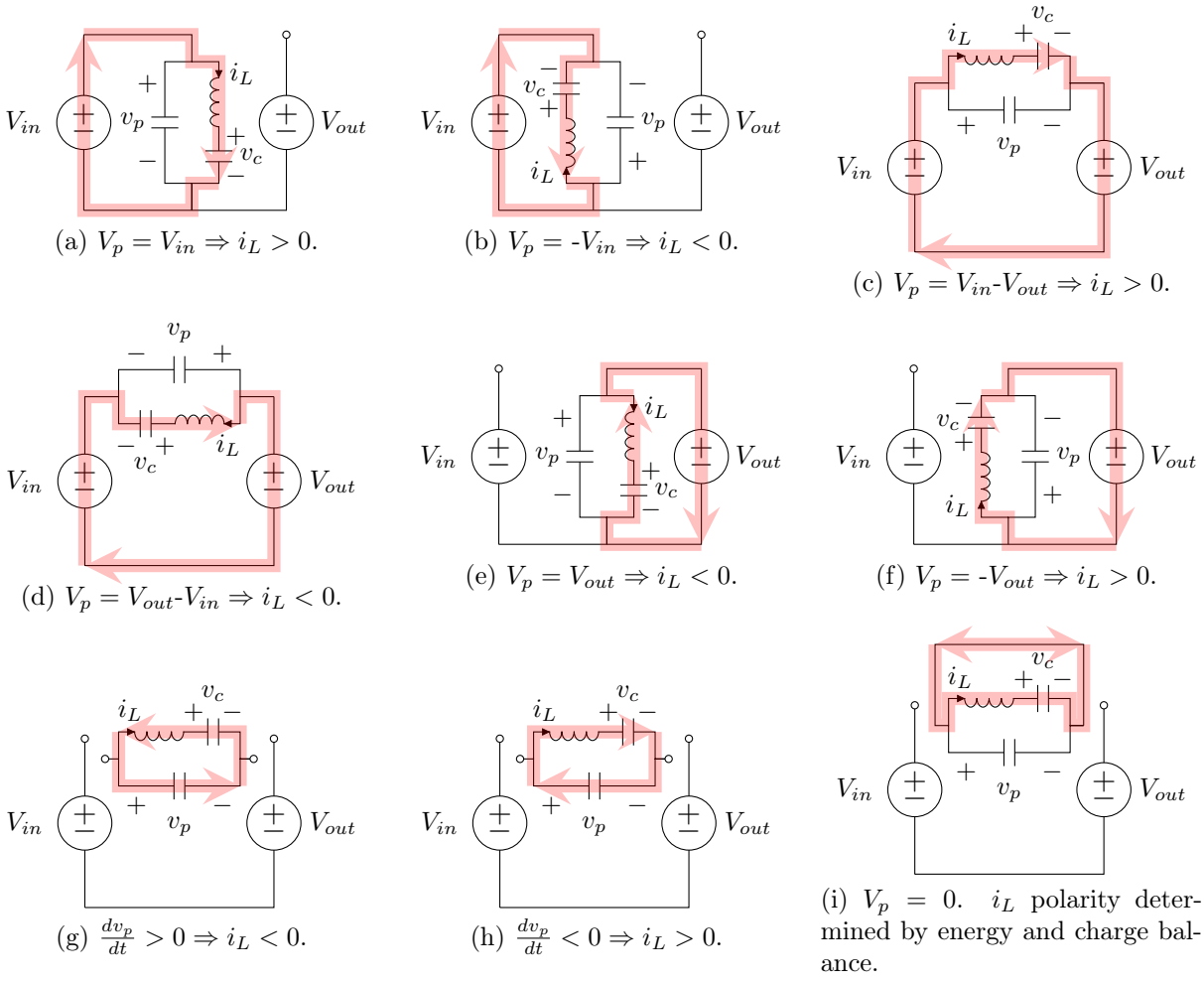

(a) $V_p = V_{in} \Rightarrow i_L > 0$.

(b) $V_p = \text{-}V_{in} \Rightarrow i_L < 0$.

(c) $V_p = V_{in}\text{-}V_{out} \Rightarrow i_L > 0$.

(d) $V_p = V_{out}\text{-}V_{in} \Rightarrow i_L < 0$.

(e) $V_p = V_{out} \Rightarrow i_L < 0$.

(f) $V_p = \text{-}V_{out} \Rightarrow i_L > 0$.

(g) $\frac{dv_p}{dt} > 0 \Rightarrow i_L < 0$.

(h) $\frac{dv_p}{dt} < 0 \Rightarrow i_L > 0$.

(i) $V_p = 0$. i_L polarity determined by energy and charge balance.

Figure 2-3: Assumed current paths for each connected stage (a)-(f), open stage (g)-(h), and zero stage (i), illustrated with an ideal PR.

- Connected stages: the PR's terminals are connected to the source/load system such that v_p is fixed (denoted with capital V_p) at some combination of V_{in} and/or V_{out}, illustrated in Figs. 2-3(a)-(f).
- Zero stages: the PR's terminals are short-circuited ($V_p = 0$) as shown in Fig. 2-3(i).
- Open stages: the PR's terminals are open-circuited, allowing v_p to increase or decrease through resonance as shown in Figs. 2-3(g)-(h).

Connected stages allow the PR to exchange energy with the source/load system, while zero and open stages are useful for redistributing energy among the PR's states. We make

the assumption that positive average power flow *from* V_{in} and/or *to* V_{out} is desired for each connected stage to minimize charge circulation. For this to be true, i_L must be on-average positive during connected stages where $V_p = V_{in}$, V_{in}-V_{out}, or -V_{out} and on-average negative for connected stages where V_p = -V_{in}, V_{out}-V_{in}, and V_{out}. Average i_L polarity constraints also apply to open stages, which require a particular charge redistribution to charge/discharge v_p. Positive i_L removes charge from C_p and therefore decreases v_p, while negative i_L increases v_p. These assumed current polarities are illustrated for each stage type in Fig. 2-3. We note that zero stages have no inherent i_L polarity requirement for positive average power flow.

2.2.2 Switching Sequence Enumeration

These stages can be arranged into *switching sequences*, defined as order-specific patterns of stages cycled throughout a switching period. To facilitate soft charging of C_p at each stage transition, we only consider switching sequences that alternate connected/zero stages with open stages. Thus, we refer to a switching sequence by the order of its connected/zero stages named by PR terminal voltage (V_p), assuming an open stage between each (e.g., V_{in}, V_{in}-V_{out}, V_{out}). To enumerate potential switching sequences, we permute the set of stages described above with the following additional constraints:

1. A minimum number of stages ($\leq$6 stages).
2. At least one stage with connection to V_{in}.
3. At least one stage with connection to V_{out}.
4. At least two connected stages (to balance energy transfer to/from the PR over a switching period).
5. No repetition of the same connected/zero stage.

These criteria limit the search to switching sequences with only even numbers of stages, with a minimum of four (including open stages). We differentiate between duplicate se-

Table 2.1: All Enumerated Four-Stage Switching Sequences

V_{in}, V_{in}-V_{out}	B,B	V_{in}-V_{out}, V_{out}-V_{in}	B,B
V_{in}, V_{out}-V_{in}	B,B	V_{in}-V_{out}, V_{out}	B,B
V_{in}, V_{out}	B,B	V_{in}-V_{out}, -V_{out}	B,B
V_{in}, -V_{out}	B,B		

Table 2.2: All Enumerated Six-Stage Switching Sequences

V_{in}, -V_{in}, V_{in}-V_{out}	A,A	V_{in}, -V_{out}, V_{in}-V_{out}	A,A
V_{in}, -V_{in}, V_{out}-V_{in}	B,C	V_{in}, -V_{out}, V_{out}-V_{in}	C,C
V_{in}, -V_{in}, V_{out}	B,C	V_{in}, -V_{out}, V_{out}	C,B
V_{in}, -V_{in}, -V_{out}	A,A	V_{in}, -V_{out}, Zero	$*$,$*$
V_{in}, V_{in}-V_{out}, V_{out}-V_{in}	B,C	V_{in}, Zero, V_{in}-V_{out}	A,B
V_{in}, V_{in}-V_{out}, V_{out}	$*$,B	V_{in}, Zero, V_{out}-V_{in}	B,$*$
V_{in}, V_{in}-V_{out}, -V_{out}	B,B	V_{in}, Zero, V_{out}	$*$,$*$
V_{in}, V_{in}-V_{out}, Zero	B,$*$	V_{in}, Zero, -V_{out}	B,B
V_{in}, V_{out}-V_{in}, V_{in}-V_{out}	A,A	V_{in}-V_{out}, V_{out}-V_{in}, V_{out}	C,B
V_{in}, V_{out}-V_{in}, V_{out}	B,$*$	V_{in}-V_{out}, V_{out}-V_{in}, -V_{out}	A,A
V_{in}, V_{out}-V_{in}, -V_{out}	A,A	V_{in}-V_{out}, V_{out}-V_{in}, Zero	B,B
V_{in}, V_{out}-V_{in}, Zero	B,A	V_{in}-V_{out}, V_{out}, -V_{out}	A,A
V_{in}, V_{out}, V_{in}-V_{out}	A,A	V_{in}-V_{out}, V_{out}, Zero	A,B
V_{in}, V_{out}, V_{out}-V_{in}	A,A	V_{in}-V_{out}, -V_{out}, V_{out}	C,B
V_{in}, V_{out}, -V_{out}	A,A	V_{in}-V_{out}, -V_{out}, Zero	$*$,B
V_{in}, V_{out}, Zero	A,A	V_{in}-V_{out}, Zero, V_{out}	$*$,B
		V_{in}-V_{out}, Zero, -V_{out}	B,A

quences as follows: Rearranging the order of a switching sequence's stages results in a different switching sequence, whereas rotating the stages (in the same order) to a different "first" stage results in the same switching sequence. Further, inverting *all* stages of a switching sequence results in the same switching sequence (with opposite PR polarity).

Enumerating all possible sequences and filtering the results according to these criteria yields 7 distinct four-stage switching sequences and 33 distinct six-stage sequences. Full lists of these sequences are shown in Tables 2.1 and 2.2, along with the subsequent sub-sections in which they are eliminated for '$V_{in} > V_{out}$, $V_{out} > V_{in}$'. Sequences marked with 'A' are

Table 2.3: Example i_L Polarity Mappings for $V_{in} > 2V_{out}$

V_p sequence A:	V_{in}	open	V_{in}-V_{out}	open	V_{out}	open
i_L polarity:	+	+	+	+	-	-
V_p sequence B:	V_{in}	open	V_{out}-V_{in}	open	$-V_{out}$	open
i_L polarity:	+	+	-	-	+	-

eliminated in Section 2.2.3, sequences marked with 'B' are eliminated in Section 2.2.4, and sequences marked with 'C' are eliminated in Section 2.2.5. The final switching sequences shown in Table 2.4 are marked with $*$.

2.2.3 Single PR Resonant Cycle

We downselect the enumerated set of switching sequences based on physical requirements for power conversion and practical considerations. We first focus on switching sequences that can be completed in only one PR resonant period (one cycle of energy exchange between L and C). A four- or six-stage sequence that spans more than one resonant period would require more redistribution of energy within the PR during open and zero stages (while dissipating energy in R), higher and/or bidirectional switch blocking requirements (if v_p peaks during an open stage), or connected stages with significant reverse power flow to avoid these.

To investigate this, the average i_L polarity constraints described in Section 2.2.1 can be mapped for each stage of a switching sequence as shown in Table 2.3, where + and - indicate positive or negative i_L as required by the necessary energy transfer or charge displacement. For a switching sequence to be completed in one PR resonant cycle, it must require only one span (one or more stages back-to-back) of positive i_L and only one span of negative i_L like Sequence A in Table 2.3. Sequence B in Table 2.3 requires multiple spans of each and therefore traverses more than one cycle. Filtering the potential switching sequences to only those that can be completed in one cycle leaves 7 four-stage and 20 six-stage switching sequences for each of $V_{in} > V_{out}$ and $V_{in} < V_{out}$.

2.2.4 Voltage Conversion Range

Periodic steady-state operation requires balance of both energy and charge on the PR across the switching period. To illustrate, the following Conservation of Energy (CoE) equation must hold for six-stage switching sequences (easily adaptable to four-stage sequences). For the n^{th} stage, E_n is the energy delivered to the PR, V_{pn} is a constant value of v_p, and q_n equals the net charge transferred by i_L (i.e., q_n has the same polarity specified for i_L):

$$E_1 + E_3 + E_5 = V_{p1}q_1 + V_{p3}q_3 + V_{p5}q_5 = 0 \tag{2.1}$$

Switching sequences for which the energy terms in this equation are either all positive or all negative (i.e., the only solution is $q_1 = q_3 = q_5 = 0$) are not capable of balancing the PR's energy and can be eliminated.

Furthermore, the following Conservation of Charge (CoC) equations must hold for C_p and C, respectively, in a six-stage sequence:

$$q_2 + q_4 + q_6 = 0 \tag{2.2}$$

$$q_1 + q_2 + q_3 + q_4 + q_5 + q_6 = 0 \tag{2.3}$$

Combining these two equations shows that the charge transfer during connected/zero stages must also be balanced:

$$q_1 + q_3 + q_5 = 0 \tag{2.4}$$

Inserting (2.4) into (2.1) results in a general equation that must be satisfied for balancing energy and charge on the PR throughout a given switching sequence. The solution to this equation *with correct q polarities* yields the complete voltage conversion range for which this balance holds and the switching sequence is useful. An example voltage conversion range derivation is shown below using this procedure, and the conversion ranges for the final proposed switching sequences are summarized in Table 2.4. Switching sequences for which this general equation cannot be satisfied without $q_1 = q_3 = q_5 = 0$ are not capable of both energy and charge balance and can be eliminated. Switching sequences for which only specific

voltage conversion ratios can satisfy this equation (e.g., $V_{in} = V_{out}$ or $V_{in} = 2V_{out}$) cannot efficiently regulate voltage and are therefore also removed. Filtering according to these criteria eliminates all four-stage switching sequences; *no four-stage switching sequences can satisfy our assumptions thus far outside of fixed voltage conversion ratios.* By contrast, 9 six-stage sequences (each with step-up and step-down versions) are capable of balancing the PR's energy and charge across wide voltage conversion ranges, which is advantageous for voltage regulation.

Example Voltage Conversion Range Derivation

We derive the range of voltage conversion ratios compatible with example switching sequence V_{in}, V_{in}-V_{out}, V_{out}, using the CoE equation (2.1) and the CoC equation (2.4). For this switching sequence, the i_L polarity assumptions made in Section 2.2.1 require q_1 and q_3 to be positive and q_5 to be negative. Thus, equations (2.1) and (2.4) become:

$$V_{in}|q_1| + (V_{in} - V_{out})|q_3| - V_{out}|q_5| = 0 \tag{2.5}$$

$$|q_1| + |q_3| = |q_5| \tag{2.6}$$

Inserting (2.6) into (2.5) yields the general equation that must be satisfied to ensure energy and charge balance on the PR with this switching sequence:

$$V_{in}|q_1| + (V_{in} - V_{out})|q_3| - V_{out}(|q_1| + |q_3|) = 0 \tag{2.7}$$

The complete set of V_{in} and V_{out} combinations for which q_1 and q_3 can be calculated to satisfy this general equation is bound by the requirement that V_{out} is a weighted average of V_{in} and V_{in}-V_{out}. This translates to the ranges $V_{in} > V_{out}$ and $V_{out} > V_{in}$-V_{out}, which combine into $\frac{1}{2} < \frac{V_{out}}{V_{in}} < 1$. Thus, this is the range of voltage conversion ratios that are supported by switching sequence V_{in}, V_{in}-V_{out}, V_{out} assuming the aforementioned constraints.

2.2.5 Switch Implementations

The circuit topologies and switch implementations needed to realize these switching sequences vary widely in terms of switch quantity and voltage blocking capability. A converter with a high number of switches is more complex and costly to implement, and switches that block bidirectional voltage are difficult to physically realize. In general, each distinct terminal connection requires its own switch, and there are three node options (positive input, positive output, ground) to which both terminals can be tied for zero stages. For the six-stage sequences in this study, implementations that require fewer than or greater than four switches require at least one bidirectional voltage blocking switch. If we filter to switching sequences that only require four unidirectional-blocking switches (inclusive of three-switch topologies with one bidirectional-blocking switch), 5 switching sequences remain each for step-up and step-down operation. The remainder of this chapter focuses on these switching sequences, summarized in Table 2.4 and discussed in Section 2.3. The corresponding circuit topologies for realizing these sequences are shown in Fig. 2-4.

2.2.6 Alternative Topology-based Enumeration

One alternative enumeration approach begins with the scope of *topologies* that can be derived from Fig. 2-2, constrained by practical assumptions. Assuming the output voltage is uniquely either greater than or less than the input voltage, the following source/load connection quantities are possible for each PR terminal:

- One source/load connection: allows a fixed node with no switches.
- Two source/load connections: creates a switch node that requires two unidirectional-blocking switches.
- Three source/load connections: creates a switch node that requires two unidirectional-blocking and one bidirectional blocking switch (for the middle-voltage node).

Since a six-stage switching sequence has three connected stages, it requires a minimum of four total terminal connections for the PR. This can be constructed with either one

terminal having one connection (a fixed node) and the other having three connections (a switch node) or both terminals having two connections each (two switch nodes). Both of these configurations can be implemented with four unidirectional blocking switches, which is the fewest number for a six-stage switching sequence. Assuming this simplicity is desired, the domain of relevant topologies can be confined to these configurations.

Enumerating topologies with two switch nodes yields Figs. 2-4(a)-(e) plus one additional structure with both PR terminals each having connections to the positive nodes of V_{in} and V_{out}. This amounts to four distinct structures if the blocking directions of the switches are left ambiguous. The structures in Figs. 2-4(a)-(e) can each support four distinct connected stages, while the additional structure can only support three (since it supports two ways to achieve a zero stage).

The set of potential switching sequences for a topology can be enumerated by permuting the structure's possible connected stages. For Figs. 2-4(a)-(e), this results in eight distinct six-stage switching sequences each (as defined by the assumptions in Section 2.2.2). These switching sequences can then be downselected based on the same resonant cycle and energy/charge balance requirements described in Sections 2.2.3 and 2.2.4. This process eliminates all but four sequences each for Figs. 2-4(a)-(d), all but three sequences for Fig. 2-4(e), and all potential sequences for the additional derived structure. The downselection result is the same as that displayed in Fig. 2-4 and Table 2.4 for these topologies, and the same process applies to Figs. 2-4(f)-(i).

2.3 Resulting Converter Implementations and Constraints

With promising PR-based converter implementations identified, we now discuss their characteristics and how their operation may be constrained for additional benefits.

2.3.1 Six-Stage Switching Sequences

Table 2.4 summarizes the step-up and step-down versions of the 5 switching sequences reached in Section 2.2 along with their associated topologies and constraints; details for

these are provided below. The sequences for $V_{in} > V_{out}$ each have time-reversal duals for $V_{in} < V_{out}$ [57], resulting in some sequences that are the same for both cases while others are different (amounting to 8 total distinct sequences). The supported voltage conversion ranges are calculated as described in Section 2.2.4. The 9 topologies for realizing these sequences are displayed in Fig. 2-4. It should be noted that some of these topologies have two switch nodes (i.e., both PR terminals each connect to two source/load system nodes), and some have only one (i.e., the other PR terminal is fixed). Topologies (*) can be realized with only two active switches, and topology (†) requires opposite v_p polarity.

To analyze switching sequences, we adopt a numbering convention for stages in which the first stage for a given switching sequence is the first listed stage as written in Table 2.4, and stage numbers increase sequentially. Thus, stages 1, 3, and 5 are connected/zero stages, and stages 2, 4, and 6 are the respective open stages following those connected/zero stages. We refer to the PR's states at the beginning of each stage with a subscript denoting the stage number; V_{pn} and i_{Ln} refer to V_p and i_L at the start of the n^{th} stage, respectively.

Degrees of freedom in the periodic steady-state operation of these switching sequences (detailed in Section 2.4) can be constrained according to desired high-efficiency behaviors. In this work, we seek to maximize performance by requiring only positive instantaneous power transfer as well as zero-voltage switching (ZVS) of power transistors. The zero crossing constraints in Table 2.4 denote the stage transitions at which i_L zero crossings must occur for minimum charge circulation (assuming unidirectional-blocking switches) as described in Section 2.3.2. The modifications of these constraints for ZVS are those described in Section 2.3.3. K refers to the charge transfer utilization factor described in Section 2.5.1.

2.3.2 Minimal Charge Circulation

To reduce loss, we constrain the periodic steady-state operation of these switching sequences in ways that eliminate excess charge circulation. This includes constraining for all-positive instantaneous power transfer both from the source and to the load. To minimize charge circulation, the average i_L polarity assumptions in Section 2.2.1 can be extended to requiring

Table 2.4: Summary of Proposed Six-Stage Switching Sequences, Topologies, and Constraints

Switching Sequence	Voltage Conversion Range	Zero Crossing Constraints	Topology (Fig. 2-4)	Modification for ZVS (required if only 2 active switches used)	K
V_{in}-V_{out}, *Zero*, V_{out}	$\frac{V_{out}}{V_{in}} < \frac{1}{2}$	$i_{L1}, i_{L4} = 0$	(a)*	$i_{L4}, i_{L6B} = 0$, $V_{p6B} = V_{in}$	$\frac{V_{in}}{2(V_{in}-V_{out})}$
	$\frac{1}{2} < \frac{V_{out}}{V_{in}} < 1$	$i_{L3}, i_{L6} = 0$	(a)	$i_{L3}, i_{L6B} = 0$, $V_{p6B} = V_{in}$	$\frac{V_{in}}{2V_{out}}$
V_{in}, V_{in}-V_{out}, V_{out}	$\frac{1}{2} < \frac{V_{out}}{V_{in}} < 1$	$i_{L1}, i_{L4} = 0$	(a)	$i_{L1}, i_{L4B} = 0$, $V_{p4B} = 0$	$\frac{V_{in}}{2V_{out}}$
V_{in}-V_{out}, -V_{out}, *Zero*	$\frac{V_{out}}{V_{in}} < 1$	$i_{L1}, i_{L4} = 0$	(c)†	$i_{L1}, i_{L4B} = 0$, $V_{p4B} = -V_{in}$	$\frac{1}{2}$
			(e)*	$i_{L4}, i_{L6B} = 0$, $V_{p6B} = V_{in}$	
			(f)*	No change	
V_{in}, *Zero*, V_{out} (explored in [58])	$1 < \frac{V_{out}}{V_{in}}$	$i_{L3}, i_{L6} = 0$	(b)*	$i_{L2B}, i_{L6} = 0$, $V_{p2B} = V_{in}$-V_{out}	$\frac{1}{2}$
			(d), (i)*	No change	
	$\frac{V_{out}}{V_{in}} < 1$	$i_{L1}, i_{L4} = 0$	(c)	$i_{L1}, i_{L4B} = 0$, $V_{p4B} = V_{out}$-V_{in}	
			(a), (h)*	No change	
V_{in}, -V_{out}, *Zero*	Any	$i_{L1}, i_{L4} = 0$	(e)	No change	$\frac{\max(V_{in}, V_{out})}{2(V_{in}+V_{out})}$
V_{in}, *Zero*, V_{out}-V_{in}	$2 < \frac{V_{out}}{V_{in}}$	$i_{L3}, i_{L6} = 0$	(d)	$i_{L3}, i_{L6B} = 0$, $V_{p6B} = V_{out}$	$\frac{V_{out}}{2(V_{out}-V_{in})}$
	$1 < \frac{V_{out}}{V_{in}} < 2$	$i_{L1}, i_{L4} = 0$	(d)*	$i_{L4}, i_{L6B} = 0$, $V_{p6B} = V_{out}$	$\frac{V_{out}}{2V_{in}}$
V_{in}, V_{out}-V_{in}, V_{out}	$1 < \frac{V_{out}}{V_{in}} < 2$	$i_{L3}, i_{L6} = 0$	(d)*	$i_{L2B}, i_{L6} = 0$, $V_{p2B} = 0$	$\frac{V_{out}}{2V_{in}}$
V_{in}, V_{in}-V_{out}, *Zero*	$1 < \frac{V_{out}}{V_{in}}$	$i_{L1}, i_{L4} = 0$	(b)*	$i_{L4}, i_{L6B} = 0$, $V_{p6B} = V_{out}$	$\frac{1}{2}$
			(e)	$i_{L1}, i_{L4B} = 0$, $V_{p4B} = -V_{out}$	
			(g)*	No change	

(*) can be realized with only two active switches, and (†) requires opposite v_p polarity.

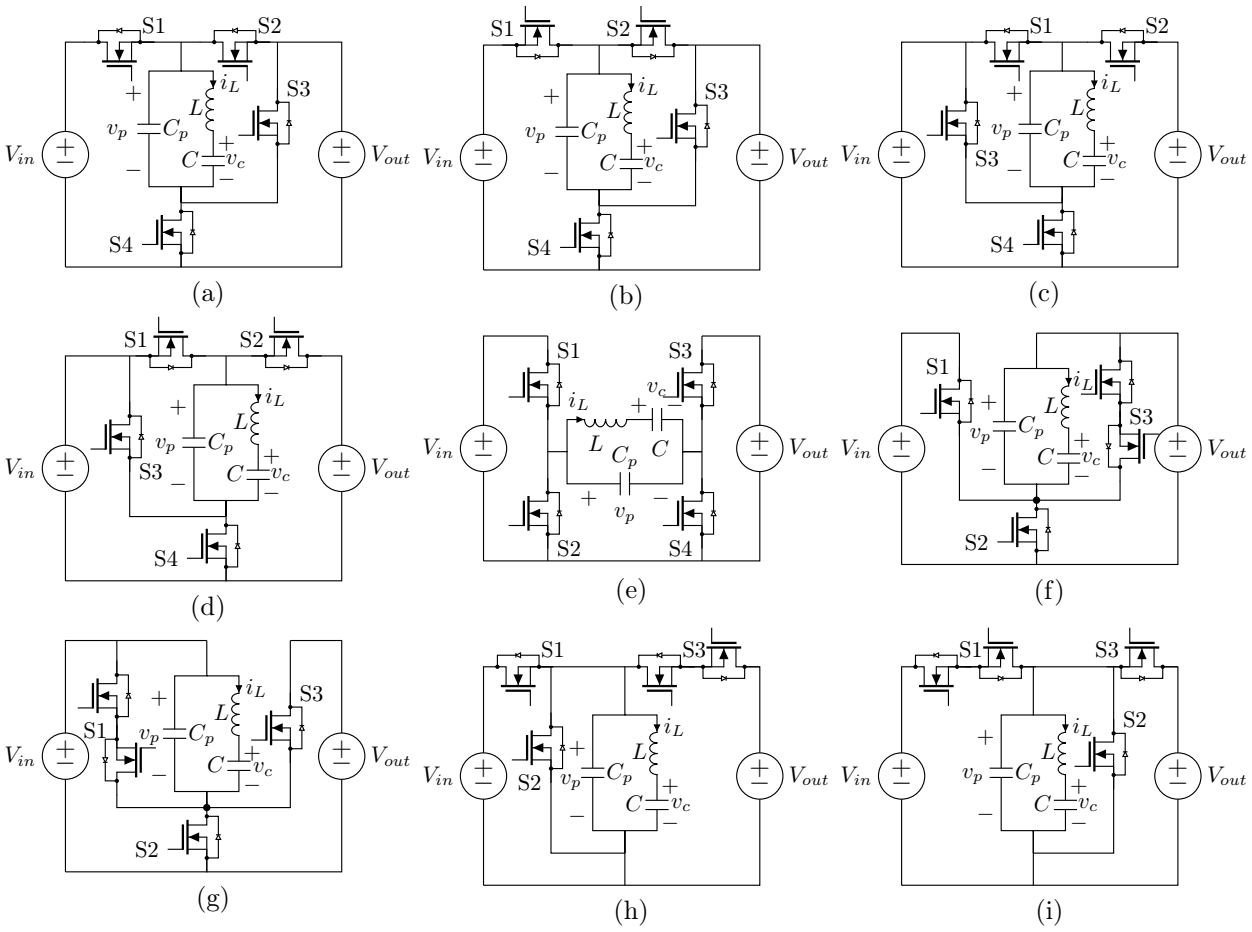

Figure 2-4: Converter topologies corresponding to the switching sequences displayed in Table 2.4. All switches are illustrated as MOSFETs, but many can be implemented passively.

these i_L polarities for the entirety of each stage, eliminating the portions of stages that do not provide net energy transfer between the PR and the source/load system or within the PR itself. This requires v_p to resonate to exactly its desired voltage, without overshoot, during open stages. Zero stages occurring near an i_L zero crossing are constrained for only unidirectional current flow with the polarity of i_L determined by CoC equation (2.4).

These constraints force the switching sequence to align with the i_L cycle such that the i_L zero crossings occur exactly at the stage transitions between positive- and negative-i_L stages. Thus, the two i_L zero crossing points can be defined for all switching sequences as summarized under "Zero Crossing Constraints" in Table 2.4, in which i_{Ln} refers to i_L at the start of the n^{th} stage.

2.3.3 Zero-Voltage Switching

All of the viable implementations summarized in Table 2.4 facilitate soft charging of the PR, but not necessarily ZVS of the switches. Topologies that have only one switch node (i.e., one terminal of the PR is tied to the source/load system) inherently require ZVS in order to soft charge the PR since C_p and all switch capacitances exist between the same switch node and a fixed DC voltage. Thus, ZVS occurs across the entire six-stage switching sequence for topologies (f)-(i) in Fig. 2-4.

For topologies that have two switch nodes (i.e., neither terminal of PR is tied to the source/load system, as in topologies (a)-(e) of Fig. 2-4), six-stage sequences require at least one open stage during which both switch nodes change voltage. Outside of specific conversion ratios, the necessary voltage changes at each of the two nodes during this open stage tend to require different time durations and/or opposite i_L polarities.

ZVS can be ensured for topologies (a)-(e) of Fig. 2-4 if the open stage during which both nodes change voltage is *split into two sections*. For the general case, this two-part open stage can be used to change the two node voltages one at a time, with a V_p constraint at the transition point as needed for ZVS. This way, the PR is tied to the source/load system by one of its terminals at all times, and the transition between the two parts of the open stage can take place at a zero crossing for i_L if the two terminal voltage transitions require opposite i_L polarities. This concept is illustrated in Section 2.4.1 using state planes.

Altering an open stage in this way to achieve ZVS in topologies (a)-(e) requires modification of the i_L zero-crossing constraints for minimal charge circulation. These modifications are displayed in Table 2.4 along with the V_p constraint for the i_L zero crossing between the open stage's two parts (subscript "B" indicates this transition point). This V_p constraint suggests the presence of a potential fourth connected stage (and therefore an eight-stage switching sequence) if held for longer than infinitesimal time duration, which is explored in Section 2.3.5.

2.3.4 Simplified Switch Implementations

Fig. 2-4 shows active switch implementations for all switches, but at least one switch in each topology can be replaced with a diode to reduce control complexity. There are two zero crossings for i_L each cycle, and a switch that turns off at a zero crossing to satisfy the i_L constraints in Table 2.4 can be implemented with a diode if it also blocks voltage in the appropriate direction. This is the case for one switch each in Figs. 2-4(f)-(i), reducing the number of active switches to two (counting the bidirectional blocking pair as one switch) for these topologies. Topologies (a), (b), (d), and (e) can also be reduced to only two active switches for certain switching sequences, with the other two switches realized with diodes. These implementations require (and help ensure) soft switching with the current constraints in Table 2.4, which greatly reduces the complexity imposed by those constraints. All topology and switching sequence combinations that can be implemented using only two active switches are distinguished with (*) next to their topologies in Table 2.4.

2.3.5 Expansion to Eight-Stage Switching Sequences

As discussed in Section 2.3.3, achieving ZVS with a six-stage switching sequence in topologies with two switch nodes (Figs. 2-4(a)-(e)) requires splitting an open stage into two sections, allowing the two terminal nodes to change voltage sequentially. The infinitesimal-duration boundary between these two sections is constrained at a defined V_p, which suggests the potential for a fourth connected stage at that point (creating an eight-stage switching sequence). Notably, if all modified six-stage switching sequences are expanded to include this specific fourth connected stage, *all sequences for a given topology yield the same eight-stage switching sequence* (same stages in the same order). Thus, all six-stage sequences proposed herein are different segments of only three eight-stage sequences:

- Figs. 2-4(a)-(b): V_{in}, V_{in}-V_{out}, Zero, V_{out} (Fig. 2-10)
- Figs. 2-4(c)-(d): V_{in}, Zero, V_{out}-V_{in}, V_{out}
- Figs. 2-4(e): V_{in}, V_{in}-V_{out}, -V_{out}, Zero

This relationship between a topology's six-stage and eight-stage sequences suggests a multi-dimensional space of operating modes with varying durations for each of the four potential connected stages. The six-stage sequences can be considered the boundaries for this space, and the eight-stage sequence spans the region from one boundary to another. Therefore, the efficiency comparison of six-stage switching sequences conducted in Section 2.5 compares the extremes of this space and points to the corners of it that most effectively use the PR. Intentional use of the eight-stage sequence provides added flexibility for tuning and an additional degree of freedom for regulation while maintaining soft charging, ZVS, and positive instantaneous power flow. The concept of an eight-stage sequence has been previously explored in the context of resonant switched-capacitor converters [59], and we employ it as part of a PR-based regulation stage in Chapter 5.

To search for other potential eight-stage sequences, we enumerate sequences for each topology structure as suggested in Section 2.2.6. This yields 8 sequences for each of the 3 structures (24 total), but only the 3 eight-stage sequences listed above survive downselection for one PR resonant cycle and enforcement of energy/charge balance.

2.4 Periodic Steady-State Operation

The periodic steady-state operation of these converter implementations can be visualized using state planes and is fully specified by a *periodic steady-state solution*. We describe these tools herein and discuss their utility for obtaining switching times for simulation and estimating efficiency.

2.4.1 State Plane Representation

The exact operation of the switching sequences detailed in Section 2.3 can be described by the trajectories of the PR's states; this is commonly leveraged in resonant converter analysis [60–64]. During each stage of a switching sequence, the PR resonates in one of three equivalent resonant circuits shown in Fig. 2-5. The PR's states at the end of a given stage

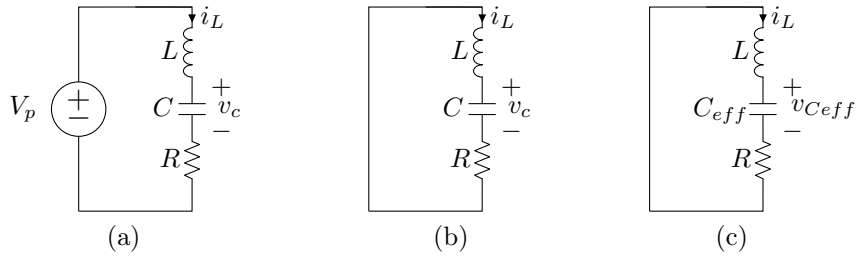

Figure 2-5: Resonant circuits for (a) connected stages, (b) zero stages, and (c) open stages.

equal the initial states for the next stage, and we can visualize the PR's states across the entire switching period with a pair of state planes as shown in Fig. 2-6.

In Fig. 2-6, the i_L vs. v_p state plane lends intuition for how the PR interacts with the source-load system, and the i_L vs. v_c plane provides insight into how each stage maps to the PR's resonant cycle. The *starting point* of each stage is indicated by number label; the positions of these labels correspond to the numbered variable states used to solve for a periodic steady-state solution in Section 2.4.2. For periodic steady-state operation, the final variable states must equal the initial variable states, creating complete loops on the state planes. For high efficiency, v_p must resonate to exactly V_p for the next connected/zero stage in time for that stage to begin (for soft charging of C_p), and all stages must have unidirectional i_L (for minimal charge circulation). The state planes of Fig. 2-6 correspond to the time-domain waveforms of Fig. 2-7, which exhibit these desired behaviors.

During all connected/zero stages (1, 3, and 5) on the state planes, v_p stays constant (V_p) at some combination of $\pm V_{in}$, $\pm V_{out}$, and 0 depending on the PR terminal connections. L and C resonate in the equivalent circuit of Fig. 2-5(a) or 2-5(b), with i_L and v_c exhibiting LC-normalized circular arcs (if with no loss) around a center point of (0, V_p) on the i_L vs. v_c plane. i_L reflects the same vertical change on the i_L vs. v_p plane at constant V_p. The PR acquires and releases energy during connected stages, and whether its energy increases or decreases depends on the polarities of V_p and i_L.

During all open stages (2, 4, and 6), all three state variables participate in resonance, and the effective capacitance reduces to the series combination of C_p and C:

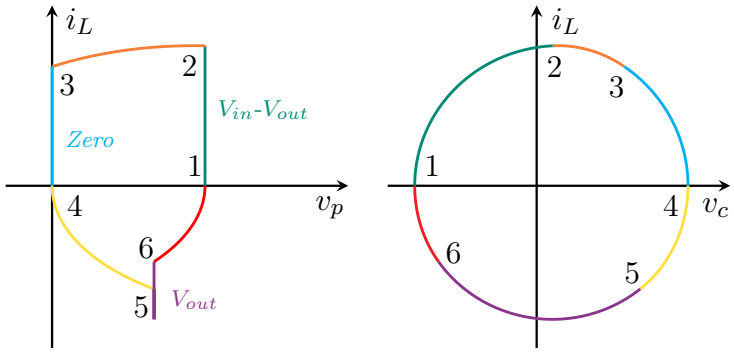

Figure 2-6: State plane example for switching sequence V_{in}-V_{out}, *Zero*, V_{out} with $V_{in} = 100$ V, $V_{out} = 40$ V, and $P_{out} = 6$ W. Numbers 1-6B correspond to the time-domain points indicated in Fig. 2-7. PR parameters: Table 2.5.

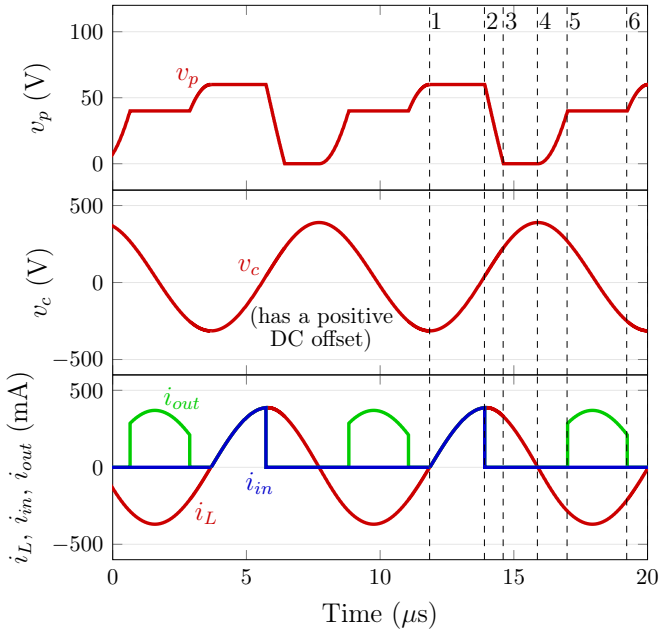

Figure 2-7: Time-domain waveforms for switching sequence V_{in}-V_{out}, *Zero*, V_{out} with $V_{in} = 100$ V, $V_{out} = 40$ V, and $P_{out} = 6$ W. Numbers 1-6B correspond to the state transition points in Fig. 2-6.

$$C_{eff} = \frac{C_p C}{C_p + C} \tag{2.8}$$

The center of resonance on the state plane during open stages is less straightforward. i_L is still centered around 0, and the center of resonance for v_{Ceff} is also 0, yielding the resonant circuit in Fig. 2-5(c). This mandates that the center of resonances (V_o) for v_p and v_c both

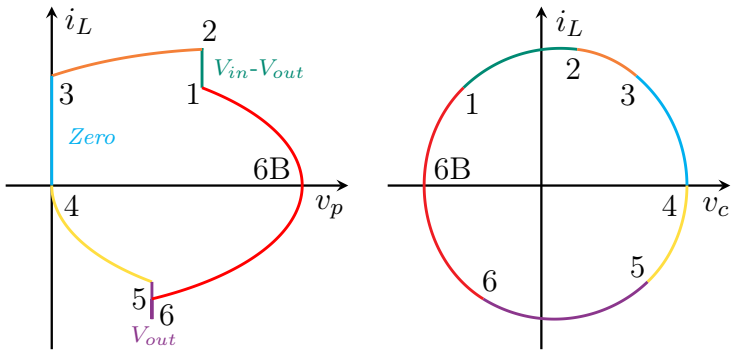

Figure 2-8: State plane example for soft-switched sequence V_{in}-V_{out}, *Zero*, V_{out} with V_{in} = 100 V, V_{out} = 40 V, and P_{out} = 6 W. Numbers 1-6B correspond to the time-domain points indicated in Fig. 2-9. PR parameters: Table 2.5.

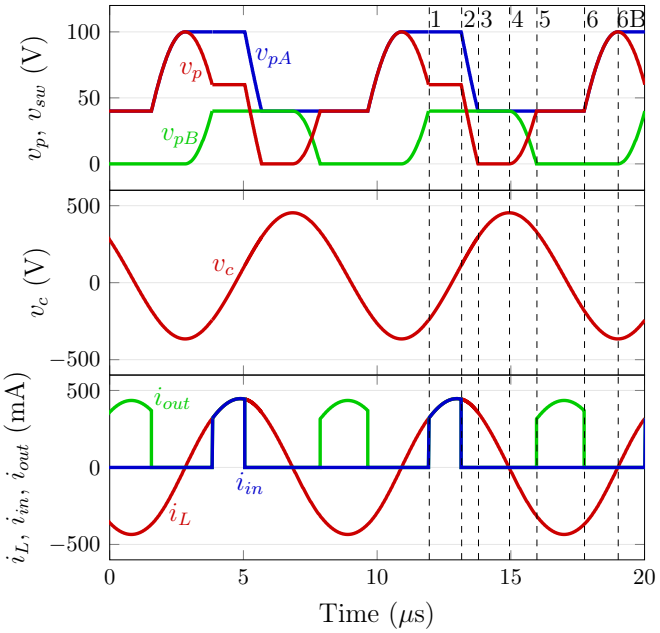

Figure 2-9: Time-domain waveforms for soft-switched sequence V_{in}-V_{out}, *Zero*, V_{out} with V_{in} = 100 V, V_{out} = 40 V, and P_{out} = 6 W. v_{pA} and v_{pB} refer to the switch nodes between S1, S2 and S3, S4, respectively, in Fig. 2-17. Numbers 1-6B correspond to the state transition points in Fig. 2-8.

be equal to the following function of capacitance and initial states for the stage, using stage 2 as an example (full derivation below):

$$V_o = \frac{C_p v_{p2} + C v_{c2}}{C_p + C} \tag{2.9}$$

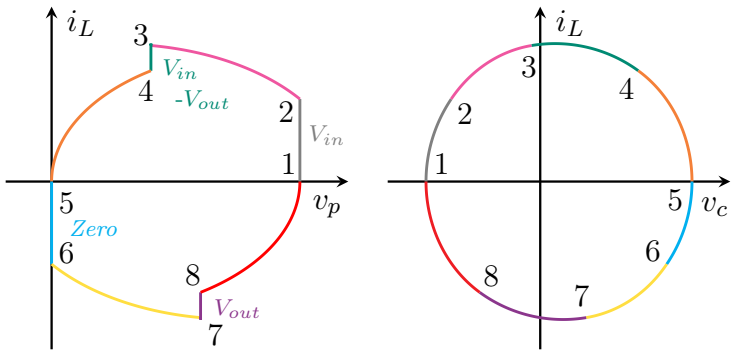

Figure 2-10: State plane example for sequence V_{in}, V_{in}-V_{out}, *Zero*, V_{out} with V_{in} = 100 V, V_{out} = 60 V, and P_{out} = 6 W. PR parameters: Table 2.5.

Table 2.5: Assumed PR Model Parameters

Parameter:	C_p	L	C	R	f_{res}
Value:	4.3 nF	1.4 mH	1.4 nF	$\leq$ 2.4 Ω	114 kHz

The C_p terms in the above equations can be modified to include parasitic capacitance if desired, which is described in Section 2.4.5. R does not affect the center of resonance for either connected or open stages, but it does damp the resonance (and therefore dissipates energy) during both.

In Fig. 2-8, we illustrate how the V_{in}-V_{out}, *Zero*, V_{out} switching sequence may be modified for ZVS as described in Section 2.3.3, assuming topology (a) of Fig. 2-4. During its two-segment sixth stage, this implementation must resonate v_p up to V_{in} for ZVS turn-on of S1 (at point 6B) before reducing v_p to V_{in}-V_{out} for soft switching of S3. The corresponding time-domain waveforms are shown in Fig. 2-9.

In Fig. 2-10, we illustrate the expansion of Fig. 2-8 into an eight-stage sequence as described in Section 2.3.5. The additional degree of freedom allotted by the eight-stage sequence may be constrained for symmetry between the positive and negative halves of the i_L cycle as described in Section 5.3, simplifying control requirements.

Open Stage Center of Resonance Derivation

The center of resonance on a state plane for v_p and v_c during open stages (denoted V_o) can be derived from the energy stored in C_p and C that does not participate in the open-stage resonance. This is calculated by subtracting the energy in C_{eff} from the energy in C_p and C at the beginning of the open stage (dependent on the variable states when the stage begins) as follows, using stage 2 in Fig. 2-6 as an example:

$$E_{Ceff} = \frac{1}{2}C_{eff}(v_{p2} - v_{c2})^2 \tag{2.10}$$

$$E_{Cp} + E_C = \frac{1}{2}C_p v_{p2}^2 + \frac{1}{2}C v_{c2}^2 \tag{2.11}$$

$$E_{Cp} + E_C - E_{Ceff} = \frac{(C_p v_{p2} + C v_{c2})^2}{2(C_p + C)} \tag{2.12}$$

The center of resonance V_o is then the voltage for which the energy in C_p and C equal this value:

$$\frac{1}{2}C_p V_o^2 + \frac{1}{2}C V_o^2 = \frac{(C_p v_{p2} + C v_{c2})^2}{2(C_p + C)} \tag{2.13}$$

$$\Rightarrow V_o = \frac{C_p v_{p2} + C v_{c2}}{C_p + C} \tag{2.14}$$

To consider parasitic capacitances in the circuit, C_p can be modified as described in Section 2.4.5.

2.4.2 Ideal Periodic Steady-State Solution

Quantifying variable states and their exact locations on a state plane requires solving the multi-stage system for periodic steady state. The ideal version of this solution (neglecting R) can be obtained with light computation and provides a close estimate of the exact solution to the extent that $R \to 0$. The exact periodic steady-state solution (considering R) must be obtained numerically as described in Section 2.4.4. The below analysis does not consider

the effects of parasitic capacitances in the circuit (e.g., switch capacitances); these can be added by modifying C_p as described in Section 2.4.5.

We can solve for the ideal periodic steady-state solution for a given switching sequence using equations that enforce CoE and CoC across the switching cycle, assuming the final variable states equal the initial variable states and that v_p always reaches the voltage necessary to soft-charge C_p. These equations rely only on the state variable values at each switching stage transition point, with their subscript numbers indicating the stage that follows (corresponding to the number labels in Fig. 2-6). Since v_p is defined for each of these points, there are two total variables for each stage (v_c and i_L).

Connected stages have the following CoE constraint, where v_p is defined (V_p) based on the PR's terminal connections. Intuitively, V_p can be considered the DC voltage offset for C as it resonates with L.

$$C(v_{c1} - V_p)^2 + Li_{L1}^2 = C(v_{c2} - V_p)^2 + Li_{L2}^2 \tag{2.15}$$

Open stages for the PR have both a CoE constraint and a CoC constraint since v_p changes through resonance with the PR's other elements.

$$C_p V_{p2}^2 + Cv_{c2}^2 + Li_{L2}^2 = C_p V_{p3}^2 + Cv_{c3}^2 + Li_{L3}^2 \tag{2.16}$$

$$C_p(V_{p3} - V_{p2}) = -C(v_{c3} - v_{c2}) \tag{2.17}$$

These equations can be solved using an analytic solver constrained by the i_L polarity requirements in Section 2.3.2. Six-stage sequences have three connected stages and three open stages, which translate to nine total equations and twelve variables. Then, the i_L zero crossing constraints displayed in Table 2.4 must be added, creating a fully constrained periodic steady-state system assuming V_{in}, V_{out}, and P_{out} are specified. Solving this ideal periodic steady-state system is exemplified in the first part of the script provided in Appendix A.1.1.

2.4.3 Ideal Switching Times

Once an ideal periodic steady-state solution has been obtained, the time duration of each stage can be calculated using the exact variable states at each stage transition. A simple strategy for this involves multiplying the resonant period of a given stage's equivalent circuit times the proportion of its resonant period completed during the stage. For a connected stage, this translates to calculating the angle between the two vectors created by the stage's start and end points (both referenced to the center of resonance (V_p,0)) on the i_L vs. v_c normalized state plane. If a connected stage occurs in only one quadrant of the state plane, that angle can be calculated and used to calculate the stage's time duration as follows:

$$t_1 = \sqrt{LC}\left(\tan^{-1}\left(\frac{i_{L2}\sqrt{L/C}}{v_{c2} - V_p}\right) - \tan^{-1}\left(\frac{i_{L1}\sqrt{L/C}}{v_{c1} - V_p}\right)\right) \tag{2.18}$$

Similarly, the time duration of an open stage can be calculated using the angle between the vectors created by the stage's i_L and inductor voltage (V_p-v_c) start and end points (both referenced to (0,0)). This takes the following form for an open stage in one quadrant of the i_L vs. V_p-v_c state plane, and can then be multiplied by the LC_{eff} resonant period to calculate time duration:

$$t_2 = \sqrt{LC_{eff}}\left(\tan^{-1}\left(\frac{i_{L3}\sqrt{L/C_{eff}}}{V_{p3} - v_{c3}}\right) - \tan^{-1}\left(\frac{i_{L2}\sqrt{L/C_{eff}}}{V_{p2} - v_{c2}}\right)\right) \tag{2.19}$$

For any stage that spans more than one quadrant of the state plane, this strategy for calculating stage time duration still applies but one must consider each quadrant when calculating the angle between the vectors.

This strategy for calculating ideal switching times is utilized in the script of Appendix A.1.1.

2.4.4 Exact Periodic Steady-State Solution

The periodic steady-state solution obtained in Section 2.4.2 does not consider the effects of R. Adding power dissipation terms to the CoE equations requires time-domain integration of i_L^2, which is complex to implement using only the transition point state variables in the

ideal system of equations. Instead, if an exact periodic steady-state solution considering R is desired, the time-domain system of differential equations governing the PR's states can be solved symbolically for each stage (producing solutions with complex exponentials) and assembled into a system of equations representing the whole switching sequence. Then, this system of equations can be solved numerically *using the ideal periodic steady-state solution as its starting point*, which is vital for reliable convergence.

Connected stages can be described by the following differential equations, where v_p is constant (V_p):

$$\frac{dv_c}{dt} = \frac{i_L}{C} \tag{2.20}$$

$$\frac{di_L}{dt} = \frac{V_p - v_c - Ri_L}{L} \tag{2.21}$$

Open stages have these same equations plus an additional equation to describe the change in v_p.

$$\frac{dv_p}{dt} = \frac{-i_L}{C_p} \tag{2.22}$$

With two equations for each connected stage and three equations for each open stage, this time-domain system has fifteen equations for a six-stage switching sequence. Its unknowns are the same transition point variable states plus the six time durations of each stage, amounting to 18 total variables. This method for obtaining an exact periodic steady-state solution considering R is much more computation-heavy than the ideal solution and should therefore only be pursued if an exact solution is absolutely necessary. We have utilized an exact periodic steady-state solution to calculate and compare expected PR efficiencies in Section 2.5.5, and an example implementation of its solver is provided in Appendix A.1.1.

2.4.5 Considering Parasitic Capacitance

In a realistic implementation, there are additional parasitic capacitances (e.g., switch capacitances) between each switch node and ac ground. These capacitances do not affect resonant

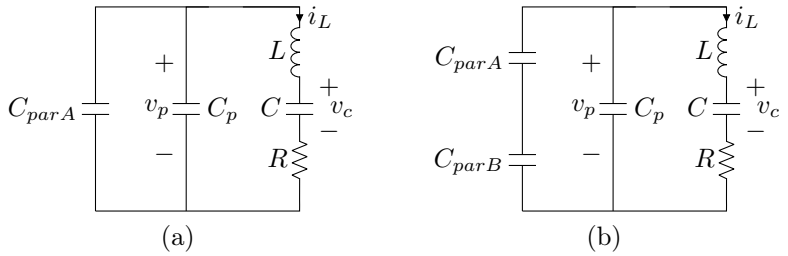

Figure 2-11: Resonant circuits considering parasitic capacitances at (a) one PR terminal and (b) both PR terminals.

behavior during connected stages, but they can play a significant role in the resonance of open stages. Fig. 2-11 contains the open stage resonant circuits when parasitic capacitances are present at one or both terminals of the PR, where C_{parA} and C_{parB} are the sums of all capacitances between switch nodes A or B (respectively) and ac ground. To consider these capacitance in the analysis herein, C_p can be modified to include them as follows:

$$C_{p+A} = C_p + C_{parA} \tag{2.23}$$

$$C_{p+A+B} = C_p + \frac{C_{parA}C_{parB}}{C_{parA} + C_{parB}} \tag{2.24}$$

2.5 PR Utilization, Amplitude of Resonance, and Efficiency

The efficiency of a PR-based converter depends on not only on the PR's properties (e.g., material, dimensions, mounting, etc.) but also how effectively its implementation uses it to process energy. To evaluate this, we examine the charge displacement pattern of each switching sequence with respect to the PR's resonant cycle and its implications for the PR's amplitude of resonance and energy processing capability.

2.5.1 Charge Transfer Utilization Factor

The efficiency of a PR-based converter depends on not only on the PR's properties (e.g., material, dimensions, loss factors, etc.) but also how effectively its implementation uses it to process energy. To evaluate this, we examine the charge transfer pattern of each switching sequence with respect to the PR's resonant cycle and its implications for the PR's amplitude of resonance and energy processing capability.

The proposed implementations in Table 2.4 vary widely in how they utilize the PR's resonant cycle. For $V_{in} > V_{out}$, some sequences such as V_{in}-V_{out}, *Zero*, V_{out} spend the majority of the PR resonant cycle delivering energy to the load (i.e., energy is delivered during both positive and negative i_L), while others such as V_{in}, -V_{out}, *Zero* devote more than an entire half-cycle to open and zero stages.

Productive use of the PR's resonant cycle can be quantified with a "charge transfer utilization factor", K, which we define as the proportion of all connected/zero stage charge displacement that is delivered to the output for $V_{in} > V_{out}$ or sourced from the input for $V_{out} > V_{in}$. This fraction can be simplified to a function of only V_{in} and V_{out} using the CoE and CoC equations for a given sequence.

Here we derive K for sequence V_{in}, V_{in}-V_{out}, V_{out}, which delivers charge to the output during stages 3 and 5:

$$K = \frac{|q_3| + |q_5|}{|q_1| + |q_3| + |q_5|} = \frac{|q_3| + |q_5|}{2|q_5|} \tag{2.25}$$

An expression for q_3 as a function of q_5 can be derived from CoE-CoC expression (2.7), re-written with q_3 and q_5:

$$V_{in}(|q_5| - |q_3|) + (V_{in} - V_{out})|q_3| - V_{out}|q_5| = 0 \tag{2.26}$$

$$\Rightarrow |q_3| = \frac{V_{in} - V_{out}}{V_{out}}|q_5| \tag{2.27}$$

Inserting (2.27) into (2.25) yields K as a function of V_{in} and V_{out}:

$$K = \frac{V_{in}}{2V_{out}} \tag{2.28}$$

The K expressions derived for all of the switching sequences are displayed in the rightmost column of Table 2.4. A higher charge transfer utilization factor K implies that a switching sequence's connected stages use the PR's resonant cycle more effectively, requiring less charge circulation to deliver the same quantity of energy to the load.

2.5.2 Total Charge Transfer

The total charge that must be displaced by the PR during each resonant cycle can be partitioned into charge transfer required of connected/zero stages (Q_{conn}) and open stages (Q_{open}). The charge that must be displaced by i_L during only the connected/zero stages (Q_{conn}) of a switching sequence is the following function of K:

$$Q_{conn} = \frac{Q_{out}}{K} = \frac{E_{out}}{KV_{out}} = \frac{P_{out}}{fKV_{out}} \tag{2.29}$$

Open stages do not deliver charge to the output but collectively charge/discharge C_p across its full voltage range V_{pp}, so the charge displaced by i_L during open stages is:

$$Q_{open} = 2C_pV_{pp} \tag{2.30}$$

Thus, the total magnitude of charge that must be displaced by i_L during each resonant cycle (Q_{total}) is the sum:

$$Q_{total} = Q_{conn} + Q_{open} = \frac{P_{out}}{fKV_{out}} + 2C_pV_{pp} \tag{2.31}$$

These charge transfer calculations enable estimation of several PR energy and efficiency characteristics as explored in the remainder of this section. If desired, the effects of parasitic capacitances can be added by modifying C_p as described in Section 2.4.5.

2.5.3 Amplitude of Resonance Model

The magnitude of charge displaced by i_L each resonant cycle (Q_{total}) can be extended to estimate the PR's maximum i_L, denoted as I_L. I_L can be considered a metric for the PR's amplitude of resonance, which has implications for energy storage, loss, and efficiency. PRs

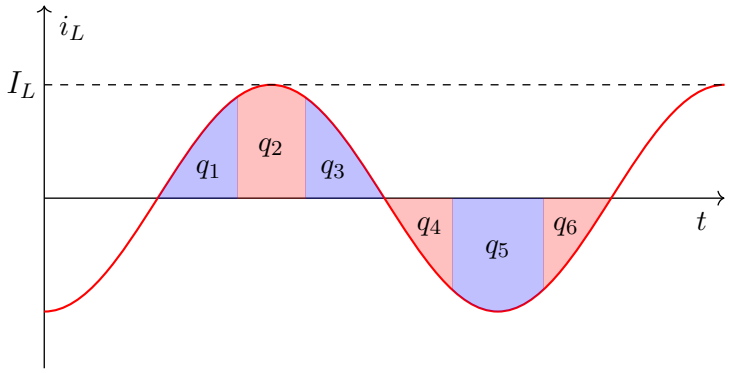

Figure 2-12: Sinusoidal approximation of i_L based on the charge transfer q_n required of each stage. Amplitude I_L is the "amplitude of resonance".

tend to have very high quality factors, so we approximate i_L to be sinusoidal as shown in Fig. 2-12. I_L can then be calculated by equating Q_{total} to the integral of i_L:

$$Q_{total} = 2\int_0^{\frac{1}{2f}} i_L dt = 2\int_0^{\frac{1}{2f}} I_L \sin(2\pi f t) dt = \frac{2I_L}{\pi f} \tag{2.32}$$

$$\Rightarrow I_L = \frac{\pi}{2} f Q_{total} = \pi\Big(\frac{P_{out}}{2KV_{out}} + fC_pV_{pp}\Big) \tag{2.33}$$

This I_L expression provides key insight into the factors that determine the PR's amplitude of resonance. Only the open stage term in this equation is dependent on PR parameters; the connected/zero stage term depends exclusively on the operating point and switching sequence. For a given PR and operating point, a higher charge transfer utilization K results in the same P_{out} delivery with a lower I_L. Also, I_L increases as P_{out} increases and vice-versa.

Fig. 2-13 plots I_L as a function of voltage conversion ratio for constant P_{out} in the step-down case and reveals significant variability with respect to the K values in Table 2.4. I_L generally increases as the voltage conversion ratio decreases, which is more drastic as V_{out} is varied since $\frac{P_{out}}{V_{out}}$ also increases in that case. $K{=}\frac{V_{in}}{2(V_{in}-V_{out})}$ and $K{=}\frac{V_{in}}{2V_{out}}$ clearly produce the lowest I_L for both the constant-V_{in} and constant-V_{out} sweeps. Thus, switching sequences associated with these K values require the lowest-amplitude resonance of the PR for the same P_{out}.

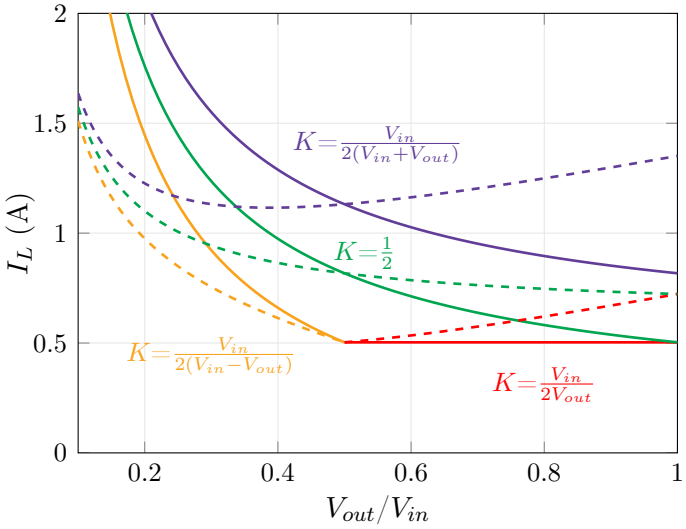

Figure 2-13: I_L vs. $\frac{V_{out}}{V_{in}}$ for various K as calculated in (2.33) with constant $V_{in} = 100$ V (solid lines) or constant $V_{out} = 50$ V (dashed lines). $P_{out} = 10$ W, $V_{pp} = V_{in}$, and f (assumed f_{res}) and C_p correspond to the PR in Table 2.5.

2.5.4 Energy Storage and Loss

I_L is the value of i_L at its assumed-sinusoidal peak, which is the point in the resonant cycle at which L holds all of the energy stored in the PR's LCR branch. Thus, the mechanical energy stored in the PR (E_{stored}) for a given switching sequence and operating point can be estimated using:

$$E_{stored} \approx \frac{1}{2} L I_L^2 \tag{2.34}$$

Similarly, the mechanical energy lost during each cycle of the PR (E_{loss}) can be estimated using I_L as follows:

$$E_{loss} \approx \int_0^{\frac{1}{f}} i_L(t)^2 R dt = \int_0^{\frac{1}{f}} (I_L \sin(2\pi f t))^2 R dt = \frac{1}{2f} I_L^2 R \tag{2.35}$$

Minimizing I_L translates to less energy storage and loss, both of which are proportional to I_L^2. Thus, I_L can be used as a general metric for comparing energy processing capability during the design process, with lower I_L values for a given operating point being more desirable for high efficiency.

2.5.5 Exact Efficiency Comparison

To further evaluate the proposed implementations in Table 2.4, we calculate and compare PR efficiency using the exact periodic steady-state solution considering R described in Section 2.4.4. The result confirms the implications of (2.33) and (2.35) and shows their utility for calculating an efficiency approximation that compares closely with the exact solution.

Fig. 2-14 plots calculated PR efficiency (only the PR - not the full converter) as a function of voltage conversion ratio for a given PR and fixed power when used in each of the configurations listed in Table 2.4. These calculations are made based on the exact periodic steady-state solution of Section 2.4.4, assuming the measured PR parameters in Table 2.5. Fig. 2-14 reveals significant efficiency differences among the implementations, but these variations align with the characteristics that minimize I_L in (2.33), especially K. High efficiency tends to be correlated with:

- Connected stages involving V_{out} (for $V_{in} > V_{out}$) or V_{in} (for $V_{out} > V_{in}$) spanning a greater portion of the PR resonant cycle.
- No zero stage, or minimal zero-stage charge transfer.
- Less charge transfer during open stages (i.e. smaller V_{pp}).

Sequences V_{in}, V_{in}-V_{out}, V_{out} and V_{in}-V_{out}, *Zero*, V_{out} advantageously utilize both the positive and negative i_L halves of the PR resonant cycle for energy transfer to the output, and they require the lowest V_{pp} (V_{out} as-is or V_{in} with soft switching) across the switching cycle in their operating regions. These sequences are the most effective for the step-down case, as predicted by I_L and now confirmed with exact efficiency in Fig. 2-14.

In the state plane context, sequences that have identical efficiencies as a function of voltage conversion ratio have shifted versions of the same i_L profile. For example, V_{in}, V_{in}-V_{out}, V_{out} and V_{in}-V_{out}, *Zero*, V_{out} have the same state planes rotated by 180° and V_p-shifted by V_{out}. These sequences also have the same K and V_{pp}, which is consistent with producing the same I_L for a given PR and operating point in (2.33) and therefore the same loss in (2.35).

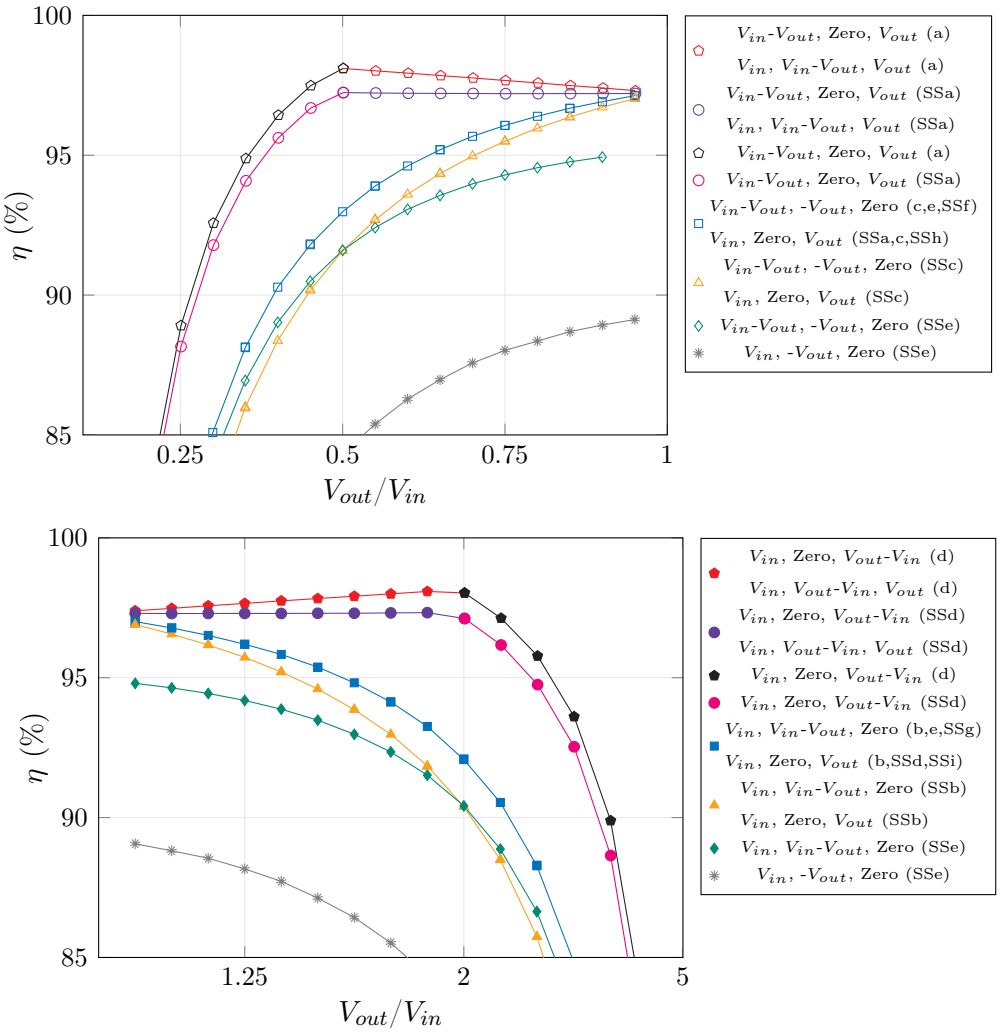

Figure 2-14: Calculated efficiency vs. $\frac{V_{out}}{V_{in}}$ of the exact periodic steady-state solution (Section 2.4.4) for the PR in Table 2.5 when used in the proposed implementations of Table 2.4. Max(V_{in},V_{out}) = 100 V and P_{out} = 10.0 W. The line markers each correspond to specific switching sequences, topologies, and potential modifications for soft switching (denoted with 'SS') as summarized in the legend.

Fig. 2-14 also shows that the modifications required for ZVS (denoted by 'SS') in topologies Fig. 2-4(a)-(e) result in a slight efficiency drop for the PR, which can be attributed to the additional v_p swing in the two-part open stage (and therefore higher V_{pp} in (2.33)). This v_p swing warrants additional charge transfer during open stages, requiring a higher I_L (and therefore higher loss in the PR) for the same energy transfer to the load. Thus, a trade-off exists between this PR efficiency drop and the loss that would be incurred by hard switching

in these topologies.

It should be noted that the proportion of energy output per cycle that is directly transferred from V_{in} to V_{out} during the same connected stage (and therefore not stored in the PR) was *not* found to be deterministic for high efficiency; this is further explored below.

Proportion of Direct Energy Transfer

The proportion of direct energy transfer for a given switching sequence and operating point can be derived using the same CoE and CoC concepts used in Section 2.2.4. In one cycle, sequence V_{in}-V_{out}, Zero, V_{out} delivers $V_{out}|q_1|$ directly from input to output and $V_{out}|q_5|$ to the output from energy stored in the PR. Thus, the proportion of direct energy transfer is $\frac{|q1|}{|q1|+|q5|}$. This can be derived from the CoE equation for V_{in}-V_{out}, Zero, V_{out} as follows:

$$(V_{in} - V_{out})|q_1| = V_{out}|q_5| \tag{2.36}$$

$$\Rightarrow \frac{|q_1|}{|q_1| + |q_5|} = \frac{V_{out}}{V_{in}} \tag{2.37}$$

The same applies to V_{in}, V_{in}-V_{out}, V_{out}, whose proportion of direct energy transfer is $\frac{|q3|}{|q3|+|q5|}$. This can be derived beginning with (2.26) and results in:

$$\Rightarrow \frac{|q_3|}{|q_3| + |q_5|} = 1 - \frac{V_{out}}{V_{in}} \tag{2.38}$$

Thus, V_{in}, V_{in}-V_{out}, V_{out} and V_{in}-V_{out}, Zero, V_{out} have opposite proportions of direct energy transfer, yet still produce the same efficiency in Fig. 2-14.

2.5.6 Efficiency Estimation

To the extent that i_L is sinusoidal, the analysis of Section 2.5.4 can be extended to estimate the efficiency of an operating point using only (2.33) as follows:

$$\eta \approx \frac{P_{out}}{P_{out} + fE_{loss}} = \frac{P_{out}}{P_{out} + \frac{1}{2}I_L^2 R} \tag{2.39}$$

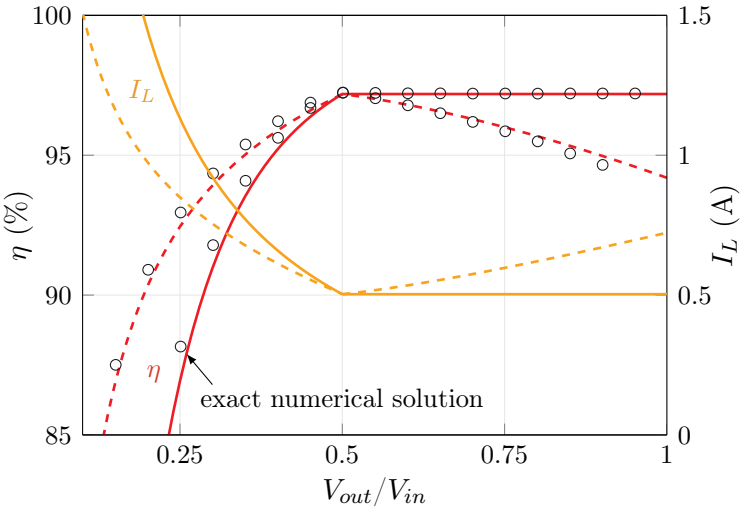

Figure 2-15: Estimated I_L (2.33) and efficiency (2.39) vs. $\frac{V_{out}}{V_{in}}$ for the PR in Table 2.5 with constant V_{in} = 100 V (solid lines) or constant V_{out} = 50 V (dashed lines). P_{out} = 10 W and $f_{assumed}$ = 131 kHz (anti-resonant frequency). The exact, numerically-solved efficiency points are overlaid on the estimated trends for direct comparison.

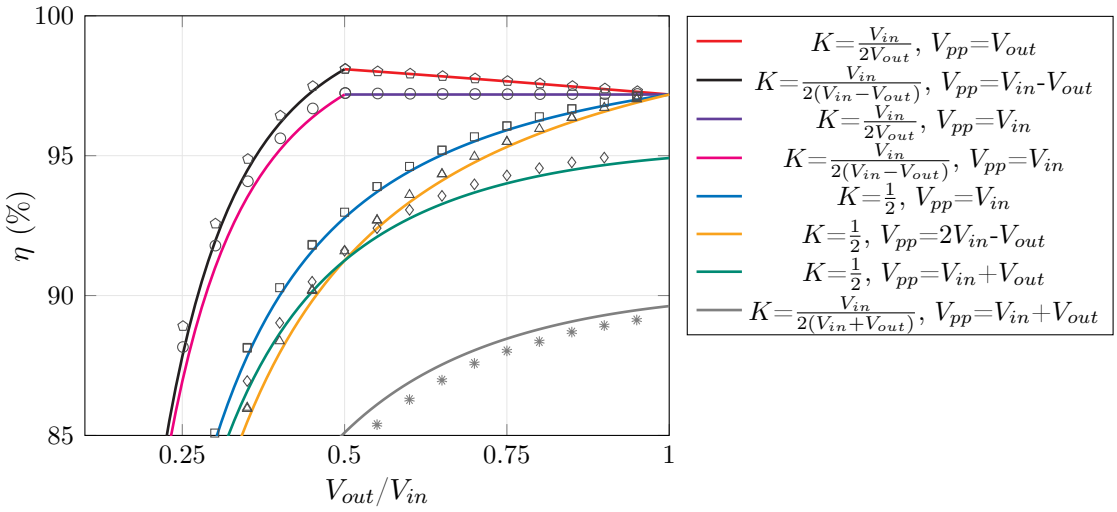

Figure 2-16: Estimated efficiency vs. $\frac{V_{out}}{V_{in}}$ using (2.39) for the PR in Table 2.5 with V_{in} = 100 V and P_{out} = 10.0 W. Different K and V_{pp} combinations are delineated by color, and the calculated points in Fig. 2-14 are overlaid on the estimated trends for direct comparison.

This relationship is illustrated in Fig. 2-15 with I_L and efficiency estimates as functions of $\frac{V_{out}}{V_{in}}$ for fixed V_{in} (solid lines) and for fixed V_{out} (dashed lines). To evaluate the validity of (2.39), the exact, numerically-obtained efficiency points are overlaid for direct comparison.

Fig. 2-15 reveals striking similarity between the two methods for predicting efficiency, attesting to the close representation of the PR's resonant behavior obtained through (2.33). This suggests that reasonable energy storage, loss, and efficiency estimations can be accessed with (2.33) without the computational burden of numerically solving the exact periodic steady-state system. Fig. 2-16 plots these estimates for the same step-down operating ranges and implementations compared in Fig. 2-14, with the points from Fig. 2-14 overlaid for direct comparison.

2.6 Example Implementation

We validate the converter implementations and analysis herein with an example design capable of realizing multiple switching sequences. This section details its construction and experimental results.

2.6.1 Prototype

We illustrate an example converter implementation using the topology in Fig. 2-4(a) and the PR modeled in Table 2.5. Table 2.4 shows that this topology serves switching sequences V_{in}-V_{out}, *Zero*, V_{out} and V_{in}, V_{in}-V_{out}, V_{out}, which have the highest K values for step-down designs and therefore the most desirable efficiencies. The soft-switched version of V_{in}-V_{out}, *Zero*, V_{out} can be reduced to just two active switches for $V_{in} > 2V_{out}$ as pictured in Fig. 2-17 while maintaining all-positive instantaneous power transfer with unidirectional-blocking switches. Thus, this implementation has both performance and practicality advantages relative to others for step-down applications.

The PR was selected based on the following criteria among available parts from APC International: (1) material with a high mechanical quality factor and (2) resonant frequency in the low hundreds of kHz (for ease of initial demonstration). We acquired samples of three off-the-shelf products, obtained estimates of their model parameter values using an impedance analyzer, solved for their relative efficiencies, and selected the APC International

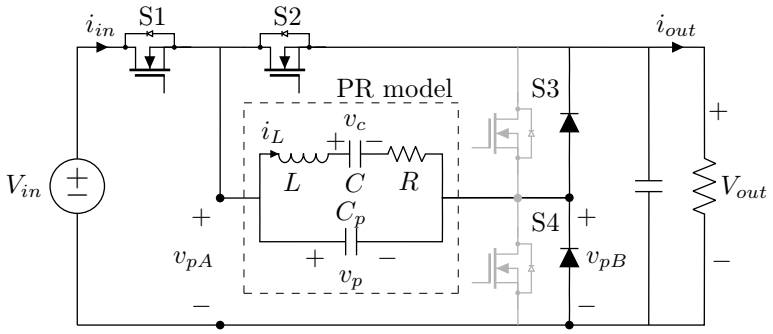

Figure 2-17: Example implementation of the topology in Fig. 2-4(a), showing S3 and S4 implemented as active switches (grayed out) or diodes.

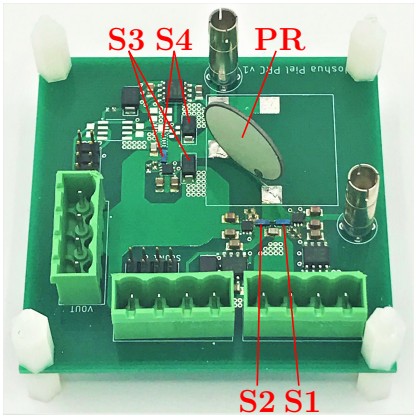

Figure 2-18: Prototype circuit board for the implementation in Fig. 2-17.

part 790 (844 material disc, diameter 19.8 mm, thickness .8 mm, radial vibration mode) as the best candidate for demonstration; the circuit model parameters for this PR are displayed in Table 2.5.

The prototype (pictured in Fig. 2-18) is implemented on a two-layer 1-oz copper board with the parts shown in Table 2.6. Its layout has parallel FET and diode footprints for S3 and S4 so either can be accommodated as shown in Fig. 2-17. We test each switching sequence using only the minimum required active switches (summarized in Table 2.7), with S3 and S4 implemented as diodes when feasible. Testing in the $\frac{V_{out}}{V_{in}} < 0.5$ region permits use of both diodes at all times. For testing in the $\frac{V_{out}}{V_{in}} > 0.5$ region, both the S3 and S4 FETs are populated but only used as listed in Table 2.7. More details about this prototype, including its PCB layout, are provided in Appendix A.3.1.

Table 2.6: Prototype Parts List

Component	Part
PR	APC International part 790
Active Switch	EPC2019 GaN FET
Schottky Diode	ON Semiconductor NRVSTA4100
Gate Driver	Texas Instruments UCC27611

Table 2.7: High-Efficiency Step-Down Switching Sequences

Switching Sequence	Voltage Conversion Range	Active Switches
V_{in}-V_{out}, *Zero*, V_{out}	$V_{in} > 2V_{out}$	S1, S2
	$2V_{out} > V_{in} > V_{out}$	S1, S2, S3
V_{in}, V_{in}-V_{out}, V_{out}	$2V_{out} > V_{in} > V_{out}$	S1, S2, S4

An isolated supply powers the gate circuitry for S1 and S2. We operate this prototype with open-loop control of all gate signals and a constant-voltage load. For each operating point, the converter's switching times are tuned for ZVS, soft charging of the PR, and all-positive instantaneous power transfer. Assuming operation is at a fixed power or frequency, there is a unique tuning point that satisfies these conditions for a six-stage sequence. The PR's properties change with temperature, so all data points are acquired at $\leq$ 40 °C and not necessarily at thermal equilibrium for higher-loss operating points.

With this prototype, only the V_{in}-V_{out}, *Zero*, V_{out} switching sequence can serve the $\frac{V_{out}}{V_{in}} < 0.5$ operating region, so we use this region to illustrate the switching sequence's functionality and validate the analysis of Sections 2.4 - 2.5. In the $\frac{V_{out}}{V_{in}} > 0.5$ region, we compare the V_{in}-V_{out}, *Zero*, V_{out} and V_{in}, V_{in}-V_{out}, V_{out} sequences and demonstrate the flexibility they provide. The eight-stage domain between these sequences in the $\frac{V_{out}}{V_{in}} > 0.5$ region is explored experimentally in Section 2.6.5.

2.6.2 Waveforms

Experimental waveforms for various operating points with $\frac{V_{out}}{V_{in}}$ less than 0.5 are displayed in Figs. 2-19 and 2-20. These waveforms greatly resemble the desired waveforms shown in Fig.

2-9, which directly compare to the operating point of Fig. 2-19(b). All waveforms exhibit ZVS and soft charging of the PR, as indicated by the resonant transitions and the exact v_p swing up to V_{in}. Some operating points have smooth waveforms, while others contain a small 2.5 MHz ripple as shown in Fig. 2-20(b) due to excitation of the PR's thickness vibration mode. Figs. 2-19(b) and 2-20(c) have nearly-identical switching times and are indistinguishable if scaled by voltage, demonstrating linear behavior in this regard. These concepts also apply to waveforms in the $\frac{V_{out}}{V_{in}} > 0.5$ operating region, some of which are displayed in Fig. 2-27 of Section 2.3.5.

Fig. 2-19 illustrates how the switching sequence adapts as $\frac{V_{out}}{V_{in}}$ decreases from 0.48 to 0.2 for the same power output. At $\frac{V_{out}}{V_{in}} = 0.48$ (Fig. 2-19(a)), the zero stage (stage 3) is almost nonexistent, and the voltage waveforms appear close to symmetric. As $\frac{V_{out}}{V_{in}}$ decreases, the zero stage becomes progressively more prominent until it dominates the V_{in}-V_{out} stage as shown for $\frac{V_{out}}{V_{in}} = 0.2$ in Fig. 2-19(c). This is how the switching sequence regulates voltage.

Fig. 2-20 shows how the switching sequence changes as power increases from 1 W (Fig. 2-20(a)) to 24 W (Fig. 2-20(c)) at the same input and output voltage. At 1 W, the connected stages are barely visible; almost all of the PR's resonant cycle is used for charge transfer during the open stages. As power increases, this charge transfer requires less time, and the connected stages become more prominent.

2.6.3 Gain

Fig. 2-21 plots the experimental $\frac{V_{out}}{V_{in}}$ as a function of frequency for different power levels in the $\frac{V_{out}}{V_{in}} < 0.5$ region. Fig. 2-25 does the same for $\frac{V_{out}}{V_{in}} > 0.5$ and shows that the two sequences serving this region operate at nearly-identical frequencies for a given operating point. For the same $\frac{V_{out}}{V_{in}}$, higher-power loads require frequencies closer to the resonant frequency (at the lower end of the frequency range). These maps illustrate how frequency may be used to regulate power at a constant $\frac{V_{out}}{V_{in}}$ or vice versa, using the final degree of freedom in the periodic steady-state solution as discussed in Section 2.4.2.

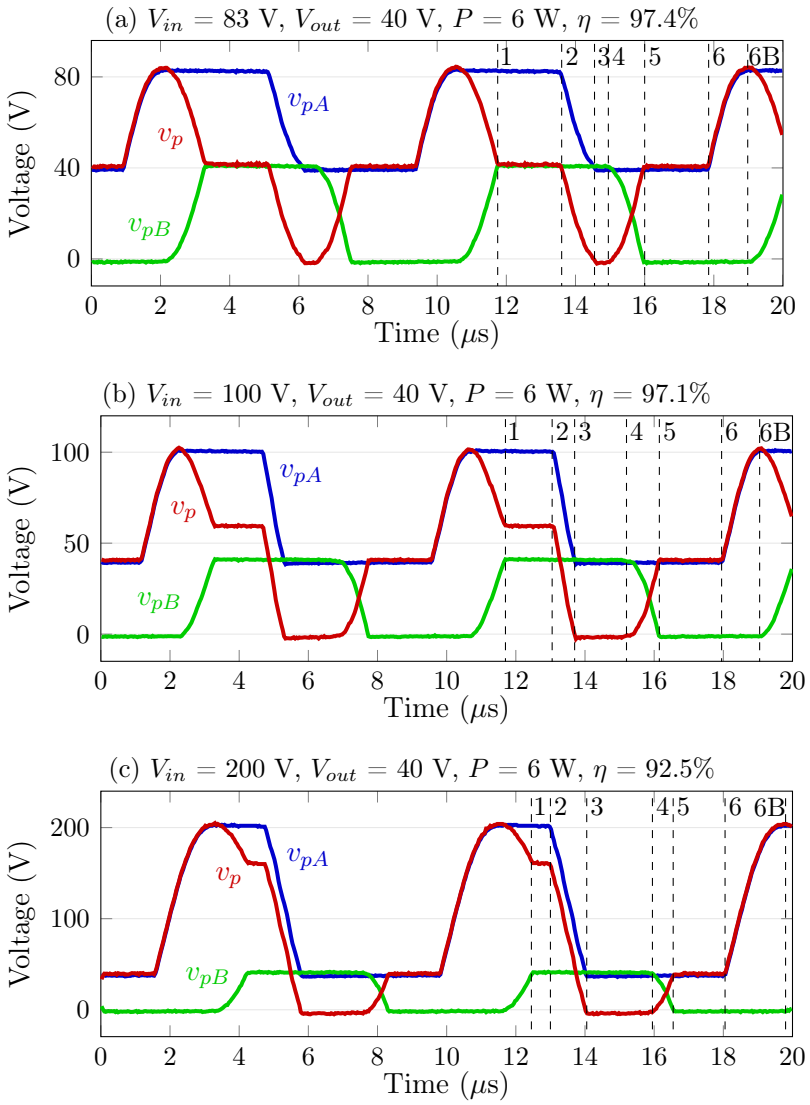

Figure 2-19: Experimental waveforms for switching sequence V_{in}-V_{out}, *Zero*, V_{out} at various $\frac{V_{out}}{V_{in}}$ with the prototype described in Section 2.6.1. Numbers 1-6B correspond to the stage transition points in Fig. 2-8.

2.6.4 Efficiency

We evaluate the prototype's performance over various $\frac{V_{out}}{V_{in}}$, load, and frequency conditions beginning with V_{in}-V_{out}, *Zero*, V_{out} in the $\frac{V_{out}}{V_{in}} < 0.5$ region. Before we discuss efficiency, it should be noted that Fig. 2-21 exhibits jagged gain curves at frequencies close to 120 kHz and 122.5 kHz, at which the PR operates in an undesired alternate vibration mode. These "spurious" modes cause downward spikes in efficiency as shown in Fig. 2-24, and

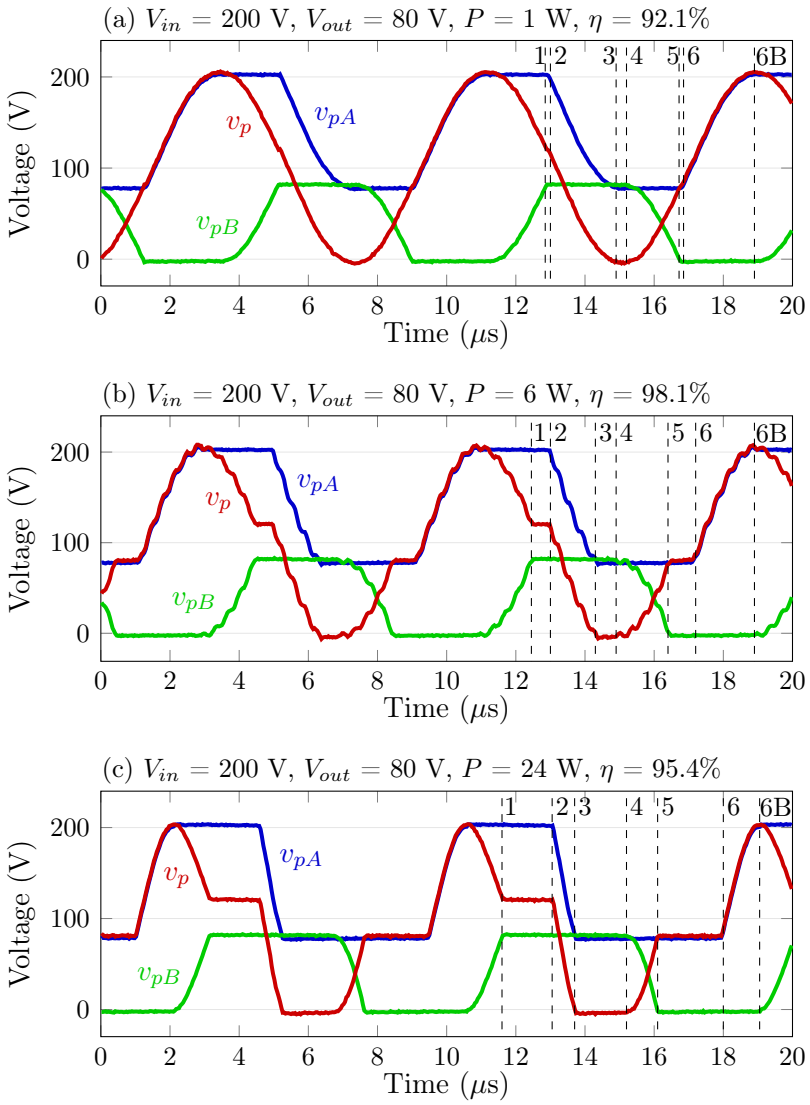

Figure 2-20: Experimental waveforms for switching sequence V_{in}-V_{out}, *Zero*, V_{out} at various power levels with the prototype described in Section 2.6.1. Numbers 1-6B correspond to the stage transition points in Fig. 2-8.

their existence depends on the PR's manufacturing variation, mounting, and other vibration modes (outside the scope of this chapter)[1]. Thus, the discussion in this section examines the observed efficiency trends ignoring these modes.

In Fig. 2-22, we plot efficiency as a function of power for different $\frac{V_{out}}{V_{in}}$ less than 0.5. Efficiency increases as $\frac{V_{out}}{V_{in}}$ approaches 0.5, which demonstrates the role of the charge transfer utilization factor K in (2.33). At $\frac{V_{out}}{V_{in}} = 0.5$, K reaches its maximum for this operating range,

[1]Efficiency drops are also observed in [58] due to harmonic content in i_L.

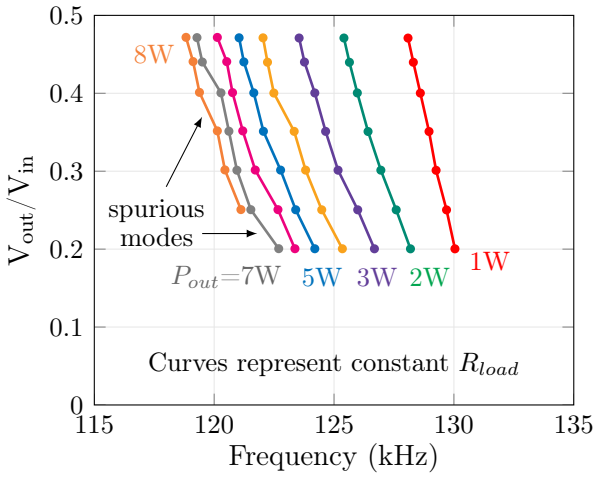

Figure 2-21: $\frac{V_{out}}{V_{in}}$ vs. frequency for different power levels (labeled) at the same V_{out} = 40 V. Same operating points as Fig. 2-22.

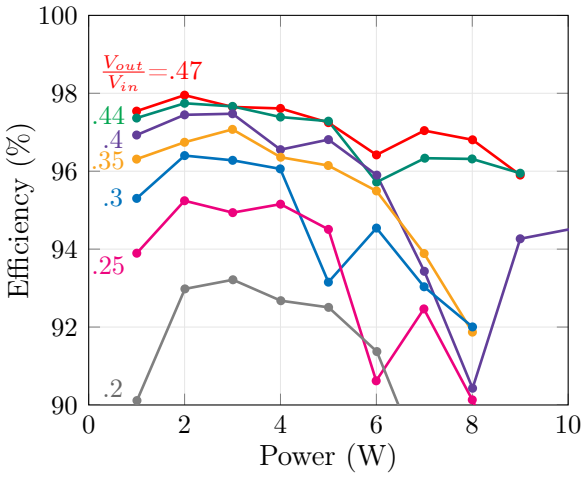

Figure 2-22: Efficiency vs. power for different $\frac{V_{out}}{V_{in}}$ ratios (labeled) at the same V_{out} = 40 V. Same operating points as Fig. 2-21.

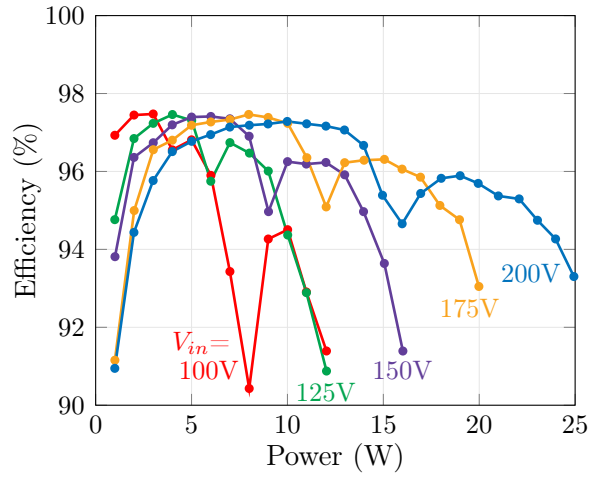

Figure 2-23: Efficiency vs. power for different input voltages (labeled) at the same $\frac{V_{out}}{V_{in}}$ = 0.4. Same operating points as Fig. 2-24.

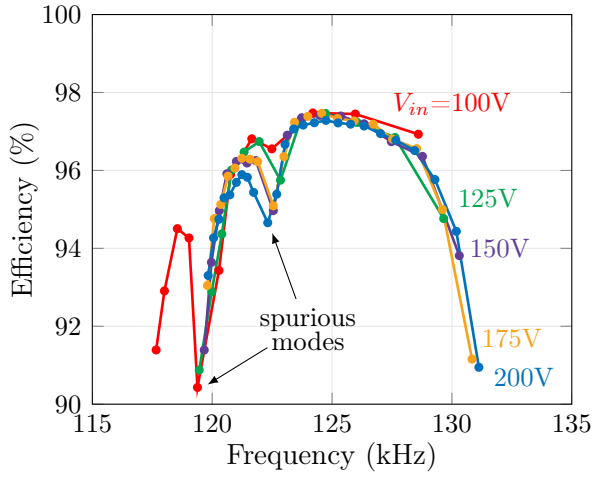

Figure 2-24: Efficiency vs. frequency for different input voltages (labeled) at the same $\frac{V_{out}}{V_{in}}$ = 0.4. Same operating points as Fig. 2-23.

which translates to lowest I_L and therefore lowest loss.

We then plot the efficiency as a function of power for various V_{in} and V_{out} combinations all with the same $\frac{V_{out}}{V_{in}}$ ratio (and therefore constant K) in Fig. 2-23. At higher voltages, higher power levels can be reached with similar efficiencies, indicating that efficiency is closely

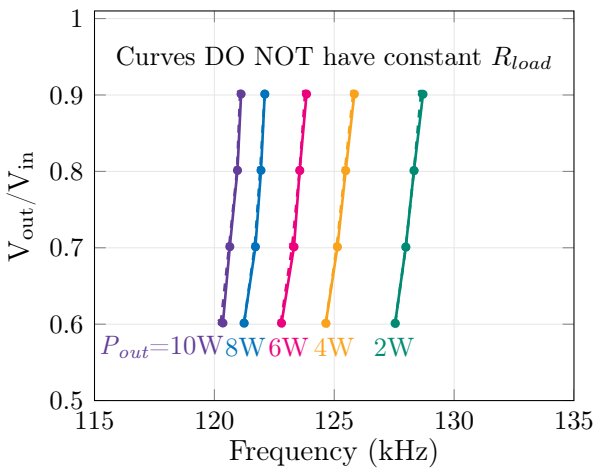

Figure 2-25: $\frac{V_{out}}{V_{in}}$ vs. frequency for different power levels (labeled) with V_{in}-V_{out}, *Zero*, V_{out} (solid lines) and V_{in}, V_{in}-V_{out}, V_{out} (dashed lines) at V_{in} = 100 V. Same operating points as Fig. 2-26.

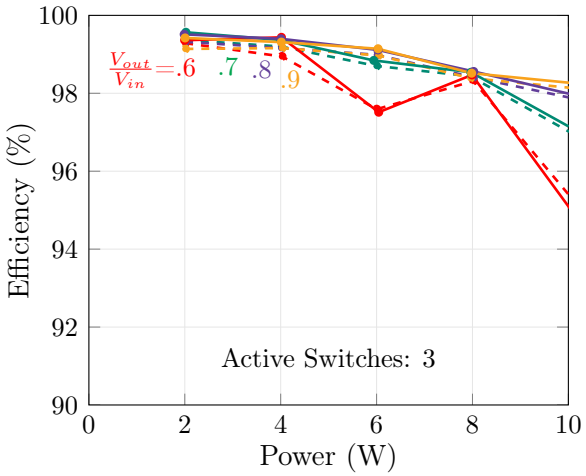

Figure 2-26: Efficiency vs. power for different $\frac{V_{out}}{V_{in}}$ with V_{in}-V_{out}, *Zero*, V_{out} (solid lines) and V_{in}, V_{in}-V_{out}, V_{out} (dashed lines) at V_{in} = 100 V. Same operating points as Fig. 2-25.

related to current. This is described by the $\frac{P_{out}}{V_{out}}$ term in (2.33), whose first term does not change as long as $\frac{P_{out}}{V_{out}}$ remains the same. The power level at which efficiency peaks also rises as voltage rises in Fig. 2-23, suggesting an "optimal" $\frac{P_{out}}{V_{out}}$ (the open stage term dominates at lower power levels and vice versa).

Fig. 2-24 contains the efficiency data in Fig. 2-23 plotted again vs. switching frequency (still all with the same $\frac{V_{out}}{V_{in}}$ and K) and reveals strikingly similar efficiency sweeps for all input/output voltage combinations. At a single frequency and $\frac{V_{out}}{V_{in}}$, both the connected stage and open stage terms in (I_L) increase linearly with voltage, as does the resulting I_L. P_{out} increases quadratically with voltage, and if loss is closely related to I_L^2, loss also increases quadratically with voltage. Thus, the same efficiency results regardless of voltage level as long as frequency and $\frac{V_{out}}{V_{in}}$ are identical. Fig. 2-24 demonstrates this behavior and therefore further validates (2.33) and the close relationship between I_L and loss.

Fig. 2-26 compares efficiency as a function of power for various $\frac{V_{out}}{V_{in}}$ greater than 0.5 for V_{in}-V_{out}, *Zero*, V_{out} (solid lines) and V_{in}, V_{in}-V_{out}, V_{out} (dashed lines) with constant V_{in}. Fig. 2-26 demonstrates that these two switching sequences have essentially identical efficiencies

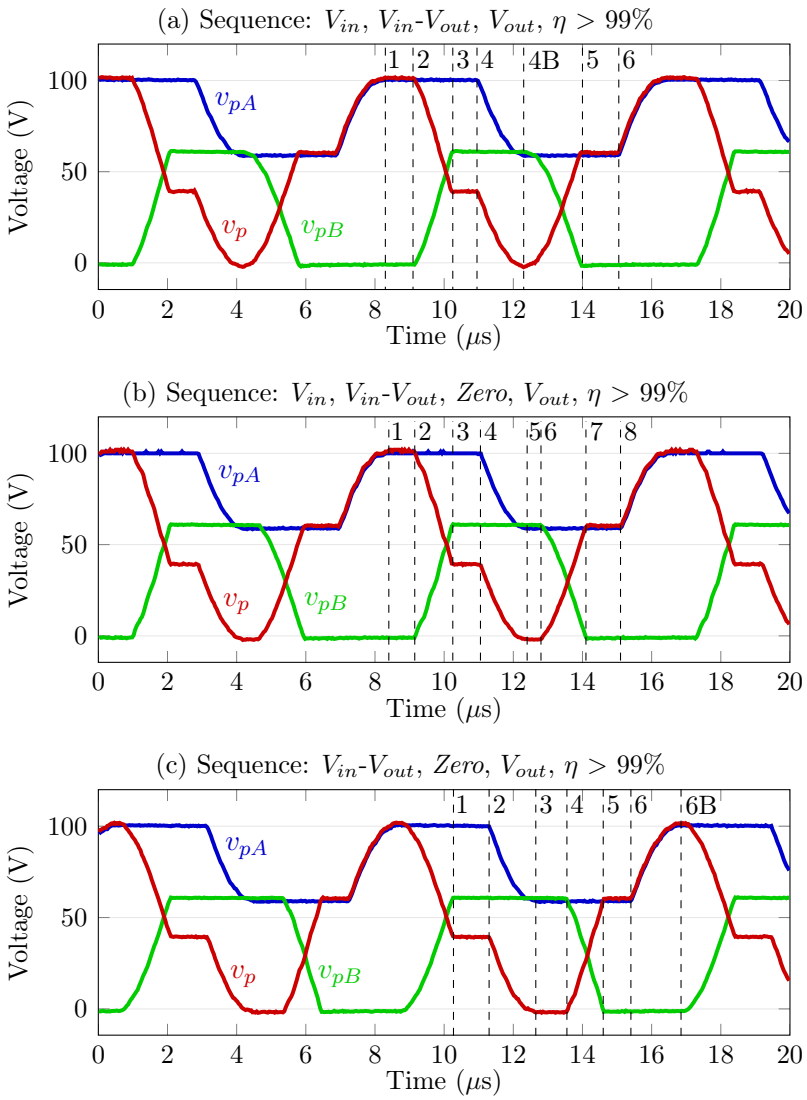

Figure 2-27: Experimental waveforms of different switching sequences for V_{in} = 100 V, V_{out} = 60 V, P = 4 W, with the prototype described in Section 2.6.1. Numbers 1-6B for (b) correspond to the stage transition points in Fig. 2-10.

even as power and $\frac{V_{out}}{V_{in}}$ vary, and that efficiency has practically no dependence on $\frac{V_{out}}{V_{in}}$ in this region of operation. Both of these behaviors again confirm the influence of K on performance; K is identical for both sequences and removes the dependence of I_L on V_{out} in this region. Thus, this PR-based converter implementation may be used in this operating region for a significant range of voltage regulation with little change in efficiency.

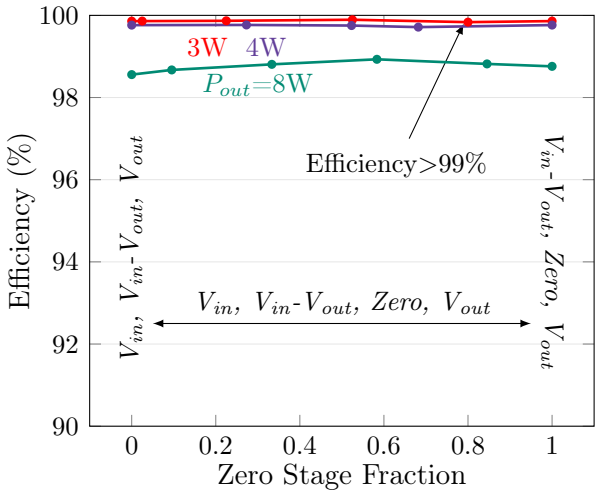

Figure 2-28: Experimental efficiency vs. zero stage fraction (1 = maximum duration) for eight-stage sequence with V_{in} = 100 V, V_{out} = 60 V, and constant power.

2.6.5 Eight-Stage Sequence

To demonstrate the V_{in}, V_{in}-V_{out}, Zero, V_{out} eight-stage sequence, we experimentally traverse the region between V_{in}-V_{out}, Zero, V_{out} and V_{in}, V_{in}-V_{out}, V_{out} while keeping V_{in}, V_{out}, and P_{out} constant. This requires incrementally increasing and decreasing the zero stage and V_{in} stage time durations and adjusting frequency to maintain a tuned operating point. Fig. 2-27(b) displays waveforms for V_{in}, V_{in}-V_{out}, Zero, V_{out}, while Figs. 2-27(a) and 2-27(c) display waveforms for the two six-stage sequences (all at the same operating point). These waveforms exhibit ZVS, soft charging of the PR, and all-positive instantaneous power transfer as desired. Fig. 2-28 plots efficiency across the continuous eight-stage region at a single operating point and shows that efficiency is virtually constant as the V_{in} and zero stages trade time duration. This aligns with the eight-stage sequence also having an identical charge transfer utilization factor K to those of the boundary six-stage sequences (K=$\frac{V_{in}}{2V_{out}}$) in this region of operation. Thus, the eight-stage region between the two six-stage sequences provides similar operating behavior with an added degree of control flexibility. The operating points of Figs. 2-27 and 2-28 engage all four of the converter's active switches (including the six-stage sequences for direction comparison), resulting in the highest reported efficiencies (>99%) for this prototype.

2.7 Conclusion

In this chapter, we have identified, analyzed, and demonstrated a set of dc-dc converter implementations capable of efficiently utilizing PRs. A systematic enumeration and downselection has revealed eight distinct six-stage switching sequences and nine practical converter topologies that rely solely on a single PR for power stage energy storage. The considered switching sequences support wide ranges of voltage conversion ratios with resonant "soft charging" of the PR's input capacitance and ZVS; this will allow efficient operation of these implementations at higher switching frequencies.

The presented analysis methods provide means to easily visualize, constrain, and evaluate the operation of these proposed implementations. Experimental testing validates that these implementations facilitate resonant soft charging of the PR's capacitance, ZVS of all switches, and minimal charge circulation, resulting in efficiencies of $\geq$96% across a wide range of operating points and peak efficiencies of >99%. The PR in this prototype is a commercially-available component, so even greater performance and power density may be reached with a PR custom-designed for power conversion, which we explore in Chapter 6. Thus, it can be concluded that PR-based converter implementations are promising alternatives to those based on traditional energy storage mechanisms and may facilitate miniaturization for high voltage, low power applications.

The work of this chapter has been published in [65–67], and these high-efficiency switching sequences (e.g., V_{in}-V_{out}, *Zero*, V_{out}) have since been utilized to achieve high performance in [68–71]. We likewise note the analyses of the V_{in}, *Zero*, V_{out} switching sequence in [58, 72] and the V_{in}-V_{out}, -V_{out}, V_{out} sequence in [73, 74]. The V_{in}-V_{out}, -V_{out}, V_{out} is eliminated in the downselection of this chapter due to topological complexity, but it provides higher efficiency than V_{in}-V_{out}, *Zero*, V_{out} for high step-down ratios.

Chapter 3

DC-DC Converter Implementations Based on Piezoelectric Transformers

3.1 Introduction

Power converter topologies and switching sequences based on piezoelectric resonators (PRs) are enumerated in Chapter 2, with one such implementation achieving >99% efficiency. Although such PR-based converter designs are promising, they exhibit decreasing efficiencies for high voltage conversion ratios. A PR-based converter switching sequence tailored to high step-down ratios is explored in [74], but even this switching has prohibitively low efficiency for extreme step-down ratios.

Piezoelectric transformers (PTs) build on the advantages of PRs in that they provide opportunities for voltage transformation and galvanic isolation. PT-based converter designs capable of ZVS without magnetics have been explored in [37, 39–52, 75]. Even with such progress, these magnetic-less PT-based converters report limited efficiency capabilities. PTs are understood to be capable of efficiencies >95% with sinusoidal drives [41, 48, 49], but PT-based dc-dc converter power-stage efficiencies tend to be drastically lower as summarized in Table 3.1. Notably, however, most of these designs rely on standard resonant converter architectures and operating techniques; there has been little investigation into alternative converter implementations dedicated to maximizing PT efficiency.

Table 3.1: Demonstrated Power-Stage Efficiencies for Magnetic-less DC-DC Converters Based on Piezoelectric Transformers

Reference	[46]	[49]	[50]	[47]	This work
Efficiency	70 %	62 %	78 %	68 %	90 %

In this chapter, we draw from the approach of Chapter 2 in that we abandon standard converter architectures and control techniques in search of dc-dc converter implementations that efficiently utilize PTs as their only energy storage components. We conduct a systematic enumeration and downselection process of isolated and non-isolated switching sequences and the necessary circuit topologies for realizing them. This investigation is confined to practical switching sequences capable of high-efficiency behaviors including ZVS, all-positive instantaneous power transfer, and minimal charge circulation across wide operating ranges. To analyze and compare implementations, we provide tools for deriving their ZVS operating regions, estimating PT efficiency, and solving for periodic steady state to calculate switching times. We then validate these analyses with an experimental prototype of one proposed implementation using a commercially available PT.

3.2 Isolated Converter Implementations

To identify high-efficiency PT-based converter implementations, we first enumerate and downselect isolated PT-based switching sequences and derive their compatible operating regions and circuit topologies. The proposed set of converter implementations opens opportunity for piezoelectrics to serve as the primary passive components in power conversion systems requiring isolation.

3.2.1 Assumed System and Stages

To enumerate isolated PT-based converter implementations, we assume an isolated dc-dc system with a constant-voltage load as shown in Fig. 3-1. This system relies on only the PT for energy storage, neglecting input and output filter components, and the PT serves as a 2-

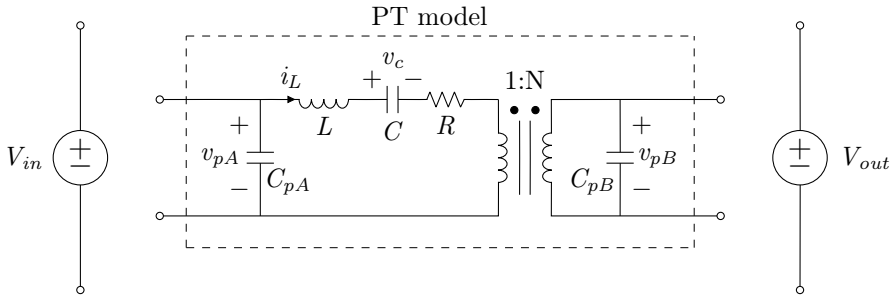

Figure 3-1: Isolated dc-dc source-load system assumed for switching sequence enumeration, with the PT represented by the reduced Mason circuit model [3]. Other terminal capacitances are neglected.

port, 4-terminal device. The PT is modeled using a reduced form of the Mason model, which includes physical terminal capacitances, an ideal transformer, and an LCR branch modeling the PT's mechanical resonance properties [3,4,76]. While this work focuses on a PT oriented for step-up operation, the presented analyses can be similarly applied to step-down PTs [77].

We begin by first identifying possible *stages* of a switching cycle. Each distinct way the terminals of the PT can be connected in the source-load system of Fig. 3-1 constitutes a possible stage. We refer to stages independently for each port of the PT, labeled by the voltage imposed on v_{pA} or v_{pB}.

As demonstrated in Section 2.3.2 for PR-based stages, we constrain the polarity of i_L in each stage for high-efficiency behaviors including ZVS, all-positive instantaneous power transfer, and minimal charge circulation. Thus, stages can be classified as follows:

- Connected stages: the PT port is connected to the source-load system such that $v_{pA} = \pm V_{in}$ or $v_{pB} = \pm V_{out}$. The polarity of i_L is constrained for all-positive instantaneous power transfer.

- Zero stages: the PT port is short-circuited, requiring v_{pA} or v_{pB} to equal zero. The polarity of i_L may be either positive (denoted *Zero+*) or negative (denoted *Zero-*), constrained for unidirectionality to avoid excess charge circulation.

- Open stages: the PT port is open-circuited, allowing v_{pA} or v_{pB} to increase or decrease through resonance. The polarity of i_L is constrained for charging/discharging C_{pA} or

Table 3.2: Potential Isolated Stages by Port and i_L Polarity

Polarity	Input Stages ($v_{pA} =$)	Output Stages ($v_{pB} =$)
$i_L > 0$	V_{in}; *Zero+*; $\frac{dv_{pA}}{dt} < 0$	V_{out}; *Zero+*; $\frac{dv_{pB}}{dt} > 0$
$i_L < 0$	-V_{in}; *Zero-*; $\frac{dv_{pA}}{dt} > 0$	-V_{out}; *Zero-*; $\frac{dv_{pB}}{dt} < 0$

C_{pB} as required for ZVS. One or both terminals may transition in this stage, either simultaneously or sequentially.

Connected stages transfer energy between the PT and the source-load system, while zero and open stages redistribute energy between the PT's states. The set of all potential stages is summarized along with i_L polarity constraints in Table 3.2.

3.2.2 Switching Sequence Enumeration

To derive isolated converter implementations, we permute these potential stages to create *switching sub-sequences* at each port, defined as order-specific arrangements of stages for a given port across a switching cycle. Then, we combine sub-sequences at each port to create full PT-wide *switching sequences*, analogous to the PR-based sequences detailed in Chapter 2. Assuming the stages and i_L constraints in Table 3.2, we enumerate possible sub-sequences with:

1. A minimum number of stages (for control simplicity).
2. At least one connected stage (for transferring energy to/from the PT).
3. Alternating connected/zero stages and open stages (for ZVS between connected/zero stages).
4. No repetition of the same connected/zero stage.
5. At least one connected/zero stage each for positive and negative i_L (for charge balance on C across the cycle).

6. One sequential span each of positive and negative i_L (for completion in one PT resonant cycle) [67].

Enumerating all possible sub-sequences and filtering according to these criteria yields two distinct 4-stage sub-sequences and two distinct 6-stage sub-sequences each for the input and output ports of the PT. We consider similar-stage sub-sequences to be distinct only if the *order* of their stages is different, regardless of which stage is listed "first". Also, we consider the inverted version of a sub-sequence (i.e., all stages having inverted voltage but in the same order) to be the same sub-sequence. Multiplied together between the two ports, the enumerated sub-sequences create 16 full switching sequences that enable ZVS and all-positive instantaneous power transfer in isolated PT-based dc-dc converters.

Throughout this work, we refer to a sub-sequence by the order of its connected/zero stage voltages (e.g., V_{out}, -V_{out}, *Zero+* for a six-stage sub-sequence), assuming the open stages between each. Full PT-based switching sequences are then denoted by "input-port sub-sequence | output-port sub-sequence" (e.g., V_{in}, -V_{in} | V_{out}, -V_{out}, *Zero+*).

3.2.3 Ideal Voltage Conversion Range

These 16 potential switching sequences can be filtered based on practical considerations such as wide operating ranges capable of the high-efficiency behaviors assumed in Chapter 2. First, the periodic steady-state operating range of a switching sequence is confined by its ability to balance energy and charge within the PT across a switching cycle. This requires the following energy balance equation to hold, using the V_{in}, -V_{in} | V_{out}, -V_{out}, *Zero+* sequence as an example:

$$V_{in}(|q_{Vin}| + |q_{-Vin}|) = \frac{V_{out}}{N}(|q_{Vout}| + |q_{-Vout}|) \tag{3.1}$$

in which we equate the energy sourced from V_{in} to the energy delivered to the load in a single cycle (assuming an ideal PT), and where q_n refers to the direction-specific quantity of charge transferred by i_L (as defined in Fig. 3-1) during stage n.

Neglecting open stages for now (i.e., neglecting charge and discharge of C_{pA} and C_{pB}),

Table 3.3: Proposed Isolated Switching Sequences, Topologies, and Constraints

Switching Sequence (Input | Output)	Topology	Ideal V_{out}/V_{in} Range	Charge Transfer Utilization Factors (K)	C_{pA}, C_{pB} Voltage Ranges (V_{ppA}, V_{ppB})
V_{in}, -V_{in} | V_{out}, *Zero+*, *Zero-*	FB-HB	$2N < \frac{V_{out}}{V_{in}} < \infty$	$K_A = 1$, $0 < K_B < \frac{1}{2}$	$2V_{in}$, V_{out}
V_{in}, -V_{in} | V_{out}, -V_{out}, *Zero+*	FB-FB	$N < \frac{V_{out}}{V_{in}} < 2N$	$K_A = 1$, $\frac{1}{2} < K_B < 1$	$2V_{in}$, $2V_{out}$
V_{in}, *Zero-* | V_{out}, *Zero+*, *Zero-*	HB-HB	$N < \frac{V_{out}}{V_{in}} < \infty$	$K_A = \frac{1}{2}$, $0 < K_B < \frac{1}{2}$	V_{in}, V_{out}
V_{in}, *Zero-* | V_{out}, -V_{out}, *Zero+*	HB-FB	$\frac{N}{2} < \frac{V_{out}}{V_{in}} < N$	$K_A = \frac{1}{2}$, $\frac{1}{2} < K_B < 1$	V_{in}, $2V_{out}$
V_{in}, -V_{in}, *Zero-* | V_{out}, *Zero-*	FB-HB	$N < \frac{V_{out}}{V_{in}} < 2N$	$\frac{1}{2} < K_A < 1$, $K_B = \frac{1}{2}$	$2V_{in}$, V_{out}
V_{in}, -V_{in}, *Zero-* | V_{out}, -V_{out}	FB-FB	$\frac{N}{2} < \frac{V_{out}}{V_{in}} < N$	$\frac{1}{2} < K_A < 1$, $K_B = 1$	$2V_{in}$, $2V_{out}$
V_{in}, *Zero+*, *Zero-* | V_{out}, *Zero-*	HB-HB	$0 < \frac{V_{out}}{V_{in}} < N$	$0 < K_A < \frac{1}{2}$, $K_B = \frac{1}{2}$	V_{in}, V_{out}
V_{in}, *Zero+*, *Zero-* | V_{out}, -V_{out}	HB-FB	$0 < \frac{V_{out}}{V_{in}} < \frac{N}{2}$	$0 < K_A < \frac{1}{2}$, $K_B = 1$	V_{in}, $2V_{out}$

charge balance on C requires positive- and negative-i_L stages to have equal-magnitude charge displacement. For the same example, this requires:

$$|q_{Vin}| = |q_{-Vin}| = |q_{Vout}| + |q_{Zero+}| = |q_{-Vout}| \tag{3.2}$$

The solution to (3.1) and (3.2) is the idealized[1] voltage conversion range supported by this switching sequence. In this case, $|q_{Vout}|$ can range from 0 to $|q_{Vin}|$ and still satisfy (3.2), allowing (3.1) to become:

$$N < \frac{V_{out}}{V_{in}} < 2N \tag{3.3}$$

This is the ideal operating range for which this switching sequence provides the desired high-efficiency behaviors. 4x6- and 6x4-stage switching sequences are capable of maintaining such behaviors across wide voltage conversion ranges, but 4x4-stage sequences support only specific conversion ratios if any. Thus, 4x4-stage sequences are less practical for most power conversion applications and are therefore eliminated from this scope. On the other hand, 6x6-stage sequences exhibit excess charge circulation (resulting in lower efficiencies) and unnecessary control complexity compared to the 4x6- and 6x4-stage sequences, so we likewise eliminate them.

[1]This voltage conversion range is ideal in that (a) it neglects loss in the PT, and (b) it neglects open stage charge transfer differences between the ports (i.e., the effects of C_{pA} and C_{pB}).

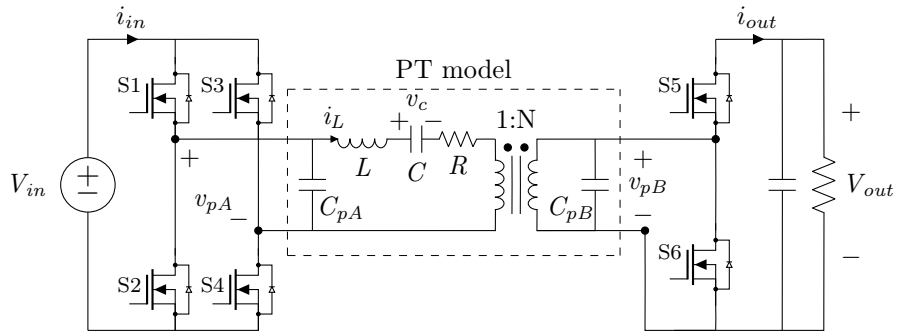

(a) FB-HB

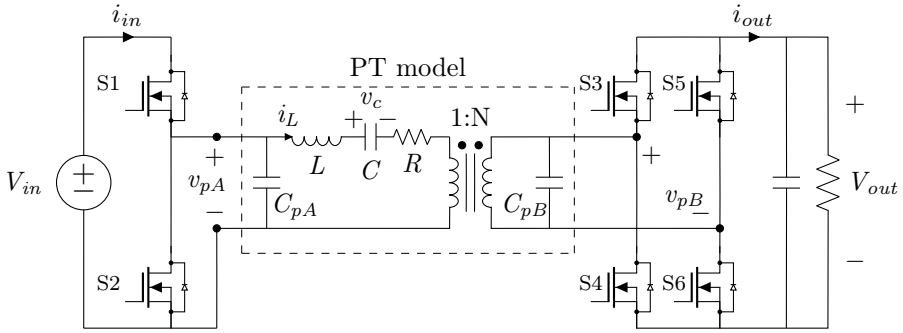

(b) HB-FB

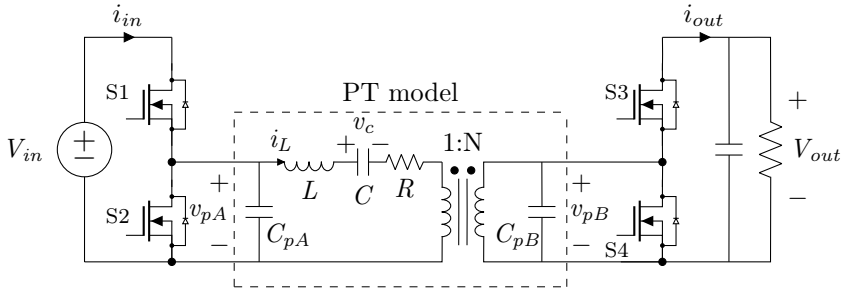

(c) HB-HB

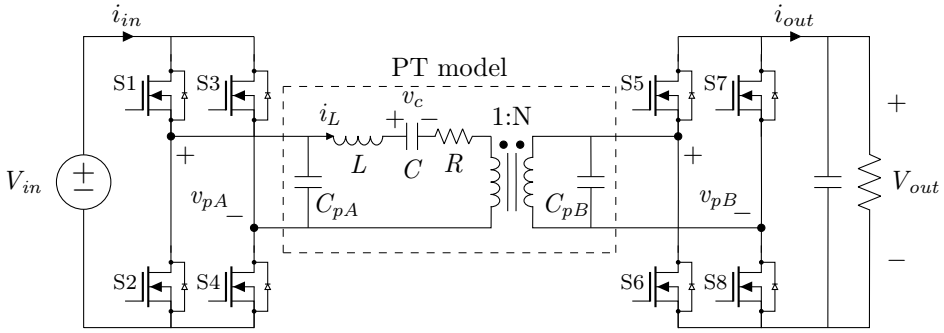

(d) FB-FB

Figure 3-2: Topologies for realizing the isolated switching sequences listed in Table 3.3.

The final eight switching sequences are displayed with their ideal voltage conversion ranges and other constraints in Table 3.3; this is the proposed set of sequences for isolated dc-dc converters.

3.2.4 Topologies

Each switching sequence in Table 3.3 can be realized with either a half-bridge or a full-bridge at each PT port as shown in the four isolated topologies of Fig. 3-2. This sub-sequence enumeration process does not discriminate between the two terminals of a single port, so topologies containing half-bridges can be similarly implemented with the opposite terminal fixed. Although these resulting topologies are common, it should be emphasized that the proposed switching sequences inform operation of these topologies for the desired high-efficiency behaviors. Also, if the rectifier in any of these topologies operates with a 4-stage sub-sequence, it may be implemented passively with diodes to simplify control.

3.3 Non-Isolated Converter Implementations

We next expand the set of proposed converter implementations to non-isolated PTs, which allow for a wider variety of switching sequences that more efficiently utilize the PT for applications not requiring isolation. The general strategy described in Section 3.2 for identifying isolated converter implementations may be adopted for enumerating and downselecting non-isolated converter implementations, though non-isolated PTs do exhibit some key differences. Unlike with isolated PTs, the common node C of a non-isolated PT introduces dependence between the two ports that warrants consideration of both ports together when deriving converter implementations. Also, because the set of potential stages, switching sequences, and topologies is larger without the isolation requirement, additional steps may be taken to downselect these based on practical needs.

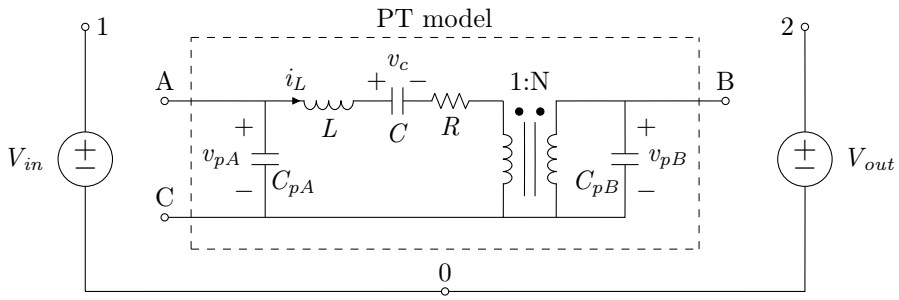

Figure 3-3: Non-isolated dc-dc source-load system assumed for switching sequence enumeration, with the PT represented by the reduced Mason circuit model [3]. Other terminal capacitances are neglected.

3.3.1 Assumed System and Terminal Configurations

To enumerate non-isolated converter implementations, we assume the common-negative dc-dc source-load system shown in Fig. 3-3; the analysis may be easily expanded to other cases. This source-load system contains only the PT for energy storage, not considering filter components at V_{in} and V_{out}. The non-isolated PT is modeled with both ports referenced to node C, creating a 2-port, 3-terminal device.

We begin by identifying connections to the source/load system for each of the three PT terminals and arranging these into potential *terminal configurations*. A terminal configuration differs from a stage in that it refers to the combination of how the PT's three terminals are each connected to the source-load system. Terminal configurations inherently specify stages for each port, but they differentiate between multiple ways these stages can be realized (e.g., at which node two terminals are tied to create a zero stage).

We focus on only connected/zero stages at both ports for these terminal configurations, assuming open stages occur between each for either or both ports as necessary. We refer to each configuration by the PT's terminal labels (A, B, and C), each followed by the terminal's source/load connection (0, 1, and 2), as defined in Fig. 3-3. For example, the configuration "A1B2C0" has terminal A connected to $+V_{in}$, terminal B connected to $+V_{out}$, and terminal C connected to the common-negative node. Permuting the three possible source/load connections for each of the three PT terminals reveals 27 potential terminal configurations for non-isolated PTs.

Table 3.4: Non-Isolated PT Terminal Configurations by i_L Polarity

Polarity	Terminal Configurations	Terminal Transitions
$i_L > 0$	A0B2C0, A1B0C0, A1B0C1, A1B1C0, A1B2C0, A1B2C1	A1 → A0, B0 → B2, C0 → C1, B1 → B2
$i_L < 0$	A0B0C1, A0B1C0, A0B1C1	A0 → A1, B2 → B0, C1 → C0, B2 → B1
Either	A0B0C0, A1B1C1	N/A

We then filter these terminal configurations assuming a step-up PT, and therefore $V_{out} > V_{in}$. Accordingly, we first reduce to configurations for which terminals A and C do not connect to node 2 ($+V_{out}$), since C_{pA} is often significantly greater than C_{pB} for step-up PTs (i.e., it would take an impractical length of time to resonate the node voltages of A or C to $+V_{out}$ for ZVS)[2]. Similar to isolated PTs, we also constrain the polarity of i_L for (1) all-positive instantaneous power transfer, again assuming i_L to be unidirectional within a single configuration, and (2) charging/discharging C_{pA} or C_{pB} for ZVS during transitions between configurations. Thus, 11 remaining configurations and 8 possible terminal transitions between them are shown with their i_L constraints in Table 3.4.

3.3.2 Switching Sequences

To enumerate switching sequences, we permute the potential terminal configurations listed in Table 3.4. Similar to isolated PTs, we assume open stages occur between the connected stages of each port to enable ZVS. Further, since supporting wide voltage conversion ranges is found to require six or more stages for both PRs in Section 2.2.4 and isolated PTs in Section 3.2, we likewise focus on six-stage sequences for non-isolated PTs. Enumerating permutations of three terminal configurations in Table 3.4 reveals 330 distinct six-stage sequences, which we then downselect for sequences with:

1. A maximum of five total terminal connections to the source/load system throughout the switching cycle (i.e., the minimum number of connections that yields viable sequences).

[2]It should be noted that this constraint is specific to step-up configurations. For step-down configurations, terminals A and C should not connect to V_{in}.

2. At least one connection to node 1 ($+V_{in}$) and one connection to node 2 ($+V_{out}$).
3. No two terminals always tied together.
4. No repetition of the same terminal configuration.
5. At least one configuration each for positive and negative i_L (for charge balance on C across the cycle).
6. One sequential span each of positive and negative i_L, considering both connected and open stages for each port (for completion in one PT resonant cycle).
7. Sequential zero stages for a given port realized at the same node in the source-load system (to avoid excess charge circulation).

Once enumerated, these switching sequences can be conceptualized by the sub-sequences of each PT port, and the ideal voltage conversion ranges for these sequences can be calculated using the same energy and charge balance strategy presented in Section 3.2.3.

We further downselect to switching sequences that would be simplest to maintain with closed-loop control, requiring as few control loops as possible. Thus, we filter to sequences for which only one PT terminal transitions between two connected stages in a single half-cycle (i.e., between two connected stages of the same i_L polarity). Only one such transition is needed for voltage regulation as described in Chapter 4, so sequences with additional transitions of this nature require additional control complexity and are therefore eliminated. This results in 4x6 stage switching sequences if the transitioning terminal is A or B, but it creates a 6x6 stage sequence if C serves as the transitioning terminal; we consider 6x6 stage sequences only in the context of this transition for non-isolated PTs.

This filtering process yields twelve switching sequences of interest for non-isolated PT-based converter implementations. These sequences are displayed in Table 3.5 in terms of each port's sub-sequences, along with their ideal voltage conversion ranges calculated using the strategy outlined in Section 3.2.3. The constraints for these sequences derived in Section 3.5 are likewise displayed in Table 3.6.

Table 3.5: Proposed Non-Isolated Switching Sequences, Topologies, and Constraints

Switching Sequence (Input | Output)	Topology (Fig. 3-4)	Ideal V_{out}/V_{in} Range
V_{in}, *Zero+*, *Zero-* | V_{out}, *Zero-*	(a)	$0 < \frac{V_{out}}{V_{in}} < N$
V_{in}, *Zero+*, *Zero-* | V_{out}, V_{in}	(b)	$1 < \frac{V_{out}}{V_{in}} < N+1$
Zero+, -V_{in}, *Zero-* | V_{out}-V_{in}, *Zero-*	(d)	$1 < \frac{V_{out}}{V_{in}} < N+1$
Zero+, -V_{in}, *Zero-* | V_{out}, -V_{in}, *Zero-*	(e)	$0 < \frac{V_{out}}{V_{in}} < N-1$
Zero+, -V_{in}, *Zero-* | V_{out}, *Zero-*, V_{in}	(f)	$1 < \frac{V_{out}}{V_{in}} < N$
V_{in}, *Zero+*, *Zero-* | V_{out}, V_{out}-V_{in}, *Zero-*	(g)	$1 < \frac{V_{out}}{V_{in}} < N$
V_{in}, *Zero-* | *Zero+*, V_{out}, *Zero-*	(a)	$N < \frac{V_{out}}{V_{in}} < \infty$
V_{in}, *Zero-* | V_{in}, V_{out}, V_{in}	(b)	$N+1 < \frac{V_{out}}{V_{in}} < \infty$
Zero+, -V_{in}, | -V_{in}, V_{out}-V_{in}, -V_{in}	(c)	$N < \frac{V_{out}}{V_{in}} < \infty$
Zero+, -V_{in}, | *Zero+*, V_{out}-V_{in}, *Zero-*	(d)	$N+1 < \frac{V_{out}}{V_{in}} < \infty$
Zero+, -V_{in}, | *Zero+*, V_{out}, -V_{in}	(e)	$N-1 < \frac{V_{out}}{V_{in}} < \infty$
V_{in}, *Zero-* | V_{in}, V_{out}, *Zero-*	(g)	$N < \frac{V_{out}}{V_{in}} < \infty$

Table 3.6: Proposed Non-Isolated Switching Sequences, Topologies, and Constraints

Switching Sequence (Input | Output)	Charge Transfer Utilization Factors (K)	Voltage Ranges (V_{ppA}, V_{ppB})
V_{in}, *Zero+*, *Zero-* | V_{out}, *Zero-*	$0 < K_A < \frac{1}{2}$, $K_{Bin} = 0$, $K_{Bout} = \frac{1}{2}$	V_{in}, V_{out}
V_{in}, *Zero+*, *Zero-* | V_{out}, V_{in}	$0 < K_A < \frac{1}{2}$, $K_{Bin} = \frac{1}{2}$, $K_{Bout} = \frac{1}{2}$	V_{in}, V_{out}-V_{in}
Zero+, -V_{in}, *Zero-* | V_{out}-V_{in}, *Zero-*	$0 < K_A < \frac{1}{2}$, $K_{Bin} = \frac{1}{2}$, $K_{Bout} = \frac{1}{2}$	V_{in}, V_{out}-V_{in}
Zero+, -V_{in}, *Zero-* | V_{out}, -V_{in}, *Zero-*	$0 < K_A < \frac{1}{2}$, $\frac{-1}{2} < K_{Bin} < 0$, $K_{Bout} = \frac{1}{2}$	V_{in}, V_{out}+V_{in}
Zero+, -V_{in}, *Zero-* | V_{out}, *Zero-*, V_{in}	$0 < K_A < \frac{1}{2}$, $0 < K_{Bin} < \frac{1}{2}$, $K_{Bout} = \frac{1}{2}$	V_{in}, V_{out}
V_{in}, *Zero+*, *Zero-* | V_{out}, V_{out}-V_{in}, *Zero-*	$0 < K_A < \frac{1}{2}$, $0 < K_{Bin} < \frac{1}{2}$, $K_{Bout} = \frac{1}{2}$	V_{in}, V_{out}
V_{in}, *Zero-* | *Zero+*, V_{out}, *Zero-*	$K_A = \frac{1}{2}$, $K_{Bin} = 0$, $0 < K_{Bout} < \frac{1}{2}$	V_{in}, V_{out}
V_{in}, *Zero-* | V_{in}, V_{out}, V_{in}	$K_A = \frac{1}{2}$, $0 < K_{Bin} < \frac{1}{2}$, $0 < K_{Bout} < \frac{1}{2}$	V_{in}, V_{out}-V_{in}
Zero+, -V_{in}, | -V_{in}, V_{out}-V_{in}, -V_{in}	$K_A = \frac{1}{2}$, $K_{Bin} = 0$, $0 < K_{Bout} < \frac{1}{2}$	V_{in}, V_{out}
Zero+, -V_{in}, | *Zero+*, V_{out}-V_{in}, *Zero-*	$K_A = \frac{1}{2}$, $0 < K_{Bin} < \frac{1}{2}$, $0 < K_{Bout} < \frac{1}{2}$	V_{in}, V_{out}-V_{in}
Zero+, -V_{in}, | *Zero+*, V_{out}, -V_{in}	$K_A = \frac{1}{2}$, $K_{Bin} = \frac{-1}{2}$, $0 < K_{Bout} < \frac{1}{2}$	V_{in}, V_{out}+V_{in}
V_{in}, *Zero-* | V_{in}, V_{out}, *Zero-*	$K_A = \frac{1}{2}$, $\frac{-1}{2} < K_{Bin} < 0$, $0 < K_{Bout} < \frac{1}{2}$	V_{in}, V_{out}

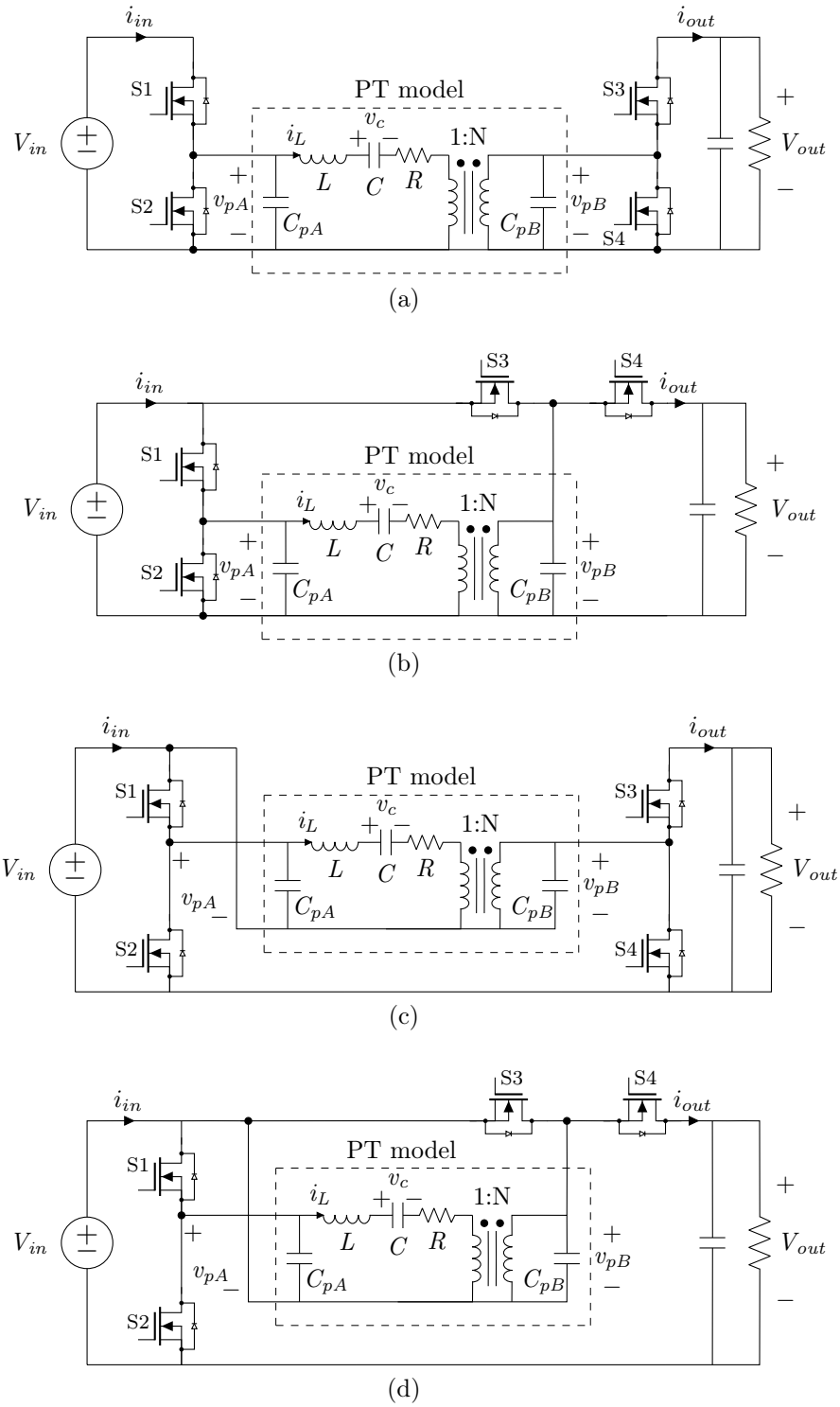

Figure 3-4: Topologies for realizing the non-isolated switching sequences listed in Table 3.5.

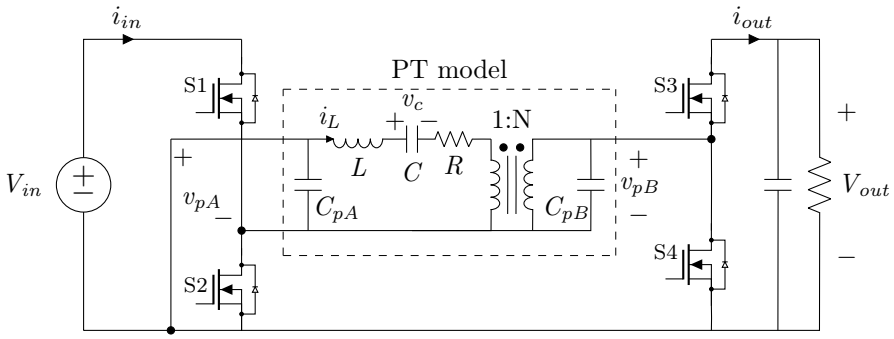

(e)

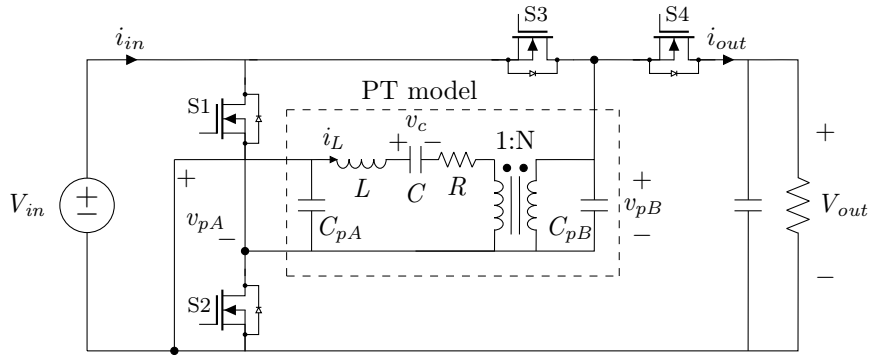

(f)

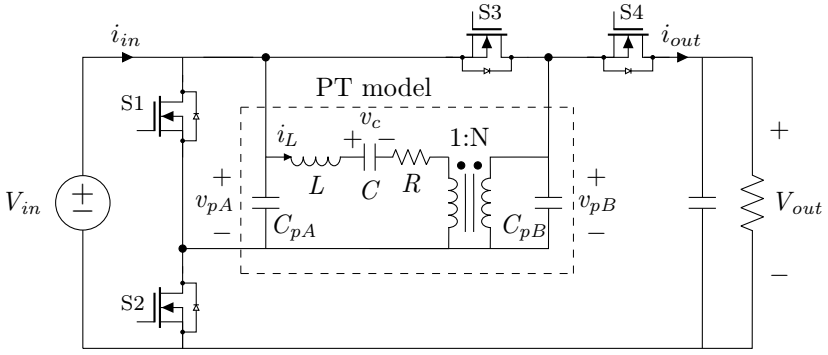

(g)

Figure 3-4: (Continued) Topologies for realizing the non-isolated switching sequences listed in Table 3.5.

3.3.3 Topologies

The non-isolated switching sequences of Table 3.5 can be realized with the topologies displayed in Fig. 3-4, each requiring four unidirectional-blocking switches. Predictably, this set of non-isolated topologies is larger than that for isolated PTs, allowing additional opportu-

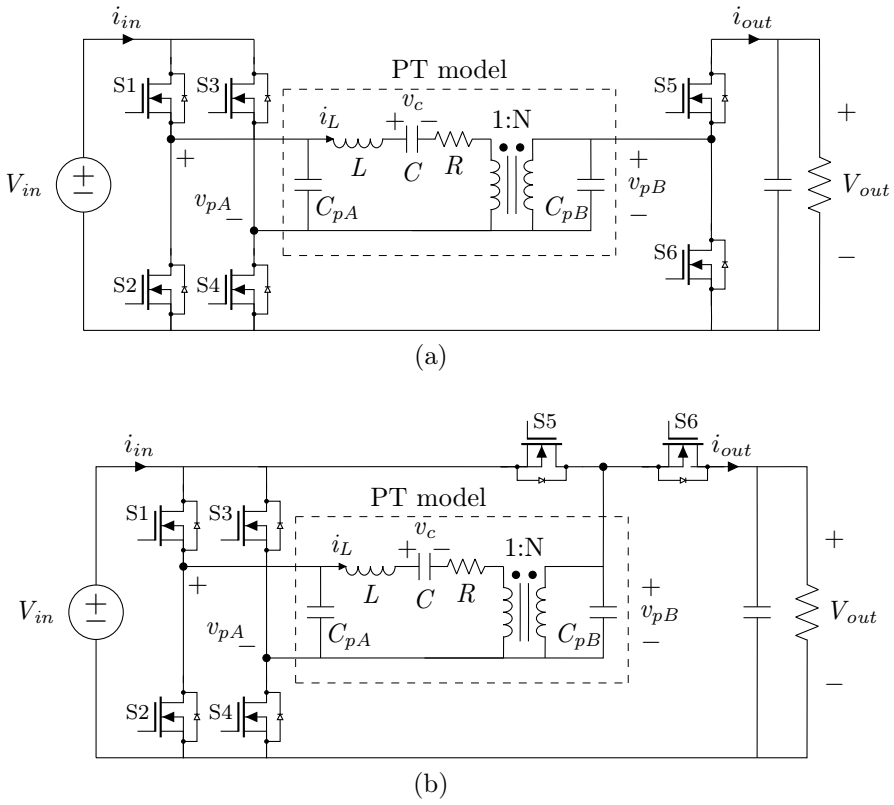

Figure 3-5: Synthesized topologies for realizing multiple non-isolated switching sequences listed in Table 3.5, along with additional sequences that require a full-bridge inverter.

nities for applications not requiring isolation. Similar to the isolated topologies, the rectifier switches of these topologies may be implemented passively if the output port uses a 4-stage sub-sequence.

To realize multiple sequences, the topologies of Fig. 3-4 may be synthesized with additional switches. Fig. 3-5 displays two example topologies that are each capable of realizing multiple switching sequences in Table 3.5. Further, each of these topologies support their own additional sets of switching sequences that require a full-bridge inverter.

Finally, the topologies of Fig. 3-4 may be similarly expanded to allow three terminal connections for node B, though this requires adding a bidirectional-blocking switch.

3.4 Periodic Steady-State Operation

Once a switching sequence has been selected, we can analyze the PT's states across its resonant cycle and constrain them for periodic steady-state operation. This can lend useful information such as switching times for simulation.

3.4.1 Resonant Cycle Segmentation

During the enumeration process, the switching sequences at each PT port were assumed to operate independently, so the timing of stage transitions at each port relative to the other is not specified. Mapping the switching sub-sequences of each port to the PT's resonant cycle is imperative for analyzing the PT's resonance and solving for periodic steady-state operation. We refer to the span of resonance between each stage transition point (at either port) as a *segment*, and segments vary based on switching sequence, operating point, and PT parameters.

To map a switching sequence to the PT's resonant cycle, we first solve a system of equations for the charge displaced by i_L during each of its stages. The connected/zero stage charge displacement for each port is established by the energy transferred to/from the source-load system and charge balance on C as further described in Section 3.5.1. For the sub-sequence V_{out}, -V_{out}, *Zero+*, this results in the following two equations:

$$|q_{V_{out}}| + |q_{-V_{out}}| = \frac{E_{out}}{V_{out}} = \frac{P_{out}}{fV_{out}} \tag{3.4}$$

$$|q_{V_{out}}| + |q_{Zero+}| = |q_{-V_{out}}| \tag{3.5}$$

These equations (four total between the two ports) fully constrain the connected/zero charge transfer quantities of a four-stage sub-sequence, but one additional constraint is needed to solve for these quantities in a six-stage sub-sequence (e.g., $|q_{V_{out}}|$, $|q_{Zero+}|$, $|q_{-V_{out}}|$ in the example above). This is obtained by equating the total connected/zero stage charge displacement from the perspective of each port as exemplified in (3.2). Thus, the charge

displacement during each of the five connected/zero stages in a 4x6- or 6x4-stage sequence can be solved using this simple system of equations.

The charge transfer of each open stage can be calculated using the change in voltage (ΔV_{pA} or ΔV_{pB}) on C_{pA} or C_{pB} required for ZVS as follows, using the output port for example:

$$|q_{\Delta V_{pB}}| = C_{pB}\Delta V_{pB}. \tag{3.6}$$

The charge transferred by i_L during each stage governs the stages' time durations, which we now utilize to determine the order of all stage transitions between the two ports and divide the resonant cycle into segments. First, both the input and output port sequences have stage transitions that must be synchronized to the PT's i_L zero crossings to satisfy the i_L polarity constraints in Tables 3.2 and 3.4. These transitions align the two switching sequences temporally.

Once the i_L zero crossing transitions have been defined, the durations of each stage neighboring the zero crossings can be compared port-to-port based on the charge that must be transferred by i_L during each individual stage. The transitions for stages requiring less charge transfer occur temporally closer to the i_L zero crossing, and stages requiring more charge transfer begin or end further in time from the zero crossing. This process can be extended to other stage transitions by adding their stages' charge transfer onto a port's existing sum and then comparing between ports.

Using this strategy, we can map the order of all stage transitions at either port throughout the switching sequence, which divide the PT's resonant cycle into segments. Knowledge of these segments is useful for analyzing the PT's resonance and constraining for periodic steady state.

3.4.2 Equivalent Resonant Circuits

Once a PT's resonant cycle has been segmented, its segments can each be analyzed using an equivalent resonant circuit. The analysis of this section stems from principles of state plane

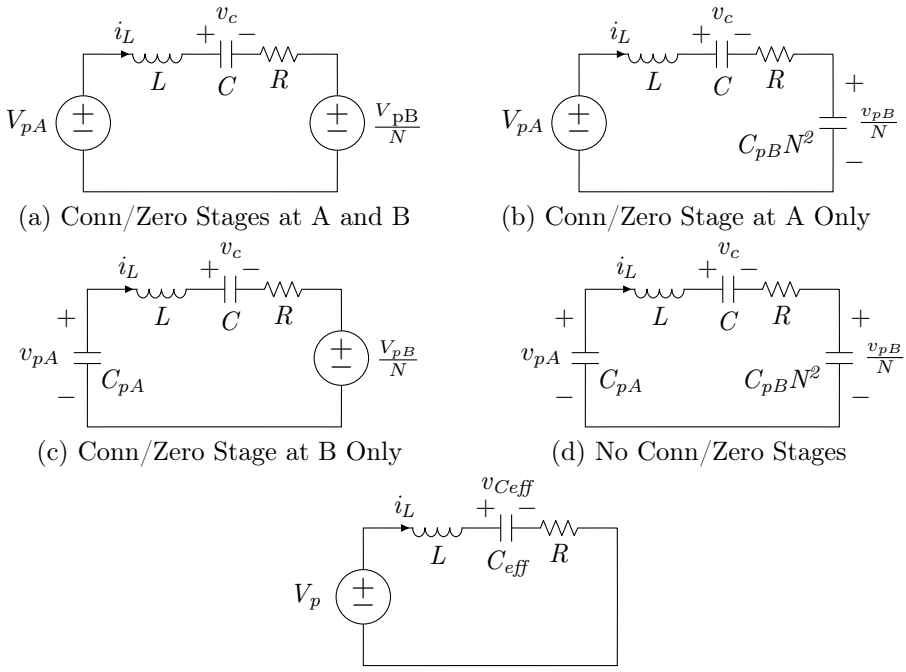

(a) Conn/Zero Stages at A and B

(b) Conn/Zero Stage at A Only

(c) Conn/Zero Stage at B Only

(d) No Conn/Zero Stages

(e) Reduced Resonant Circuit

Figure 3-6: Equivalent circuits for PT resonance based on port connections.

Table 3.7: Parameters for Reduced Resonant Circuit (Fig. 3-6(e))

Connected/Zero Stage Ports	V_p	C_{eff}	$v_{C_{eff}}$
A and B	V_{pA}-$\frac{V_{pB}}{N}$	C	v_c
A Only	V_{pA}	$\frac{CC_{pB}N^2}{C+C_{pB}N^2}$	$v_c + \frac{v_{pB}}{N}$
B Only	-$\frac{V_{pB}}{N}$	$\frac{CC_{pA}}{C+C_{pA}}$	$v_c - v_{pA}$
none	0	$\frac{CC_{pA}C_{pB}N^2}{C+C_{pA}+C_{pB}N^2}$	$v_c - v_{pA} + \frac{v_{pB}}{N}$

analysis illustrated for PRs in [67] and for isolated step-down PTs in [77].

There are four potential equivalent resonant circuits corresponding to connected/zero stages or open stages at each port; these are shown in Figs. 3-6(a)-(d) with voltage sources representing connected/zero stage voltages and terminal capacitances (C_{pA} or C_{pB}) present during open stages. The PT resonates in a single resonant circuit for the duration of each segment, switching to a new resonant circuit at each segment transition.

To simplify analysis, all four resonant circuits can be reduced to the equivalent circuit of Fig. 3-6(e) with an aggregate offset voltage V_p and an effective capacitance C_{eff} using the

parameters listed in Table 3.7. This reduced resonant circuit serves as a tool for standardizing stage behaviors when solving for periodic steady state.

3.4.3 Ideal Periodic Steady-State Solution

The periodic steady-state solution of the PT's state trajectories quantifies exactly how a switching sequence must operate to realize its intended efficiency advantages. An ideal periodic steady-state solution (assuming $R = 0$) can be obtained analytically with light computation and provides a close estimate of the exact solution to the extent that $R \to 0$.

To solve for an ideal periodic steady-state solution, we apply Conservation of Energy (CoE) and Conservation of Charge (CoC) equations to the PT's state variables during each segment, assuming the final states equal the first states and that ZVS occurs at each stage transition. These equations rely on only the states at each stage transition point and can be crafted segment-by-segment in the order determined in Section 3.4.1. Using the reduced resonant circuit of Fig. 3-6(e), every segment has the following CoE constraint:

$$C_{eff}(v_{C_{eff}1} - V_p)^2 + Li_{L1}^2 = C_{eff}(v_{C_{eff}2} - V_p)^2 + Li_{L2}^2 \tag{3.7}$$

in which states marked with "1" correspond to the beginning of the segment and states marked with "2" correspond to the end of the segment.

Segments with open stages have additional CoC constraint(s) depending on which additional capacitances (C_{pA} and/or C_{pB}) participate in resonance. For open stages at the input, the following CoC equation applies:

$$C(v_{c2} - v_{c1}) = -C_{pA}(v_{pA2} - v_{pA1}) \tag{3.8}$$

Open stages at the output likewise require:

$$C(v_{c2} - v_{c1}) = NC_{pB}(v_{pB2} - v_{pB1}) \tag{3.9}$$

Thus, each segment adds $1 + n$ equations to the system, where n equals the number of port capacitances resonating.

From here, the i_L polarity constraints listed in Tables 3.2 and 3.4 can be added by setting i_L equal to zero at the appropriate segment transition points; this constrains two i_L transition states for each port. For a 4x6- or 6x4-stage sequence, this leaves one remaining degree of freedom (assuming V_{in} and V_{out} have already been defined) that dictates the power delivered to the load. Using these constraints, one can solve this system of equations for the ideal periodic steady-state solution of all transition point states. For a given PT, sequence combination, and operating point, this solution describes the single set of state trajectories that provides all of the advantageous behaviors discussed herein, amounting to maximum efficiency. Appendix A.1.2 exemplifies solving for this ideal periodic steady-state solution in the first part of the provided script.

3.4.4 Ideal Switching Times

The ideal time duration of each segment across a switching cycle can be extracted from the PT's transition point states in the ideal periodic steady-state solution. One approach for this involves multiplying a segment's resonant period times the proportion of this resonant period that it completes. This requires calculating the "angle" between the segment's start and end points, both referenced from the circuit's center of resonance. In the reduced resonant circuit of Fig. 3-6(e), L and C_{eff} resonate around a center point of $i_L = 0$ and $v_{C_{eff}} = V_p$. We define an impedance-normalized vector U_x for each transition x to be:

$$U_x = \left(v_{C_{eff}x} - V_p,\ \ i_{Lx}\sqrt{\frac{L}{C_{eff}}},\ \ 0 \right) \tag{3.10}$$

in which V_p and C_{eff} are specific to the segment of interest, even for the same transition point. The angle between two neighboring transition point vectors can be calculated using the four-quadrant inverse tangent function. Its proportion of the period (out of 2π) can then be multiplied by the segment's resonant period to calculate the segment's time duration:

$$t_{1-2} = \sqrt{LC_{eff}}\,\text{atan2}\left(\frac{||U_1 \times U_2||}{U_1 \cdot U_2} \right) \tag{3.11}$$

We should note that frequency is *not* an independent control variable; it is collectively

determined by these switching times. These ideal switching time calculations are utilized in the periodic steady-state solution script provided in Appendix A.1.2.

3.4.5 Exact Periodic Steady-State Solution

Calculating an exact periodic steady-state solution considering loss due to R requires time-domain integration of i_L^2, which is not easily implemented using only the PT states at each stage transition. If needed, an exact periodic steady-state solution can be obtained by symbolically solving the PT's system of time-domain differential equations that govern its states during each segment. This produces a system of complex exponentials, which can then be solved numerically for the exact solution using the ideal solution as a starting point to aid convergence.

Similar to the ideal periodic steady-state solution, the system of exact differential equations can be assembled segment-by-segment as in Section 3.4.1. This system has the same transition point state variables as the ideal system, plus the segments' time durations as variables. After applying all equations and constraints for a 4x6- or 6x4-stage sequence combination, one degree of freedom remains for modulating power. The exact periodic steady-state solution is useful for calculating switching times for loss-inclusive simulations. A MATLAB script that solves for exact periodic steady-state solutions of the V_{in}, -V_{in} | V_{out}, -V_{out}, *Zero+* switching sequence is provided in Appendix A.1.2.

3.5 PT ZVS Region, Amplitude of Resonance, and Efficiency

PT-based converter switching sequences can be intuitively analyzed using PT charge displacement patterns, which lend useful information about the PT's ZVS region, amplitude of resonance, and efficiency.

3.5.1 Charge Transfer Utilization Factor

The PT-based switching sequences in Tables 3.3 and 3.5 vary widely in how effectively they utilize the PT's resonant cycle to transfer energy. We quantify the productivity of a single port's sub-sequence with a "charge transfer utilization factor", K. Following the definition of Chapter 2, K is the proportion of a sub-sequence's connected and zero stage charge transfer that sources energy from the source or delivers energy to the load. K_A refers to the input port sub-sequence sourcing energy from V_{in}, and K_B refers to the output port sub-sequence delivering energy to V_{out} for isolated PTs. For non-isolated PTs, K_{Bin} and K_{Bout} respectively refer to the output port sourcing energy from V_{in} and delivering energy to V_{out}.

We illustrate these concepts with an example isolated sequence V_{in}, -V_{in} | V_{out}, -V_{out}, *Zero+*, which is visualized across the i_L cycle in Fig. 3-7. For the output port of this sequence, K_B is calculated to be:

$$K_B = \frac{Q_{conn(Vout)}}{Q_{conn} + Q_{zero}} = \frac{|q_{V_{out}}| + |q_{-V_{out}}|}{|q_{V_{out}}| + |q_{-V_{out}}| + |q_{Zero+}|} \tag{3.12}$$

The applicable range for K is bounded by charge balance on capacitance C, which requires the total charge transferred by positive- and negative-i_L to be equal. For an individual port, positive and negative open stage charge transfer is balanced for C_{pA} or C_{pB}, so positive and negative connected/zero stage charge transfer must also be balanced for C. For the above example:

$$|q_{Vout}| + |q_{Zero+}| = |q_{-Vout}| \tag{3.13}$$

Thus, for this example switching sequence, $|q_{Vout}|$ can range from 0 to $|q_{-Vout}|$, which confines K_B to the range $\frac{1}{2} < K_B < 1$. A similar derivation for K_A yields $K_A = 1$.

When deriving K_{Bin} and K_{Bout} for non-isolated PT sub-sequences, only connected stages involving V_{in} and V_{out}, respectively, are considered in the numerator of (3.12). K_{Bin} may be positive or negative depending on whether the output port contributes to or counters energy sourced from V_{in}.

The K values for all switching sequences are displayed in Tables 3.3 and 3.6; 4-stage sub-sequences have fixed K values, while 6-stage sub-sequences support ranges of K.

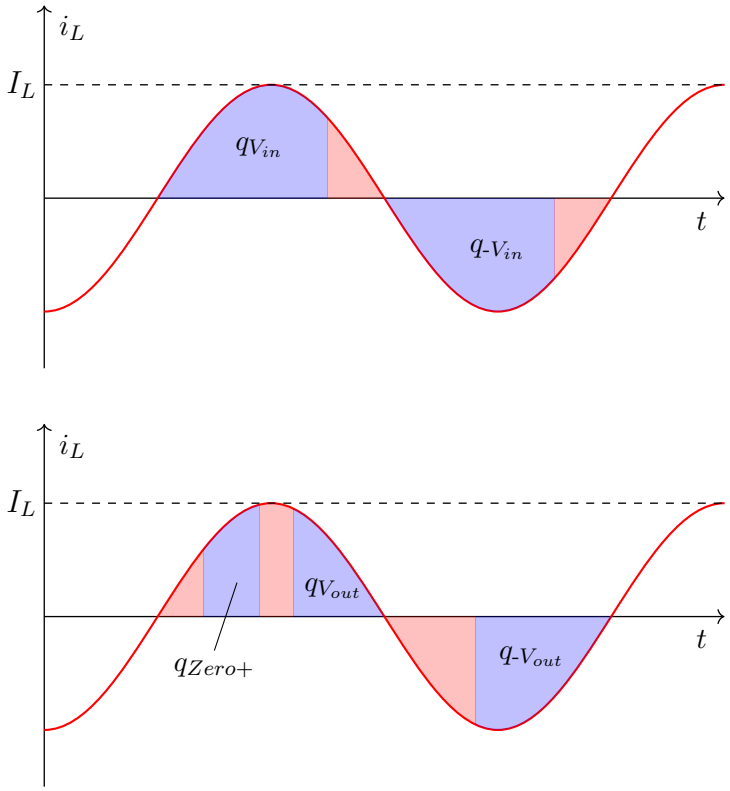

Figure 3-7: Sinusoidal approximation of i_L based on the charge transfer q_n required of each stage, from the perspective of the input (top) and output (bottom) ports of an isolated PT. Connected/zero stages are shaded purple, open stages are shaded red, and I_L is the amplitude of resonance. Example sequence: V_{in}, -V_{in} | V_{out}, -V_{out}, *Zero+*.

3.5.2 Total Charge Transfer

Fig. 3-7 illustrates how an assumed-sinusoidal i_L cycle can be segmented by input port stages (top plot) or output port stages (bottom plot) for a given switching sequence. The shaded regions under the i_L curve (i.e., the sectional integrals of i_L) equal the charge displaced during each stage. From the perspective of either port, the magnitude of charge transferred by i_L during one resonant cycle can be partitioned into connected/zero stage charge displacement ($Q_{conn} + Q_{zero}$) and open stage charge displacement (Q_{open}) [67].

A sub-sequence's connected/zero stage charge displacement is the following function of charge sourced/delivered and K, using the input port of the isolated sequence in Fig. 3-7 as an example:

$$Q_{conn} + Q_{zero} = \frac{Q_{in}}{K_A} = \frac{E_{in}}{K_A V_{in}} = \frac{P_{in}}{f K_A V_{in}} \tag{3.14}$$

in which f may be assumed within the PT's inductive region[3].

A sub-sequence's open stages collectively charge and discharge C_{pA} or C_{pB} across its full peak-to-peak voltage range V_{ppA} or V_{ppB}, respectively, and these ranges are displayed for each switching sequence in Tables 3.3 and 3.6. This results in the following open stage charge displacement for the isolated sequence's input port:

$$Q_{open} = 2 C_{pA} V_{ppA} \tag{3.15}$$

Thus, the total magnitude of charge that must be transferred by i_L during each cycle (Q_{total}) is:

$$Q_{total} = Q_{conn} + Q_{zero} + Q_{open} = \frac{P_{in}}{f K_A V_{in}} + 2 C_{pA} V_{ppA} \tag{3.16}$$

If we were to instead compute Q_{total} from the perspective of the output port for this example,

$$Q_{total} = N\left(\frac{P_{out}}{f K_B V_{out}} + 2 C_{pB} V_{ppB}\right) \tag{3.17}$$

For non-isolated sequences, $K_B = K_{Bout}$ may be substituted into (3.17) for calculating Q_{total} from the output port's perspective. K_{Bin} impacts the connected/zero stage charge transfer required of the input port's sub-sequence, which must be considered when deriving Q_{total} from the input port's perspective. For that case,

$$Q_{total} = \frac{\frac{P_{in}}{f V_{in}} + 2 K_A C_{pA} V_{ppA} + 2 K_{Bin} C_{pB} V_{ppB}}{K_A + \frac{K_{Bin}}{N}} \tag{3.18}$$

Q_{total} provides means to easily assess the PT's total charge transfer, which we use to derive the PT's ZVS region in Section 3.5.3 and amplitude of resonance in Section 3.5.4.

3.5.3 Zero-Voltage Switching Region

Ensuring a switching sequence is capable of ZVS is the first step in evaluating its suitability for a given operating point and PT. In addition to switch capacitances, the PT terminal

[3]The inductive region for a PT is narrow with respect to frequency, so the exact f assumed in this calculation has little effect on the result as long as it falls within the PT's inductive region.

capacitances C_{pA} and C_{pB} must resonate to exactly their next-stage voltages for ZVS during open stages. Here we determine the operating region for which a given switching sequence is capable of ZVS considering this open stage charge displacement. This analysis assumes C_{pA} and C_{pB} dominate their respective switch node capacitances, though neighboring switch capacitances may be added to C_{pA} and C_{pB} if significant.

We can examine a given switching sequence's ZVS region by first calculating the total charge transferred by i_L (detailed in Section 3.5.2) from the perspective of each port. This calculation considers the charge displacement necessary for all stages of the switching sequence, including open stages for ZVS, assuming the aforementioned constraints (e.g., i_L polarities) are preserved. For the isolated case,

$$Q_{total} = \frac{P_{in}}{fK_A V_{in}} + 2V_{ppA}C_{pA} = N\big(\frac{P_{out}}{fK_B V_{out}} + 2V_{ppB}C_{pB}\big) \tag{3.19}$$

and for the non-isolated case,

$$\begin{aligned} Q_{total} &= \frac{\frac{P_{in}}{fV_{in}} + 2K_A C_{pA} V_{ppA} + 2K_{Bin} C_{pB} V_{ppB}}{K_A + \frac{K_{Bin}}{N}} \\ &= N\big(\frac{P_{out}}{fK_{Bout} V_{out}} + 2V_{ppB}C_{pB}\big) \end{aligned} \tag{3.20}$$

The two sides of these Q_{total} equations are equal by definition and reveal likely-significant differences in the charge displacement requirements for each PT port. For a given operating point, the switching sequence compensates these differences by varying K_A and/or K_B (K_A, K_{Bin}, and/or K_{Bout} for the non-isolated case), which are fixed for 4-stage sequences and confined to specific ranges for 6-stage sequences. Thus, these ranges for K dictate the operating region for which (3.19) and (3.20) are true, which defines the switching sequence's ZVS region.

Equipped with PT parameters and a given switching sequence's V_{ppA}, V_{ppB}, and K boundaries, we can solve (3.19) or (3.20) for the range of operating points capable of ZVS. Neglecting R in the PT (i.e., $P_{in} = P_{out}$), Fig. 3-8 maps the ZVS regions of three neighboring isolated switching sequences on power and voltage gain axes; this is a useful representation for visualizing the operating regions served by different switching sequences. These sequences

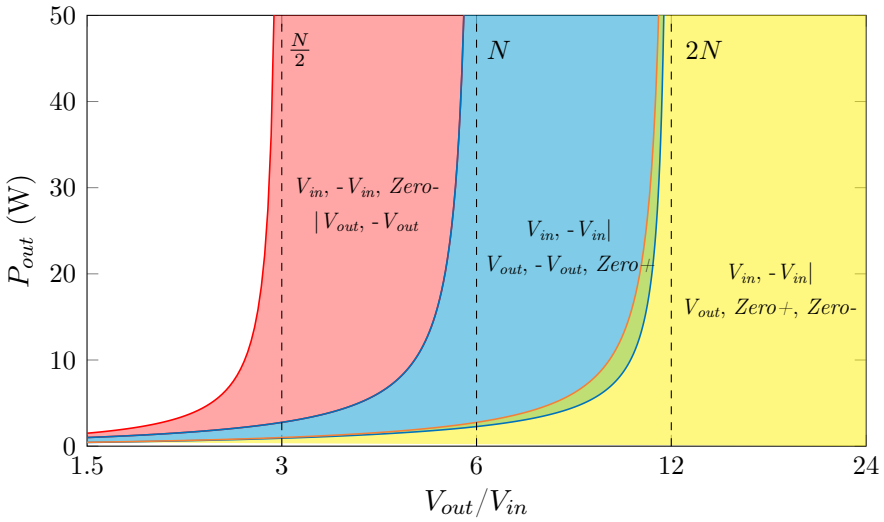

Figure 3-8: ZVS region defined by (3.19) for three isolated switching sequences, assuming the manufacturer-provided PT parameters in Table 3.8 and $V_{in} = 100$ V. Ideal boundaries are marked with dotted lines.

Table 3.8: Example PT Parameter Values

Parameter	Manufacturer-Provided [78]	On-board Measurement
C_{pA}	960 pF	1.6 nF (with switches)
C_{pB}	8 pF	83 pF (with diodes)
L	59 mH	44 mH
C	60 pF	72 pF
R	24 Ω	27 Ω
N	6	6 (assumed)

allow for a continuous range of ZVS, with boundaries between FB and HB sequences overlapping. As power increases, connected/zero stages dominate the PT's charge transfer, and the boundaries for these ZVS regions approach their ideal V_{out}/V_{in} range asymptotes (calculated in Section 3.2.3). Known nonidealities such as loss and parasitic capacitance can be implemented in (3.19) through P_{in} or P_{out} and C_{pA} or C_{pB}, respectively, but neither disrupt the continuity of ZVS across sequence combinations.

3.5.4 Amplitude of Resonance Model

The total charge displaced by i_L in one resonance cycle can be utilized to estimate the amplitude of i_L (I_L), which quantifies the PT's amplitude of resonance as described for PRs in Chapter 2. If we assume i_L to be sinusoidal as illustrated in Fig. 3-7, I_L can be calculated by equating Q_{total} to the integral of $|i_L|$ over one cycle:

$$Q_{total} = 2\int_0^{\frac{1}{2f}} i_L dt = 2\int_0^{\frac{1}{2f}} I_L \sin(2\pi f t) dt = \frac{2I_L}{\pi f} \tag{3.21}$$

$$\Rightarrow I_L = \frac{\pi}{2} f Q_{total} = \pi\Big(\frac{P_{in}}{2K_A V_{in}} + f C_{pA} V_{ppA}\Big) \tag{3.22}$$

using the input port of an isolated PT as an example, though I_L may also be computed with Q_{total} of (3.17) or (3.18). I_L may be calculated from the perspective of either PT port, but doing so using a 4-stage-sequence port allows simpler computation with constant K value(s). For six-stage sequences, K varies within a defined range as shown in Section 3.5.1 but can be computed based on the operating point as detailed in [67]. This is also required for non-isolated switching sequences for which both K_{Bin} and K_{Bout} are unfixed[4].

I_L provides important insight into the PT's energy storage and loss, and we employ it to analytically estimate efficiency in Section 3.5.5.

3.5.5 Efficiency Estimation

Within topological and ZVS constraints, a switching sequence may be selected for a given PT and operating region based on achievable efficiency. Calculating the PT's exact efficiency for a given switching sequence is not directly accessible without an exact periodic steady-state solution, which requires heavy computation as detailed in Section 3.4.5. Thus, this section explores tools for analytically estimating PT efficiency.

The dominant loss mechanism for a piezoelectric component vibrating in the proximity of its resonant frequency tends to be mechanical loss [79], which we model with the series resis-

[4]For PTs with $N >> 1$, $K_{Bin} \approx 1 - \frac{NV_{in}}{2V_{out}}$ for the V_{in}, *Zero-* | V_{in}, V_{out}, V_{in} sequence, $K_{Bin} \approx \frac{NV_{in}}{2V_{out}}$ for the *Zero+*, -V_{in}, | *Zero+*, V_{out}-V_{in}, *Zero-* sequence, and $K_{Bin} \approx -\frac{1}{2} + \frac{NV_{in}}{2V_{out}}$ for the V_{in}, *Zero-* | V_{in}, V_{out}, *Zero-* sequence (based on the strategy for deriving K in Chapter 2).

tance R in the reduced Mason model. Thus, we focus on the PT's mechanical efficiency for estimating the performance of a PT-based converter implementation. Mechanical efficiency can be estimated using the amplitude of resonance in (3.22) as follows [67]:

$$\eta = \frac{P_{out}}{P_{out} + fE_{loss}} \approx \frac{P_{out}}{P_{out} + \frac{1}{2}I_L^2 R} \tag{3.23}$$

Using this estimation technique, Fig. 3-9 compares the efficiencies of all switching sequences in Tables 3.3 and 3.6 across their respective ZVS regions (as derived in Section 3.5.3) using the manufacturer-provided PT parameters in Table 3.8. Beginning at $\frac{V_{out}}{V_{in}} = N$, Fig. 3-9 illustrates how efficiency changes with voltage conversion ratio when varying only V_{in} (dashed lines) or only V_{out} (solid lines) for each sequence. The efficiency trends are not symmetrical due to offsets in their ZVS boundaries, but they do demonstrate considerably wide gain ranges with high efficiency.

Fig. 3-9 also reveals significant differences in obtainable efficiency between the sequences themselves. For a given operating point and PT, (3.23) shows that I_L should be minimized for high efficiency. However, sequence characteristics that minimize I_L are in direct conflict (i.e., a full-bridge sequence enables higher K than a half-bridge sequence but requires twice the open stage charge transfer), creating a trade-off that must be evaluated by the designer. Full-bridge sequences achieve highest efficiencies for the power level of Fig. 3-9(a), though half-bridge sequences are capable of these efficiencies at a lower power level as shown in Fig. 3-9(b) (sequences plotted in black and gray are directly comparable between the plots since they can be equally realized with or without isolation). Further, Fig. 3-9(b) illustrates how some non-isolated sequences are capable of higher efficiencies than isolation-compatible sequences if permitted by the application. For both plots, the specific implementation that achieves highest efficiency varies based on operating point and PT properties, underscoring the utility of this estimation technique.

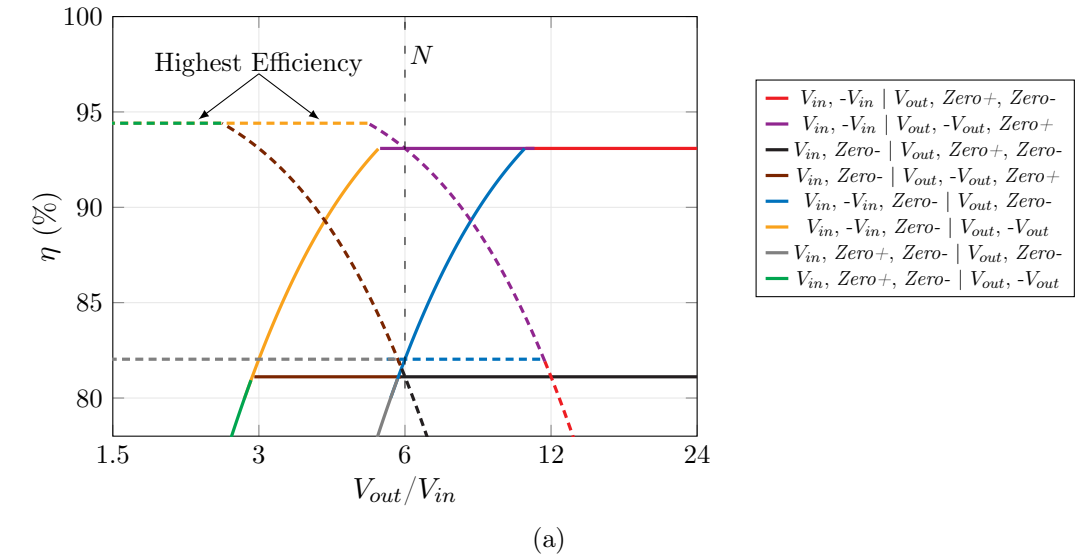

(a)

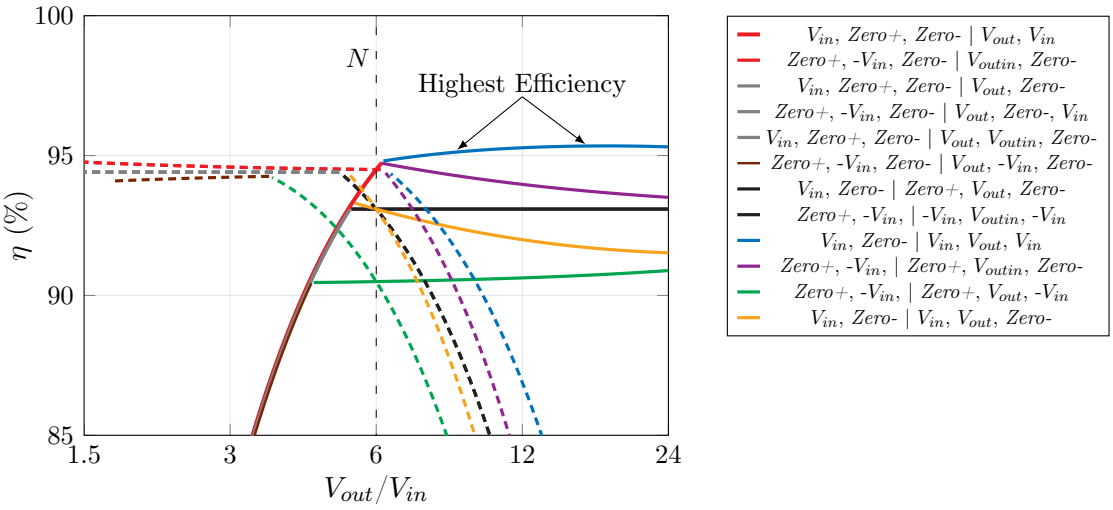

(b)

Figure 3-9: Estimated efficiency vs. $\frac{V_{out}}{V_{in}}$ for varying only V_{in} (dashed lines, V_{out} = 400 V) or only V_{out} (solid lines, V_{in} = 66.7 V) for (a) isolated sequences in Table 3.3 with P_{out} = 8 W, and (b) non-isolated sequences in Table 3.5 with P_{out} = 2 W. Efficiency estimates based on (3.23), assuming the manufacturer-provided PT parameters in Table 3.8 and the ZVS regions of (3.19) and (3.20). Sequences marked by the same color within a plot have indistinguishable efficiency characteristics, though only black and gray correspond between (a) and (b). In legend, $V_{outin} = V_{out}$-V_{in}.

3.5.6 Peak Efficiency

Evaluating the peak achievable efficiency for a given switching sequence and PT is also useful when selecting and designing an implementation. To estimate peak efficiency, we can directly maximize η with respect to operating point parameters. For a switching sequence with a fixed K_B or K_{Bout} (i.e., a 4-stage sub-sequence), efficiency is maximized with respect to P_{out} when

$$P_{out} = 2fC_{pB}V_{ppB}V_{out}K_B \tag{3.24}$$

which provides peak efficiency of

$$\eta_{peak} = \frac{1}{1 + \frac{2\pi^2 fN^2 RC_{pB}V_{ppB}}{K_B V_{out}}} \tag{3.25}$$

for which $K_B = K_{Bout}$ may be substituted for non-isolated sequences. For switching sequences with fixed K_A, this maximum efficiency and corresponding power condition can be similarly derived to be functions of C_{pA}, V_{in}, V_{ppA}, and K_A (and other relevant parameters related to K_{Bin}, if applicable).

PT-based converters can be designed to achieve maximum efficiency for a nominal operating point by satisfying (3.24). For example, to increase the maximum-efficiency power level for a given voltage specification, the designer may choose a PT with a higher fC_{pB} product or a switching sequence with a higher $V_{ppB}K_B$ product.

It should be noted that the peak efficiency operating point in (3.25) is only achievable if it falls within the switching sequence's ZVS region. Fig. 3-10 displays the peak efficiency and ZVS-boundary efficiency for the V_{in}, *Zero+*, *Zero-* | V_{out}, V_{in} switching sequence with the on-board measured PT parameters in Table 3.8. For $\frac{V_{out}}{V_{in}} > 3$, the peak efficiency operating point falls within the ZVS region and can be achieved along with several other high-efficiency operating points surrounding the peak. For $\frac{V_{out}}{V_{in}} < 3$, the ZVS boundary prevents peak efficiency from being reached, confining the achievable efficiency with ZVS to a lower value.

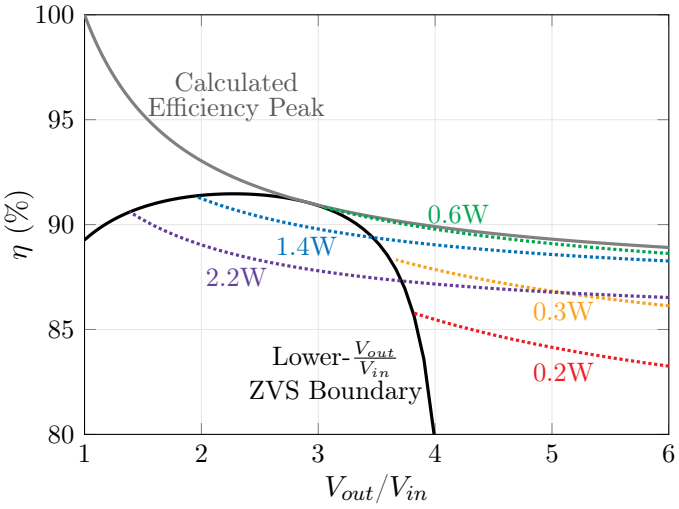

Figure 3-10: Achievable efficiency vs. $\frac{V_{out}}{V_{in}}$ for sequence V_{in}, *Zero+*, *Zero-* | V_{out}, V_{in} considering the ZVS boundary of (3.20), assuming the on-board PT parameters in Table 3.8 and V_{out} = 360 V. Example power levels marked by color.

3.6 Experimental Validation

We illustrate an example converter implementation and validate the analyses of this chapter with a 180 - 500 V experimental prototype. Here we detail this prototype's construction and performance.

3.6.1 Prototype

For this prototype design, we select the non-isolated V_{in}, *Zero+*, *Zero-* | V_{out}, V_{in} switching sequence. This is one of the highest-performing sequences in the $\frac{V_{out}}{V_{in}} < N$ range according to Fig. 3-9(b), and because it regulates with its input port (i.e., K_{Bout} is fixed), it can be implemented with a circuit topology having only two active switches such as Fig. 3-11.

We implement the topology of Fig. 3-11 on a two-layer 1-oz copper board as shown in Fig. 3-12, with the parts listed in Table 3.9. The STEMiNC PT is selected from commercially available PTs based on performance capability using the efficiency estimation method of Section 3.5.5. Since C_{pA} and C_{pB} are relatively small for this PT, both the active switches and Schottky diodes are selected for minimal output capacitance to minimize their contributions

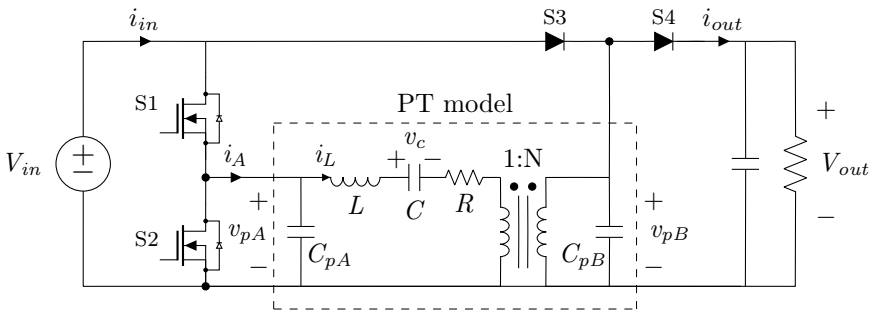

Figure 3-11: Example implementation of the topology in Fig. 3-4(b), with S3 and S4 implemented as diodes.

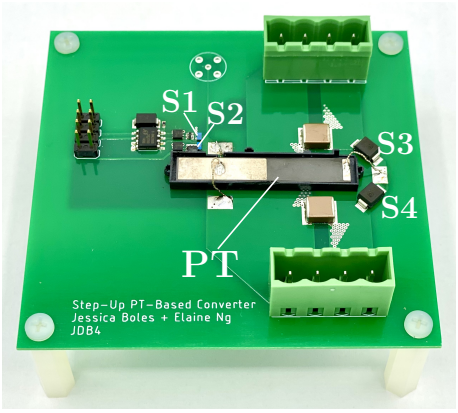

Figure 3-12: Prototype circuit board for the topology of Fig. 3-11.

Table 3.9: Prototype Parts List

Component	Part
PT	STEMiNC SMSTF50P2S6
Active Switch	EPC2012C GaN FET
Schottky Diode	Genesic Semiconductor GB01SLT06-214
Gate Driver	Texas Instruments UCC27611

to the switch node capacitances. Once mounted on the board with all components, the PT's effective parameters are characterized using an impedance analyzer (with no external voltage bias, and 1 Vpp excitation) to have the on-board values provided in Table 3.8. More details about this prototype, including its PCB layout, are provided in Appendix A.3.2.

We operate this prototype with open-loop control of all gate signals, which we manually tune for the desired switching sequence and its high-efficiency behaviors. Since this work

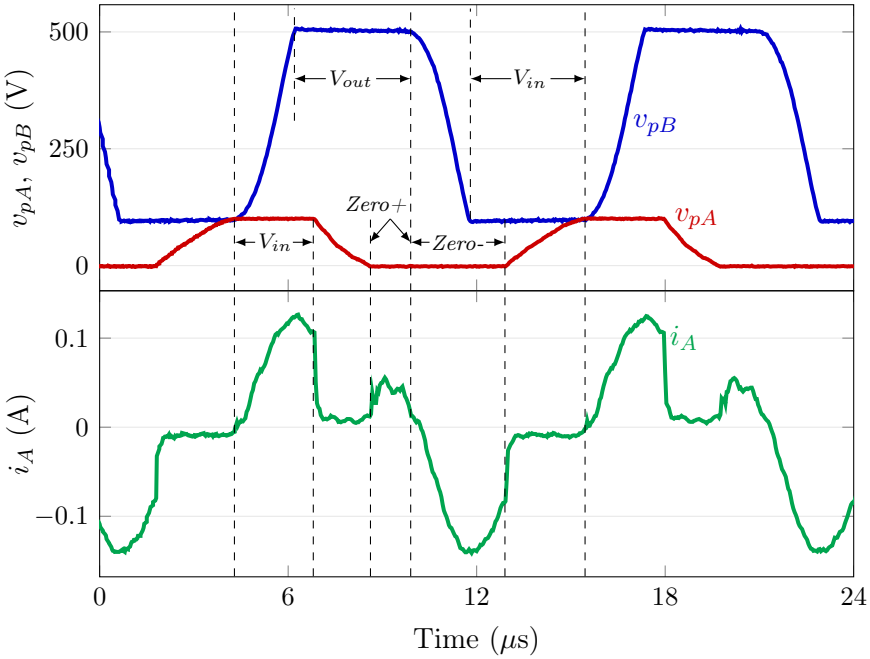

Figure 3-13: Experimental waveforms for switching sequence V_{in}, *Zero+*, *Zero-* | V_{out}, V_{in} operating at $V_{in} = 100$ V, $V_{out} = 500$ V, and $P_{out} = 1.5$ W. Stages are labeled in black, and v_{pA}, v_{pB}, and i_A are defined in Fig. 3-11.

focuses on steady-state operation rather than start-up or dynamic behavior, the open-loop switching times are applied as-is at start-up and suffice for establishing the desired steady-state operation. The effect of an oscilloscope probe on the PT's output port capacitance is non-negligible, so this probe is removed for the experimental results of Fig. 3-15. Further, because the PT's properties have high dependence on temperature, the results of Fig. 3-15 are acquired shortly after powering up the converter and not necessarily at thermal equilibrium.

3.6.2 Waveforms

This prototype's experimental waveforms are displayed in Fig. 3-13. These waveforms illustrate key elements of the switching sequence's high-efficiency behaviors. The resonant transitions of v_{pA} and v_{pB} between connected stages indicate ZVS, and the positioning of these stages with reference to the inverter's output current i_A demonstrates all-positive in-

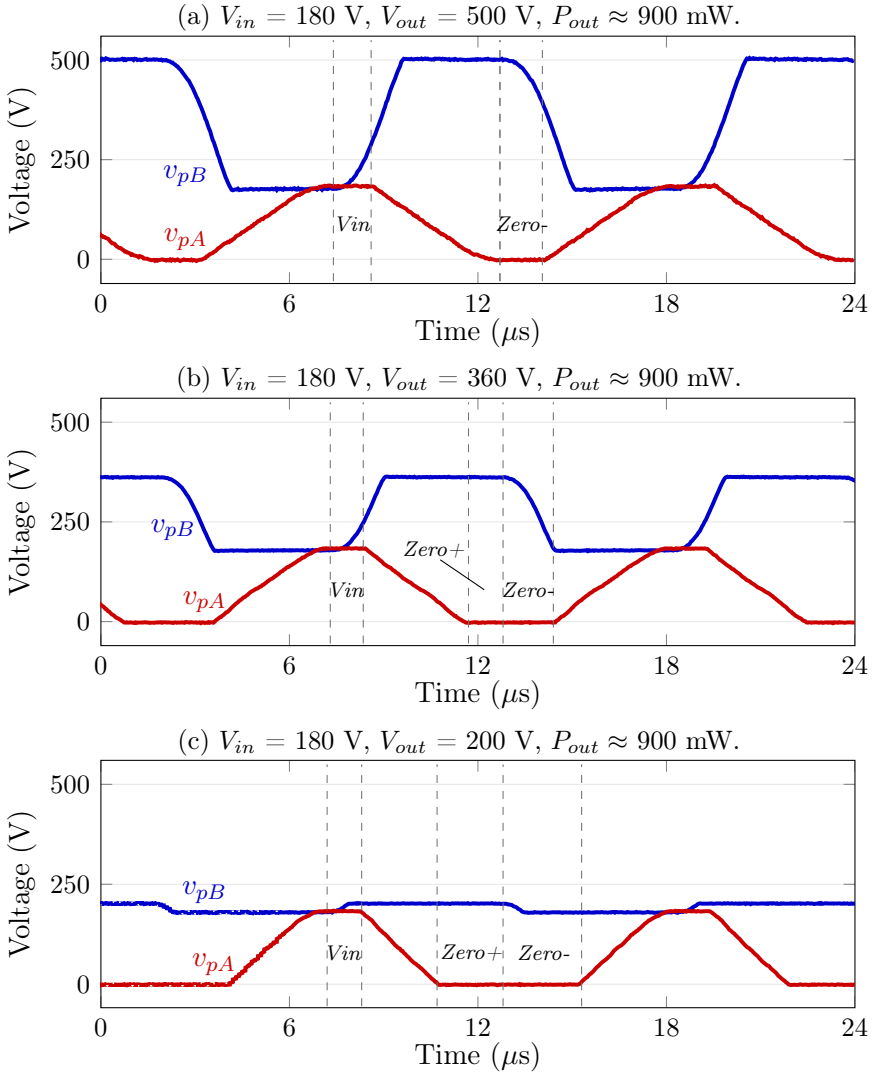

Figure 3-14: Experimental waveforms for switching sequence V_{in}, *Zero+*, *Zero-* | V_{out}, V_{in} operating at 900 mW and V_{in} = 180 V for (a) $\frac{V_{out}}{V_{in}}$=2.78, (b) $\frac{V_{out}}{V_{in}}$=2, and (c) $\frac{V_{out}}{V_{in}}$=1.11 with the prototype described in Section 3.6.1. Stages of the input-port sub-sequence are labeled.

stantaneous power transfer and unidirectional current within each stage to minimize charge circulation. It is also shown that i_A drops to near-zero during open stages, indicating that most of i_L is being used to charge/discharge C_{pA} and therefore validating that C_{pA} is dominant over switch capacitances as assumed for ZVS analysis in Section 3.5.3.

Fig. 3-14 illustrates how the switching sequence adapts for different voltage gains with constant V_{in} and P_{out}. Between these operating points, the input port's *Zero+* stage drastically changes in length, ultimately disappearing in Fig. 3-14(a). This translates to a change

Table 3.10: Estimated Power Stage Loss Breakdown

PT	Switch $R_{ds,on}$	Diode V_{fwd}	Total	η
60 mW	77 μW	4 mW	64 mW	90.3 %

Operating point: V_{in} = 120 V, V_{out} = 360 V, P_{out} = 0.6 W, I_L = 67 mA

in K_A, which can serve as a control handle for regulating V_{out} as discussed in Chapter 4.

3.6.3 Gain

Fig. 3-15(a) plots experimental $\frac{V_{out}}{V_{in}}$ as a function of frequency for different power levels, and each curve represents a constant load resistance. The proposed sequences require operation in the PT's inductive region, which is slightly above its resonant frequency (≈89 kHz for this PT). Fig. 3-15(a) maps how these switching sequences adapt for different V_{out} and/or power, analogous to selecting K_A or constraining the final degree of freedom in the periodic steady-state solution of Section 3.4.3. For the same $\frac{V_{out}}{V_{in}}$, higher power and/or voltage is achieved with frequencies at the low end of the inductive region (closer to the resonant frequency), and lower voltage/power is obtained at higher frequencies (but not exceeding the anti-resonant frequency).

3.6.4 ZVS and Efficiency

We evaluate the prototype's performance over various $\frac{V_{out}}{V_{in}}$ and power levels. Table 3.10 shows the estimated power-stage loss breakdown for an example operating point, revealing the PT to be the dominant source of loss. Fig. 3-15(b) plots power-stage efficiency vs. $\frac{V_{out}}{V_{in}}$ according to output power, keeping V_{out} constant and varying V_{in}. The relatively flat efficiency slope for a given power level echoes the estimated trend for PT efficiency in Figs. 3-9(b) and 3-10. For constant V_{out}, this sequence is capable of wide $\frac{V_{out}}{V_{in}}$ ranges with little efficiency penalty.

In 3-15(b), each power sweep is conducted for the full $2 < \frac{V_{out}}{V_{in}} < 6$ range to the extent that ZVS can be achieved. For $P_{out} < 0.8$ W, the ZVS boundary is encountered before the sweep can be completed at low $\frac{V_{out}}{V_{in}}$. Thus, we overlay this switching sequence's modeled ZVS

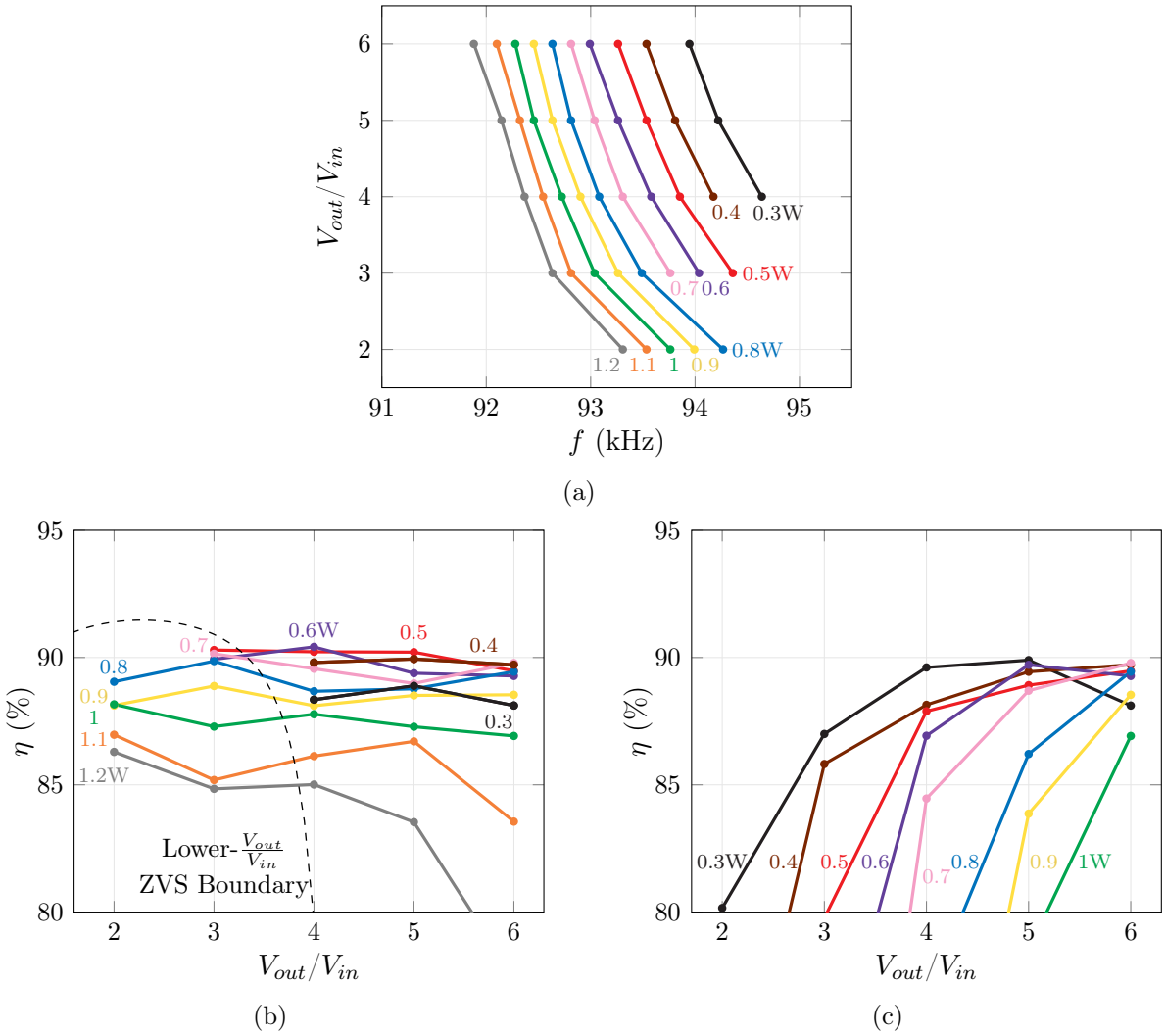

Figure 3-15: (a) Experimental $\frac{V_{out}}{V_{in}}$ vs. frequency for constant $V_{out} = 360$ V and various power levels (marked). Curves represent constant load resistances. (b) Experimental power-stage efficiency vs. $\frac{V_{out}}{V_{in}}$ for constant $V_{out} = 360$ V and various power levels (marked). ZVS boundary calculated using (3.20). (c) Experimental power-stage efficiency vs. $\frac{V_{out}}{V_{in}}$ for constant $V_{in} = 100$ V and various power levels (marked). Efficiencies do not consider auxiliary power.

boundary from Fig. 3-10 (given the on-board PT model characteristics provided in Table 3.8), which appropriately traces the observed ZVS boundary. Further, the experimental efficiency peaks with respect to power for $\frac{V_{out}}{V_{in}}$ greater than the ZVS boundary, as also modeled in Fig. 3-10.

Fig. 3-15(c) similarly displays efficiency vs. $\frac{V_{out}}{V_{in}}$ according to power level for constant V_{in} and varying V_{out}. In this case, efficiency drastically drops as $\frac{V_{out}}{V_{in}}$ decreases, a trend that is

also reflected in Fig. 3-9(b) for this sequence. Although this may be unattractive for some applications, Fig. 3-9 suggests the opposite trend to be true for other sequences serving the $\frac{V_{out}}{V_{in}} > N$ region (i.e., these sequences would be capable of high-efficiency voltage regulation with constant V_{in}).

Overall, the efficiency trends of this prototype validate the estimated trends of Section 3.5.5, constrained by the ZVS boundary derived in Section 3.5.3. The peak experimental efficiencies track the modeled values, though with steeper decline with respect to power than expected. In addition to non-PT losses in the circuit, this discrepancy can be attributed to the charge transfer analysis of Section 3.5 neglecting R; the calculated value for I_L does not consider the additional charge displacement necessary to make up for loss in the PT and therefore degrades in validity with higher loss. This discrepancy may also be due to differences between the PT's small-signal and large-signal characteristics with respect to amplitude of resonance.

The efficiencies obtained for this prototype exceed the whole-converter efficiencies reported for most magnetic-less PT-based dc-dc converters in the literature, attesting to the high performance capabilities of the proposed switching sequences. The power levels corresponding to these efficiencies is limited by the off-the-shelf PT; this dependence on PT parameters, along with strategies for increasing power capability, is discussed in Section 3.5.6. Further gains in efficiency and power handling capability may be achieved through optimization of the PT itself as explored in Chapter 8.

3.7 Conclusion

In this chapter, we have systematically enumerated isolated and non-isolated dc-dc converter implementations that rely solely on a PT for energy storage. This process yields eight isolated switching sequences and twelve non-isolated switching sequences that facilitate high-efficiency behaviors across wide operating ranges. Such high-efficiency behaviors include ZVS, all-positive instantaneous power transfer, and minimum charge circulation. These switching sequences can be realized with practical topologies, many of which may

be implemented with only two active switches. Once a converter implementation has been selected, we can solve for periodic steady-state switching times that may be used for ideal simulation of a desired converter topology and switching sequence. The amplitude of resonance model and charge transfer analysis can be employed to quantify PT cycle utilization, derive ZVS boundaries, and estimate PT efficiency; these steps are useful for selecting the most appropriate converter implementation and/or PT for a given application.

This analysis is validated in an experimental prototype based on a commercially available PT. The proposed switching sequences enable higher whole-converter efficiencies than reported for most magnetic-less PT-based converters through strategic utilization of the PT. Assuming further optimization of the PT (as explored in Chapter 8), PT-based converters are favorable for high-voltage, low-power applications, especially those requiring significant conversion ratios and/or isolation.

The work of this chapter has been published in [77, 80, 81], and further discussion of this approach can be found in Master of Engineering thesis [82].

Chapter 4

Closed-Loop Control of Piezoelectric-Based DC-DC Converters

4.1 Introduction

High-efficiency PR- and PT-based converter implementations are proposed and demonstrated in Chapters 2 and 3, respectively. These converter implementations are distinguished by six-stage switching sequences that enable high-efficiency behaviors such as soft charging, ZVS, all-positive instantaneous power transfer, and minimal charge circulation across wide operating regions. While these six-stage sequences are advantageous for realizing the efficiency capabilities of piezoelectrics, they are more complex than standard power converter operating modes (including those of previous piezoelectric-based converters [29,75,83–89]). Closed-loop control for these six-stage switching sequences is challenging in that it requires frequency modulation, pulse-width modulation, and dead time control, with additional control required for active rectification. To add, piezoelectrics contain at least three states with two always resonating, and piezoelectric material properties are highly dependent on temperature.

Closed-loop control strategies have been developed for six-stage switching sequences in [58,90]. These methods are implemented with voltage-sensed switching, in which the switch on-time durations are the primary control variables and frequency is determined passively.

Although voltage-sensed switching has been used in high-frequency power converters (e.g., [91, 92]), hardware limitations may constrain the upper bound for switching frequency with these methods.

In this chapter, we explore closed-loop control strategies for six-stage switching sequences in the context of PR-based dc-dc converters, including viable control methods for high-frequency operation. We first describe and model the voltage regulation capability of a six-stage switching sequence assuming all high-efficiency behaviors are maintained. Then, we propose closed-loop control strategies for both regulating voltage and maintaining each of the switching sequence's high-efficiency behaviors, which we validate in an experimental prototype. Although these strategies are developed in the context of specific PR-based switching sequence, they may be generally applied to any PR- or PT-based six-stage switching sequence requiring two half-bridges.

The work of this chapter was conducted primarily by Joshua Piel with my supervision. This chapter is intended to serve as a summary, and the reader is encouraged to reference Joshua Piel's Master of Engineering thesis [93] for more details.

4.2 Output Voltage Regulation

Before we discuss full closed-loop control strategies for six-stage switching sequences, we first describe how these sequences adapt for different voltage conversion ratios, how this can be leveraged for voltage regulation, and how their high-level dynamics can be modeled.

4.2.1 Regulation in a Six-Stage Switching Sequence

The periodic steady-state operation of a six-stage switching sequence is constrained by its high-efficiency behaviors, which dictate its necessary switching times as described in Sections 2.4 and 3.4. For a given V_{in} and load, this system of switching constraints contains only one degree of freedom for regulating v_{out}. Frequency is not an independent control handle and is instead determined by the time duration required to complete all stages.

The mechanism by which these switching sequences regulate output voltage can be illustrated through their energy and charge balance equations derived in Sections 2.2.4 and 3.2.3. For example, the V_{in}-V_{out}, *Zero*, V_{out} PR-based switching sequence requires the following equation to hold for energy and charge balance on the PR (following the derivation of Section 2.2.4):

$$(V_{in} - V_{out})|q_1| - V_{out}(|q_1| + |q_3|) = 0 \tag{4.1}$$

where q_1 and q_3 are the quantities of charge displaced by i_L during stages 1 and 3, respectively, with stage numbers defined as in Chapter 2.

Stages 1 and 3 in this switching sequence both require positive i_L for high efficiency, so these stages are confined to the positive half of the assumed-sinusoidal i_L cycle. Thus, for different V_{out} with respect to V_{in}, the relative durations of stages 1 and 3 within the positive i_L half-cycle can be modulated such that q_1 and $q3$ satisfy (4.1). In the topology of Fig. 4-1, this translates to modulating the S1 and S2 on-times, or their duty cycle. Example waveforms for the V_{in}-V_{out}, *Zero*, V_{out} sequence in this topology are displayed in Fig. 4-2.

All six-stage switching sequences in the context of Chapters 2 and 3 require one such half-bridge or switch pair employing duty cycle modulation to maintain energy and charge balance. We refer to this half-bridge as the "regulating" half-bridge and other half-bridge(s) as "non-regulating" half-bridge(s) within a given topology. Regulating and non-regulating half-bridges play distinct roles in closed-loop control of these switching sequences as detailed in Section 4.3.

4.2.2 Dynamic Model

The output voltage dynamics of a piezoelectric-based switching sequence can be modeled by assuming the S1 on-time duration ($S1_{on}$) is the only control handle and the switching sequence's other high-efficiency behaviors are perfectly maintained. This state space model requires only two states: v_{out} and the piezoelectric component's amplitude of resonance I_L (i.e., the amplitude of $i_L(t)$) described in Sections 2.5 and 3.5 and visualized in Fig. 4-3.

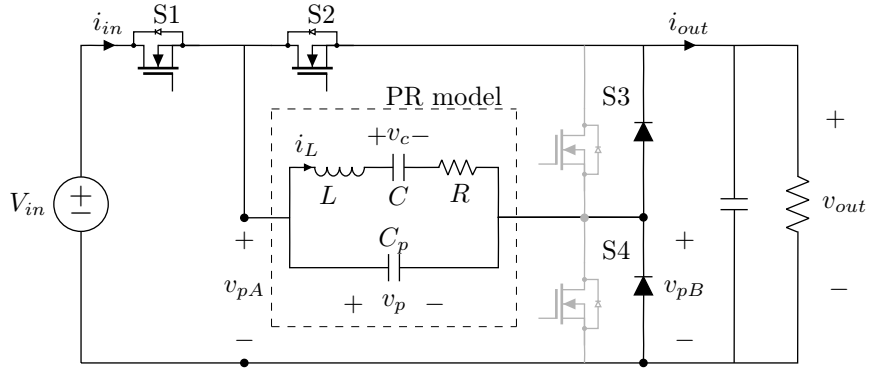

Figure 4-1: PR converter topology for switching sequence V_{in}-V_{out}, *Zero*, V_{out}, with the PR model enclosed in dotted lines.

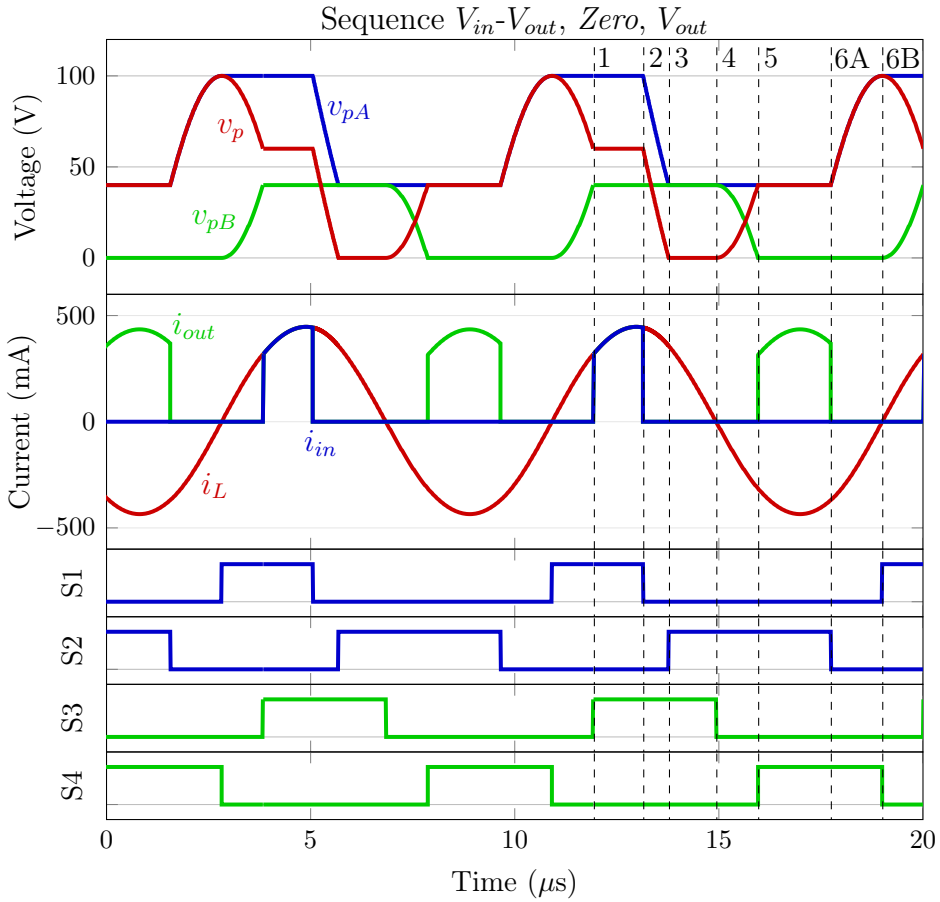

Figure 4-2: Simulated waveforms of V_{in}-V_{out}, *Zero*, V_{out} for $V_{in} = 100$ V, $V_{out} = 40$ V, and $P_{out} = 6$ W. Numbers 1-6B designate stage transitions.

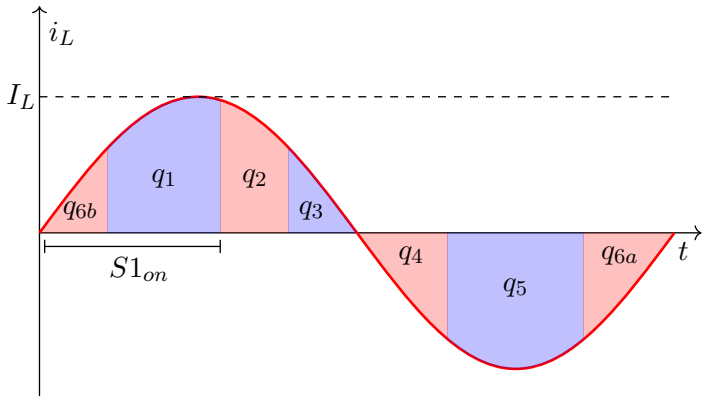

Figure 4-3: Assumed-sinusoidal i_L and amplitude of resonance I_L for the V_{in}-V_{out}, *Zero*, V_{out} switching sequence. The charge displaced during each stage n is labeled with q_n, corresponding to stage numbers defined in Fig. 4-2. Figure source: Joshua Piel.

In deriving this model, we assume an ideal component and a constant switching period T (i.e., the range of compatible frequencies is confined to the component's inductive region), and v_{out} and I_L are assumed to be constant within a single switching period. In addition to tracking v_{out}, we would like to track the dynamic evolution of I_L, which varies slowly with respect to an individual switching period.

For the V_{in}-V_{out}, *Zero*, V_{out} switching sequence and the topology of Fig. 4-1, we derive the state trajectory of v_{out} by enforcing charge balance on the load capacitance. Every switching period, the PR delivers $|q_1| + |q_5|$ to this capacitance, constituting an average PR output current of $\frac{|q_1|+|q_5|}{T}$. The average load current supplied by this capacitance is $\frac{v_{out}}{R_{load}}$. Thus, the state evolution of v_{out} can be described by

$$\frac{dv_{out}}{dt} = \frac{1}{C_{out}} \left(\frac{|q_1| + |q_5|}{T} - \frac{v_{out}}{R_{load}} \right) \tag{4.2}$$

We derive the dynamic behavior of I_L by equating the net energy supplied by the source-load system to a change in the PR's stored energy. Every switching period, the system delivers $(V_{in} - v_{out})|q_1|$ to the PR and extracts $v_{out}|q_5|$. This translates to the following model for the quantity of energy stored in the PR (E_{stored}):

$$\frac{dE_{stored}}{dt} = \frac{(V_{in} - v_{out})|q_1| - v_{out}|q_5|}{T} \tag{4.3}$$

Assuming most energy is stored in the PR's mechanical states, we can approximate $E_{stored} \approx \frac{1}{2}LI_L^2$. The rate of change for E_{stored} within this definition depends on the time derivative of I_L:

$$\frac{dE_{stored}}{dt} = \frac{d(\frac{1}{2}LI_L^2)}{dt} = LI_L\frac{dI_L}{dt} \tag{4.4}$$

This approximation assumes the change in energy stored in C_p is negligible compared to the change in energy stored in L when i_L is at its peak. Combining (4.3) and (4.4) yields the following state trajectory for I_L:

$$\frac{dI_L}{dt} = \frac{1}{TLI_L}\big(\,(V_{in} - v_{out})\,|q_1| - v_{out}|q_5|\big) \tag{4.5}$$

which completes the following state-space model:

$$\begin{cases} \dfrac{dv_{out}}{dt} = \dfrac{1}{C_{out}}\left(\dfrac{|q_1| + |q_5|}{T} - \dfrac{v_{out}}{R_{load}}\right) \\ \dfrac{dI_L}{dt} = \dfrac{1}{TLI_L}\big(\,(V_{in} - v_{out})\,|q_1| - v_{out}|q_5|\big) \end{cases} \tag{4.6}$$

Charge displacement quantities q_1 and q_5 can be derived by integrating i_L across stages 1 and 5, respectively. For connected/zero stages, this is typically achieved by integrating i_L across a known time duration including the desired stage and subtracting the charge displaced by other included intervals such as open stages. The charge displaced during an open stage is:

$$q_n = C_p(V_{p(n+1)} - V_{p(n)}) \tag{4.7}$$

in which $V_{p(n+1)}$ is the connected/zero-stage voltage V_p of the stage after n, respectively.

To derive $|q_1|$, we integrate i_L across $S1_{on}$ as visualized in Fig. 4-3 and then subtract q_{6b}, resulting in:

$$|q_1| = \frac{TI_L}{2\pi}\left(1 - \cos\left(\frac{2\pi}{T}S1_{on}\right)\right) - C_p v_{out} \tag{4.8}$$

We likewise derive $|q_5|$ by integrating i_L across its negative half-cycle (for its absolute value) and then subtracting q_4 and q_{6a}, resulting in:

$$|q_5| = \frac{TI_L}{\pi} - C_p V_{in} \tag{4.9}$$

These charge displacement quantities are functions of only control handle $S1_{on}$, states I_L and v_{out}, and assumed constants. Inserting (4.8) and (4.9) into (4.6) completes the state-space model in terms of these quantities.

This dynamic model is useful for evaluating a switching sequence's transient performance assuming all other timing aspects of the switching sequence are perfectly maintained. State equations (4.6) can be linearized around an operating point to simulate the switching sequence's behavior with closed-loop output voltage regulation as validated in [93,94]. We note that maintaining the switching sequence's high-efficiency behaviors while regulating voltage requires the full closed-loop control methods discussed in Section 4.3.

4.3 Closed-Loop Control Methods

Six-stage switching sequences require detailed control strategies to both regulate output voltage and maintain the switching sequence's high-efficiency behaviors. Here we present two control strategies for the regulating half-bridge, and an accompanying strategy for the non-regulating half-bridge.

4.3.1 Sensed Control of Regulating Half Bridge

One control method for six-stage switching sequences involves triggering on the regulating half-bridge switches in response to sensed voltage measurements, using the switch on-durations $S1_{on}$ and $S2_{on}$ as primary control variables. We illustrate this "sensed control" concept for the V_{in}-V_{out}, *Zero*, V_{out} sequence in Fig. 4-4, in which S1 and S2 are turned on by sensing v_{pB} and v_{pA}, respectively. $S1_{on}$ and $S2_{on}$ are governed by independent feedback loops for output voltage regulation and maintaining the switching sequence's high-efficiency

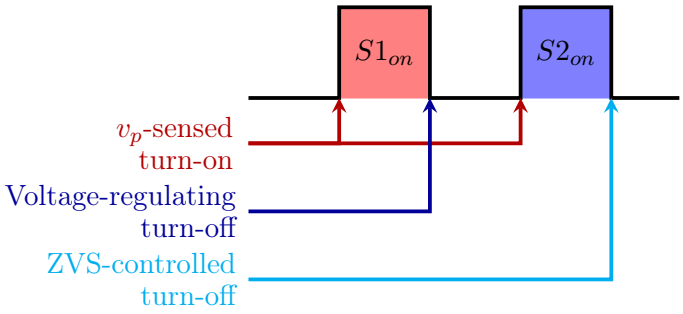

Figure 4-4: Roles of switch transitions and control variables during sensed control. Figure source: Joshua Piel.

behaviors, respectively.

To elaborate, S1 is triggered on at an i_L zero crossing, marking the beginning of stage 6B and synchronizing the switching period to the PR's resonant cycle. This i_L zero crossing is detected by v_{pB} rising above zero when S4 (assumed to be a diode) begins blocking voltage. $S1_{on}$ is then controlled based on the error between v_{out} and command output voltage V_{cmd} as shown in Fig. 4-5 and Table 4.1.

S2 is triggered on when v_{pA} drops to v_{out}, marking the beginning of stage 3. $S2_{on}$ is controlled based on the error between v_{pA} and V_{in} at the i_L zero crossing that triggers on S1. Controlling for $v_{pA} = V_{in}$ ensures both ZVS and all-positive instantaneous power transfer (i.e., v_{pA} is not greater than V_{in} at this point due to reverse body-diode conduction), which are both important for maximizing the switching sequence's efficiency.

We note that this sensed control strategy passively determines the converter's switching frequency. Voltage-sensed switching strategies have been utilized in high-frequency converters, but hardware limitations may constrain their upper frequency bounds.

4.3.2 Static Control of Regulating Half Bridge

An alternative control method for six-stage switching sequences is "static control", in which the switching period, duty cycle, and dead times for the regulating half-bridge are actively set by the controller rather than determined by triggering. This strategy involves four control variables as visualized in Fig. 4-6: $S1_{on}$, S1 dead time $S1_{dt}$, S2 dead time $S2_{dt}$, and the

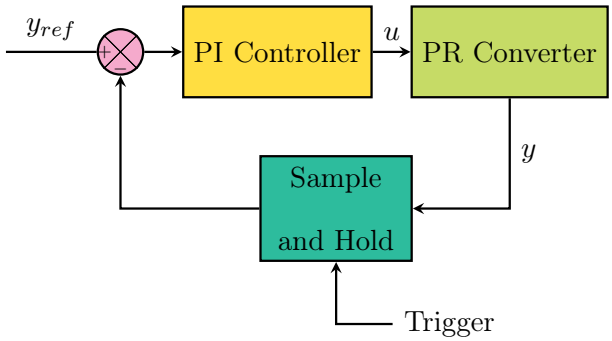

Figure 4-5: Control loops used in both sensed and static control, with corresponding values of y, y_{ref}, and u are provided in Table 4.1. Every PR cycle, the output y from the converter is sampled at the trigger point, just before the specified switch turns on. Figure source: Joshua Piel.

Table 4.1: Control Loop Parameters for Static and Sensed Control

Control Method	Control Variable (u)	Measured Output (y)	Desired Value (y_{ref})	Trigger (Switch Turn-on)
Sensed	$S1_{on}$	v_{out}	V_{cmd}	—
	$S2_{on}$	v_{pA}	V_{in}	$S1$
Static	$S1_{on}$	v_{out}	V_{cmd}	—
	$S1_{dt}$	v_{pA}	V_{in}	$S1$
	$S2_{dt}$	v_{pA}	v_{out}	$S2$
	T	t_{α}	$\frac{1}{2}t_{\beta}$	—
	$S3_{dt}$	v_{pB}	v_{out}	$S3$

switching period T. We note that $S2_{on}$ is collectively determined by these four control variables.

In this static control strategy, $S1_{on}$ is likewise modulated for regulating v_{out} to V_{cmd}. $S1_{dt}$ and $S2_{dt}$ are controlled for ZVS, using the errors between v_{pA} and V_{in} (just before S1 turns on) as well as v_{pA} and v_{out} (just before S2 turns on), respectively. T is controlled such that the turn-on of S1 aligns with the i_L zero crossing, synchronizing the switching period to the PR's resonant cycle.

In a six-stage switching sequence, an i_L zero crossing occurring at the transition between two open stages can be tracked geometrically. In an open-circuited PR, $\frac{dv_p}{dt} = -\frac{i_L}{C_p}$, implying that v_p is either maximum or minimum during an i_L zero crossing and temporally symmetric

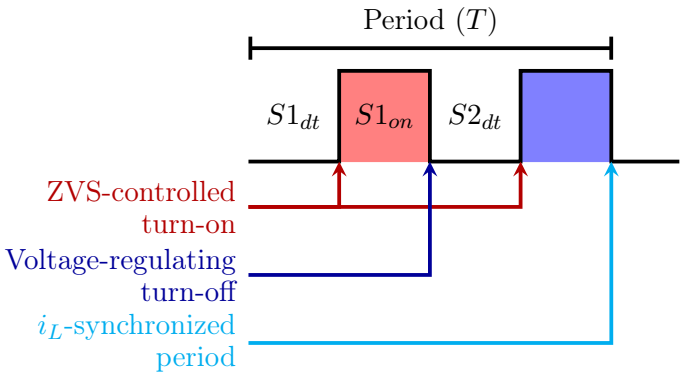

Figure 4-6: Roles of switch transitions and control variables during static control. Figure source: Joshua Piel.

around this peak. Thus, the maximum or minimum occurs temporally halfway between two points of same voltage v_p occurring before and after it.

As illustrated in Fig. 4-7 for the V_{in}-V_{out}, *Zero*, V_{out} sequence, we leverage this strategy to track the i_L zero crossing with respect to the switching cycle. The i_L zero crossing can be assumed to occur temporally halfway between when v_p rises $V_{in} - V_{out}$ in stage 6a and when v_p decreases back to $V_{in} - V_{out}$ in stage 6b. Using existing voltage measurements, these points occur when v_{pA} rises above $V_{in} - V_{out}$ in stage 6a and when v_{pB} falls to V_{out} at the end of stage 6b. The turn-on of S1 is intended to coincide with the i_L zero crossing as shown in Fig 4-7 but can become misaligned as the PR's resonant period increases or decreases as shown in Fig. 4-8. Thus, T is controlled such that the turn-on of S1 aligns with this timing estimation of the i_L zero crossing.

This static control strategy is more robust than the sensed-switching strategy to high-frequency noise, interference due to spurious modes, and comparator delays, making it more suitable for use at high switching frequencies. We note that the symmetry assumption at the foundation of this method depends on the resonating switch capacitances of stages 6a and 6b being equal or negligible compared to C_p. Additional i_L synchronization strategies are discussed in [75] in the context of PT-based converters.

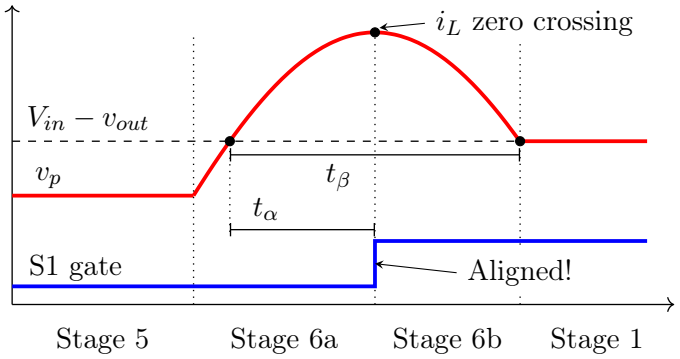

Figure 4-7: Symmetry-based i_L zero crossing detection for the V_{in}-V_{out}, *Zero*, V_{out} switching sequence. In this example, S1's turn-on is exactly aligned with the i_L zero crossing, so $t_\alpha = \frac{1}{2}t_\beta$. Figure source: Joshua Piel.

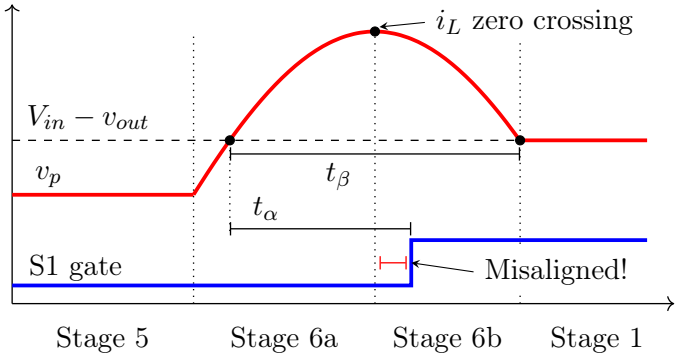

Figure 4-8: Symmetry-based i_L zero crossing detection for the V_{in}-V_{out}, *Zero*, V_{out} switching sequence. In this example, S1's turn-on occurs after the i_L zero crossing, so $t_\alpha > \frac{1}{2}t_\beta$. Figure source: Joshua Piel.

4.3.3 Synchronous Control of Non-Regulating Half Bridge

Non-regulating rectifiers for several switching sequences described in Chapters 2 and 3 may be implemented passively with diodes to simplify control. For the V_{in}-V_{out}, *Zero*, V_{out} sequence, this applies to S3 and S4 in the topology of Fig. 4-1 for the $\frac{V_{out}}{V_{in}} < \frac{1}{2}$ operating region. However, maximizing efficiency requires active implementation of all switches to avoid loss incurred by diode forward voltage drops. Here we discuss a non-regulating half-bridge control strategy compatible with the static control method detailed in Section 4.3.2.

Non-regulating half bridges are synchronized to the period of the regulating half bridge. Although they have their own duty cycles, dead times, and phase shift with respect to the

regulating half bridge, only one additional control handle is needed beyond the static control implementation described in Section 4.3.2. For the V_{in}-V_{out}, *Zero*, V_{out} sequence, the phase shift between half bridges is constrained by S4 turning off exactly when S1 turns on, which is already controlled to align with the i_L zero crossing in the static control framework. Further, the duty cycle of a non-regulating half bridge can be approximated as 50%, and its dead times can be approximated as equal since both open stages border i_L zero crossings and displace the same quantity of charge. Thus, the switching times for a non-regulating half bridge can be constructed with only one additional control variable for dead time.

In the context of V_{in}-V_{out}, *Zero*, V_{out}, we refer to the non-regulating half bridge dead time as $S3_{dt}$. Similar to $S1_{dt}$ and $S2_{dt}$, $S3_{dt}$ is controlled for ZVS using the error between v_{pB} and v_{out} (just before S3 turns on). We note that controlling $S3_{dt}$ simplifies the i_L zero crossing detection for static control since it directly defines the time duration of stage 6b.

4.4 Example Implementation

We validate the static control strategy described in Section 4.3 using the V_{in}-V_{out}, *Zero*, V_{out} PR-based switching sequence. Here we describe the prototype's implementation details and its experimental results.

4.4.1 Prototype

For validation of closed-loop control, we re-purpose the prototype board of Chapter 2 to have a larger, lower-frequency PR (APC International part 1553). This prototype is pictured in Fig. 4-9 and consists of the parts and PR model parameters listed in Table 4.2. This PR has a smooth impedance characteristic throughout its inductive region and requires a switching frequency of approximately 80 kHz.

The prototype's controller is implemented digitally using the Texas Instruments F28379D Control Card microcontroller and its built-in PWM modules, ADCs, and comparators. The gate signals for S1 and S2 are generated by independent PWM modules configured for a

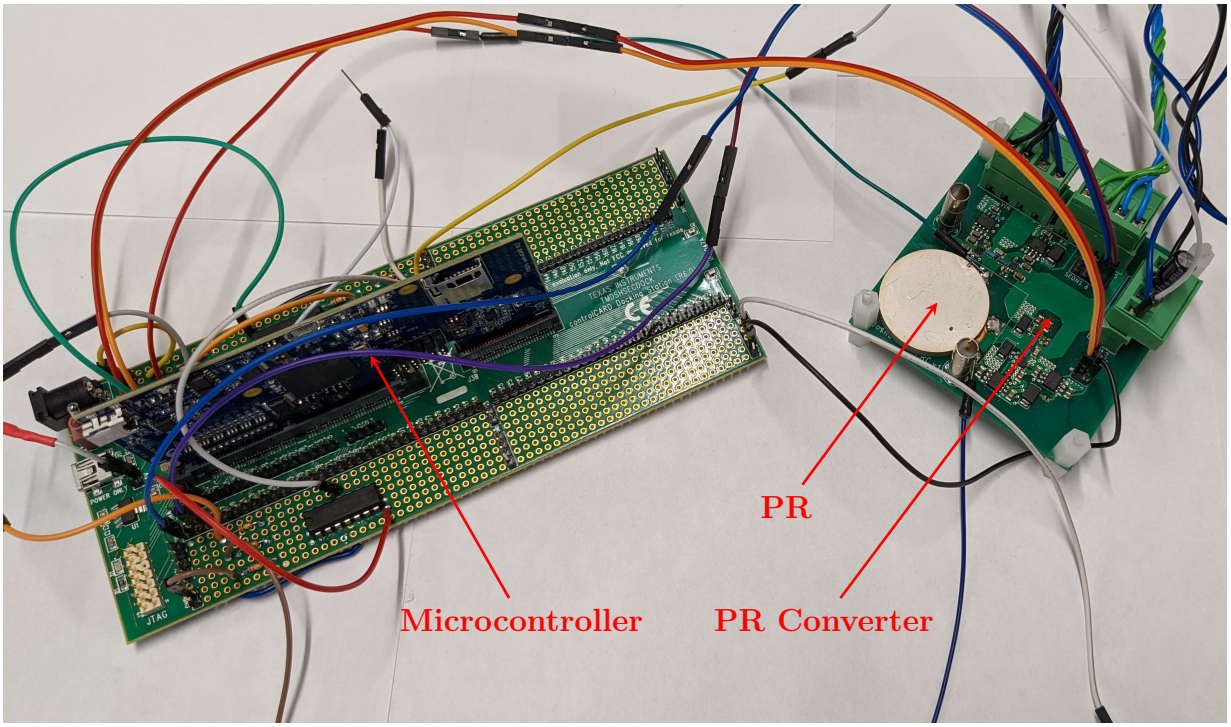

Figure 4-9: Photo of the experimental setup. Figure source: Joshua Piel.

specified T, $S1_{on}$, $S1_{dt}$, and $S2_{dt}$ with a resolution of 10 ns. Gate signals for S3 and S4 are likewise generated by PWM modules with the same T, a specified $S3_{dt}$ for both switches, and with S4 turning off exactly when S1 turns on. Feedback loops for these five control variables are implemented with ADCs for sensing, comparators for evaluating error, and discrete-time PI compensators with saturation bounds to prevent invalid switching waveforms.

The sensing circuits for v_{pA}, v_{pB}, and v_{out} consist of voltage dividers (with resistance greater than 100 kΩ) and buffers using a Texas Instruments TL974IN op-amp with a 12 MHz unity gain bandwidth. The v_{out} sensing circuit has an additional low-pass filter based on a Sallen-Key topology with a cutoff frequency of 15 kHz and a quality factor of $\frac{1}{\sqrt{2}}$. The PWM modules trigger sampling of the ADCs at the switch turn-on points displayed in Table 4.1, and v_{out} is sampled once per cycle. To evaluate the error between the turn-on of S1 and the i_L zero crossing, t_α and t_β (defined in Fig. 4-7) are computed using counter modules and a finite state machine within the microcontroller's Configurable Logic Block.

The startup sequence for this control strategy is beyond the scope of this work, so open-

Table 4.2: Experimental Prototype Parts and Parameters

Parameter	Value
PR	APC International part 1553
C_p	1.41 nF
C_r	510 pF
L	8.73 mH
R	2.3 Ω
Switches	EPC2019 GaN FET
Diodes	On Semiconductor NSTA4100
Gate Drivers	Texas Instruments UCC27611
Input Capacitance	45 μF
Output Capacitance	115 μF

loop switching times are used at startup to establish the PR's resonant cycle. The feedback loops described above are enabled after a fixed time delay.

Further implementation details for this prototype can be accessed in [93].

4.4.2 Experimental Results

Periodic steady-state waveforms for the prototype operating with closed-loop control are shown in Figs. 4-10 and 4-11. Fig. 4-10 demonstrates each of switching sequence's high-efficiency behaviors with closed-loop control of only the regulating half bridge; the rectifier is implemented passively. These waveforms demonstrate ZVS and soft charging, apparent in the resonant voltage transitions, as well as all-positive instantaneous power transfer and minimum charge circulation. Fig. 4-11 shows periodic steady-state operation with both the regulating and non-regulating half bridges operating in closed-loop, demonstrating the same high-efficiency behaviors.

Finally, we cycle the prototype through load steps to demonstrate its transient response. Fig. 4-12 contains the converter's transient behavior following a load step from half to full load, exhibiting a peak deviation of 7.5% and a 2% settling time of 14.6ms. Fig. 4-13 displays the prototype's transient response to the opposite step from full to half load, showing a peak

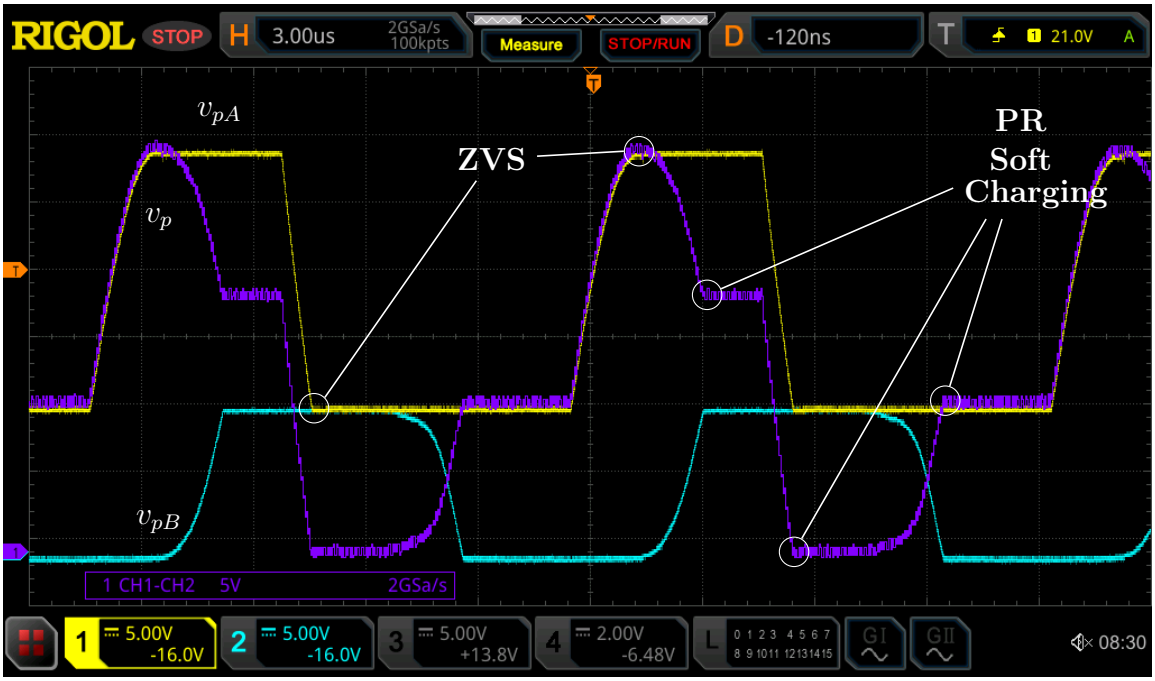

Figure 4-10: Experimental waveforms for the prototype in Fig. 4-9 with closed-loop control of the regulating half bridge. $V_{in} = 30$ V, $v_{out} = 10.4$ V, and $R_{load} = 600\ \Omega$. Figure source: Joshua Piel.

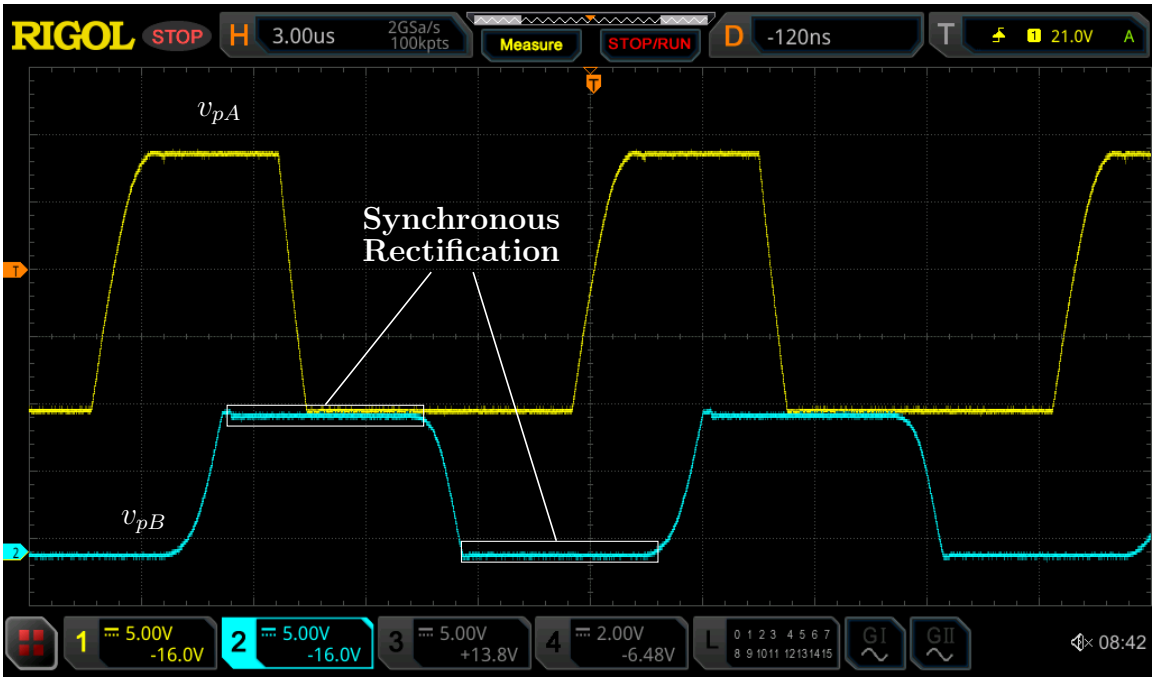

Figure 4-11: Experimental waveforms for the prototype in Fig. 4-9 with closed-loop control of both half bridges. $V_{in} = 30$ V, $v_{out} = 10.4$ V, and $R_{load} = 600\ \Omega$. Figure source: Joshua Piel.

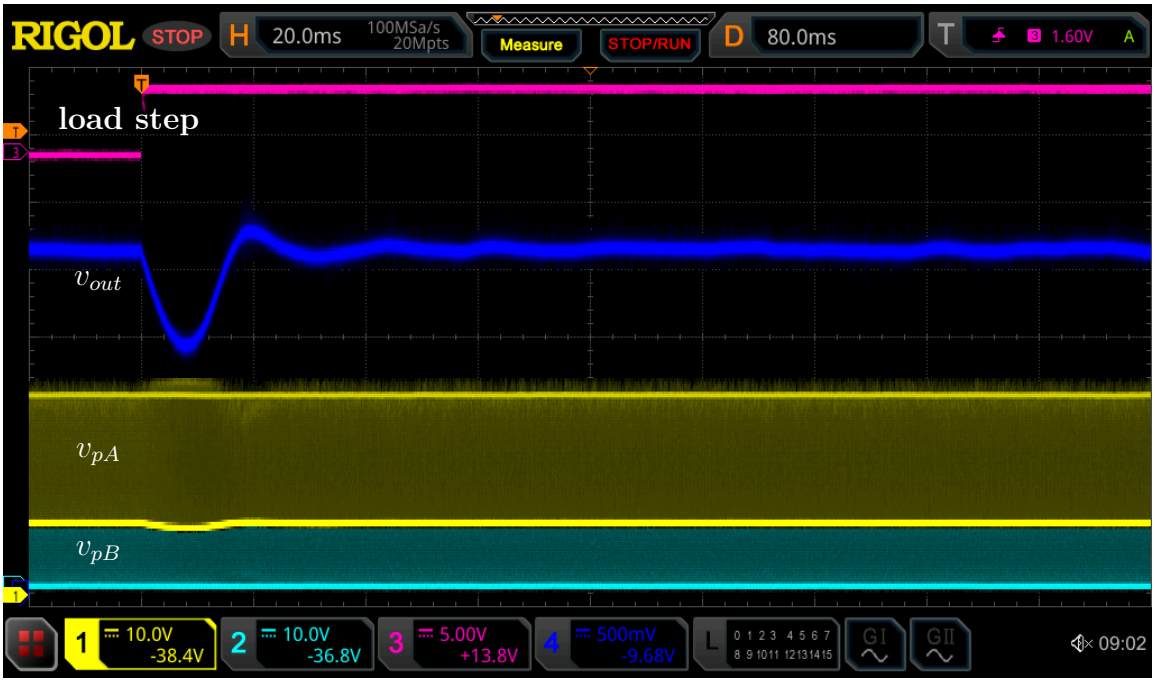

Figure 4-12: Experimental transient response to R_{load} step from 600 Ω to 300 Ω with V_{in} = 30 V and V_{cmd} = 10.4 V. The peak deviation from steady state is 770 mV (7.5% of V_{cmd}) and the 2% settling time is 14.6 ms. Figure source: Joshua Piel.

Figure 4-13: Experimental transient response to R_{load} step from 300 Ω to 600 Ω with V_{in} = 30 V and V_{cmd} = 10.4 V. The peak deviation from steady state is 600 mV (5.8% of V_{cmd}) and the 2% settling time is 18.4 ms. Figure source: Joshua Piel.

deviation of 5.8% and a 2% settling time of 18.4ms. We note that this prototype's transient response could be further improved through optimization of the control coefficients. Beyond this prototype, greater performance could be achieved through use of higher-frequency PRs.

4.5 Conclusion

To facilitate practical use of the high-efficiency switching sequences proposed in Chapters 2 and 3, this chapter proposes multiple closed-loop control methods for six-stage switching sequences. These strategies are capable of both regulating the output voltage and maintaining the switching sequence's high-efficiency behaviors including ZVS, soft charging of the PR's capacitance, and minimal charge circulation. The proposed control methods rely on only voltage measurements and are simple enough for implementation on a digital microcontroller, which we validate experimentally. Closed-loop control is critical for practical use of these six-stage switching sequences, and these proposed methods are promising solutions for implementing such.

The work of this chapter has been published in [93, 94].

Chapter 5

Hybridization with Switched-Capacitor DC-DC Converters

5.1 Introduction

Magnetic-less dc-dc converter implementations based on piezoelectric resonators (PRs) and piezoelectric transformers (PTs) are demonstrated in Chapters 2 and 3, respectively. While PR-based converters are capable of very high efficiencies across wide operating ranges, their efficiency advantages wane at extreme voltage conversion ratios. PTs are advantageous in that they provide inherent voltage transformation, but commercially available PTs are not competitive with PRs in terms of efficiency as illustrated in the experimental prototype of Chapter 3.

Switched-capacitor (SC) converters and hybrid SC/magnetic circuits are widely utilized in non-isolated settings for realizing high voltage conversion ratios with high efficiency and power density [8–14]. Without the presence of magnetics, however, the efficiency advantage of SC-based converters is confined to specific integer conversion ratios. This constitutes an opportunity to hybridize SC-based and PR-based power conversion and leverage their reciprocal advantages to maintain high efficiency and power density for a continuous range of large voltage conversion ratios.

In this chapter, we propose a two-stage PR/SC-based dc-dc converter architecture that serves as one example of such hybridization. This structure consists of a PR-based regulation stage and an SC-based transformation stage, drawing on previous two-stage SC-based architectures leveraging magnetics [9, 10]. For the PR-based regulation stage, we detail use of an eight-stage switching sequence as a means to reduce control complexity. These concepts are demonstrated in an experimental prototype that greatly exceeds the efficiency capability of purely PR-based and PT-based designs for its voltage conversion ratio.

The work of this chapter was conducted primarily by Babuabel Wanyeki with my supervision. This chapter is intended to serve as a summary, and the reader is encouraged to reference Babuabel Wanyeki's Master of Engineering thesis [95] for more details.

5.2 Two-Stage Converter Architecture

We first provide an overview of the two-stage PR/SC-based converter architecture and discuss considerations for how the two stages are ordered.

5.2.1 Two-Stage Concept

Two-stage power converter architectures incorporating SC-based converters are becoming increasingly common, often leveraging magnetics for voltage regulation [9, 10]. We propose a two-stage power conversion concept in which a SC-based stage is similarly utilized for high-efficiency voltage transformation, and a piezoelectric-based stage provides voltage regulation with high efficiency. These stages are cascaded (e.g., as visualized in Fig. 5-1), and they are individually optimized with their own switching frequency and control (though additional coordination between stages may be included). This allows each stage to be independently designed for maximum efficiency and/or power density.

The circuit topologies and operating modes within each of these stages may be selected from previously-established architectures. Several PR-based converter implementations detailed in Chapter 2 are capable of providing high efficiency in the $\frac{1}{2} < \frac{V_{out}}{V_{in}} < 1$ operating

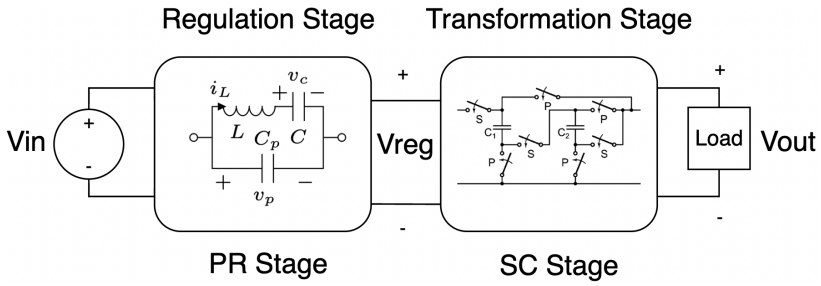

Figure 5-1: Conceptual diagram of the proposed two-stage PR/SC-based converter architecture. Figure source: Babuabel Wanyeki.

region, with gradually decreasing efficiency for $\frac{V_{out}}{V_{in}} < \frac{1}{2}$. We detail a symmetric eight-stage version of these switching sequences with reduced control complexity in Section 5.3. The SC stage may be selected from a wide variety of high-efficiency topologies [14]. As leveraged in some SC/magnetic converters, the two stages may also be merged for additional benefits (e.g., to enable soft charging of the SC stage).

5.2.2 Stage Ordering

For this two-stage converter architecture, there are trade-offs associated with the stage ordering. One may either place the regulation stage (the PR stage) before or after the transformation stage (the SC stage). Most two-stage architectures conduct voltage regulation in close proximity to the load for fast transient response, and hence place the regulation stage after the transformation stage. In this configuration, the regulation stage also acts as a controlled current-source at the output of the transformation stage, which is particularly advantageous for SC-based transformation stages achieving soft charging for high efficiency [9, 13]. However, this configuration requires the regulation stage to handle the lowest voltages and highest currents in a two-stage step-down configuration. While this can be advantageous with magnetics-based regulation stages, bulk PRs tend to have very high characteristic impedance and therefore achieve peak efficiency at high voltage, low current operating points. While PRs may be designed to achieve maximum efficiency at any specific operating point as detailed in Chapter 6, low-characteristic-impedance PRs tend to require extremely planar form factors with greater footprint area.

The high characteristic impedance of presently available bulk PRs motivates placement of a PR-based regulation stage at the higher-voltage end of a converter architecture. For a step-down configuration, this implies that the regulation stage precedes the transformation stage as shown in Fig. 5-1. While its transient response may not be as impressive, this ordering provides opportunity for higher efficiency and power density. The PR in this configuration requires lower footprint area to reach its maximum efficiency point according to the design conditions of Chapter 6, and the SC stage likewise benefits from its components having lower voltage ratings.

5.3 Piezoelectric-Based Regulation Stage

Piezoelectric-based conversion stages require specific operating sequences for high efficiency. Here we present operating characteristics and analysis tools for an eight-stage switching sequence, which serves as a simpler alternative to six-stage sequences.

5.3.1 Eight-Stage Switching Sequence

The PR-based six-stage switching sequences detailed in Chapter 2 provide very high PR efficiency at the expense of complex control. As described in Chapter 4, closed-loop control of these six-stage sequences for voltage regulation and maintaining their high-efficiency behaviors requires five feedback loops, assuming four active switches. In the context of the V_{in}-V_{out}, *Zero*, V_{out} switching sequence and topology of Fig. 5-2, these control variables include the switching period T, the S1 on-time $S1_{on}$, the S1 dead time $S1_{dt}$, the S2 dead time $S2_{dt}$, and the S3/S4 dead time $S3_{dt}$. Five control variables are necessary in part because six-stage switching sequences have asymmetric switching times between the positive-i_L and negative-i_L halves of the switching period.

As also discussed in Chapter 2, these high-efficiency six-stage switching sequences may be expanded into eight-stage sequences capable of similarly-high efficiencies. One such example is the V_{in}, V_{in}-V_{out}, *Zero*, V_{out} sequence, which contains the same stages as V_{in}-V_{out}, *Zero*,

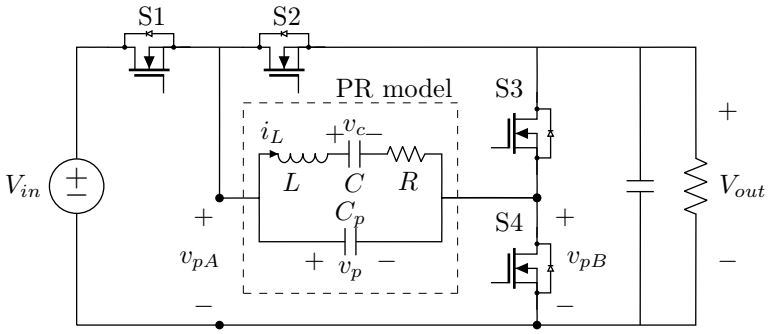

Figure 5-2: Topology corresponding to the V_{in}, V_{in}-V_{out}, *Zero*, V_{out} switching sequence proposed in Chapter 2.

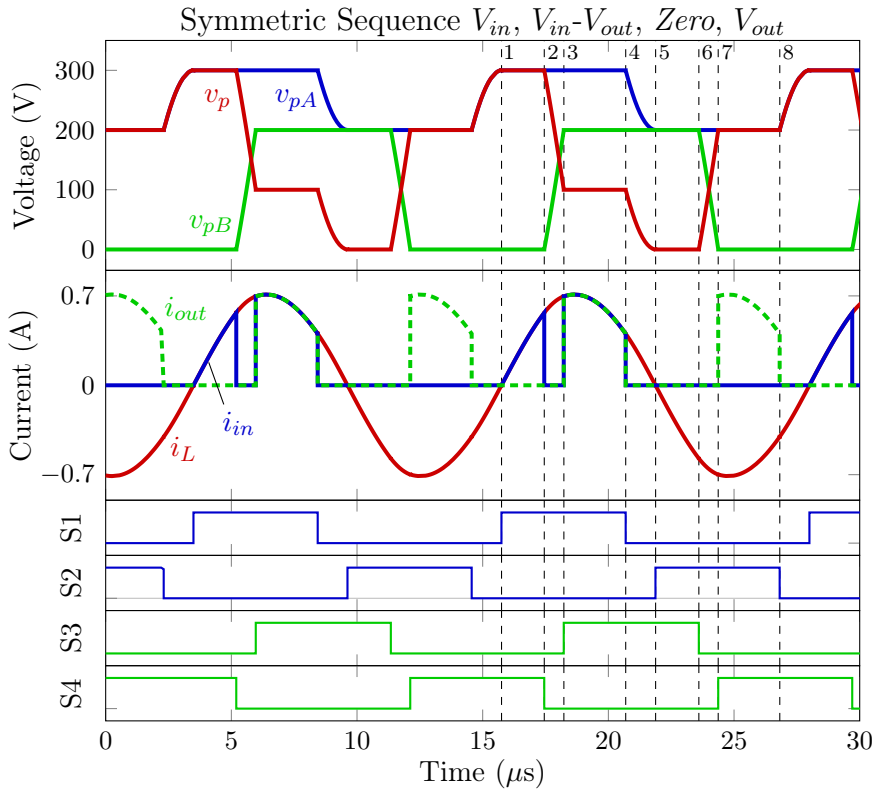

Figure 5-3: Example waveforms for switching sequence V_{in}, V_{in}-V_{out}, *Zero*, V_{out} with PR parameters in Table 5.1. $V_{in} = 300$ V, $V_{out} = 200$ V, $P_{out} = 50$ W.

V_{out} except with a non-zero-duration V_{in} stage between the turn-on of S1 and the turn-off of S4 as shown in Fig. 5-3. Adding a connected stage to a switching sequence provides an additional degree of freedom in its periodic steady-state solution as described in Section 2.4, and this additional degree of freedom may be used to constrain the switching sequence for

Table 5.1: Calculated Prototype PR Model Parameters

C_p	L	C	R
2.5 nF	2.6 mH	1.7 nF	0.8 Ω

near-symmetry between its two halves. This symmetry is reflected in the periodic steady-state waveforms of Fig. 5-3.

5.3.2 Voltage Regulation

We analyze this symmetric eight-stage sequence by first examining its energy and charge balance characteristics as generalized for six-stage sequences in Chapter 2. Maintaining the six-stage sequences' high-efficiency behaviors like minimum charge circulation requires i_L to be positive during the V_{in} and V_{in}-V_{out} stages and negative during the V_{out} stage. Thus, the following equation must hold for energy balance on the PR throughout a switching period:

$$V_{in}|q_1| + (V_{in} - V_{out})|q_3| - V_{out}|q_7| = 0 \tag{5.1}$$

where q_n is the charge displaced by i_L during the nth stage with stage numbers defined and visualized in Figs. 5-3 and 5-4, respectively.

For symmetry between the switching sequence's two halves, we leverage the eight-stage sequence's extra degree of freedom to constrain $|q_1| = |q_5|$ and $|q_3| = |q_7|$. This allows the following simplification of (5.1):

$$\frac{V_{out}}{V_{in}} = \frac{|q_1| + |q_3|}{2|q_3|} \tag{5.2}$$

In this symmetric eight-stage sequence, stages 1 and 3 are confined to the positive half of the i_L cycle. Thus, for different V_{out} with respect to V_{in}, the relative time durations of stages 1 and 3 can be adjusted within the positive i_L half cycle such that q_1 and q_3 satisfy (5.2). To preserve the sequence's symmetry, this is conducted by modulating the phase shift between the converter's half-bridges in the topology of Fig. 5-2. This phase shift is therefore the primary control handle for output voltage regulation in the V_{in}, V_{in}-V_{out}, *Zero*,

V_{out} sequence. We note that a similar concept has been leveraged for voltage regulation in resonant switched-capacitor converters in [59].

Assuming (5.2) is maintained with the aforementioned constraints for q_1 and q_3, the range of voltage conversion ratios supported by the symmetric V_{in}, V_{in}-V_{out}, *Zero*, V_{out} sequence is:

$$\frac{1}{2} < \frac{V_{out}}{V_{in}} < \infty \tag{5.3}$$

allowing step-down operation for $\frac{1}{2} < \frac{V_{out}}{V_{in}} < 1$.

This symmetric eight-stage sequence is advantageous in that both of its duty cycles can be fixed at approximately 50% and the required dead times for S1 and S2 are equivalent. It therefore requires only four total control variables for both voltage regulation and maintaining its high-efficiency behaviors: period T, S1/S2 dead time $S1_{dt}$, S3/S4 dead time $S3_{dt}$, and phase shift ϕ. This constitutes simpler control requirements than the six-stage sequences described in Chapter 4.

5.3.3 PR Utilization and Amplitude of Resonance Model

As described in Chapters 2 and 3, the amplitude of resonance model is a useful tool for analyzing a piezoelectric component's utilization and efficiency for a given switching sequence; we visualize the amplitude of resonance for an eight-stage sequence in Fig. 5-4. Use of this model first requires a switching sequence's charge transfer utilization factor K, defined as the proportion of connected/zero stage charge displacement that delivers energy to the load for step-down operation. The eight-stage V_{in}, V_{in}-V_{out}, *Zero*, V_{out} switching sequence has the following K:

$$K = \frac{|q_3| + |q_7|}{|q_1| + |q_3| + |q_5| + |q_7|} = \frac{|q_3|}{|q_1| + |q_3|} \tag{5.4}$$

in which we have simplified for $|q_1| = |q_5|$ and $|q_3| = |q_7|$ as described in Section 5.3.2. Inserting (5.2) then yields

$$K = \frac{V_{in}}{2V_{out}} \tag{5.5}$$

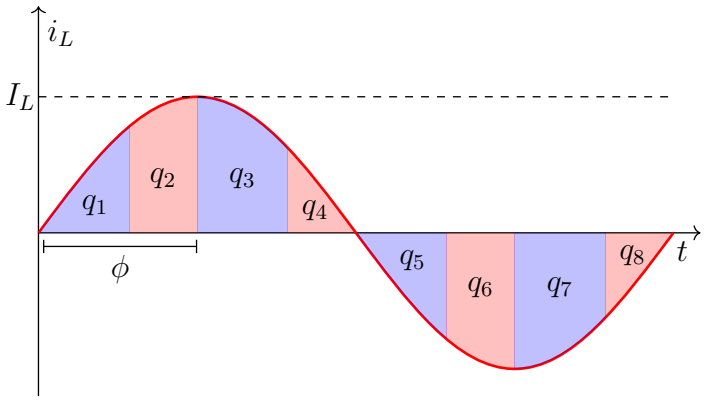

Figure 5-4: Assumed-sinusoidal i_L and amplitude of resonance I_L for the V_{in}, V_{in}-V_{out}, *Zero*, V_{out} switching sequence. The charge displaced during each stage n is labeled with q_n, corresponding to stage numbers defined in Fig. 5-3.

We note this is the same K as the six-stage V_{in}-V_{out}, *Zero*, V_{out} sequence, resulting in the same amplitude of resonance model as derived in Chapter 2 and later assumed in Chapter 6:

$$I_L = \pi \left(\frac{P_{out}}{V_{in}} + f C_p V_{in} \right) \tag{5.6}$$

The efficiency characteristic of this symmetric eight-stage sequence is therefore the same as that of the V_{in}-V_{out}, *Zero*, V_{out} sequence in the $\frac{1}{2} < \frac{V_{out}}{V_{in}} < 1$ operation region; specifically, efficiency is constant with respect to V_{out} for a given V_{in} and P_{out}. Thus, this symmetric eight-stage sequence provides the same efficiency advantage as a regulation stage with lower control complexity.

5.4 Example Implementation

Here we detail an example implementation of this two-stage converter concept with a piezoelectric-based regulation stage, along with its experimental results.

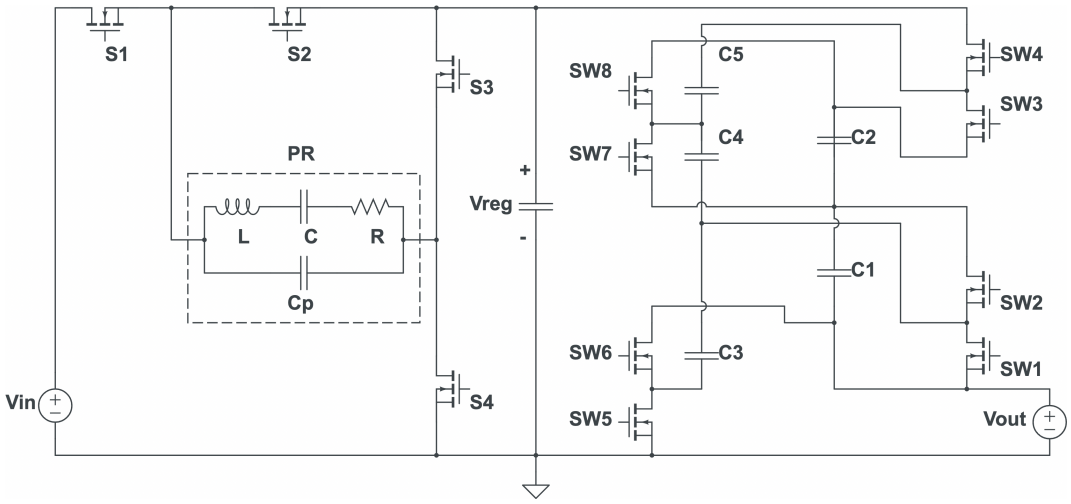

Figure 5-5: Two-stage PR/SC-based dc-dc converter topology. Figure source: Babuabel Wanyeki.

5.4.1 Prototype

To validate this two-stage PR/SC-based converter concept, we design an experimental prototype rated for 210 V $< V_{in} <$ 390 V, $V_{out} = 50$ V, and $P_{out} = 50$ W. This prototype contains the power stage architecture of Fig. 5-5 in which the piezoelectric-based regulation stage precedes the switched-capacitor-based transformation stage. The regulation stage utilizes the topology and eight-stage switching sequence detailed in Section 5.3, as this implementation offers high efficiency capability with simpler control requirements than six-stage switching sequences. The transformation stage is implemented with a 4:1 ladder topology. Case studies into different topologies in [95] reveals the ladder and series-parallel topologies to be most efficient for this design space, and the ladder offers additional advantages including simpler gate driver needs and low voltage ratings for all switches and capacitors.

This prototype is implemented on a 4-layer, 1.6mm printed circuit board as shown in Fig. 5-6 with the power stage parts listed in Table 5.2. The PR is selected from commercially available components based on the criteria outlined in Chapter 6; APC International part 1757 consists of a high-efficiency PZT material operating in the radial vibration mode and is capable of handling the desired power and voltage levels within acceptable stress and loss density limits. The regulation stage switches are selected such that their drain-source

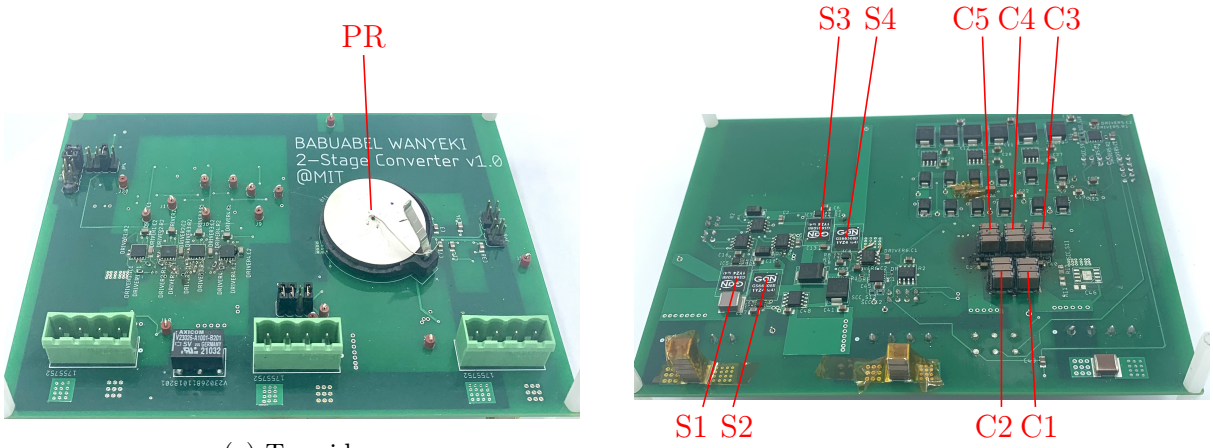

(a) Top side.

(b) Bottom side.

Figure 5-6: Prototype circuit board for the topology of Fig. 5-5. Figure source: Babuabel Wanyeki.

Table 5.2: Abbreviated Prototype Parts List

Component	Value
PR	APC International part 1757
Battery Holder	BH3000
Transistor	GS66508B-MR
Gate Driver	UCC27611DRVT
Isolator	SI8620BB-B-ISR
TDK Capacitors	CAA573X7S2A476M640LH
Transistor	EPC2036
Half-bridge Gate Driver	LM5113QDPRRQ1

capacitances and on-resistances are negligible in comparison to those of the PR. The transformation stage capacitors and switches are selected based on an optimization leveraging standard switched-capacitor converter design techniques as explained in [14, 95]. More details on the gate circuitry and hotel power supply for each stage are provided in [95]. We note that this prototype has been designed with the aim of demonstrating functionality with maximal efficiency rather than maximal power density or transient performance.

We operate this prototype with open-loop switching times for both stages and a constant-voltage load. The PR-based regulation stage operates between 78.5 and 83.5 kHz, with gate signals generated with an internally-developed control board based on T, ϕ, $S1_{dt}$, and

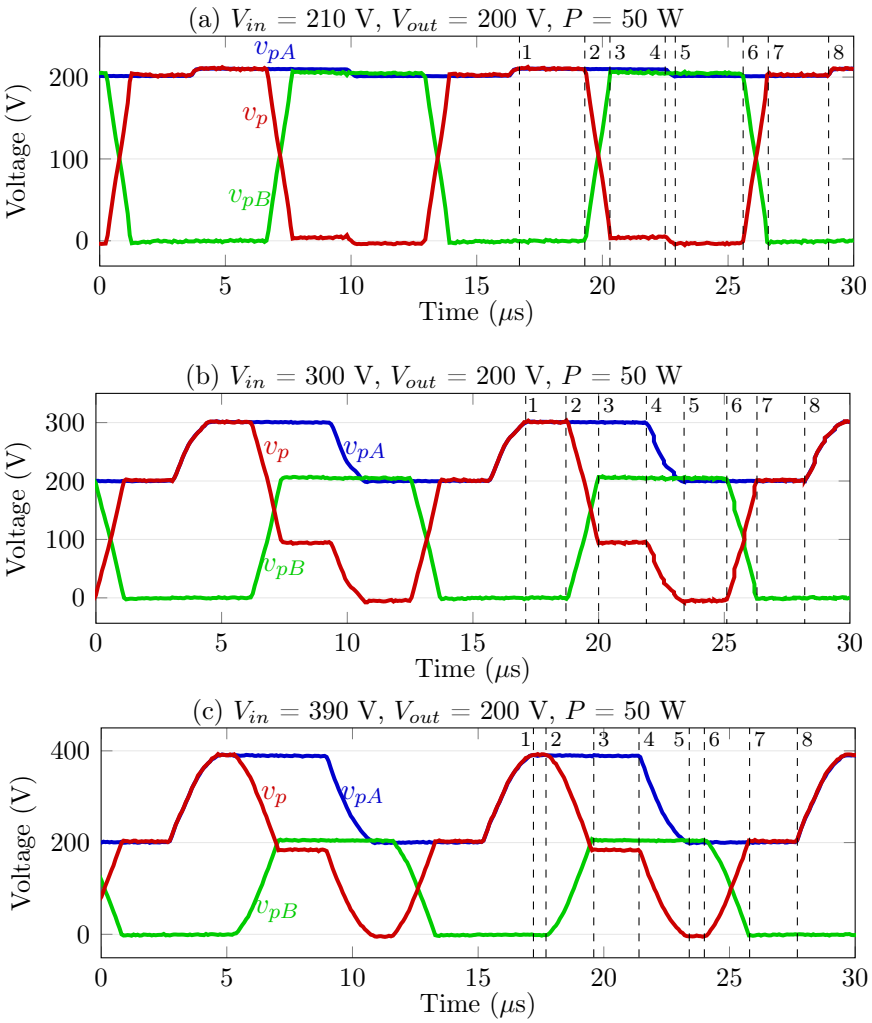

Figure 5-7: Experimental PR-stage waveforms at various $\frac{V_{out}}{V_{in}}$ with switching sequence V_{in}, V_{in}-V_{out}, *Zero*, V_{out} in the prototype described in Section 5.4.1. Figure source: Babuabel Wanyeki.

$S3_{dt}$. The duty cycle between $S1$ and $S2$ is slightly modulated to correct for time-duration differences between positive and negative i_L half-cycles, though this is not considered an active control variable. The switched-capacitor-based transformation stage operates at 253 kHz with gate signals produced by a function generator. We note that the transformation stage frequency is selected as part of an optimization detailed in [95], while the regulation stage frequency is tied to the selected PR's inductive region. Thus, which stage's operating frequency exceeds the other is arbitrary in the context of this prototype.

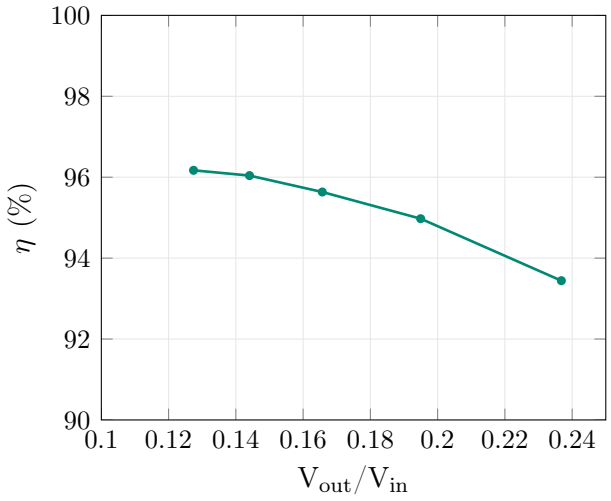

Figure 5-8: Measured power-stage efficiency vs. $\frac{V_{out}}{V_{in}}$ for the prototype described in Section 5.4.1 with $V_{out} = 50$ V and $P_{out} = 50$ W. Figure source: Babuabel Wanyeki.

5.4.2 Experimental Results

Experimental waveforms for the prototype's PR-based regulation stage are displayed in Fig. 5-7. These waveforms exhibit the desired high-efficiency behaviors of the eight-stage switching sequence including soft charging of the PR and ZVS, following closely in form with the example waveforms of Fig. 5-3. With phase shift as the primary control handle for regulation, the V_{in} and $Zero$ stages (stages 1 and 5 in Fig. 5-7) lengthen as $V_{in} \rightarrow V_{out}$ and nearly disappear as $V_{in} \rightarrow 2V_{out}$.

Experimental power stage efficiency for this prototype at 50 W is displayed in Fig. 5-8. This prototype exhibits high efficiencies across a continuous range of high conversion ratios thanks to the reciprocal advantages of the PR-based and SC-based stages, with the PR stage approaching its minimum loss ratio at $V_{in} = 390$ V. The peak efficiency of this prototype (>96 %) greatly surpasses those of the PR-based and PT-based prototypes in Chapters 2 and 3 at comparable conversion ratios, highlighting the value of PR/SC hybridization.

5.5 Conclusion

In this chapter, we have proposed and demonstrated a two-stage PR/SC-based converter architecture as a strategy for hybridizing PR-based and SC-based power conversion. This concept leverages the reciprocal advantages of PRs and SCs to support a wide range of high voltage conversion ratios with high efficiency. We utilize an eight-stage switching sequence in the PR-based regulation stage as a means to achieve the efficiency benefits of six-stage sequences proposed in Chapter 2 with simpler control requirements. We validate this concept in an experimental prototype that achieves high efficiencies across wide operating ranges, in excess of those obtainable by PR-based or PT-based converters at such voltage conversion ratios.

We note there are a variety of other avenues through which PR-based and SC-based power conversion may be hybridized to leverage their individual advantages. In this prototype alone, an even wider range of high-efficiency voltage regulation could be obtained by discretely changing the gain of the SC-based transformation stage. Although this particular experimental prototype is not optimized for power density, these results suggest hybrid PR/SC-based converter architectures to be auspicious for applications requiring both extreme voltage conversion and efficient voltage regulation.

The work of this chapter is described in more detail in the thesis [95].

Part II

Piezoelectric Component Design

Chapter 6

Piezoelectric Resonator Design

6.1 Introduction

The efficiency promise of power conversion based on only piezoelectric passive components is evident in the magnetic-less dc-dc converter designs realized in [58,67,69,74] with single-port piezoelectric resonators (PRs). In Chapter 2, we enumerate practical PR-based converter implementations that achieve high efficiency through strategic utilization of the PR's resonant cycle, resulting in experimental efficiencies exceeding 99%. Other PR-based converter implementations are demonstrated in [58,74], and [69] explores use of high-frequency lithium niobate PRs to achieve high power density. However, criteria for selecting piezoelectric materials and/or designing PRs themselves remain murky in the context of power conversion, and metrics developed for other applications serve different interests.

In this chapter, we present figures of merit (FOMs) for piezoelectric materials and vibration modes specifically for use as passive components in power electronics. Focusing on PRs, we derive FOMs for achievable efficiency and power handling density, which are shown to depend on only material properties assuming a realistic converter control sequence. These FOMs likewise correspond to geometry conditions for realizing both maximum efficiency and power density in a PR design. We demonstrate use of these FOMs and geometry conditions to compare commercially available materials and vibration modes, and we validate their

Table 6.1: Material State Definitions

u	Mechanical Displacement (m)
T	Mechanical Stress (N/m^2)
S	Mechanical Strain
E	Electric Field Strength (N/m)
D	Electric Flux Density (C/m^2)

Table 6.2: Material Property Definitions

Q_m	Mechanical Quality Factor
k	Electromechanical Coupling Factor
v_a	Acoustic Velocity (m/s)
ρ	Mass Density (kg/m^3)
ε	Dielectric Constant (F/m)
s	Compliance Constant (m^2/N)
d	Piezoelectric Charge Constant (C/N)
c	Elastic Modulus (N/m^2)
e	Piezoelectric Strain Modulus (C/m^2)
σ	Poisson's Ratio
T_{max}	Maximum Mechanical Stress (N/m^2)
S_{max}	Maximum Mechanical Strain
E_{max}	Max. Electric Field Strength (N/m)

utility with both numerical solutions and experimental results.

6.2 Piezoelectric Resonator Model

To develop PR design strategies for power conversion, we first define the PR structures and vibration modes of focus and derive their equivalent circuit models.

6.2.1 Assumed Component Structures

PRs can be produced in a variety of shapes and electrode patterns, and each configuration has a unique set of compatible vibration modes depending the PR's polarization direction, electrode placement, and boundary conditions. In this chapter, we focus on the component structures pictured in Fig. 6-1. These PRs are assumed to each vibrate in their fundamental modes marked in red in Fig. 6-1 with no externally-applied stress (i.e., all surfaces are assumed to be traction-free). These vibration modes can be grouped into two categories that permeate throughout this chapter: modes for which the applied and induced electric fields are parallel (||), and modes for which these fields are perpendicular (+). For material property tensors, it should be noted that the "3" direction corresponds to the polarization axis.

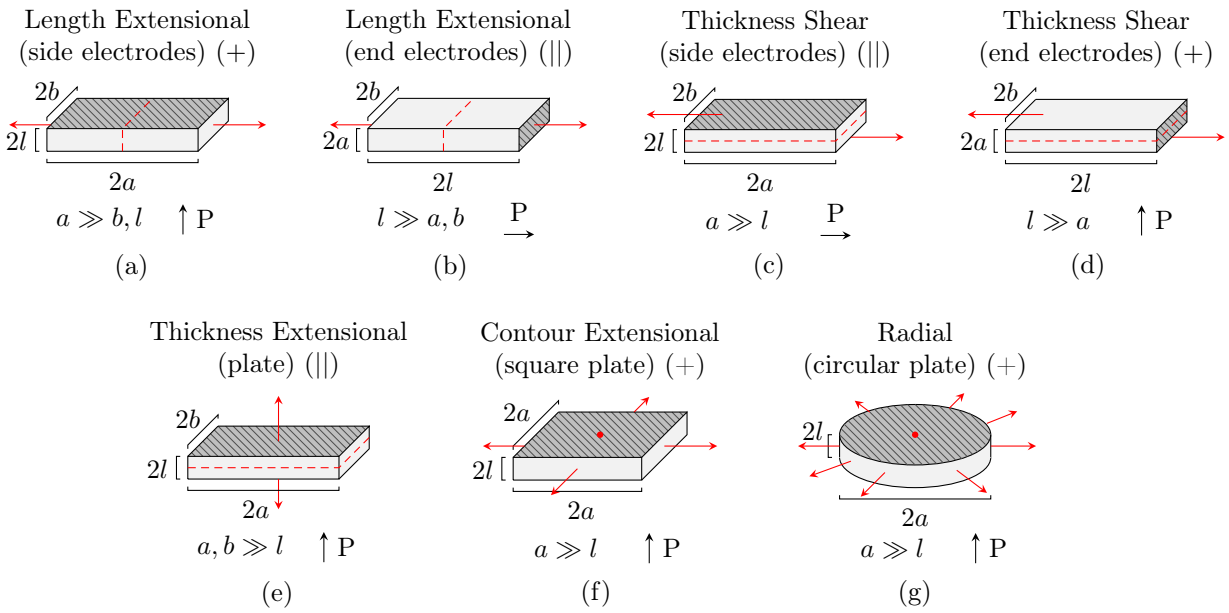

Figure 6-1: Considered PR vibration modes with electrodes denoted by shaded areas, displacement direction(s) marked with red arrows, and nodes / nodal planes marked with red dots / dashed lines, respectively. The polarization direction of the PR is denoted with 'P', and each electrode is assumed to have area A with distance $2l$ between electrodes. All surfaces are assumed to be traction-free, and the origin is assumed to be at the PR's center for analysis in Section 6.2.

6.2.2 Model Overview

Piezoelectric materials are governed by coupled constitutive relations between mechanical strain (S), mechanical stress (T), electric field strength (E), and electric flux density (D) due to the direct and converse piezoelectric effects [2, 96]:

$$\mathbf{S} = \mathbf{s}^E\mathbf{T} + \mathbf{d}^t\mathbf{E} \tag{6.1}$$

$$\mathbf{D} = \mathbf{d}\mathbf{T} + \boldsymbol{\varepsilon}^T\mathbf{E} \tag{6.2}$$

in which bold quantities represent tensors. Parameters for these equations are defined in Tables 6.1 and 6.2. Superscripts of S, T, E, or D for these parameters indicate the state held constant during measurement (e.g., $\mathbf{s}^E$ indicates compliance at a zero or constant electric field), and t refers to the transpose.

A piezoelectric material is likewise bound to the Newtonian equation of motion:

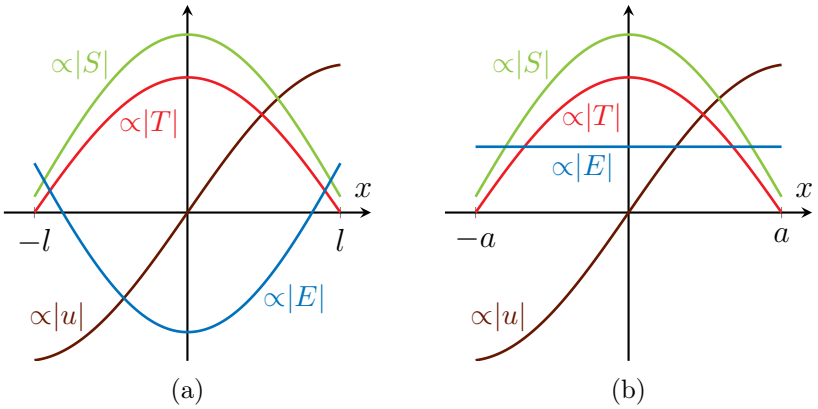

Figure 6-2: Relative amplitudes of u, S, T, and E along the axis of G_f in a PR for (a) vibration modes in which the applied and induced electric fields are parallel ($||$) and (b) vibration modes in which the applied and induced electric fields are perpendicular ($+$).

$$\nabla \cdot \mathbf{T} = \rho \ddot{\mathbf{u}}, \tag{6.3}$$

along with strain-displacement definition $\mathbf{S} = \frac{1}{2}(\nabla \mathbf{u} + \mathbf{u}\nabla)$ and Gauss's Law $\nabla \cdot \mathbf{D} = 0$. To illustrate the behaviors for each vibration mode, we adopt a generalized notation for all parameters without indices; the tensor components pertinent to each vibration mode (using Voigt notation) are displayed in Table 6.3. We likewise refer to a location along the l-dimension axis for parallel modes and a-dimension axis for perpendicular modes as generally "x"; this x axis corresponds to the frequency-setting dimension (i.e., G_f as described below).

Together, these equations constitute an acoustic wave equation that dictates sinusoidal time- and space-dependent solutions for u, S, T, and E as visualized with relative amplitudes in Fig. 6-2. These states have similar spacial dependencies across x for each vibration mode, though their specific directions may be different. With all surfaces in Fig. 6-1 assumed to be traction-free, the maximum amplitudes of S, T, and E each occur at the center of the PR (at $x = 0$).

The frequency f of the acoustic wave propagating through the PR is expressed as

$$f = \frac{\kappa}{2\pi} v_a = G_f \frac{\kappa_o}{2\pi} v_a \tag{6.4}$$

in which κ is the wave number (in rad/m) and v_a is the acoustic velocity (in m/s) of the

Table 6.3: Material Tensor Components for each Vibration Mode [2]

Mode	v_a	d	s^E	ε^T	k
Length Ext. (s)	$\sqrt{\frac{1}{\rho s_{11}^E}}$	d_{31}	s_{11}^E	ε_{33}^T	$k_{31}=\frac{d_{31}}{\sqrt{s_{11}^E \varepsilon_{33}^T}}$
Length Ext. (e)	$\sqrt{\frac{1}{\rho s_{33}^D}}$	d_{33}	s_{33}^E	ε_{33}^T	$k_{33}=\frac{d_{33}}{\sqrt{s_{33}^E \varepsilon_{33}^T}}$
Thickness shear (side)	$\sqrt{\frac{1}{\rho s_{55}^D}}$	d_{15}	s_{55}^E	ε_{11}^T	$k_{15}=\frac{d_{15}}{\sqrt{s_{55}^E \varepsilon_{11}^T}}$
Thickness shear (end)	$\sqrt{\frac{1}{\rho s_{55}^E}}$	d_{15}	s_{55}^E	ε_{11}^T	$k_{15}=\frac{d_{15}}{\sqrt{s_{55}^E \varepsilon_{11}^T}}$
Thickness Extensional	$\sqrt{\frac{c_{33}^D}{\rho}}$	**	**	**	$k_t=\frac{e_{33}}{\sqrt{c_{33}^D \varepsilon_{33}^S}}$
Contour Extensional	$\sqrt{\frac{1}{\rho s_{11}^E (1-\sigma^2)}}$	d_{31}	s_{11}^E	ε_{33}^T	$k_p=\sqrt{\frac{2k_{31}^2}{1-\sigma}}$
Radial	$\sqrt{\frac{1}{\rho s_{11}^E (1-\sigma^2)}}$	d_{31}	s_{11}^E	ε_{33}^T	$k_p=\sqrt{\frac{2k_{31}^2}{1-\sigma}}$

Measurement condition conversions [2]:
$\varepsilon_{11}^S = (1-k_{15}^2)\varepsilon_{11}^T$ $\quad \varepsilon_{33}^S = (1-k_{33}^2)\varepsilon_{33}^T$ $\quad s_{11}^D = (1-k_{31}^2)s_{11}^E$
$s_{33}^D = (1-k_{33}^2)s_{33}^E$ $\quad s_{55}^D = (1-k_{15}^2)s_{55}^E$ $\quad c_{33}^E = (1-k_t^2)c_{33}^D$
**Thickness extensional mode is commonly represented by e_{33}, c_{33}^E, and ε_{33}^S.

PR material [2]. G_f is a geometry term based the PR's frequency-setting dimension, defined for parallel and perpendicular vibration modes in Table 6.4. We also define κ_o to be the geometry-normalized wave number (in rad), where $\kappa_o = \frac{\kappa}{G_f}$.

The PR's electrical impedance can be likewise derived from the acoustic wave solution and is shown in Fig. 6-3(a) as a function of f. The PR exhibits inductive behavior in the region between the resonant (f_r) and anti-resonant (f_{ar}) frequencies; this region is of most interest to power conversion since inductive loading enables zero-voltage switching (ZVS) and other high-efficiency behaviors described in Chapter 2. The inductive region spans the following ranges of κ_o for parallel ($||$) and perpendicular ($+$) vibration modes, respectively:

$$\frac{\gamma_{o||}}{2} < \kappa_{o||} < \frac{\pi}{2} \tag{6.5}$$

$$\frac{\pi}{2} < \kappa_{o+} < \frac{\gamma_{o+}}{2} \tag{6.6}$$

for which factor γ_o is displayed in Table 6.4.

The PR impedance characteristic shown in Fig. 6-3(a) can be modeled by an equivalent

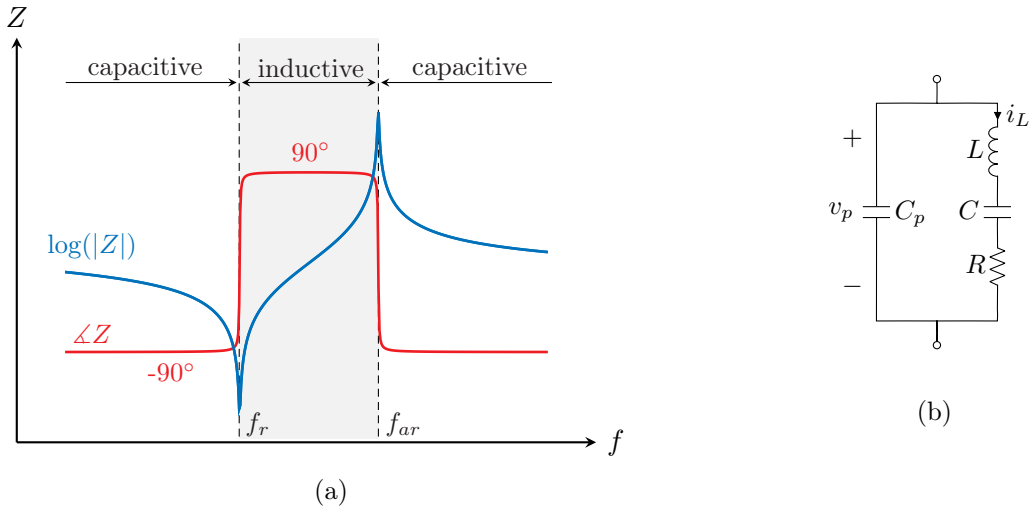

Figure 6-3: (a) PR impedance in the proximity of a vibration mode, where f_r is the resonant frequency and f_{ar} is the anti-resonant frequency. (b) Butterworth-Van Dyke circuit model for PRs [1]. Parameters are defined in Table 6.4 [2].

Table 6.4: Piezoelectric Resonator Model Parameters [2]

Parameter	Parallel (||)	Perpendicular (+)
G_f	$\frac{1}{l}$	$\frac{1}{a}$
γ_o	$\sqrt{\pi^2 - 8k^2}$	$\sqrt{\pi^2 + 8\frac{k^2}{1-k^2}}$
C_p	$\varepsilon^T(1-k^2)\frac{A}{2l}$	$\varepsilon^T(1-k^2)\frac{A}{2l}$
C	$\frac{8k^2}{\pi^2-8k^2}C_{p\|\|}$	$\frac{8k^2}{\pi^2(1-k^2)}C_{p+}$
L	$\frac{1}{2G_f^2k^2v_a^2C_{p\|\|}}$	$\frac{1-k^2}{2G_f^2k^2v_a^2C_{p+}}$
R	$\frac{1}{Q_m}\sqrt{\frac{L_{\|\|}}{C_{\|\|}}}$	$\frac{1}{Q_m}\sqrt{\frac{L_+}{C_+}}$

For thickness mode, $C_p = \varepsilon^S\frac{A}{2l}$. For radial mode parameters, see Table 6.8.

electrical circuit (i.e., the Butterworth-Van Dyke model [1]) illustrated in Fig. 6-3(b). For excitation of a PR's fundamental frequency, this model has the parameters shown in Table 6.4, which are generalized to parallel and perpendicular vibration modes [2, 16, 97]. A is the electrode area, $2l$ is the distance between the electrodes, and the material parameters of interest are shown for each vibration mode in Table 6.3. This electrical model serves as the basis for how we conceptualize the PR's behavior: f_r corresponds to series resonance between

L and C, and f_{ar} occurs at parallel resonance between C_p and the series combination of L and C. The model's full derivation for all considered modes can be found in [2].

6.2.3 One-Dimensional Stress/Strain Modes

We now examine this model derivation for specific vibration modes. Most vibration modes considered (length extensional, thickness shear, and thickness extensional) can be modeled by one-dimensional stress/strain, in which we consider only one tensor component for each PR state in (6.1)-(6.2), (6.3). For this case, the coupled constitutive relations take the reduced form:

$$S = s^E T + dE \tag{6.7}$$

$$D = dT + \varepsilon^T E \tag{6.8}$$

With the equation of motion (6.3), (6.7)-(6.8) create an acoustic wave equation for mechanical displacement u:

$$\frac{\partial^2 u}{\partial t^2} = v_a^2 \frac{\partial^2 u}{\partial x^2} \tag{6.9}$$

The PR is assumed to resonate in the proximity of its lowest-frequency vibration mode for traction-free boundaries in Fig. 6-1. Thus, the acoustic wave solution is sinusoidal in form:

$$u = \Delta \sin(\kappa x) e^{j\omega t} \tag{6.10}$$

Inserting (6.10) into the constitutive relations and enforcing traction-free boundaries yields the solutions for S, T, and E; these solutions are displayed for each mode in Table 6.5. These solutions provide means to analyze the PR's mechanical and electrical limits, which we utilize in Sections 6.4.3 and 6.4.4. Also, parameters for the Butterworth-Van Dyke circuit model (Fig. 6-3(b)) can be derived from E and correspond to Table 6.4 [2].

Table 6.5: One-Dimensional Vibration Mode Derivations

	Length Ext. (s) and Thickness Shear (e)	Length Ext. (e) and Thickness Shear (s)	Thickness Extensional
S	$\kappa\Delta\cos(\kappa x)e^{j\omega t}$	$\kappa\Delta\cos(\kappa x)e^{j\omega t}$	$\kappa\Delta\cos(\kappa x)e^{j\omega t}$
T	$\frac{1}{s^E}\kappa\Delta\left(\cos(\kappa x)-\cos(\kappa_o)\right)e^{j\omega t}$	$\frac{1}{s^D}\kappa\Delta\left(\cos(\kappa x)-\cos(\kappa_o)\right)e^{j\omega t}$	$c^D\kappa\Delta\left(\cos(\kappa x)-\cos(\kappa_o)\right)e^{j\omega t}$
E	$\frac{\kappa\Delta}{d}\left(\cos(\kappa_o)\right)e^{j\omega t}$	$\frac{\kappa\Delta}{d(1-k^2)}\left(-k^2\cos(\kappa x)+\cos(\kappa_o)\right)e^{j\omega t}$	$\frac{c^D\kappa\Delta}{e(1-k^2)}\left(-k^2\cos(\kappa x)+\cos(\kappa_o)\right)e^{j\omega t}$
I_L	$\kappa AG_f\frac{v_a d}{s^E}\Delta\sin(\kappa_o)$	$\kappa AG_f\frac{v_a d}{s^E}\Delta\sin(\kappa_o)$	$\kappa AG_f v_a e\Delta\sin(\kappa_o)$
Δ_S	$\frac{1}{\kappa}S_{max}$	$\frac{1}{\kappa}S_{max}$	$\frac{1}{\kappa}S_{max}$
Δ_T	$\frac{s^E}{\kappa}\frac{1}{1-\cos(\kappa_o)}T_{max}$	$\frac{s^D}{\kappa}\frac{1}{1-\cos(\kappa_o)}T_{max}$	$\frac{1}{c^D\kappa}\frac{1}{1-\cos(\kappa_o)}T_{max}$
Δ_E	$\frac{d}{\kappa}\frac{1}{\cos(\kappa_o)}E_{max}$	$\frac{d}{\kappa}\frac{(1-k^2)}{(\cos(\kappa_o)-k^2)}E_{max}$	$\frac{e}{c^D\kappa}\frac{1}{(\cos(\kappa_o)-k^2)}E_{max}$
I_{LmaxS}	$AG_f\frac{v_a d}{s^E}S_{max}\sin(\kappa_o)$	$AG_f e v_a S_{max}\sin(\kappa_o)$	$AG_f\frac{v_a d}{s^E}S_{max}\sin(\kappa_o)$
I_{LmaxT}	$AG_f v_a d T_{max}\cot(\frac{\kappa_o}{2})$	$AG_f v_a d(1-k^2)T_{max}\cot(\frac{\kappa_o}{2})$	$AG_f v_a\frac{e}{c^D}T_{max}\cot(\frac{\kappa_o}{2})$
I_{LmaxE}	$AG_f k^2\varepsilon^T v_a E_{max}\tan(\kappa_o)$	$AG_f k^2\varepsilon^S v_a E_{max}\frac{\sin(\kappa_o)}{\cos(\kappa_o)-k^2}$	$AG_f k^2\varepsilon^S v_a E_{max}\frac{\sin(\kappa_o)}{\cos(\kappa_o)-k^2}$

6.2.4 Contour Extensional Mode

For contour extensional mode, we assume the PR to be under plane stress (i.e., we consider only the normal stress components along the two axes perpendicular to the applied electric field). We denote these normal stresses with T_1 and T_2, and their coordinate plane is defined by the red displacement lines in Fig. 6-1(f) with the origin at the center of the PR. The constitutive relations then have the form [2]:

$$T_1 = \frac{1}{s_{11}^E(1-\sigma^2)}\Big(\frac{\partial u_1}{\partial x_1}+\sigma\frac{\partial u_2}{\partial x_2}\Big)-\frac{d_{31}}{s_{11}^E(1-\sigma)}E \tag{6.11}$$

$$T_2 = \frac{1}{s_{11}^E(1-\sigma^2)}\Big(\sigma\frac{\partial u_1}{\partial x_1}+\frac{\partial u_2}{\partial x_2}\Big)-\frac{d_{31}}{s_{11}^E(1-\sigma)}E \tag{6.12}$$

$$D = \frac{d_{31}}{s_{11}^E(1-\sigma)}(\frac{\partial u_1}{\partial x_1}+\frac{\partial u_2}{\partial x_2})+\varepsilon_{33}^T(1-k_p^2)E \tag{6.13}$$

With (6.3), these equations constitute an acoustic wave equation for mechanical displacement u. Its solution can be approximated by two separate waves, which we assume to be identical along their respective dimensions [2]:

$$u_1 = \Delta\sin(\kappa x_1)e^{j\omega t} \tag{6.14}$$

$$u_2 = \Delta\sin(\kappa x_2)e^{j\omega t} \tag{6.15}$$

Table 6.6: Planar Vibration Mode Derivations

	Contour Extensional	Radial
S	$S_1 = \kappa\Delta\cos(\kappa x_1)e^{j\omega t}$ $S_2 = \kappa\Delta\cos(\kappa x_2)e^{j\omega t}$	$S_{rr} = \frac{\kappa}{2}\Delta(J_0(\kappa r) - J_2(\kappa r))e^{j\omega t}$ $S_{\theta\theta} = \frac{1}{r}\Delta J_1(\kappa r)e^{j\omega t}$
T	$T_1 = \frac{\kappa\Delta e^{j\omega t}}{s_{11}^E(1-\sigma^2)}\Big(\cos(\kappa x_1)+\sigma\cos(\kappa x_2)-(1+\sigma)\cos(\kappa_o)\Big)$ $T_2 = \frac{\kappa\Delta e^{j\omega t}}{s_{11}^E(1-\sigma^2)}\Big(\sigma\cos(\kappa x_1)+\cos(\kappa x_2)-(1+\sigma)\cos(\kappa_o)\Big)$	$T_{rr} = \frac{\Delta e^{j\omega t}}{s_{11}^E(1-\sigma^2)}\Big(\frac{\kappa}{2}\big(J_0(\kappa r)-J_2(\kappa r)\big)+\frac{\sigma}{r}J_1(\kappa r)-\kappa\Psi\Big)$ $T_{\theta\theta} = \frac{\Delta e^{j\omega t}}{s_{11}^E(1-\sigma^2)}\Big(\frac{\kappa\sigma}{2}\big(J_0(\kappa r)-J_2(\kappa r)\big)+\frac{1}{r}J_1(\kappa r)-\kappa\Psi\Big)$
E	$\frac{\kappa\Delta}{d_{31}}\left(\cos(\kappa_o)\right)e^{j\omega t}$	$\frac{\kappa\Delta}{d_{31}(1+\sigma)}\Psi e^{j\omega t}$
I_L	$2\kappa AG_f\frac{v_a d_{31}}{s_{11}^E(1-\sigma)}\Delta\sin(\kappa_o)$	$\kappa_o v_a\frac{2\pi d_{31}}{s_{11}^E(1-\sigma)}\Delta J_1(\kappa_o)$
Δ_S	$\frac{1}{\kappa}S_{max}$	$\frac{2}{\kappa}S_{max}$
Δ_T	$\frac{s_{11}^E(1-\sigma)}{\kappa(1-\cos(\kappa_o))}T_{max}$	$\frac{s_{11}^E(1-\sigma^2)}{\kappa(\frac{1}{2}(1+\sigma)-\Psi)}T_{max}$
Δ_E	$\frac{d_{31}}{\kappa}\frac{1}{\cos(\kappa_o)}E_{max}$	$\frac{d_{31}(1+\sigma)}{\kappa\Psi}E_{max}$
I_{LmaxS}	$2AG_f v_a\frac{d_{31}}{s_{11}^E(1-\sigma)}S_{max}\sin(\kappa_o)$	$AG_f\frac{4d_{31}v_a}{s_{11}^E(1-\sigma)}S_{max}J_1(\kappa_o)$
I_{LmaxT}	$2AG_f v_a d_{31}T_{max}\cot(\frac{\kappa_o}{2})$	$AG_f\frac{2v_a d_{31}(1+\sigma)}{\frac{1}{2}(1+\sigma)-\Psi}T_{max}J_1(\kappa_o)$
I_{LmaxE}	$AG_f v_a k_p^2\varepsilon_{33}^T E_{max}\tan(\kappa_o)$	$AG_f v_a k_p^2\varepsilon_{33}^T(1+\sigma)E_{max}\frac{J_1(\kappa_o)}{\Psi}$

Inserting (6.14) and (6.15) into (6.11) and (6.12) and enforcing the boundary conditions of $T_1 = 0$ at $x_1 = \pm a$ and $T_2 = 0$ at $x_2 = \pm a$ provides the analytical solution shown in Table 6.6 for the PR's S, T, and E states. This solution follows the relative amplitudes illustrated in Fig. 6-2(b) and yields the circuit model parameters displayed in Table 6.4.

6.2.5 Radial Mode

For the radial vibration mode, we consider only planar stress components parallel to the electrodes; E is again applied only in the polarization direction. This time, we adopt a cylindrical coordinate system in which r is the radial coordinate and θ is the hoop coordinate. Thus, the constitutive relations are [2]:

$$T_{rr} = \frac{1}{s_{11}^E(1-\sigma^2)}\Big(\frac{\partial u_r}{\partial r}+\sigma\frac{u_r}{r}\Big) - \frac{d_{31}}{s_{11}^E(1-\sigma)}E \tag{6.16}$$

$$T_{\theta\theta} = \frac{1}{s_{11}^E(1-\sigma^2)}\Big(\sigma\frac{\partial u_r}{\partial r}+\frac{u_r}{r}\Big) - \frac{d_{31}}{s_{11}^E(1-\sigma)}E \tag{6.17}$$

$$D = \frac{d_{31}}{s_{11}^E(1-\sigma)}\Big(\frac{\partial u_r}{\partial r}+\frac{u_r}{r}\Big) + \varepsilon_{33}^T(1-k_p^2)E \tag{6.18}$$

Together with the equation of motion (6.3), these constitute a wave equation for mechanical displacement u_r with solution

$$u_r = \Delta J_1(\kappa r) e^{j\omega t} \tag{6.19}$$

for which J_n is the Bessel function of first kind and nth order. Inserting (6.19) into (6.16) and enforcing the boundary condition $T_{rr} = 0$ at $r = a$ yields the analytical solution in Table 6.6 for the PR's S, T, and E states, which follows the illustration in Fig. 6-2(b) for $x = r$. In this solution, we have substituted

$$\Psi = \frac{1}{2} J_0(\kappa_o) - \frac{1}{2} J_2(\kappa_o) + \frac{\sigma}{\kappa_o} J_1(\kappa_o) \tag{6.20}$$

The geometry-normalized wave numbers corresponding to f_r and f_{ar} in radial mode are solutions to the following transcendental equations, respectively [2]:

$$\kappa_{o,r} \frac{J_0(\kappa_{o,r})}{J_1(\kappa_{o,r})} = 1 - \sigma \tag{6.21}$$

$$\kappa_{o,ar} \frac{J_0(\kappa_{o,ar})}{J_1(\kappa_{o,ar})} = 1 - \sigma - \frac{k_p^2}{1 - k_p^2}(1 + \sigma) \tag{6.22}$$

If needed, Bessel functions $J_0(\kappa_o)$, $J_1(\kappa_o)$, and $J_2(\kappa_o)$ can be approximated by series expansions around $\kappa_{o,r}$; second-order expansions around $\kappa_o = 2$ are shown in Table 6.7. The geometry-normalized wave number that corresponds to the minimum-loss-ratio operating frequency is then:

$$\bar{\kappa}_o = \frac{2\kappa_{o,r}\kappa_{o,ar}}{\kappa_{o,r} + \kappa_{o,ar}} \tag{6.23}$$

Finally, E in Table 6.6 can be reduced to the circuit model of Fig. 6-3(b) with the parameters shown in Table 6.8.

Table 6.7: Bessel Function Expansions

Function	Expansion Around $\kappa_o = 2$
$\kappa_o \frac{J_0(\kappa_o)}{J_1(\kappa_o)}$	$0.776 - 1.525(\kappa_o - 2) - 0.789(\kappa_o - 2)^2$
$J_0(\kappa_o)$	$0.224 - 0.577(\kappa_o - 2) - 0.0322(\kappa_o - 2)^2$
$J_1(\kappa_o)$	$0.577 - 0.645(\kappa_o - 2) - 0.2(\kappa_o - 2)^2$
$J_2(\kappa_o)$	$0.353 - 0.224(\kappa_o - 2) - 0.0560(\kappa_o - 2)^2$

Table 6.8: Circuit Model Parameters for Radial Vibration Mode [2]

Parameter	Radial Mode Expression
G_f	$\frac{1}{a}$
C_p	$\varepsilon^T(1 - k_p^2)\frac{A}{2l}$
C	$\frac{2(1+\sigma)}{\kappa_{o,r}^2-(1-\sigma^2)} \frac{k_p^2}{1-k_p^2} C_p$
L	$\frac{1}{2G_f^2 v_a^2 C_p} \frac{1-k_p^2}{k_p^2} \frac{\kappa_{o,r}^2-(1-\sigma^2)}{\kappa_{o,r}^2(1+\sigma)}$
R	$\frac{1}{Q_m}\sqrt{\frac{L}{C}}$

6.3 Amplitude of Resonance Model

In addition to the PR model itself, how the PR behaves in a power converter is an important consideration for PR design. Here we model the PR's amplitude of resonance for a given switching sequence and operating point and derive its limits.

6.3.1 Assumed Converter Operation

To model PR behavior as utilized in a converter, we assume operation based on either of the highest-efficiency step-down switching sequences analyzed in Chapter 2. These sequences are each comprised of six stages: three "connected/zero stages" (i.e., stages in which the PR is connected to the source-load system) alternated with three "open stages" (stages in which the PR is open-circuited and C_p charges/discharges through resonance). Further, these switching sequences are constrained for high-efficiency behaviors including soft charging of the PR's C_p during open stages, ZVS of all switches, and minimum charge circulation.

These highest-efficiency switching sequences are capable of constant-efficiency voltage

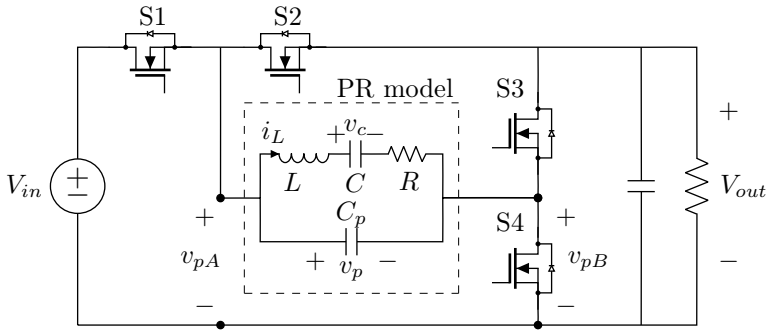

Figure 6-4: Topology corresponding to the V_{in}-V_{out}, *Zero*, V_{out} switching sequence proposed in Chapter 2.

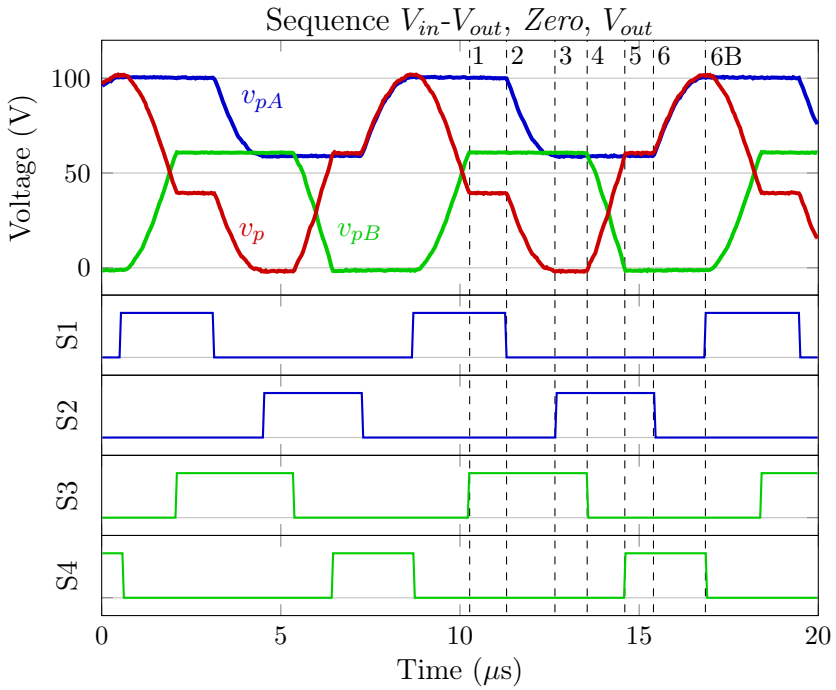

Figure 6-5: Experimental waveforms and associated switch signals for switching sequence V_{in}-V_{out}, *Zero*, V_{out} proposed in Chapter 2. Numbers 1-6B designate connected/zero stages (odd) and open stages (even). $V_{in} = 100$ V, $V_{out} = 60$ V, $P_{out} = 4$ W.

regulation for $\frac{1}{2} \leq \frac{V_{out}}{V_{in}} \leq 1$. One such switching sequence is referred to as V_{in}-V_{out}, *Zero*, V_{out}, named according to its connected/zero stage voltages as described in Chapter 2. An example topology for realizing this sequence is visualized in Fig. 6-4 with corresponding waveforms in Fig. 6-5; we utilize this implementation for experimental validation in Section 6.6.

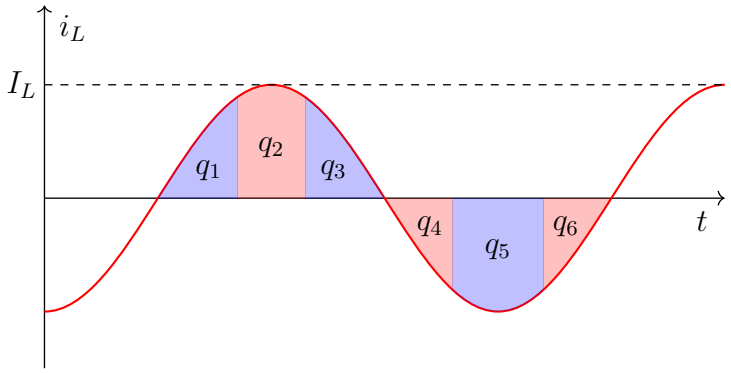

Figure 6-6: Sinusoidal approximation of i_L and resulting amplitude of resonance I_L, based on the charge transfer q_n required of each switching stage n as described in Chapter 2.

6.3.2 Amplitude of Resonance Model

As introduced in Chapter 2, the amplitude of a PR's assumed-sinusoidal i_L provides insight into its amplitude of mechanical resonance for a given switching sequence and operating point. This amplitude of resonance then dictates the PR's mechanical energy storage and loss.

The PR's ideal amplitude of resonance (I_L) can be calculated from the total magnitude of charge displaced by i_L during each resonant cycle (Q_{total}) as illustrated in Fig. 6-6. This charge transfer calculation depends on the converter's specific switching sequence and considers both connected/zero stages and open stages for realistic representation as described in Chapter 2. The highest-efficiency sequences discussed in Section 6.3.1 have the following I_L, which varies based on operating point:

$$I_L := \frac{\pi}{2} f Q_{total} = \pi \left(\frac{P_{out}}{V_{in}} + f C_p V_{in} \right) \tag{6.24}$$

where $P_{out} = \frac{V_{out}^2}{R_{load}}$ as shown in Fig. 6-4.

In accordance with the switching sequences discussed in Section 6.3.1, this I_L equation assumes soft charging/discharging of the PR's C_p, ZVS of all switches, all-positive instantaneous power transfer, and minimal charge circulation for high efficiency. Thus, (6.24) models the PR's amplitude of resonance for typical converter operation, which we assume

throughout this chapter.

6.3.3 Material Limits

A PR's maximum amplitude of resonance (I_{Lmax}) may be determined by its material's limits for strain (S_{max}), stress (T_{max}), and electric field strength (E_{max}). Such potential limits include yield stress and strain, as well as coercive field (i.e., the electric field strength at which depolarization occurs).

We can derive the relationship between I_L and the PR's physical states using the constitutive relations (6.1)-(6.2) and the equation of motion (6.3). This requires first deriving the relationship between I_L and the PR's maximum displacement amplitude (Δ) using constitutive relations (6.1)-(6.2) and the solutions in Tables 6.5-6.6. For a one-dimensional vibration mode, inserting (6.7) into (6.8) yields:

$$D = \frac{d}{s^E}\frac{\partial u}{\partial x} + \varepsilon^T\left(1-k^2\right)E \tag{6.25}$$

Integrating both sides of (6.25) across electrode area A for charge displacement and distance $2l$ for voltage gives:

$$Q = AG_f\frac{d}{s^E}u(G_f^{-1}) + \frac{A}{2l}\varepsilon^T\left(1-k^2\right)v_{p,1} \tag{6.26}$$

for which $v_{p,1}$ is the first-harmonic approximation of v_p. Finally, taking the time derivative yields:

$$i_{in} = j\omega AG_f\frac{d}{s^E}u(G_f^{-1}) + C_p\frac{dv_{p,1}}{dt} \tag{6.27}$$

in which i_{in} can be considered the current entering the PR through its top terminal as modeled in Fig. 6-3(b). For planar modes, this process results in a similar form as (6.27) for contour extensional mode and the following form for radial mode:

$$i_{in} = j\omega a\frac{2\pi d_{31}}{s_{11}^E(1-\sigma)}\Delta J_1(\kappa_o)e^{j\omega t} + C_p\frac{dv_{p,1}}{dt} \tag{6.28}$$

These expressions for i_{in} correspond to Fig. 6-3(b) such that I_L equals the magnitude of the first term in (6.27) or (6.28). This results in the following relationship between I_L and Δ for one-dimensional modes:

$$I_L = \kappa A G_f \frac{v_a d}{s^E} \Delta \sin(\kappa_o) \tag{6.29}$$

with I_L for planar modes likewise shown in Table 6.6.

From here, S, T and E can each be related to I_L through Δ. As shown in Fig. 6-2, the maximum S, T and E each occur at $x = 0$, so we rearrange their respective equations in Tables 6.5 and 6.6 and focus on $x = 0$ to reach Δ_S, Δ_T, and Δ_E as functions of S_{max}, T_{max} and E_{max}, respectively (S_{max} and T_{max} refer to the maximum principal strains and stresses for planar modes; this requires taking the limit as $r \to 0$ for radial mode). Each Δ can then be directly inserted into I_L, resulting in the strain-limited (I^S_{Lmax}), stress-limited (I^T_{Lmax}), and E-limited (I^E_{Lmax}) maximum amplitudes of resonance displayed in Tables 6.5 and 6.6.

It is shown that I^S_{Lmax}, I^T_{Lmax}, and I^E_{Lmax} have identical geometry terms, so their geometry-normalized values (referred to as I^S_{Lmaxo}, I^T_{Lmaxo} and I^E_{Lmaxo}, respectively) are summarized for each considered vibration mode in Table 6.9. The lowest-magnitude limit can be considered the geometry-normalized maximum for I_L:

$$I_{Lmaxo} := \frac{I_{Lmax}}{AG_f} = \min(I^S_{Lmaxo}, I^T_{Lmaxo}, I^E_{Lmaxo}) \tag{6.30}$$

Thus, the geometry-normalized limit I_{Lmaxo} (and which physical limit constrains it) can be determined based on only material parameters and limits. I_{Lmaxo} is employed to determine maximum power handling density in Sections 6.4.3 and 6.4.4.

6.3.4 Areal Loss Density Limit

Thermal limitations may confine a PR's amplitude of resonance to lower bounds than its material's physical limits, so we likewise derive an I_L limit based on areal loss density. Material-dependent losses in the PR include mechanical loss and dielectric loss; since mechanical loss tends to dominate close to resonance [79], we focus on only mechanical loss

Table 6.9: Maximum Amplitudes of Resonance Based on Material and Thermal Limits

Vibration Mode	I^S_{Lmaxo}	I^T_{Lmaxo}	I^E_{Lmaxo}	I^H_{Lmaxo}
Length Extensional (s)	$v_a \frac{d_{31}}{s^E_{11}} S_{max} \sin(\kappa_o)$	$v_a d_{31} T_{max} \cot(\frac{\kappa_o}{2})$	$v_a k^2_{31} \varepsilon^T_{33} E_{max} \tan(\kappa_o)$	$\sqrt{\frac{4Q_m k^2_{31} \varepsilon^T_{33} v_a}{\pi}} H$
Length Extensional (e)	$v_a \frac{d_{33}}{s^E_{33}} S_{max} \sin(\kappa_o)$	$v_a d_{33}(1-k^2_{33}) T_{max} \cot(\frac{\kappa_o}{2})$	$v_a k^2_{33} \varepsilon^S_{33} E_{max} \frac{\sin(\kappa_o)}{\cos(\kappa_o)-k^2_{33}}$	$\sqrt{\frac{4Q_m k^2_{33} \varepsilon^S_{33} v_a}{\gamma_o}} H$
Thickness Shear (side)	$v_a \frac{d_{15}}{s^E_{55}} S_{max} \sin(\kappa_o)$	$v_a d_{15}(1-k^2_{15}) T_{max} \cot(\frac{\kappa_o}{2})$	$v_a k^2_{15} \varepsilon^S_{11} E_{max} \frac{\sin(\kappa_o)}{\cos(\kappa_o)-k^2_{15}}$	$\sqrt{\frac{4Q_m k^2_{15} \varepsilon^S_{11} v_a}{\gamma_o}} H$
Thickness Shear (end)	$v_a \frac{d_{15}}{s^E_{55}} S_{max} \sin(\kappa_o)$	$v_a d_{15} T_{max} \cot(\frac{\kappa_o}{2})$	$v_a k^2_{15} \varepsilon^T_{11} E_{max} \tan(\kappa_o)$	$\sqrt{\frac{4Q_m k^2_{15} \varepsilon^T_{11} v_a}{\pi}} H$
Thickness Extensional	$v_a e_{33} S_{max} \sin(\kappa_o)$	$v_a \frac{e_{33}(1-k^2_t)}{c^E_{33}} T_{max} \cot(\frac{\kappa_o}{2})$	$v_a k^2_t \varepsilon^S_{33} E_{max} \frac{\sin(\kappa_o)}{\cos(\kappa_o)-k^2_t}$	$\sqrt{\frac{4Q_m k^2_t \varepsilon^S_{33} v_a}{\gamma_o}} H$
Contour Extensional	$\frac{2d_{31} v_a}{s^E_{11}(1-\sigma)} S_{max} \sin(\kappa_o)$	$2 v_a d_{31} T_{max} \cot(\frac{\kappa_o}{2})$	$v_a k^2_p \varepsilon^T_{33} E_{max} \tan(\kappa_o)$	$\sqrt{\frac{4Q_m k^2_p \varepsilon^T_{33} v_a}{\pi}} H$
Radial	$\frac{4d_{31} v_a}{s^E_{11}(1-\sigma)} S_{max} J_1(\kappa_o)$	$\frac{2 v_a d_{31}(1+\sigma)}{\frac{1}{2}(1+\sigma)-\Psi} T_{max} J_1(\kappa_o)$	$v_a k^2_p \varepsilon^T_{33}(1+\sigma) E_{max} \frac{J_1(\kappa_o)}{\Psi}$	$\sqrt{\frac{2Q_m k^2_p \varepsilon^T_{33} v_a}{\frac{\kappa_{o,r}}{1+\sigma} - \frac{1-\sigma}{\kappa_{o,r}}}} H$

Numerical subscripts indicate the tensor components relevant for each mode [2]. For I^H_{Lmaxo}, we have substituted $H = \left(\frac{P_{loss}}{A_s}\right)_{max}$. For radial mode, Section 6.2.5 contains the definition for Ψ and series expansions for Bessel functions.

in the context of this thesis. We estimate mechanical loss using I_L and R as described in Chapter 2:

$$P_{loss} := \frac{1}{2} I_L^2 R \tag{6.31}$$

While (6.31) typically relies on a small-signal measurement or datasheet value for R, it is the best estimate of loss that is generally available.

For an I_L limit based on areal loss density, we assume that most PR heat extraction occurs through a surface with area A_s, and that a thermal management design can safely accommodate a certain quantity of PR loss per A_s. This areal loss density relates to the PR's operation as follows:

$$\frac{P_{loss}}{A_s} = \frac{1}{2} \frac{I_L^2 R}{A_s} = \frac{1}{2} I_{Lo}^2 R_o \tag{6.32}$$

in which we have extracted geometry parameters from I_L and R, assuming $A_s = A$ for parallel ($||$) modes, $A_s = G_f A l$ for perpendicular ($+$) modes as defined in Table 6.11, and R_o for all

modes as defined in Table 6.10 (where $R_o = GR$, in which G contains all geometry terms as later defined in Section 6.4.1). For these assumed surfaces, all geometry terms cancel and (6.32) shows a direct relationship between areal loss density and I_{Lo}. This equation can be rearranged to define a loss-limited maximum (denoted with H) for I_{Lo}:

$$I_{Lmaxo}^{H} = \sqrt{\frac{2}{R_o}\left(\frac{P_{loss}}{A_s}\right)_{max}} \tag{6.33}$$

For perpendicular modes in which both non-l dimensions are equal, we note that an areal loss density based on A can be scaled to A_s using $\frac{P_{loss}}{A_s} = \frac{\widehat{G}}{4}\frac{P_{loss}}{A}$ (for contour extensional mode) or $\frac{\widehat{G}}{\pi}\frac{P_{loss}}{A}$ (for radial mode). This assumes a PR design will adhere to $\widehat{G}$, the condition for G corresponding to maximum efficiency as derived in Section 6.4.1.

I_{Lmaxo}^{H} is displayed in Table 6.9 for each mode and can be directly compared to I_{Lmaxo}^{S}, I_{Lmaxo}^{T} and I_{Lmaxo}^{E} in (6.30) to determine I_{Lmaxo}. It can also be utilized in Sections 6.4.3 and 6.4.4 to calculate loss-limited energy and power handling densities.

6.4 Material and Vibration Mode Figures of Merit

With models established for both the PR and its behavior in a power converter, we now derive figures of merit for piezoelectric materials and vibration modes based on efficiency and power density capability. These figures of merit also correspond to geometry conditions that may be leveraged for selecting PR dimensions.

6.4.1 Mechanical Efficiency Figure of Merit

To quantitatively compare piezoelectric materials and vibration modes for power conversion, we first focus on achievable PR efficiency; this has implications for both operating cost and thermal management. Efficiency can be expressed as

$$\eta := \frac{P_{out}}{P_{out} + P_{loss}} = \frac{1}{1 + \frac{P_{loss}}{P_{out}}} \tag{6.34}$$

Thus, the impact of piezoelectric material properties on efficiency can be examined through *loss ratio* P_{loss}/P_{out}, which is desired to be as low as possible. As discussed in Section 6.3.4, we focus on only mechanical loss for this FOM.

The mechanical loss ratio of a PR can be expressed as follows, assuming P_{loss} in (6.31) and I_L in (6.24):

$$\frac{P_{loss}}{P_{out}} = \frac{\frac{1}{2}I_L^2 R}{P_{out}} = \frac{\pi^2}{2}\Big(\frac{P_{out}}{V_{in}^2}R + 2BR + \frac{V_{in}^2 B^2}{P_{out}}R\Big) \tag{6.35}$$

in which we have lumped PR-dependent terms into "frequency-capacitance product" B for conciseness:

$$B := fC_p \tag{6.36}$$

B represents the only term in the amplitude of resonance model that is specific to the PR, including both material properties and geometry terms.

Loss ratio equation (6.35) has only two operating point parameters (V_{in} and P_{out}) and two PR-dependent parameters (B and R). We can explicitly separate the PR's material and geometry properties by extracting all geometry parameters from B and R, leaving only the material-dependent B_o and R_o, respectively:

$$B = \frac{G_f A}{l}B_o = GB_o \tag{6.37}$$

$$R = \frac{l}{G_f A}R_o = \frac{R_o}{G} \tag{6.38}$$

B and R depend on the same geometry terms, which we collectively define as G. G therefore represents the only PR geometry term in the amplitude of resonance model:

$$G := G_f \frac{A}{l} \tag{6.39}$$

G, B_o, and R_o are displayed for each vibration mode in Table 6.10. It should be noted that we treat Q_m as a material property provided by the manufacturer for the purposes of this study, though Q_m realistically varies from this value based on PR shape, vibration mode, and mounting structure.

Table 6.10: Mechanical Efficiency Figures of Merit and Relevant Parameters

Vibration Mode	G	B_o	R_o	FOM_M	γ_o
Length Extensional (s)	$\frac{4b}{l}$	$\varepsilon_{33}^T(1-k_{31}^2)\frac{\kappa_o v_a}{4\pi}$	$\frac{\pi}{2Q_m k_{31}^2 \varepsilon_{33}^T v_a}$	$4Q_m \frac{k_{31}^2}{1-k_{31}^2}\frac{1}{\pi^2\bar{\kappa}_o}$	$\sqrt{\pi^2+8\frac{k_{31}^2}{1-k_{31}^2}}$
Length Extensional (e)	$\frac{A}{l^2}$	$\varepsilon_{33}^T(1-k_{33}^2)\frac{\kappa_o v_a}{4\pi}$	$\frac{\gamma_o}{2Q_m k_{33}^2 \varepsilon_{33}^T(1-k_{33}^2)v_a}$	$4Q_m k_{33}^2 \frac{1}{\pi\gamma_o\bar{\kappa}_o}$	$\sqrt{\pi^2-8k_{33}^2}$
Thickness Shear (side)	$\frac{A}{l^2}$	$\varepsilon_{11}^S \frac{\kappa_o v_a}{4\pi}$	$\frac{\gamma_o}{2Q_m k_{15}^2 \varepsilon_{11}^S v_a}$	$4Q_m k_{15}^2 \frac{1}{\pi\gamma_o\bar{\kappa}_o}$	$\sqrt{\pi^2-8k_{15}^2}$
Thickness Shear (end)	$\frac{4b}{l}$	$\varepsilon_{11}^S \frac{\kappa_o v_a}{4\pi}$	$\frac{\pi}{2Q_m k_{15}^2 \varepsilon_{11}^T v_a}$	$4Q_m \frac{k_{15}^2}{1-k_{15}^2}\frac{1}{\pi^2\bar{\kappa}_o}$	$\sqrt{\pi^2+8\frac{k_{15}^2}{1-k_{15}^2}}$
Thickness Extensional	$\frac{A}{l^2}$	$\varepsilon_{33}^S \frac{\kappa_o v_a}{4\pi}$	$\frac{\gamma_o}{2Q_m k_t^2 \varepsilon_{33}^S v_a}$	$4Q_m k_t^2 \frac{1}{\pi\gamma_o\bar{\kappa}_o}$	$\sqrt{\pi^2-8k_t^2}$
Contour Extensional	$\frac{4a}{l}$	$\varepsilon_{33}^T(1-k_p^2)\frac{\kappa_o v_a}{4\pi}$	$\frac{\pi}{2Q_m k_p^2 \varepsilon_{33}^T v_a}$	$4Q_m \frac{k_p^2}{1-k_p^2}\frac{1}{\pi^2\bar{\kappa}_o}$	$\sqrt{\pi^2+8\frac{k_p^2}{1-k_p^2}}$
Radial	$\frac{\pi a}{l}$	$\varepsilon_{33}^T(1-k_p^2)\frac{\kappa_o v_a}{4\pi}$	$\frac{\kappa_{o,r}^2-(1-\sigma^2)}{Q_m\kappa_{o,r}(1+\sigma)k_p^2\varepsilon_{33}^T v_a}$	$Q_m \frac{k_p^2}{1-k_p^2}\frac{2}{\pi\bar{\kappa}_o}\frac{\kappa_{o,r}(1+\sigma)}{\kappa_{o,r}^2-(1-\sigma^2)}$	Section 6.2.5

Numerical subscripts indicate the tensor components relevant for each mode [2]. From (6.45), $\bar{\kappa}_o = \frac{\pi\gamma_o}{\pi+\gamma_o}$ (see Section 6.2.5 for radial mode).

With geometry terms extracted, (6.35) can be rewritten as

$$\frac{P_{loss}}{P_{out}} = \frac{\pi^2}{2}\left(\frac{P_{out}}{V_{in}^2}\frac{R_o}{G} + 2B_oR_o + \frac{V_{in}^2}{P_{out}}GB_o^2R_o\right) \tag{6.40}$$

To derive the minimum mechanical loss ratio, we assume that the designer has the flexibility to choose the PR's geometric dimensions. The loss ratio equation reached in (6.40) is a second-order equation with respect to G as illustrated in Fig. 6-7(a). Minimizing (6.40) with respect to G reveals the following G condition (denoted by $\widehat{G}$) and corresponding minimum mechanical loss ratio:

$$\widehat{G} = \frac{P_{out}}{V_{in}^2 B_o} = \frac{V_{out}^2}{V_{in}^2 B_o R_{load}} \tag{6.41}$$

$$\Rightarrow \quad \left(\frac{P_{loss}}{P_{out}}\right)_{min} = 2\pi^2 B_o R_o \tag{6.42}$$

The condition in (6.41) cancels the operating point, load, and PR geometry parameters in the loss ratio equation (6.42), so *the minimum achievable mechanical loss ratio for a PR depends on only its material properties* (i.e., quantities assumed in Table 6.2). Taking the inverse of (6.42), the following unitless factor can be therefore considered a mechanical efficiency FOM (FOM_M) for a PR material and vibration mode:

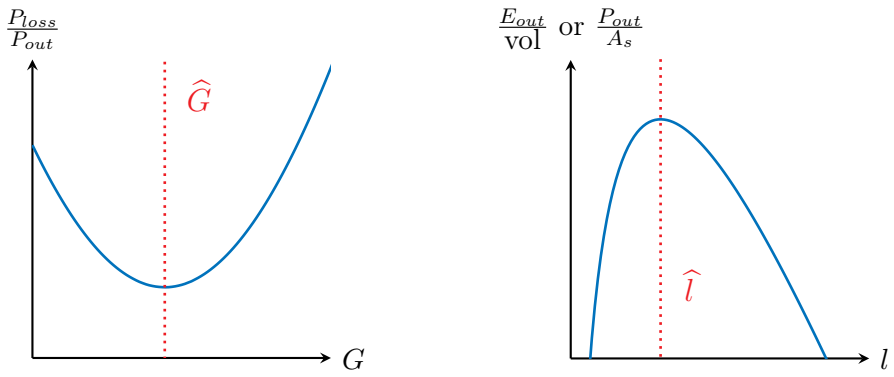

(a) (b)

Figure 6-7: On logarithmic axes, PR (a) loss ratio minimum and (b) volumetric energy handling density (or areal power handling density) maximum.

$$\text{FOM}_M := \frac{1}{2\pi^2 B_o R_o} \tag{6.43}$$

FOM_M is desired to be as large as possible, and it is summarized in Table 6.10 for the considered vibration modes.

6.4.2 Maximum-Efficiency Operating Frequency

Though B_o and R_o have no geometry dependence, B_o depends on κ_o, which spans the ranges of (6.5) and (6.6) for the inductive region shown in Fig. 6-3(a). Although the switching sequence described in Section 6.3.1 naturally spans this inductive region, frequency is *not* an independent control variable. To maintain the high-efficiency behaviors described in Section 6.3.1, the exact operating frequency (and therefore exact κ_o) is dictated by the operating point as described in Chapter 2.

Thus, we determine the frequency and κ_o that correspond to the minimum loss ratio operating point in (6.41)-(6.42) for use in the FOMs and geometry conditions of this section (though this is also useful for broader converter design). Inserting $\widehat{G}$ into (6.24) reveals both addends of I_L to be equal for this condition, which implies that the PR's charge transfer is split evenly between connected/zero stages (resonating at f_r with period $\frac{1}{f_r}$) and open stages (resonating at f_{ar} with period $\frac{1}{f_{ar}}$). Thus, both stage types require half of their respective

periods (for each transferring $\frac{1}{2}Q_{total}$), so the total period adds to $\frac{1}{\bar{f}} = \frac{1}{2f_r} + \frac{1}{2f_{ar}}$. This reveals the highest-efficiency operating frequency to be the harmonic mean of f_r and f_{ar}:

$$\bar{f} := \frac{2f_r f_{ar}}{f_r + f_{ar}} \tag{6.44}$$

which has the following geometry-normalized wave number (also derived for radial mode in Section 6.2.5):

$$\bar{\kappa}_o := \frac{\pi\gamma_o}{\pi + \gamma_o} \tag{6.45}$$

Thus, assuming the switching sequence constraints listed in Section 6.3.1 are met, this is the operating frequency for which (6.41) is satisfied and the minimum loss ratio occurs. This is the operating frequency assumed for the remainder of this chapter.

We note that the frequency of an arbitrary operating point may be estimated using a Fourier-based approach as detailed in [98].

6.4.3 Volumetric Energy Handling Density Figure of Merit

A second point of comparison for piezoelectric materials and vibration modes is achievable power handling density, which poses a boundary for converter miniaturization. Useful power density metrics must consider how the PR is to be utilized in a converter (i.e., not just energy storage capability), so we again assume the amplitude of resonance model in Section 6.3. To model the PR's power handling capability as a function of operating constraints, (6.24) can be rearranged such that power delivered to the load is the following function of I_L:

$$P_{out} = \frac{1}{\pi}V_{in}I_L - C_p f V_{in}^2 = \frac{1}{\pi}V_{in}I_L - BV_{in}^2 \tag{6.46}$$

Volumetric power density is a common metric for converter power handling capability with respect to size. The PR's volumetric power density can be derived by first dividing (6.46) by volume, where vol $= 2Al$:

$$\frac{P_{out}}{\text{vol}} = \frac{P_{out}}{2Al} = G_f\left(\frac{1}{2\pi l}V_{in}I_{Lmaxo} - \frac{1}{2l^2}B_o V_{in}^2\right) \tag{6.47}$$

in which I_L has been set equal to I_{Lmax} and geometry terms have been separated from material properties.

It is evident that a PR's volumetric power density is directly proportional to G_f, and therefore f. The operating frequency of a converter determines its driving and control requirements, so we elect to normalize (6.47) to f for even comparison between PR vibration modes with respect to converter capability. Such normalization results in the following expression for volumetric *energy handling* density, defined as the quantity of energy delivered to the load in one resonant cycle divided by volume (not to be confused with energy storage density):

$$\frac{E_{out}}{\text{vol}} = \frac{P_{out}}{\text{vol} \cdot f} = \frac{1}{\kappa_o v_a}\left(\frac{1}{l} V_{in} I_{Lmaxo} - \frac{\pi}{l^2} B_o V_{in}^2\right) \tag{6.48}$$

We can then maximize this expression by assuming the designer has the flexibility to choose l. Maximizing (6.48) with respect to l as illustrated in Fig. 6-7(b) results in the following l condition (denoted $\widehat{l}$) and maximum volumetric energy handling density:

$$\widehat{l} = 2\pi \frac{B_o V_{in}}{I_{Lmaxo}} \tag{6.49}$$

$$\Rightarrow \quad \left(\frac{E_{out}}{\text{vol}}\right)_{max} = \frac{I_{Lmaxo}^2}{4\pi \kappa_o v_a B_o} \tag{6.50}$$

Thus, all operating point and geometry terms cancel in (6.50), and the maximum volumetric energy handling density of a PR depends on only its material properties (defined in Table 6.2). The following can therefore be considered a volumetric energy handling density FOM for direct comparison between PR materials and vibration modes:

$$\text{FOM}_{VED} := \frac{I_{Lmaxo}^2}{4\pi \kappa_o v_a B_o} \tag{6.51}$$

which has units J/m^3. FOM_{VED} is summarized for various PR vibration modes in Table 6.11; we suggest use of the minimum-loss wave number $\bar{\kappa}_o$ as detailed in Section 6.4.2. The corresponding volumetric power density can be calculated by multiplying FOM_{VED} by a desired operating frequency, though this frequency depends on $\widehat{l}$ for parallel modes[1].

[1]For parallel modes, maximum volumetric power density occurs for $l = \frac{3}{4}\widehat{l}$, though with diminishing

Table 6.11: Power Density Figures of Merit and Relevant Parameters

Vibration Mode	FOM_{VED}	FOM_{APD}	A_s
Length Extensional (side)	$\frac{I_{Lmaxo}^2}{\bar{\kappa}_o^2 v_a^2 \varepsilon_{33}^T (1-k_{31}^2)}$	$\frac{I_{Lmaxo}^2}{\pi \bar{\kappa}_o \varepsilon_{33}^T (1-k_{31}^2) v_a}$	$4bl$
Length Extensional (end)	$\frac{I_{Lmaxo}^2}{\bar{\kappa}_o^2 v_a^2 \varepsilon_{33}^T (1-k_{33}^2)}$	$\frac{I_{Lmaxo}^2}{\pi \bar{\kappa}_o \varepsilon_{33}^T (1-k_{33}^2) v_a}$	A
Thickness Shear (side)	$\frac{I_{Lmaxo}^2}{\bar{\kappa}_o^2 v_a^2 \varepsilon_{11}^S}$	$\frac{I_{Lmaxo}^2}{\pi \bar{\kappa}_o \varepsilon_{11}^S v_a}$	A
Thickness Shear (end)	$\frac{I_{Lmaxo}^2}{\bar{\kappa}_o^2 v_a^2 \varepsilon_{11}^S}$	$\frac{I_{Lmaxo}^2}{\pi \bar{\kappa}_o \varepsilon_{11}^S v_a}$	$4bl$
Thickness Extensional	$\frac{I_{Lmaxo}^2}{\bar{\kappa}_o^2 v_a^2 \varepsilon_{33}^S}$	$\frac{I_{Lmaxo}^2}{\pi \bar{\kappa}_o \varepsilon_{33}^S v_a}$	A
Contour Extensional	$\frac{I_{Lmaxo}^2}{\bar{\kappa}_o^2 v_a^2 \varepsilon_{33}^T (1-k_p^2)}$	$\frac{I_{Lmaxo}^2}{\pi \bar{\kappa}_o \varepsilon_{33}^T (1-k_p^2) v_a}$	$4al$
Radial	$\frac{I_{Lmaxo}^2}{\bar{\kappa}_o^2 v_a^2 \varepsilon_{33}^T (1-k_p^2)}$	$\frac{I_{Lmaxo}^2}{\pi \bar{\kappa}_o \varepsilon_{33}^T (1-k_p^2) v_a}$	πal

Numerical subscripts indicate the tensor components relevant for each mode [2]. From (6.45), $\bar{\kappa}_o = \frac{\pi \gamma_o}{\pi + \gamma_o}$ (see Section 6.2.5 for radial mode).

6.4.4 Areal Power Handling Density Figure of Merit

In some applications, power handling capability per footprint area may be more useful to the designer than volumetric energy handling density. Areal power density also becomes more relevant for highly-planar PR designs, as often dictated by $\widehat{G}$ in (6.41) for maximum efficiency. Like Section 6.3.4, we assume the area of interest $A_s = A$ for parallel modes and $A_s = G_f A l$ for perpendicular modes as displayed in Table 6.11. Similar to (6.47), the areal power density can be written as follows with $I_L = I_{Lmax}$ and geometry terms extracted:

$$\frac{P_{out}}{A_s} = \frac{1}{\pi l} V_{in} I_{Lmaxo} - \frac{1}{l^2} B_o V_{in}^2 \tag{6.52}$$

This expression can be likewise maximized with respect to l, resulting in the same $\widehat{l}$ condition and the following maximum areal power density:

$$\widehat{l} = \frac{2\pi B_o V_{in}}{I_{Lmaxo}} \tag{6.53}$$

$$\Rightarrow \quad \left(\frac{P_{out}}{A_s}\right)_{max} = \frac{I_{Lmaxo}^2}{4\pi^2 B_o} \tag{6.54}$$

returns with respect to frequency for $l < \widehat{l}$. The volumetric power density at $l = \frac{3}{4}\widehat{l}$ is ≈18.5 % greater than that at $l = \widehat{l}$.

Like the maximum volumetric energy handling density in (6.50), the maximum areal power density for a PR depends on only its material properties. Thus, (6.54) serves as an areal power handling density FOM for PR materials and vibration modes:

$$\mathrm{FOM}_{APD||} := \frac{I_{Lmaxo}^2}{4\pi^2 B_o} \tag{6.55}$$

with units W/m^2. FOM_{APD} equals FOM_{VED} scaled by $\frac{\kappa_o v_a}{\pi}$ and is likewise summarized in Table 6.11 for each considered vibration mode. It should be noted that FOM_{APD} assumes the area A_s corresponds to the PR's relevant footprint, though the validity of this assumption depends on the PR's shape, vibration mode, and mounting structure. For contour and radial modes (i.e., modes for which both non-l dimensions are equal), FOM_{APD} may be respectively scaled by $\frac{4}{\widehat{G}}$ and $\frac{\pi}{\widehat{G}}$ for representative areal power densities based on A, assuming a PR design will adhere to the $\widehat{G}$ condition for maximum efficiency. Since $\widehat{G}$ varies by operating point, this scaled FOM_{APD} for such configurations may introduce dependence on operating point information.

6.5 Piezoelectric Resonator Design

Equipped with FOMs and geometry conditions for maximum efficiency and power density, we now demonstrate use of these tools for PR design and discuss their implications for material and vibration mode selection. We note that the results of these material and vibration mode studies are meant to be more demonstrative of the FOMs than prescriptive of the materials; the results are sensitive to variation between manufacturers in terms of measurement procedure and/or reporting of material properties (particularly for E_{max} and Q_m). This topic merits a detailed experimental characterization of such materials and vibration modes, which is beyond the scope of this thesis.

6.5.1 Geometry Conditions

The PR design process begins with co-selection of a piezoelectric material and vibration mode. Then, as derived in Section 6.4, a PR's dimensions can be designed to achieve both its minimum mechanical loss ratio and maximum power density at a nominal operating point by satisfying $G = \widehat{G}$ and $l = \widehat{l}$, respectively. The PR shapes produced by these geometry conditions vary drastically with material and vibration mode and therefore warrant consideration in the selection process.

The maximum-efficiency geometry condition $\widehat{G}$ derived in (6.41) increases proportionally with P_{out} and inversely with V_{in}^2 and B_o. The order of magnitude of B_o ranges from 10^{-8} to 10^{-6} for most piezoelectric materials, which requires $\widehat{G} >> 1$ in (6.41) for most power conversion applications. Thus, $\widehat{G}$ often dictates l to be the shortest geometric dimension, resulting in primarily planar PR designs. Modes for which l is not the shortest dimension have limited utility for power conversion; their relative dimensions assumed in Fig. 6-1 can only be maintained for low $\widehat{G}$, which corresponds to very high $\frac{V_{in}^2}{P_{out}}$.

Parallel vibration modes can be particularly advantageous for satisfying large $\widehat{G}$ values in that both the numerator (A) and denominator (l^2) of G have squared length dimensions. The length dimensions comprising G for perpendicular modes are only to the first power, requiring more extreme planar shapes to satisfy the same $\widehat{G}$. This difference is less pronounced at lower $\widehat{G}$ values but more exaggerated for higher $\widehat{G}$, making parallel modes more footprint-effective for high power applications. As $\widehat{G}$ approaches infinity, all modes besides length extensional (end electrodes) are capable of designs that meet the relative dimension assumptions in Fig. 6-1. As $\widehat{G}$ approaches zero, the set of compatible modes reduces to just the two length extensional modes and thickness shear (end electrodes) mode.

Assuming a PR is designed to satisfy $G = \widehat{G}$ and $l = \widehat{l}$, we examine how its dimensions must scale for different voltage levels and power levels assuming a fixed B_o and I_{Lmaxo}. The results of these case studies are displayed for multiple types of vibration modes in Table 6.12. We first scale V_{in} by factor α (with constant P_{out}) and display the dependence of the PR's dimensions on α such that the geometry conditions remain satisfied. We repeat this

Table 6.12: Piezoelectric Resonator Design Scaling with Operating Point

Case Study	Vibration Mode Type	$\widehat{l}$	$\widehat{G}$	A	a	b	vol	f
Scale V_{in} by α	Parallel	α	α^{-2}	1	**	**	α	α^{-1}
	Perpendicular ($a = b$)*	α	α^{-2}	α^{-2}	α^{-1}	α^{-1}	α^{-1}	α
	Perpendicular ($a \neq b$)	α	α^{-2}	α^{-1}	1	α^{-1}	1	1
Scale P_{out} by α	Parallel	1	α	α	**	**	α	1
	Perpendicular ($a = b$)*	1	α	α^2	α	α	α^2	α^{-1}
	Perpendicular ($a \neq b$)	1	α	α	1	α	α	1

*The 'Perpendicular ($a = b$)' mode type is inclusive of perpendicular modes for which both planar dimensions are a.
**The scaling of a and b for parallel modes is unspecified but must satisfy the scaling of A.

exercise for scaling of P_{out} by factor α (with constant V_{in}), and we note that whether this power scaling is realized through voltage, current, or load scaling is irrelevant to the result.

Table 6.12 reveals significant differences in how the dimensions of parallel and perpendicular vibration modes scale to maintain $G = \widehat{G}$ and $l = \widehat{l}$ at different operating points. Designing a PR for higher V_{in} requires an increase in l for all modes, but perpendicular modes require a simultaneous decrease in A to maintain $G = \widehat{G}$. For all modes, designing a PR for higher P_{out} requires an increase in A but not l. The powers to which these dimensions scale with operating point varies between mode types and may affect the designer's choice of vibration mode in the presence of area, height, volume, and frequency constraints.

The PR design strategy of satisfying $G = \widehat{G}$ and $l = \widehat{l}$ assumes that the resulting design occurs within an acceptable frequency range for the intended application. If a design is instead confined to a certain frequency or frequency limit, the designer may constrain the frequency-setting dimension G_f accordingly and still satisfy $G = \widehat{G}$ with a remaining degree of freedom in the PR's dimensions. This will sacrifice the PR's power density capability but maintain its maximum efficiency at the nominal operating point.

6.5.2 Piezoelectric Material Comparison

To illustrate use of the FOMs derived in Section 6.4, we evaluate commercially available variants of hard PZT, the most widely-utilized piezoelectric material for sensing, actuation,

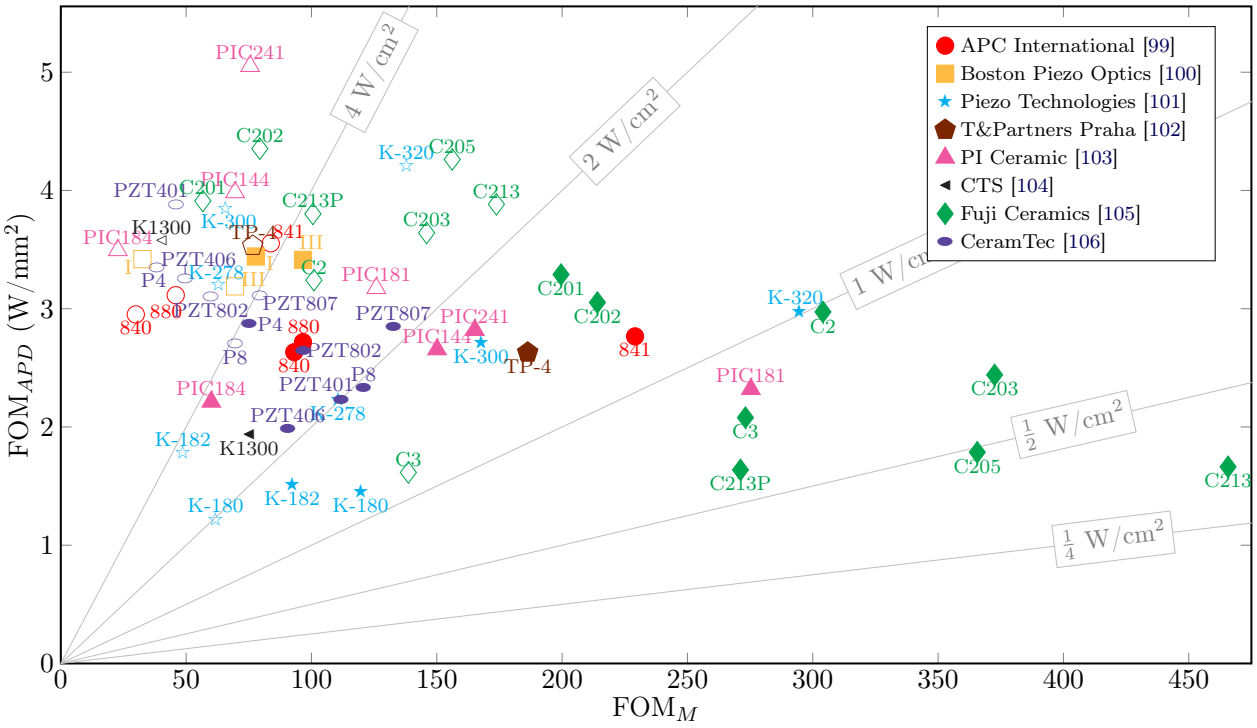

Figure 6-8: Comparison of hard PZT materials for power conversion based on FOM_M and FOM_{APD}, overlaid with areal-loss-density contour lines. Filled and unfilled markers indicate the thickness shear (side electrodes) and thickness extensional vibration modes, respectively.

transduction, and energy harvesting applications. We compare hard PZT materials based on efficiency and power density for the thickness extensional and thickness shear vibration modes (with side electrodes), which requires collecting and/or calculating the following properties for 30 hard PZT materials from eight different manufacturers: Q_m, ε_{33}^S, ε_{11}^S, k_t, k_{15}, and v_a for each mode ($v_a = \frac{\pi N}{\kappa_{o,r}}$, where N is the manufacturer-provided frequency constant). Sinusoidal amplitude E_{max} is conservatively estimated to be 500 V/mm for all materials, and power density capability is assumed to be limited by this E_{max} using I_{Lmaxo}^E.

We use these properties to calculate FOM_M and FOM_{APD} for both modes with each material. Fig. 6-8 displays these results with one FOM on each axis, and the considered materials exhibit wide variation in terms of capability. The thickness extensional mode (denoted by unfilled markers) generally demonstrates higher power density capability given the same E_{max}, and thickness shear mode (denoted by filled markers) shows higher efficiency capability given the same Q_m.

Figure 6-8 is further overlaid with areal-loss-density contour lines to help identify thermal management limits, which vary based on design and application constraints. For a given areal loss density limit, all points above the corresponding contour line can be projected downward (in the -y direction, keeping constant FOM_M) onto the allowable loss density line itself; this new point conveys their maximum power densities given the assumed limit. It can be inferred that many materials would in fact never reach the assumed E_{max} limit without aggressive thermal management; for a given thermal capability, higher power density is instead enabled by a higher FOM_M. In the context of this study, this implies that the thickness shear mode enables higher power densities than the thickness extensional mode for practical areal loss density constraints ($\leq$ 1 W/cm^2). Of course, these comparisons are based on small-signal material properties and do not account for nonlinearities in loss.

6.5.3 Vibration Mode Comparison

We compare the seven vibration modes discussed herein for hard PZT and lithium niobate ($LiNbO_3$), a second piezoelectric material of emerging interest for power conversion [15, 69]. This case study relies on material properties from [107] and [108], respectively (we assume these properties as provided, though different crystal cuts can be similarly compared). We calculate FOM_M, FOM_{VED}, and FOM_{APD} for each vibration mode and display them in Table 6.13. The same Q_m and E_{max} are assumed for all modes of each material; Q_m is assumed to be 2200 for PIC181 and 10000 for $LiNbO_3$ as reported in the datasheets, and E_{max} is assumed to be 633 V/mm for PIC181 and 7000 V/mm for $LiNbO_3$ (1/3 the coercive field of each material). An areal loss density limit of 1 W/cm^2 is also assumed, so the displayed FOMs are based on the lower of these two limits as described in Sections 6.3.3 and 6.3.4. FOMs that have been scaled by $\frac{\widehat{G}}{4}$ or $\frac{\widehat{G}}{\pi}$ are marked with asterisks in Table 6.13; these FOMs assume V_{in} = 100 V and P_{out} = 10 W.

Table 6.13 shows the modes of each material to have significantly varying capabilities with respect to mechanical efficiency, volumetric energy handling density, and areal power density. Higher FOM_M is associated with higher k^2 (since the same Q_m is assumed for all

Table 6.13: Vibration Mode Comparison for Hard PZT and Lithium Niobate

Mode	Hard PZT (PIC181)					Lithium Niobate				
	FOM_M	FOM_{VED} (J/m^3)	FOM_{APD} (W/cm^2)	$\widehat{G}$*	Theoretical Design*	FOM_M	FOM_{VED} (J/m^3)	FOM_{APD} (W/cm^2)	$\widehat{G}$*	Theoretical Design*
Length Ext. (s)	63.4	377	63.4	264	l=240μm, b=16mm	1.26	4.14	1.26	5190	l=390μm, b=510mm
Length Ext. (e)	345	1930	345	395	N/A	74.0	224	74.0	4910	N/A
Thickness Shear (s)	303	2740	302	553	l=77μm, $\sqrt{\frac{A}{4}}$=910μm	1810	7360	1810	4160	l=12μm, $\sqrt{\frac{A}{4}}$=370μm
Thickness Shear (e)	338	3210	337	581	l=71μm, b=10mm	2090	9110	2090	4440	l=10μm, b=12mm
Thickness Extensional	138	631	138	330	l=150μm, $\sqrt{\frac{A}{4}}$=1.3mm	72.0	198	72.0	4450	l=56μm, $\sqrt{\frac{A}{4}}$=1.9mm
Contour Extensional	229	13200	33.0*	302	l=36μm, a=2.8mm	3.14	12900*	3.14	5090	l=7μm, a=8.9mm
Radial	223	15600	52.8*	230	l=34μm, a=2.5mm	3.12	10200*	3.12	4030	l=8μm, a=10mm

*Assuming an example operating point of V_{in}=100V and P_{out}=10W. At this operating point, power density is E-limited only for PZT contour ext. and radial modes.

modes of the same material), and particularly high FOM_Ms are shown for $LiNbO_3$ shear modes. Most vibration modes have loss-limited power densities as indicated by FOM_{APD} tracking FOM_M given the assumed areal loss density limit. Perpendicular vibration modes tend to have higher FOM_{VED} compared to parallel modes, which implies that perpendicular modes are capable of higher volumetric power densities for a given frequency. Also worth noting is that some modes would have to operate at more than an order of magnitude higher frequency than others to achieve the same volumetric power density. These results are independent of the assumed operating point for all vibration modes except for contour extensional and radial.

For each mode in Table 6.13, we display $\widehat{G}$ and a corresponding theoretical design based on $\widehat{G}$ and $\widehat{l}$ for V_{in} = 100 V and P_{out} = 10 W; designs that violate the relative dimension assumptions in Fig. 6-1 are marked with "N/A". These $\widehat{G}$ and theoretical designs further highlight differences between $LiNbO_3$, hard PZT, and their parallel and perpendicular vibration modes. $LiNbO_3$ generally requires an order of magnitude higher $\widehat{G}$ than PZT, resulting in more planar-shaped geometries that often require more footprint area and/or higher oper-

Table 6.14: Vibration Mode Comparison Summary

Material	Hard PZT		Lithium Niobate	
Vibration Mode	Parallel	Perpendicular	Parallel	Perpendicular
FOM_M	High	High	Very High	Low
FOM_{VED}	Medium	Very High	High	Very High
FOM_{APD}	High	Medium	Very High	Low
Required Shape	Planar	Very Planar	Very Planar	Extremely Planar

ating frequencies for similar density. In general, perpendicular modes likewise require more extreme planar shapes for the same $\widehat{G}$ compared to parallel modes due to their linear (rather than squared) length dimensions comprising $\widehat{G}$. As described in Section 6.5.1, this effect would have been more exaggerated for an operating point corresponding to a greater $\widehat{G}$, and less pronounced for an operating point corresponding to a lower $\widehat{G}$.

The FOMs and theoretical designs of Table 6.13 suggest the most promising parallel vibration modes for PZT to be thickness shear (side electrodes) and thickness extensional, and the most auspicious perpendicular vibration modes for PZT to be contour extensional and radial. The highest-performing vibration mode for the considered crystal cut of Lithium Niobate is the thickness shear (side electrodes), though other high-performing modes such as a quasi-thickness extensional modes are possible with other crystal orientations. In Table 6.14, we summarize the comparison of Table 6.13 considering only these four promising vibration modes. PZT has a high FOM_M and therefore a high efficiency capability, but Lithium Niobate parallel modes offer opportunity for even higher efficiency to the extent that their theoretical quality factors can be realized. Designs constrained by footprint area should utilize parallel vibration modes, which have significantly higher FOM_{APD} than perpendicular modes. Designs that are instead constrained by volume or frequency should employ perpendicular vibration modes, which have greater FOM_{VED} and are therefore capable of greater volumetric power densities at lower frequencies. All considered vibration modes require planar shapes, but the extent to which they are planar (i.e., the extent to which dimensions a and b are significantly greater than l) vary and should be considered with manufacturing

and form factor constraints.

Thus, the most appropriate piezoelectric materials and vibration modes depend heavily on the target application space. In addition to PZT and $LiNbO_3$, there are numerous other piezoelectric materials that may be similarly evaluated for power conversion using these FOMs and geometry conditions.

6.6 Numerical and Experimental Validation

To evaluate their utility, we validate the FOMs and geometry conditions derived herein with numerically-obtained periodic steady-state solutions (PSSS) of converter behavior and experimental results.

6.6.1 Periodic Steady-State Solution

The switching sequence described in Section 6.3.1 is assumed to operate in periodic steady-state, which implies that the PR's states cycle through the same trajectories every switching cycle. As described in Section 2.4, we can quantify these trajectories in a periodic steady-state solution, which varies based on circuit model parameters and operating point (V_{in}, V_{out}, and P_{out}). An "exact" periodic steady-state solution (i.e., considering R in Fig. 6-3(b)) can obtained by numerically solving the set of differential equations that govern the PR's states during each stage of a switching sequence. A periodic steady-state solution has no dependence on the amplitude of resonance model or other derivations herein.

With an exact periodic steady-state solution, we can extract useful information from the PR's state trajectories like loss and output power for validating the derived FOMs. As such, we first validate the minimum loss ratio and maximum power densities with periodic steady-state solutions based on geometry and material data for 572 APC International discrete PR parts listed on [109]; these parts consist of round and rectangular PRs of varying dimensions, spanning nine total materials. For each part, we:

1. Calculate its circuit model parameters (as shown in Table 6.4) for a given vibration

mode.

2. Based on its dimensions, determine V_{in} and P_{out} corresponding to its minimum loss ratio and maximum energy handling density using (6.41) and (6.49), assuming I_{Lmax} to be limited by an areal loss density of 1 W/cm^2.

3. For this operating point, solve for the exact periodic steady-state solution as detailed in Section 2.4, constraining the converter switching sequence for the high-efficiency behaviors corresponding to (6.24) and $V_{out} = 0.55V_{in}$. This voltage conversion ratio selection is arbitrary since I_L is predicted to be independent of V_{out} for $V_{in} > V_{out} > \frac{1}{2}V_{in}$ according to (6.24). An example MATLAB script for obtaining the exact periodic steady-state solution is provided in Appendix A.1.1.

4. Extract P_{out} from the periodic steady-state solution by integrating the PR's i_L trajectory during load-connected stages and then multiplying by $V_{out} \cdot f$. Extract P_{loss} from the periodic steady-state solution by integrating the square of the PR's i_L trajectory during all stages and then multiplying by $R \cdot f$.

Ultimately, *all discrete parts of the same material and vibration mode yield the same minimum loss ratio, maximum energy handling density, and maximum areal power density*; these quantities translate directly to FOM$_M$, FOM$_{VED}$, and FOM$_{APD}$, respectively. In Table 6.15, periodic steady-state solution results for the length extensional mode (end electrodes) are compared with their derived estimates and demonstrate very small error for all low-loss-ratio materials. Accordingly, the periodic steady-state solution validates the following:

- FOM$_M$, $\left(\frac{P_{loss}}{P_{out}}\right)_{min}$, $\widehat{G}$, and $\bar{\kappa}_o$.
- FOM$_{VED}$, FOM$_{APD}$, and $\widehat{l}$.
- The independence of $\bar{\kappa}_o$, $\left(\frac{P_{loss}}{P_{out}}\right)_{min}$, $\left(\frac{E_{out}}{\text{vol}}\right)_{max}$, $\left(\frac{P_{out}}{A_s}\right)_{max}$, and $\frac{P_{loss}}{A_s}$ from PR geometry and operating point information.
- The dependence of $\frac{E_{out}}{\text{vol}}$, $\frac{P_{out}}{A_s}$, and $\frac{P_{loss}}{A_s}$ on normalized amplitude of resonance I_{Lo}.

Table 6.15: Figure of Merit Validation via Periodic Steady-State Solution

APC Material	Q_m	k_{33}	κ_o vs. (6.45) (radians)		$\frac{P_{loss}}{P_{out}}$ vs. $\frac{1}{\text{FOM}_M}$		$\frac{E_{out}}{\text{vol}}$ vs. FOM_{VED} (J/m^3)		$\frac{P_{out}}{A_s}$ vs. FOM_{APD} (W/cm^2)		$\frac{P_{loss}}{A_s}$ vs. 1.00 (W/cm^2)
840	500	0.72	1.371	1.364	.0102	.0102	429.6	432.3	97.97	98.07	1.002
841	1400	0.68	1.389	1.385	.0041	.0041	1073	1079	241.0	241.9	0.9912
842	600	0.71*	1.373	1.366	.0086	.0086	499.3	502.0	116.3	116.3	1.001
844	1500	0.65*	1.404	1.405	.0043	.0044	1009	1009	228.6	228.6	.9940
840-844 Average Error:			0.31 %		0.37%		0.45 %		0.13 %		0.43 %
880	1000	0.62	1.433	1.436	.0083	.0083	523.2	523.7	119.5	120.0	.9939
881	1000	0.73*	1.360	1.350	.0047	.0047	906.4	910.4	213.6	212.9	1.002
880-881 Average Error:			0.50 %		0.20%		0.26 %		0.33 %		0.39 %

Not shown: Soft PZT materials 850, 851, and 855 have loss ratios up to 0.069, with an average error (compared to (6.42)) of up to 6%. These materials have significantly more loss than hard PZT and are therefore less conducive to power conversion. (*) Calculated using $k_{33}^2 = Y_{33}^E d_{33}^2 / \varepsilon_{33}^T$.

Table 6.16: Extended Figure of Merit Validation via Periodic Steady-State Solution

Vibration Mode	APC Material	$\frac{P_{loss}}{P_{out}}$ vs. $\frac{1}{\text{FOM}_M}$		κ_o vs. (6.45) (radians)		$\frac{E_{out}}{\text{vol}}$ vs. FOM_{VED} (J/m^3)		$\frac{P_{out}}{A_s}$ vs. FOM_{APD} (W/cm^2)		$\frac{P_{loss}}{A_s}$ vs. 1.00 (W/cm^2)
Length Ext. (side)	840	.0602	.0570	1.607	1.613	112.3	112.1	17.52	17.54	1.054
	841	.0236	.0232	1.603	1.608	248.5	247.8	43.12	43.13	1.018
	880	.0414	.0399	1.597	1.601	142.0	142.4	24.91	25.04	1.032
Thickness Shear (side)	840	.0108	.0107	1.379	1.373	803.2	809.4	92.80	93.14	.9992
	841	.0043	.0044	1.395	1.394	1986	1979	230.1	229.1	.9984
	880	.0103	.0103	1.455	1.461	840.2	836.3	96.68	96.62	1.000
Thickness Shear (end)	840	.0093	.0092	1.810	1.795	1004	1009	108.7	108.4	1.006
	841	.0038	.0038	1.776	1.769	2377	2396	260.2	261.3	.9918
	880	.0096	.0096	1.683	1.689	938.2	932.8	104.3	104.1	1.001
Thickness Extensional	842	.0243	.0240	1.483	1.490	195.1	193.5	41.88	41.70	1.019
	844	.0096	.0096	1.483	1.490	485.5	483.6	104.2	104.3	.9999
	881	.0160	.0159	1.491	1.497	293.8	293.2	62.79	62.94	1.005
Contour Extensional	840	.0159	.0158	1.708	1.712	271.8	272.4	62.96	63.22	1.001
	841	.0054	.0054	1.715	1.718	826.1	826.7	185.3	185.8	.9921
	880	.0124	.0123	1.658	1.665	362.1	361.2	80.99	81.16	1.000
Radial	840	.0163	.0161	2.221	2.092	269.5	271.0	62.3	62.30	1.014
	841	.0056	.0056	2.292	2.276	809.5	811.1	180.1	180.1	1.008
	880	.0126	.0125	2.147	2.148	355.4	357.0	79.45	79.85	1.002

Periodic steady-state solution results validating the length extensional mode (end electrodes) FOMs are shown in Table 6.15, and results for all other vibration modes demonstrate similar alignment as shown in Table 6.16. Thus, FOM_M, FOM_{VED}, and FOM_{APD} serve as representative metrics for comparing the capabilities of low-loss piezoelectric materials.

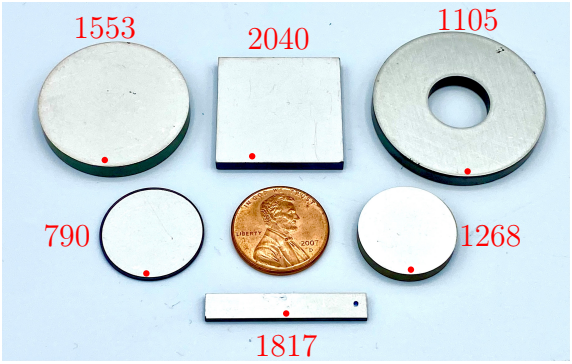

Figure 6-9: PRs tested for experimental FOM validation. The wire attachment location is marked with a red dot for each PR. Parts 790 and 1817 are mounted in an upright position on the board of Fig. 6-10 with two wires mechanically supporting the PR as in Chapter 2. All other PRs are positioned horizontally with the bottom electrode making contact with the copper ribbon and the other attached with a non-rigid wire.

We note that the energy and power density quantities are validated for all materials based on areal loss density constraint (6.32), though the practical relevance of considered area A_s in this calculation depends on the specific vibration mode and mounting structure.

6.6.2 Experimental Results

We validate the mechanical efficiency FOM experimentally using six of the PR parts considered in Section 6.6.1. These PRs consist of APC International's highest-FOM$_M$ materials (841, 844, 880, and 881) in different shapes and sizes as pictured in Fig. 6-9. These parts are selected to be low in frequency (< 600 kHz) to minimize frequency-dependent loss and potential damping effects due to mounting during validation. With each PR, we perform the following:

1. Plot the PR's impedance characteristic (i.e., Fig. 6-3(a)) for a given vibration mode using an impedance analyzer.

2. Estimate Q_m, k, and C_p based on the impedance characteristic, as detailed in Section 6.6.3.

3. Calculate the minimum loss ratio for the estimated Q_m and k using (6.42). Calculate

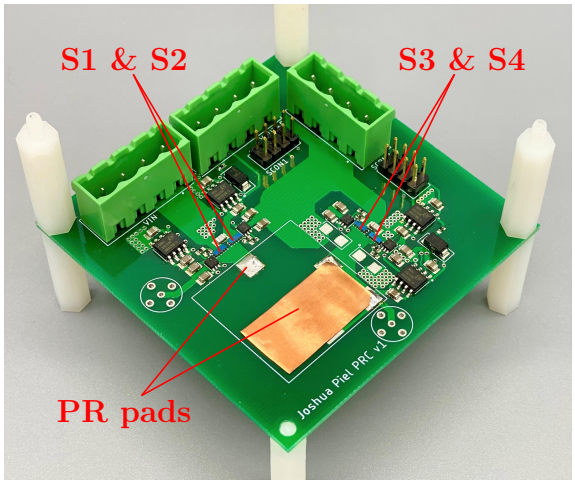

Figure 6-10: Experimental prototype board, re-purposed from Chapter 2. All switches are EPC2019 GaN FETs, driven with Texas Instruments UCC27611 gate drivers. An isolated supply powers the gate circuitry for S1 and S2. More details about this prototype, including its PCB layout, are provided in Appendix A.3.1.

the minimum-loss-ratio P_{out} using (6.41), assuming $V_{in} = 100$ V and charge-equivalent switch capacitances of 250 pF (requiring 500 pF total to be added to C_p) [110].

4. Run the PR in the prototype converter shown in Fig. 6-10 with the V_{in}-V_{out}, *Zero*, V_{out} switching sequence, constrained for the high-efficiency behaviors assumed in Section 6.3.1. This prototype and switching sequence have the topology and waveforms of Fig. 6-4 and 6-5, respectively. $V_{in} = 100$ V and $V_{out} = 60$ V, implemented with a constant-voltage load. All switching times are open-loop and manually tuned; for a given V_{in}, V_{in}, and P_{out}, there is a unique tuning point that satisfies the assumptions of Section 6.3.1.

5. Sweep through multiple power levels surrounding the calculated P_{out} to identify the minimum loss ratio and corresponding P_{in}, P_{out}, and f, maintaining the same V_{in} and V_{out} and re-tuning switching times as needed for the high-efficiency behaviors assumed in Section 6.3.1.

The results of these experiments, along with material, vibration mode, and frequency information for each PR, are displayed in Table 6.17. The estimated PR loss ratio (or

Table 6.17: Experimental Figure of Merit Validation

Part No.	Material	Vibration Mode	Q_m	k	C_p (nF)	f vs. (6.44) (kHz)		P_{out} vs. (6.41) (W)		$\frac{P_{loss}}{P_{out}}$ vs. $\frac{1}{\text{FOM}_M}$ (PR only)		η
1817	841	Length Ext. (s)	700	.32	.993	56.8	56.7	0.59	0.85	.0559	.0503	94.7 %
1105	841	Thickness Ext.	2500	.31	.602	605	596	4.0	6.6	.0221	.0156	97.8 %
2040	880	Contour Ext.	1600	.52	1.64	81.1	80.9	1.6	1.7	.0101	.0069	99.0 %
1553	841	Radial	1700	.58	1.50	80.9	80.9	1.6	1.6	.0080	.0049	99.2 %
790	844	Radial	1400	.55	3.53	124	122	4.1	4.9	.0090	.0069	99.1 %
1268	881	Radial	1600	.52	.643	129	129	1.3	1.5	.0088	.0072	99.1 %

In this table, Q_m, k, and C_p are obtained by PR characterization. (6.44), (6.41), and $\frac{1}{\text{FOM}_M}$ are calculated using these characterized quantities along with characterized f_r and f_{ar} and other manufacturer-provided material properties. f, P_{out}, $\frac{P_{loss}}{P_{out}}$, and η are measured during operation of the converter prototype at its minimum loss ratio.

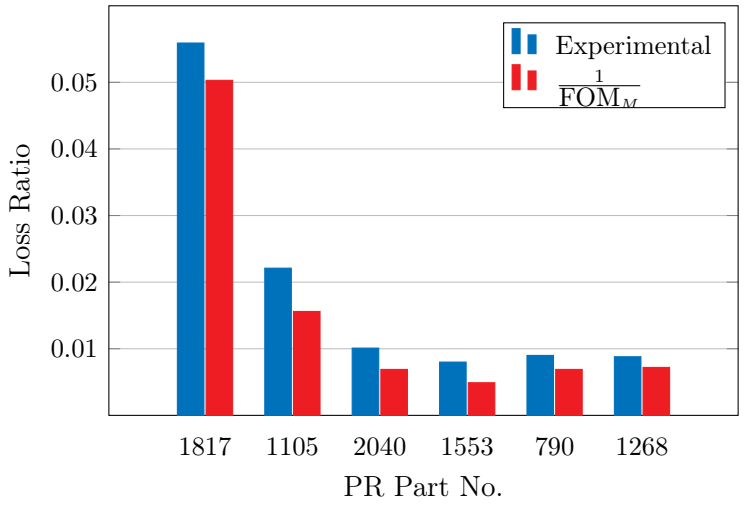

Figure 6-11: Experimental power-stage minimum loss ratio compared to $\frac{1}{\text{FOM}_M}$ for the PRs of Fig. 6-9, operated in the converter prototype of Fig. 6-10.

$\frac{1}{\text{FOM}_M}$) tracks the trend of the experimental whole-converter loss ratio as visualized in Fig. 6-11, albeit a slight underestimation. Sources for the observed discrepancies include other circuit losses (e.g., switch loss), as well as differences between the PR's small-signal (as characterized) and large-signal (as tested) characteristics. Thus, (6.42) provides a close approximation of the loss ratio to be expected by a given material and vibration mode, validating the utility of FOM_M.

6.6.3 PR Characterization

For experimental validation, we characterize each PR using a procedure outlined in [2] in order to calculate its FOMs based on physical properties. Q_m is calculated based on the PR's 3dB bandwidth at resonance as measured using a small-signal impedance analyzer :

$$Q_m = \frac{f_r}{\mathrm{BW}_{3dB}} \tag{6.56}$$

Further, the effective k is calculated based on the observed resonant and anti-resonant frequencies:

$$k_{eff} = \sqrt{\frac{f_{ar}^2 - f_r^2}{f_{ar}^2}} \tag{6.57}$$

This enables the following mode-specific k calculations [2]:

$$k_{||}^2 = \frac{\pi}{2}\sqrt{1-k_{eff}^2}\cot(\frac{\pi}{2}\sqrt{1-k_{eff}^2}) \tag{6.58}$$

$$k_{+}^2 = \frac{1}{1-\frac{2}{\pi}\sqrt{1-k_{eff}^2}\tan(\frac{\pi}{2}\frac{1}{\sqrt{1-k_{eff}^2}})} \tag{6.59}$$

$$k_{p(radial)}^2 = \frac{(1-\sigma)J_1(\kappa_{ar}) - \kappa_{ar}J_0(\kappa_{ar})}{2J_1(\kappa_{ar}) - \kappa_{ar}J_0(\kappa_{ar})} \tag{6.60}$$

C_p and other circuit parameters are extracted by matching Fig. 6-3(b) to the impedance characteristic. More details on this characterization procedure can be found in [2].

6.7 Conclusions

To evaluate piezoelectric materials and vibration modes for power conversion, we have established FOMs for achievable efficiency (FOM_M), volumetric energy handling density (FOM_{VED}), and areal power density (FOM_{APD}) based on realistic PR utilization in a converter. These FOMs depend on only material properties and areal loss density limits (if considered), and they correspond to PR geometry conditions $\widehat{G}$ and $\widehat{l}$ for realizing both maximum efficiency and maximum power density in a PR design.

The derived FOM_M depends on only k^2 and Q_m, and its corresponding geometry condition $\widehat{G}$ dictates the relative PR dimensions corresponding to maximum efficiency for a given operating point. Parallel modes are particularly advantageous for satisfying $\widehat{G}$ with less-extreme planar shapes. Which vibration modes are compatible with a given operating space is likewise dictated by $\widehat{G}$, favoring vibration modes with l as their smallest dimensions for most realistic converter applications. Further, the operating frequency at which maximum efficiency occurs is found to be the harmonic mean of the PR's resonant and anti-resonant frequencies for the assumed operation.

The derived FOM_{VED} and FOM_{APD} are constrained by the PR's geometry-normalized amplitude of resonance I_{Lmaxo}, which can be calculated based on material limits or an acceptable areal loss density. FOM_{VED} is normalized to frequency, which permits direct comparison between vibration modes for a given converter switching and control requirement. FOM_{APD} provides insight into footprint requirements for planar-shaped PRs, though the utility of this FOM depends on whether its assumed area corresponds to the footprint area of a given PR configuration; some modes require scaling by a multiple of $\frac{1}{\widehat{G}}$ for a representative footprint density. Both of these FOMs have the same geometry condition $\widehat{l}$ for maximum power density at a given operating point.

We illustrate the utility of the proposed FOMs and geometry conditions to compare the capabilities of 30 PZT-based materials and seven PR vibration modes for PZT and lithium niobate. These materials and vibration modes vary immensely with respect to the FOMs, though higher FOM_M often enables higher power densities for realistic areal loss density limits. With the same Q_m assumed for each mode, the shear modes demonstrate the highest FOM_M, particularly for lithium niobate. Perpendicular modes are generally capable of higher FOM_{VED} but tend to be more planar, requiring more footprint area than parallel modes to satisfy $\widehat{G}$. Lithium niobate also necessitates more extreme planar dimensions than PZT to meet $\widehat{G}$, requiring more footprint area and/or higher frequency for the same volumetric power density.

We validate these FOMs and their geometry conditions using a periodic steady-state numerical solver and experimental results with commercially available PTs. All PRs of the

same material and vibration mode yield the same minimum loss ratio, maximum energy handling density, and maximum areal power density for a given areal loss density, validating the independence of these quantities from PR geometry and operating point information. The proposed FOMs are demonstrated to be highly representative metrics for the achievable efficiencies and power densities of piezoelectric materials and vibration modes, and their corresponding geometry conditions are verified to facilitate both maximum efficiency and maximum power density in a PR design. Further, the displayed FOM values throughout this work attest to the aptitude of piezoelectrics for power conversion in terms of efficiency and power density capabilities.

Aspects of the work in this chapter have been published in [111, 112], and [69, 70] have since also explored PR material selection and design.

Chapter 7

Piezoelectric Resonator Augmentation

7.1 Introduction

Piezoelectric resonators (PRs) have been leveraged to realize magnetic-less dc-dc power conversion with high efficiency in [58, 67, 69, 74]. In Chapter 2, we enumerate and analyze high-efficiency converter implementations based on PRs, and we assume one such high-efficiency operating sequence to derive PR design tools in Chapter 6. These design tools include figures of merit for piezoelectric materials and vibration modes, along with geometry conditions corresponding to maximum efficiency and power density for an optimized PR design. These recent developments position PRs as promising alternatives to magnetics in terms of efficiency and power density even in their typical, "bare" forms.

In this chapter, we analytically explore opportunity to build on this promise through PR "augmentation", which we define as the addition of non-piezoelectric material layers to the dynamic surfaces of a PR to create a composite electromechanical energy storage component. We focus on a PR structure augmented with thin layers of mass, and we derive the effects of these mass layers on its equivalent circuit model, efficiency, and power density capabilities. We then provide a design process for maximally realizing the benefits of mass augmentation in a PR design, which we validate in simulation.

The work of this chapter was conducted primarily by Joseph Bonavia with my supervision.

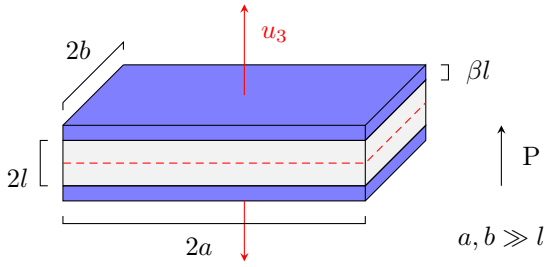

Figure 7-1: Thickness vibration mode of a mass-augmented PR, in which a layer of mass of thickness βl (blue) has been added to both electrode surfaces. The origin is assumed to be the center of the PR. Figure source: Joseph Bonavia.

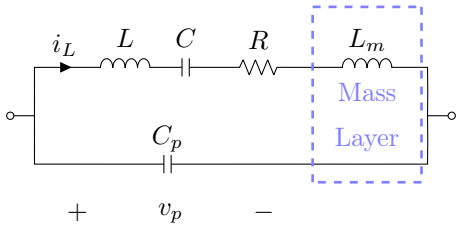

Figure 7-2: Equivalent circuit model for a mass-augmented PR, in which L_m represents added inertial inductance due to the mass. Figure source: Joseph Bonavia.

7.2 Augmented Piezoelectric Resonator Model

To evaluate PR augmentation for power conversion, we first derive the equivalent circuit model for an augmented PR.

7.2.1 Assumed Component Structure

In this chapter, we assume the mass-augmented PR configuration illustrated in Fig. 7-1. The PR vibrates in its thickness mode with all surfaces assumed to be traction-free. A thin layer of mass m_m is attached to each of the PR's electrode surfaces ($x_3 = l$ and $x_3 = -l$), and we assume each mass layer to act as a rigid (non-deformable) body. Dimensions a, b, and l apply to only the piezoelectric material itself and follow the same definitions as Chapter 6. Each mass layer has thickness βl, where β is a scaling factor between the piezoelectric material thickness and the mass thickness. We note that a subscript "m" is used throughout this chapter to denote properties of this mass layer.

Table 7.1: Equivalent Circuit Model Parameters

C_p	C	L	L_m	R
$\varepsilon_{33}^S \frac{2ab}{l}$	$\frac{8C_p k_t^2}{\gamma_o^2}$	$\frac{l^2}{2C_p k_t^2 v_a^2}$	$2\beta\frac{\rho_m}{\rho}L$	$\frac{1}{4Q_M}\frac{l\gamma_o}{C_p k_t^2 v_a}$

where $\gamma_o = \sqrt{\pi^2 - 8k_t^2}$

7.2.2 Equivalent Circuit Model

As described in Chapter 6, the set of vibration modes for a PR is defined by an acoustic wave equation and its boundary conditions. To derive an equivalent circuit model for a mass-augmented PR, we assume excitation of only the PR's fundamental thickness vibration mode. The wave equation is assumed to have a sinusoidal solution for the PR's displacement u_3:

$$u_3(x_3, t) = \Delta \sin(\kappa x_3) e^{j\omega t} \tag{7.1}$$

in which Δ is the displacement amplitude, κ is the wave number, and ω is the acoustic wave's angular frequency.

We apply the following boundary condition for the mass layers, derived from Newton's Second Law for a rigid body:

$$T_3(x_3 = \pm l) = -\frac{m_m \ddot{u_3}}{4ab} = -\rho_m \beta l \frac{\partial^2 u_3}{\partial t^2} \tag{7.2}$$

As for bare PRs in Chapter 6, we derive expressions for the piezoelectric material's stress, strain, and electric field strength by inserting (7.1) and (7.2) into the material's constitutive relations. We integrate the electric field strength E along $2l$ and the electric displacement D along surface $4ab$ to find the PR's voltage and current, respectively, which we then divide for impedance. This impedance has the electrical circuit model displayed in Fig. 7-2 with the parameters in Table 7.1. The model parameters are the same as those for a bare PR as derived in Chapter 6 except for an additional inertial inductance due to the mass:

$$L_m = 2\beta\frac{\rho_m}{\rho}L \tag{7.3}$$

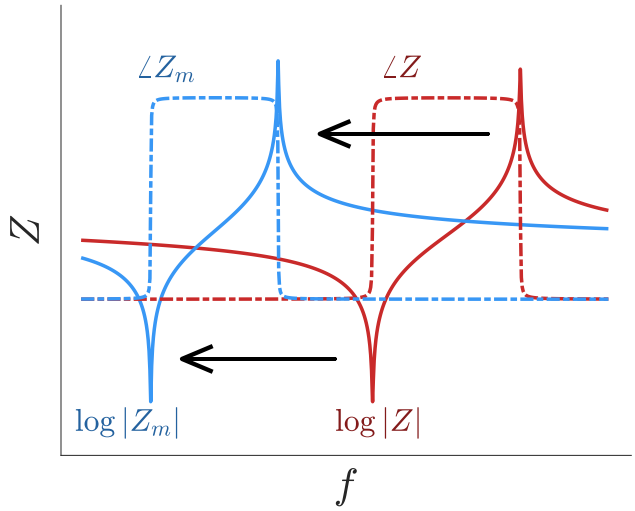

Figure 7-3: Illustration of a PR's impedance shift due to mass augmentation. Figure source: Joseph Bonavia.

This result is similar to those of derivations in [113, 114] for sensing applications. This additional inductance in the circuit model shifts the PR impedance characteristic downward in frequency as visualized in Fig. 7-3.

7.2.3 Rigid Body Condition

In this equivalent circuit model derivation, we have assumed the mass layers to be rigid bodies and that the acoustic wave propagates through only the piezoelectric material. Realistically, the acoustic wave does propagate through the mass to some degree with the same frequency as that of the piezoelectric material. This requires that

$$\omega = \kappa v_a = \frac{\kappa_o v_a}{l} = \frac{\kappa_{o,m} v_{a,m}}{\beta l} \tag{7.4}$$

where κ_o and $\kappa_{o,m}$ are geometry-normalized wave numbers corresponding to the piezoelectric material and the mass, respectively, and v_a and $v_{a,m}$ are the respective acoustic velocities of the piezoelectric material and mass.

There are multiple ways to evaluate the validity of the rigid body assumption. One such strategy is to derive the condition for which $\kappa_{o,m}$ is small, or that the proportion of the acoustic wave that propagates through the mass is small. This requires that

$$\kappa_{o,m} << 1 \tag{7.5}$$

and inserting (7.4) into (7.5) then yields the following rigid body condition:

$$\frac{v_a}{v_{a,m}}\beta\kappa_o << 1 \tag{7.6}$$

A similar rigid body condition is derived in [115] using dimensional analysis, resulting in

$$\frac{v_a^2}{v_{a,m}^2}\beta^2\kappa_o^2 << 1 \tag{7.7}$$

Thus, as the thickness of the added mass layer increases, or as its acoustic velocity decreases, the rigid body assumption breaks down and a non-negligible proportion of the acoustic wave propagates through the mass. In this regime, the rigid boundary conditions assumed in Section 7.2.2 must be reevaluated and acoustic loss in the mass layer must be considered.

7.3 Effects of Augmentation

With a model established, we now evaluate the effects of augmentation on a PR's efficiency, normalized amplitude of resonance, and power density assuming the same amplitude of resonance model as Chapter 6.

7.3.1 Effect on Efficiency

In Chapter 6, we derive the minimum loss ratio for a PR operating in a power converter to be

$$LR_{min} \coloneqq \left(\frac{P_{loss}}{P_{out}}\right)_{min} = \frac{\pi\bar{\kappa}_o\gamma_o}{4Q_m k_t^2} \tag{7.8}$$

in which Q_m is the mechanical quality factor, k_t is the thickness mode electromechanical coupling coefficient, $\gamma_o = \sqrt{\pi^2 - 8k_t^2}$, and $\bar{\kappa}_o$ is the maximum-efficiency normalized wave

number:

$$\bar{\kappa}_o = \frac{\pi\gamma_o}{\pi + \gamma_o} \tag{7.9}$$

We can conduct the same loss ratio minimization with respect to geometry for a mass-augmented PR. If the added mass layers are rigid bodies, we can assume all loss to occur in the piezoelectric material itself. We further assume that the value of R for a specific dimension of piezoelectric material is the same with or without mass augmentation. Thus, the form of the minimum loss ratio in (7.8) remains the same.

That being said, the presence of L_m in the electrical circuit model derived in Section 7.2.2 scales the maximum-efficiency normalized wave number by

$$\frac{\bar{\kappa}_{o,m}}{\bar{\kappa}_{o,bare}} = \mathbb{R}_{\bar{\kappa_o}} = \frac{1}{\sqrt{1+2\Lambda}}, \tag{7.10}$$

in which Λ is the "mass ratio" between the added mass layers and the bare PR, defined as

$$\Lambda = \beta\frac{\rho_m}{\rho} \tag{7.11}$$

As a result, the minimum loss ratio decreases with augmentation as follows:

$$\frac{LR_{min,m}}{LR_{min,bare}} = \mathbb{R}_{\mathrm{LR}} = \mathbb{R}_{\bar{\kappa_o}} = \frac{1}{\sqrt{1+2\Lambda}} \tag{7.12}$$

This suggests that the minimum loss ratio for an augmented PR decreases monotonically with the mass ratio as visualized in Fig. 7-4, thereby increasing the PR's achievable efficiency.

7.3.2 Effect on Normalized Amplitude of Resonance

In Chapter 6, we show that the power density capability of a PR depends on its geometry-normalized amplitude of resonance, I_{Lmaxo}. I_{Lmaxo} can be derived from a piezoelectric material's constitutive relations to be the following function of Δ_{max}:

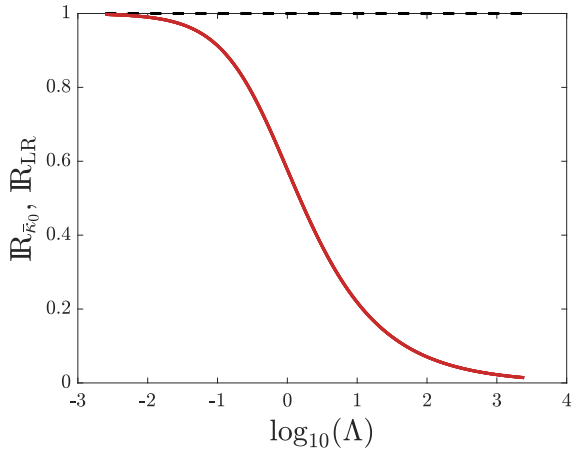

Figure 7-4: Geometry-normalized wave number and minimum loss ratio scaling as a function of mass ratio Λ for a mass-augmented PR. Figure source: Joseph Bonavia.

$$I_{Lmaxo} = \Delta_{max} e_{33} v_a \kappa \sin(\kappa_o) \tag{7.13}$$

in which e_{33} is the piezoelectric strain modulus. Δ_{max} is the maximum displacement amplitude for a PR and can be calculated based on material limits (e.g, failure stress, coercive electric field, etc.) and practical limits (e.g., heat dissipation, failure of adhesive layers, etc.). Thus, I_{Lmaxo} is a function of only material properties and these limits.

In the case of a mass-augmented PR, (7.13) remains the same, but the relationship between Δ_{max} and maximum stress T_{max} or maximum electric field strength E_{max} has dependence on Λ and k_t. Therefore, we define the scaling of I_{Lmaxo} with mass augmentation to be

$$\mathbb{R}^{\mathrm{T,E}}_{\mathrm{I_{Lmaxo}}} = \frac{I^{T,E}_{Lmaxo,m}}{I^{T,E}_{Lmaxo,bare}} \tag{7.14}$$

in which superscripts indicate the limiting factor for I_{Lmaxo}. These I_{Lmaxo} limits are summarized in Table 7.2 for the mass-augmented case. The forms of $\mathbb{R}^{\mathrm{T}}_{\mathrm{I_{Lmaxo}}}$ and $\mathbb{R}^{\mathrm{E}}_{\mathrm{I_{Lmaxo}}}$ are displayed in Fig. 7-5, and both monotonically decrease with respect to Λ.

Rather than material limits, I_{Lmaxo} may be instead limited by a maximum loss density

Table 7.2: Geometry-Normalized Maximum Amplitudes of Resonance

	I^T_{Lmaxo}	$I^E_{Lo,max}$	I^H_{Lmaxo}
Non-Augmented	$\frac{e_{33}v_a}{c^D_{33}}\cot(\frac{\bar{\kappa}_o}{2})T_{max}$	$k_t^2\varepsilon^S_{33}\frac{\sin(\bar{\kappa}_o)}{\cos(\bar{\kappa}_o)-k_t^2}v_aE_{max}$	$\sqrt{4Q_M\frac{\varepsilon^S_{33}k_t^2v_a}{\gamma_o}H_{max}}$
Mass-Augmented	$\frac{e_{33}v_a}{c^D_{33}}\frac{\sin(\bar{\kappa}_o)T_{max}}{1-\cos\bar{\kappa}_o+\Lambda\bar{\kappa}_o\sin(\bar{\kappa}_o)}$	$k_t^2\varepsilon^S_{33}\frac{\sin(\bar{\kappa}_o)v_aE_{max}}{\cos(\bar{\kappa}_o)-k_t^2-\Lambda\bar{\kappa}_o\sin(\bar{\kappa}_o)}$	$\sqrt{4Q_M\frac{\varepsilon^S_{33}k_t^2v_a}{\gamma_o}H_{max}}$

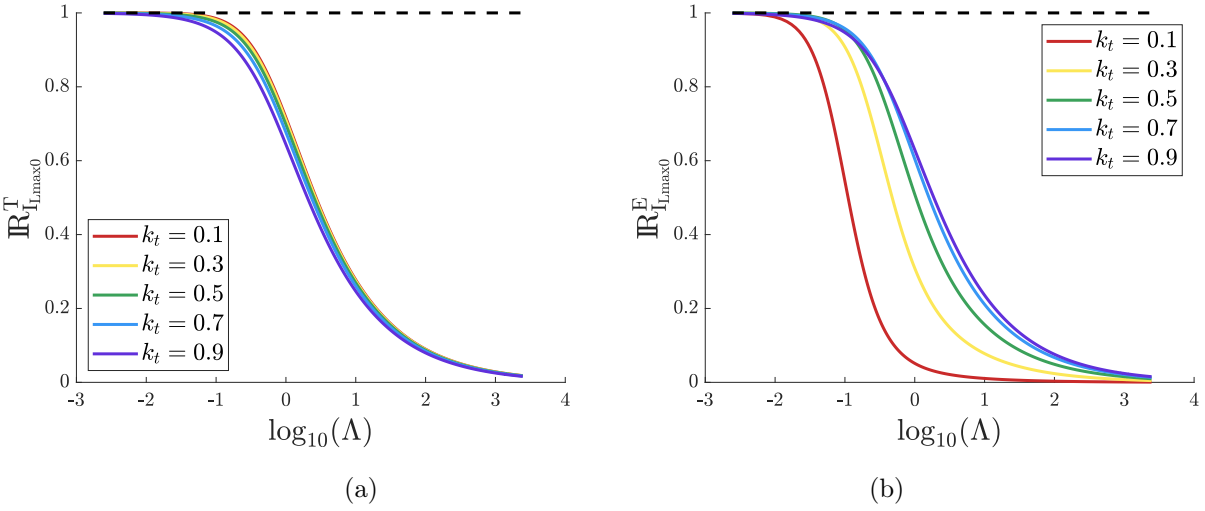

(a) (b)

Figure 7-5: (a) Stress-limited geometry-normalized I_{Lmaxo} scaling as a function of mass ratio Λ for various coupling coefficients k_t. (b) E-limited geometry-normalized I_{Lmaxo} scaling as a function of mass ratio Λ for various coupling coefficients k_t. Figure source: Joseph Bonavia.

H_{max} (in W/cm^2) corresponding to maximum thermal dissipation. For a bare PR, this limit is derived in Chapter 6 to be

$$I^H_{Lmaxo} = \sqrt{\frac{2}{R_o}H_{Max}} \tag{7.15}$$

in which R_o is the geometry-normalized R defined in Chapter 6. Since mass augmentation has been assumed to have no impact on R in this analysis, I^H_{Lmaxo} has no dependence on Λ and $\mathbb{R}^H_{I_{Lmax0}} = 1$. I^H_{Lmaxo} is likewise displayed in Table 7.2.

7.3.3 Effect on Power Density

There are two quantities with which we evaluate power density in Chapter 6: volumetric energy handling density ($\frac{P_{out}}{f*volume}$) and areal power density ($\frac{P_{out}}{area}$). The maximum volumetric energy handling density for a PR is shown to be the following function of material properties and I_{Lmaxo}:

$$VED_{max} = \frac{I_{Lmaxo}^2}{\bar{\kappa}_o^2 \varepsilon_{33}^S v_a^2} \tag{7.16}$$

Maximum areal power density is similarly shown to be

$$APD_{max} = \frac{I_{Lmaxo}^2}{4\pi^2 B_o} = \frac{I_{Lo,max}^2}{\pi \bar{\kappa}_o \varepsilon_{33}^S v_a} \tag{7.17}$$

where ε_{33}^S is the constant-strain permittivity.

For a mass-augmented PR, we first examine the scaling of these quantities for I_{Lmaxo} limited by stress T_{max} or electric field strength E_{max}. For volumetric power density, the form of (7.16) remains unchanged except for a volume scaling of $(1+\beta)$ to account for the additional mass. $\bar{\kappa}_o$ and $I_{Lmaxo}^{T,E}$ also scale as described in previous sections, amounting to an overall scaling of

$$\mathbb{R}_{\mathrm{VED}}^{\mathrm{T,E}} = (\mathbb{R}_{\mathrm{I_{Lmaxo}}}^{\mathrm{T,E}})^2 \frac{1+2\Lambda}{1+\frac{\rho}{\rho_{\mathrm{m}}}\Lambda} \tag{7.18}$$

The maximum areal power densities corresponding to T_{max} and E_{max} scale similarly except without the volume adjustment (i.e., the footprint area remains the same), resulting in:

$$\mathbb{R}_{\mathrm{APD}}^{\mathrm{T,E}} = (\mathbb{R}_{\mathrm{I_{Lmaxo}}}^{\mathrm{T,E}})^2 \sqrt{1+2\Lambda} \tag{7.19}$$

These trends are plotted in Figs. 7-6 and 7-7. While the achievable power density quantities do not monotonically increase, there is an optimal mass ratio Λ for which they may be maximized.

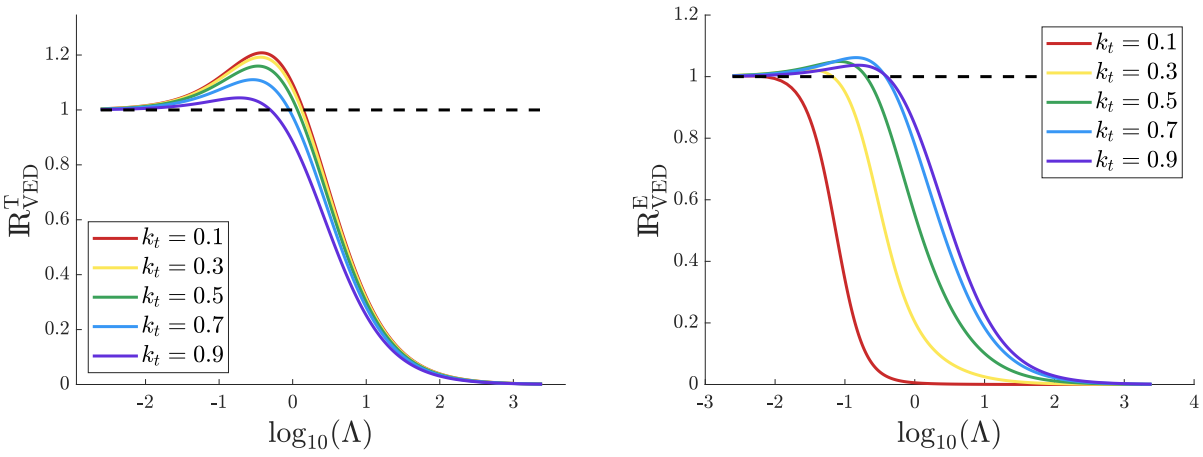

Figure 7-6: (a) Stress-limited volumetric energy handling density scaling as a function of mass ratio Λ for various coupling coefficients k_t. (b) E-limited volumetric energy handling density scaling as a function of mass ratio Λ for various coupling coefficients k_t. Figure source: Joseph Bonavia.

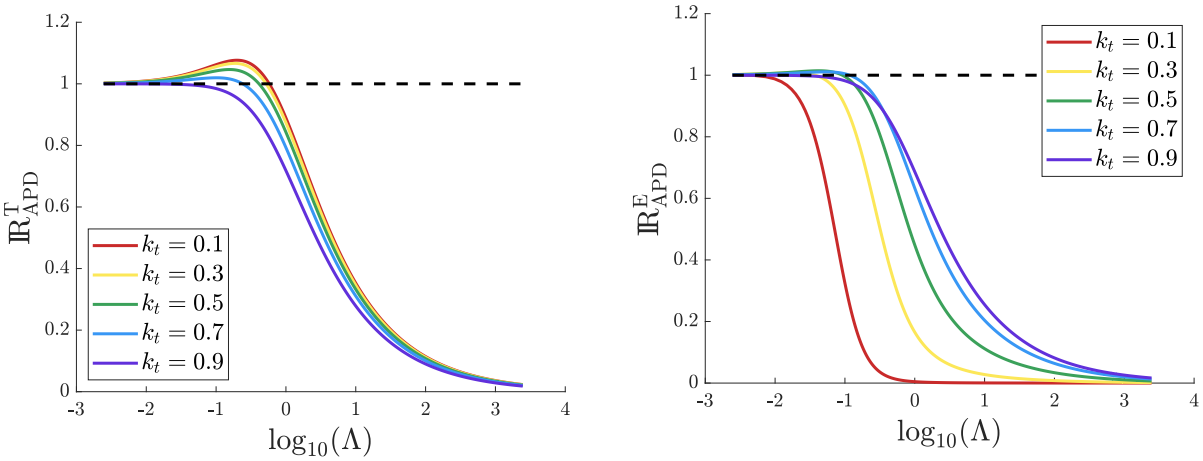

Figure 7-7: (a) Stress-limited areal power density scaling as a function of mass ratio Λ for various coupling coefficients k_t. (b) E-limited areal power density scaling as a function of mass ratio Λ for various coupling coefficients k_t. Figure source: Joseph Bonavia.

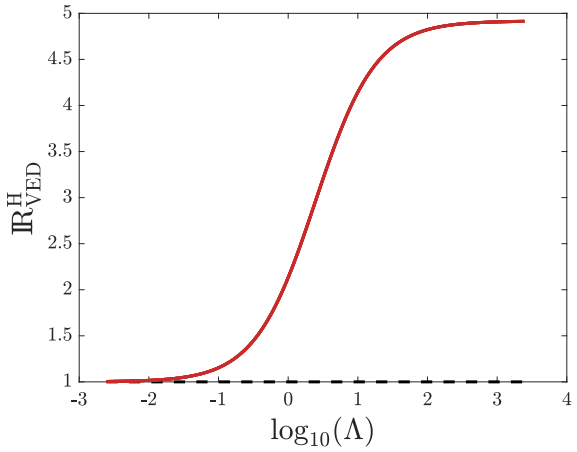

Figure 7-8: Loss-density-limited volumetric energy handling density scaling as a function of mass ratio Λ, where $2\frac{\rho_m}{\rho} = 4.9172$. Figure source: Joseph Bonavia.

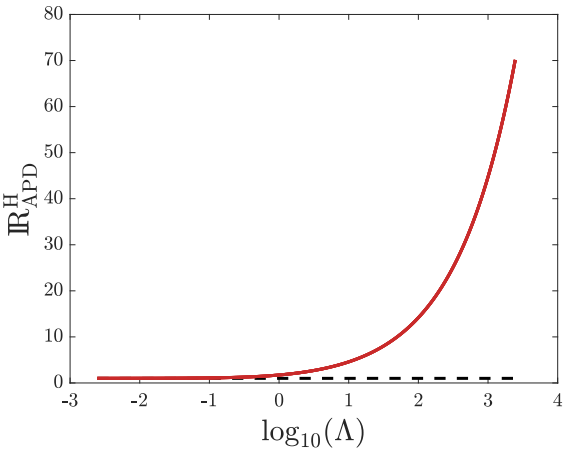

Figure 7-9: Loss-density-limited areal power density scaling as a function of mass ratio Λ. Figure source: Joseph Bonavia.

We similarly examine the scaling of loss-limited power density for a mass-augmented PR. Volumetric energy handling density in this case scales with only volume and $\bar{\kappa}_o$, resulting in

$$\frac{VED^H_{max,m}}{VED^H_{max,bare}} = \mathbb{R}^{\mathrm{H}}_{\mathrm{VED}} = \frac{1+2\Lambda}{1+\beta} = \frac{1+2\Lambda}{1+\frac{\rho}{\rho_{\mathrm{m}}}\Lambda} \tag{7.20}$$

The trend for this scaling characteristic is visualized in Fig. 7-8 and is shown to increase monotonically toward the following limit:

$$\lim_{\Lambda\to+\infty} \mathbb{R}^{\mathrm{H}}_{\mathrm{VED}} = 2\frac{\rho_{\mathrm{m}}}{\rho} \tag{7.21}$$

This suggests that the upper limit for loss-limited volumetric energy handling density can be maximized by selecting a high-density material for the mass layers.

Loss-limited areal power density scales with only $\bar{\kappa}_o$, resulting in

$$\frac{APD^H_{max,m}}{APD^H_{max,bare}} = \mathbb{R}^{\mathrm{H}}_{\mathrm{APD}} = \sqrt{1+2\Lambda} \tag{7.22}$$

which is plotted in Fig. 7-9.

This analysis reveals the loss-limited power density case to benefit the most from PR

augmentation. Power density constrained by stress or electric field may also be increased for a certain range of Λ.

7.4 Augmented Piezoelectric Resonator Design

This analysis suggests that mass-augmented PRs may be designed to have higher efficiencies and power densities than functionally-equivalent bare PRs. Here we detail the design process for mass-augmented PRs, which we then validate in simulation.

7.4.1 Design Process

A mass-augmented PR is first designed by selecting mass ratio Λ. The case studies in Chapter 6 suggests I_{Lmaxo} to be loss-limited for most bare PRs. I^H_{Lmaxo} is independent of Λ, but other limits such as I^T_{Lmaxo} and I^E_{Lmaxo} decrease as Λ increases. As visualized in Fig. 7-10, one of these limits eventually decreases below I^H_{Lmaxo} at high Λ and becomes the dominant power density constraint for the PR. Λ should be selected to be as high as possible before the other limits become relevant. We consider the optimal point to be the intersection between I^H_{Lmaxo} and the decreasing limit as highlighted in Fig. 7-10.

With Λ selected, the designer should then verify the rigid body assumption using the condition derived in Section 7.2.3. (7.7) may be re-written in terms of Λ and material properties as follows:

$$\Phi = \frac{\rho}{\rho_m}\frac{c^D_{33}}{c^D_{33,m}}\frac{\Lambda^2}{1+2\Lambda}\bar{\kappa}_o^2 << 1 \tag{7.23}$$

where ρ is density and c^D_{33} is the elastic modulus given constant electric displacement. We suggest use of $\Phi < 0.1$ as a design threshold, above which loss due to wave propagation through the mass becomes non-negligible.

The component's dimensions $G = \frac{4ab}{l^2}$ and l can then be selected to satisfy the geometry conditions for minimum loss ratio and maximum power density, respectively, at a nominal operating point. Minimum loss ratio (7.8) and maximum power densities (7.16) and (7.17)

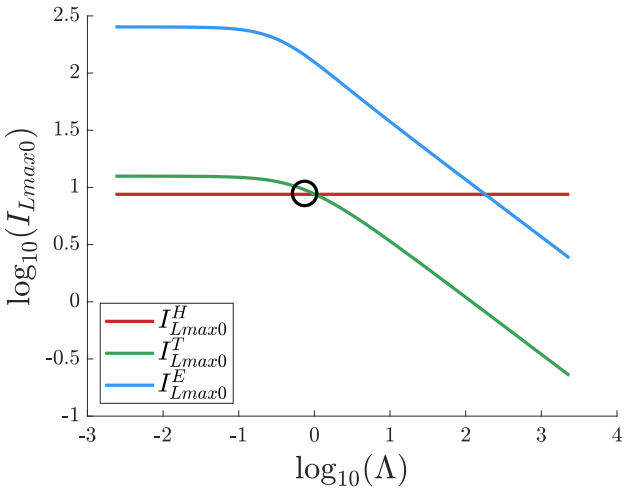

Figure 7-10: I_{Lmaxo} corresponding to different limits vs. Λ. The minimum I_{Lmaxo} for a given Λ serves as the power density limit. For the design of Section 7.4.2, we choose a value of Λ at the boundary between I_{Lmaxo}'s stress and loss limit ($\Lambda = 0.9$). This example uses PZT-8 and assumes $H = 1\frac{W}{cm^2}$. Figure source: Joseph Bonavia.

correspond to the following conditions, denoted with $\hat{}$:

$$\widehat{G} = \frac{P_{out}}{V_{in}^2}\frac{4\pi}{\bar{\kappa}_o v_a \varepsilon_{33}^S} \tag{7.24}$$

$$\widehat{l} = V_{in}\frac{\bar{\kappa}_o v_a \varepsilon_{33}^S}{2I_{Lmaxo}} \tag{7.25}$$

The only factor in (7.24) and (7.25) dependent on Λ is $\bar{\kappa}_o$, which decreases with respect to Λ. Thus, with these design conditions, a larger mass ratio results in a thinner, more planar component.

The accuracy of $\bar{\kappa}_o$ during these steps may be enhanced through an improved tangent approximation for the circuit model derivation detailed in Appendix A of [115]. This strategy involves scaling the tangent term's partial fraction expansion by an error-reduction factor α, which can be selected using the chart of Fig. 7-11. The result is then the following model for $\bar{\kappa}_o$:

$$\bar{\kappa}_o = \frac{\pi\sqrt{\pi^2 - 8\alpha k_t^2}}{\pi + \sqrt{\pi^2 - 8\alpha k_t^2}}\sqrt{\frac{1}{1 + 2\alpha\Lambda}} \tag{7.26}$$

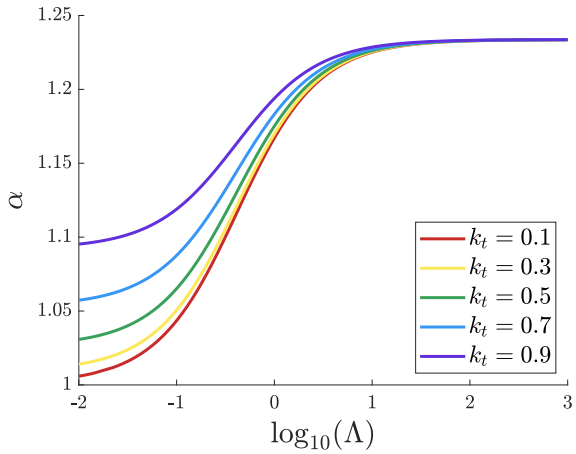

Figure 7-11: Error-reduction factor α as a function of Λ for various k_t. Figure source: Joseph Bonavia.

Table 7.3: Assumed Material Properties for PZT-8 and Tungsten

PZT-8		Tungsten	
ρ	7600 kg/m^3	ρ_m	17800 kg/m^3
$\frac{\varepsilon_{33}^S}{\varepsilon_o}$	4.972 nF/m	$c_{33,m}$	460 GPa
c_{33}^D	131.7 GPa	σ_m	0.28
e_{33}	13.91 C/m^2		
Q_m	1000		
T_{max}	30 MPa		
E_{max}	7 kV/mm		

7.4.2 Validation via Simulation

To validate this design process, we design both a bare and an augmented PR to operate in the highest-efficiency converter switching sequence assumed in Chapter 6 with $V_{in} = 100$ V and $P_{out} = 1$ kW. The bare PR is designed using PZT-8 and the geometry conditions of Chapter 6. The mass-augmented PR is designed with PZT-8 and tungsten using the strategy described in Section 7.4.1; tungsten is a strong candidate for this mass layer due to its high stiffness and density compared to PZT-8, and its material properties (based on COMSOL's material library) are displayed in Table 7.3.

Table 7.4: Bare and Augmented PR Design Comparison

	Bare	Augmented	$\frac{\text{Augmented}}{\text{Bare}}$
PZT-8 Thickness	202 μm	133 μm	0.562
Total Thickness	202 μm	157 μm	0.777
Electrode Area	14.5 cm^2	8.18 cm^2	0.562
Width (Square)	1.91 cm	1.43 cm	0.749
Volume	0.587 cm^3	0.256 cm^3	**0.436**
Mass	4.46 mg	2.68 mg	0.599
Operating Frequency	5.57 MHz	5.57 MHz	**1**
Model LR	0.0146	0.0082	**0.562**

$V_{in} = 100$ V, $P_{out} = 1$ kW, $\frac{\rho_m}{\rho} = 2.34$, $\beta = 0.384$, $\Lambda = 0.9$

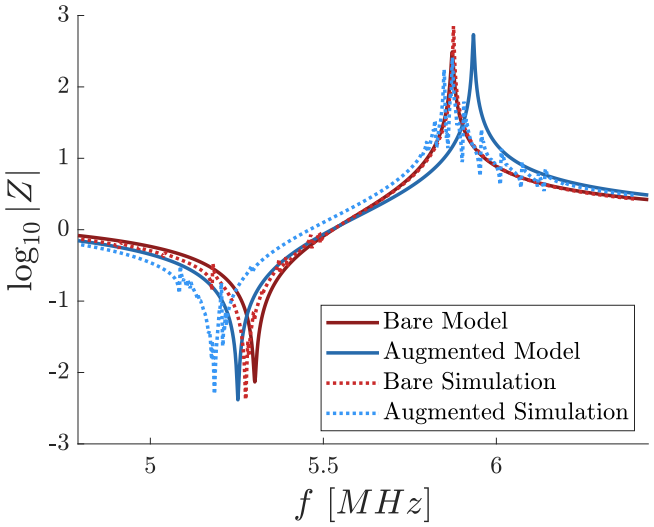

Figure 7-12: Simulated and modeled impedance magnitudes for the bare PR and augmented PR designs summarized in Table 7.4, vibrating in the thickness extensional mode. Figure source: Joseph Bonavia.

Following the procedure of Section 7.4.1, we select Λ for the mass-augmented PR based on the point at which I_{Lmaxo} becomes stress-limited as visualized in Fig. 7-10. For the specified operating point, this occurs at $\Lambda = 0.9$ and $\beta = 0.384$. This design point satisfied the rigid body condition in (7.23) with $\Phi = 0.0899 < 0.1$. Next, we select $\alpha = 1.17$ from the chart of Fig. 7-11 for modeling $\bar{\kappa}_o$ with (7.26) and then choose the augmented PR's

dimensions to satisfy (7.25) and (7.24).

Both the bare and mass-augmented PR designs are summarized in Table 7.4. We simulate these two designs in the frequency domain using COMSOL, and we display both their modeled and simulated impedance characteristics in Fig. 7-12. The resonant frequencies and inductive regions for these two designs are nearly equivalent, and the proposed model is closely aligned with the simulated impedance. However, the mass-augmented PR has only 56% the footprint area and 44% the volume of the bare PR, demonstrating a significant increase in power density. Further, the augmented PR has the same maximum-efficiency frequency but is estimated to operate with 56% lower power loss. This case study validates mass augmentation as a promising strategy for achieving significantly higher power density in PRs while retaining the same functionality and frequency of operation.

7.5 Conclusion

In this chapter, we have analytically shown that augmenting a PR with thin layers of mass can drastically improve its efficiency and power density capabilities. This opportunity is greatest for PRs constrained by loss density, for which mass augmentation may increase efficiency, volumetric energy handling density, and areal power density monotonically with respect to the PR's mass ratio. We note that this result depends on an assumption that a given PR's R is the same regardless of whether its surfaces are augmented with mass, which must be vetted in future work. Still, this theoretical study suggests mass augmentation to build on the established advantages of bare PRs, providing a promising path forward for miniaturization.

Aspects of the work in this chapter have been published in [115].

Chapter 8

Piezoelectric Transformer Design

8.1 Introduction

In Chapter 3, we detail a variety of high-efficiency magnetic-less converter implementations based on isolated and non-isolated PTs. However, even the highest-efficiency of these switching sequences is capable of only 90% efficiency in the experimental prototype of Chapter 3, which is based on a commercially available PT. This marks a significant gap in achievable efficiency between commercially available PRs and PTs. Thus, high-performance magnetic-less power conversion based on PTs will require major advancement of PTs in addition to the high-efficiency converter implementations of Chapter 3. PT design has seen significantly more investigation in the context of power conversion than PRs [4, 18, 76, 116–122], but fundamental criteria for selecting materials, vibration modes, and geometric dimensions are still lacking.

In this chapter, we draw on the PR design strategies proposed in Chapter 6 to develop PT design tools for maximizing efficiency and power density. PTs have both more degrees of freedom and more design considerations than PRs (e.g., maintaining ZVS at both ports) that amount to greater complexity in the design process. Assuming a high-efficiency PT-based converter implementation proposed in Chapter 3, we derive geometry conditions for achieving maximum efficiency and maximum power density within a PT's ZVS region. We

then illustrate use of these tools in an example PT design, which we validate via simulation.

The work of this chapter was conducted primarily by Elaine Ng with my supervision. This chapter is intended to serve as a summary, and the reader is encouraged to reference Elaine Ng's Master of Engineering thesis [82] for more details.

8.2 Piezoelectric Transformer Model

To develop PT design strategies, we first assume a high-efficiency PT structure and derive its equivalent circuit model.

8.2.1 Assumed Component Structure

PTs can be conceptualized as mechanically-coupled PRs, and we evaluate piezoelectric materials and vibration modes in the context of PRs in Chapter 6. The highest-efficiency vibration mode for PZT is the length extensional mode with end electrodes, which corresponds to the k_{33} coupling coefficient. To leverage this efficiency capability in a PT, we therefore assume a PT structure in which both parts vibrate in this length extensional mode as visualized in Fig. 8-1. This structure is commonly referred to as a k_{33}-k_{33} mode PT.

In the PT structure of Fig. 8-1, both sides have length l between their electrodes, and the electrode area of one side is a scaling factor α times that of the other part. The design strategies herein are independent of how this scaling factor is implemented geometrically (by scaling of a, b, or both), so we assume only the height to be different between the two sides with a scaling factor of α. We add an ideal insulation layer between the PT's two sides for isolation, a strategy that has been previously explored [4]. We assume perfect mechanical coupling between the PT's two sides (neglecting the mechanical aspects of the electrodes and insulation layer), and all other surfaces are assumed to be traction-free.

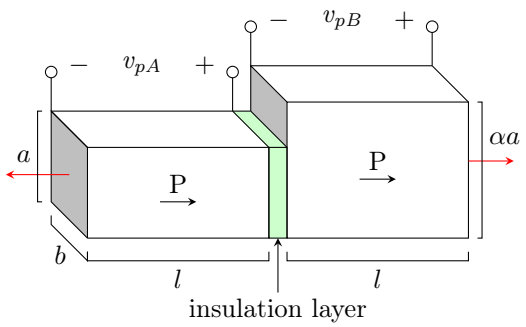

Figure 8-1: Assumed PT structure in which both parts vibrate in the length extensional mode. Visible electrodes are denoted by shaded areas, and displacement directions are marked with red arrows. The polarization direction of each part is denoted with 'P'. The insulation layer is assumed to be a perfect insulator with negligible thickness and is ignored in the analysis of this chapter. All surfaces are assumed to have no externally-applied stress (i.e., all surfaces are traction-free).

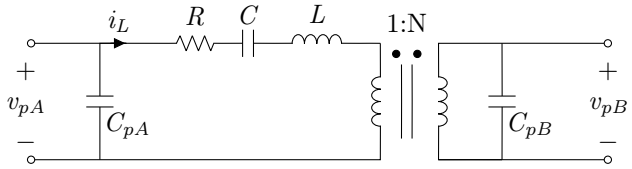

Figure 8-2: Reduced Mason circuit model for isolated PTs [3], with model parameters for the structure in Fig. 8-1 displayed in Table 8.1.

Table 8.1: Equivalent Circuit Model Parameters

C_{pA}	C_{pB}	C	L	R	N
$\varepsilon_{33}^S \frac{ab}{l}$	αC_{pA}	$\frac{8k_{33}^2 C_{pA}}{\pi^2(1+\alpha)}$	$\frac{l^2(1+\alpha)(\pi^2+8k_{33}^2)}{8\pi^2 v_a^2 k_{33}^2 C_{pA}}$	$\frac{\pi l(1+\alpha)}{8Q_m v_a k_{33}^2 C_{pA}}$	$\frac{1}{\alpha}$

8.2.2 Equivalent Circuit Model

PTs are commonly modeled using the reduced Mason model shown in Fig. 8-2. This circuit is derived by first modeling the PT's two parts as independent PRs and then combining these models via boundary conditions. At their interface, the two PRs are assumed to have equal velocity and opposite force. The combined circuit model can then be reduced to the version shown in Fig. 8-2. More details on this derivation can be found in [4].

Deriving an equivalent circuit for the component structure in Fig. 8-1 yields the model parameters displayed in Table 8.1. The PT is assumed to operate in its lowest-frequency

full-wave vibration mode, in which the acoustic wave completes a full sinusoidal cycle along the PT's dimension of $2l$. This corresponds to a geometry-normalized wave number in the proximity of π for each PT side; we therefore assume this normalized wave number to be exactly π to simplify the model derivation[1]. Further, PRs vibrating in parallel vibration modes as defined in Chapter 6 have an additional term in their LCR branch that is often modeled as a negative capacitance (we implement this term in the denominator of C for PRs in previous chapters). In this PT model, we consider this extra term to be an added inductance and lump it into L in Table 8.1.

8.3 ZVS Region and Amplitude of Resonance Model

We next model the PT's utilization and limits in a power converter using the amplitude of resonance model.

8.3.1 Assumed Converter Operation

Switching sequences and topologies for magnetic-less PT-based converters are enumerated and analyzed in Chapter 3. These switching sequences are capable of high-efficiency behaviors such as ZVS and minimal charge circulation across wide operating regions. One such sequence for an isolated PT is the V_{in}, -V_{in} | V_{out}, -V_{out}, *Zero+* sequence, named for the sequential voltages of its energy transfer stages for the input and output ports (separated by '|'). According to the analysis of Section 3.5.6, the power level corresponding to peak efficiency for this switching sequence is among the highest of isolated switching sequences analyzed in Chapter 3.

The V_{in}, -V_{in} | V_{out}, -V_{out}, *Zero+* switching sequence can be realized with a full-bridge/full-bridge topology shown in Fig. 8-3, and an example of its switching waveforms are shown in

[1]For the length extensional vibration mode and other parallel modes described in Chapter 6, a normalized wave number of π corresponds to the anti-resonant frequency (i.e., the upper frequency boundary of the inductive region). Therefore, π can be considered an overestimation of the actual normalized wave number (and corresponding frequency) used for converter operation.

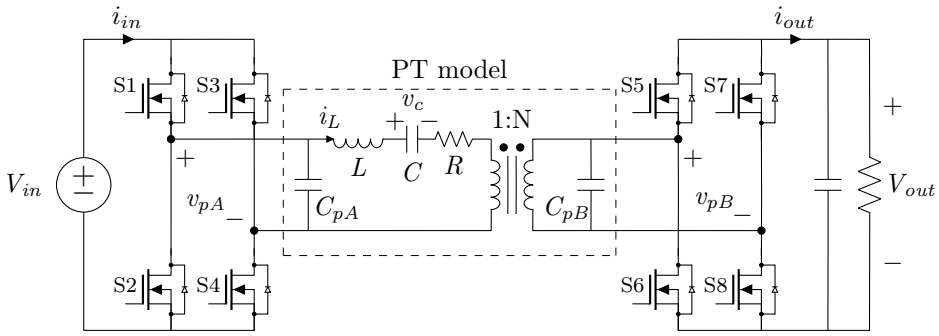

Figure 8-3: Circuit topology for implementing the V_{in}, -V_{in} | V_{out}, -V_{out}, *Zero+* switching sequence.

the simulated waveforms of Fig. 8-6. More details on this switching sequence can be found in Chapter 3.

8.3.2 ZVS Region

As described in Chapter 3, several aspects of a PT's behavior in a power converter can be modeled based on the charge it displaces during each stage of a given switching sequence. This analysis may be used to estimate the boundaries of a PT's ZVS region, defined as the operating region for which ZVS is possible assuming all other high-efficiency behaviors are maintained. PTs differ from PRs in that the boundaries of this region diverge from their ideal values at low power due to differences in the PT's terminal capacitances.

Section 3.5.3 describes how the ZVS region may be derived for a given PT and switching sequence based on the total charge displaced by i_L during a resonant period. This charge displacement is visualized in Fig. 8-4 from the perspective of each port for the V_{in}, -V_{in} | V_{out}, -V_{out}, *Zero+* sequence assumed in this chapter. For this sequence, the ZVS region is defined by

$$\frac{P_{in}}{fV_{in}} + 4V_{in}C_{pA} = N\left(\frac{P_{out}}{fK_BV_{out}} + 4V_{out}C_{pB}\right) \tag{8.1}$$

in which f may be assumed to be the PT's resonant frequency, K_B has the range $\frac{1}{2} < K_B < 1$, and other parameters correspond to Fig. 8-3.

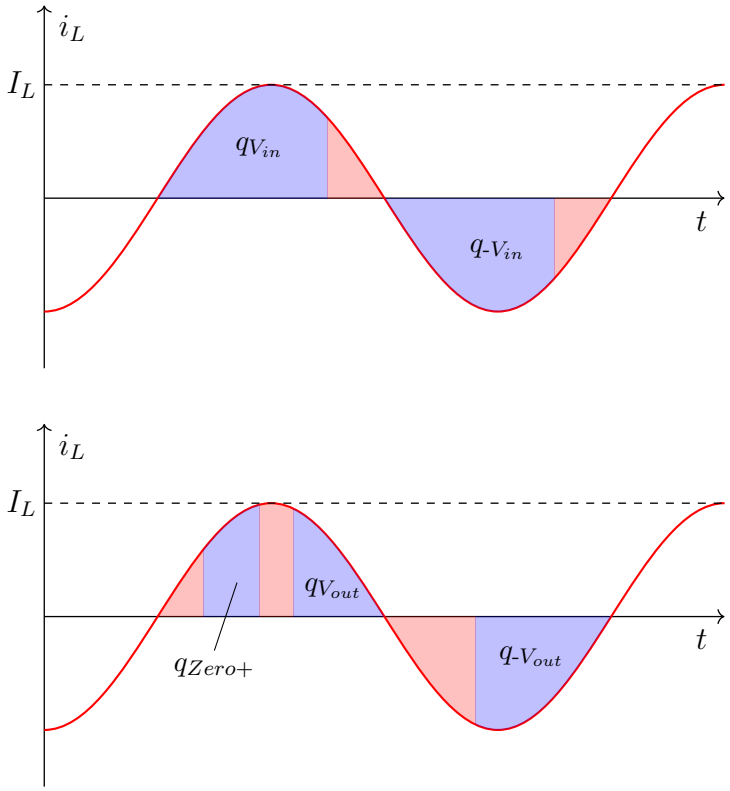

Figure 8-4: Sinusoidal approximation of i_L based on the charge displaced q during each stage, from the perspective of the input (top) and output (bottom) ports of an isolated PT. Example sequence: V_{in}, -V_{in} | V_{out}, -V_{out}, *Zero+*. Connected/zero stages shaded purple; open stages shaded red.

(8.1) is based on the total charge displaced by i_L across a resonant cycle being equal from the perspective of either port, with differences being compensated by K_B. If (8.1) can be satisfied with K_B in the range $\frac{1}{2} < K_B < 1$, ZVS can be achieved. Thus, the boundaries of K_B therefore dictate a switching sequence's ZVS region boundaries.

8.3.3 Amplitude of Resonance Model

A second tool for modeling PT behavior is the amplitude of resonance model, which is likewise derived based on charge displacement in Chapter 3. The amplitude of resonance refers to the amplitude of the assumed-sinusoidal i_L in the PT's resonant branch as visualized in Fig. 8-4. For the V_{in}, -V_{in} | V_{out}, -V_{out}, *Zero+* sequence, I_L has the form

$$I_L = \pi\Big(\frac{P_{in}}{2V_{in}} + 2fC_{pA}V_{in}\Big) \tag{8.2}$$

which can also be rearranged to be

$$P_{out} = \frac{2}{\pi}I_L V_{in} - 4fC_{pA}V_{in}^2 \tag{8.3}$$

in which we have approximated $P_{in} \approx P_{out}$. These expressions are utilized to model loss and power handling in Section 8.4.

8.3.4 Areal Loss Density Limit

In Chapter 6, the maximum power density for a PR is derived to be a function of material properties and limit I_{Lmaxo}. I_{Lmaxo} is the geometry-normalized amplitude of resonance and can be directly related to material limits (e.g., for stress and electric field strength) and practical limits (e.g., for thermal dissipation) via only material properties. Following the procedure in Chapter 6 for PRs, we derive I_{Lmaxo} for PTs from the perspective of the input port by extracting all geometry terms from I_L, resulting in the following relationship:

$$I_{Lmaxo} \coloneqq \frac{l}{ab}I_L \tag{8.4}$$

The case study of Chapter 6 reveals the power densities of PZT PRs operating in the length extensional mode to be limited by loss density H_{max}, defined as $\frac{P_{loss}}{area}$, assuming most heat is extracted through the specified surface area. We therefore derive the loss-density-limited I_{Lmaxo} in the context of PTs from the perspective of the input port:

$$H_{max} \coloneqq \frac{P_{loss}}{ab} = \frac{1}{2}\frac{I_L^2 R}{ab} = \frac{1}{2}I_{Lo}^2 R_o \tag{8.5}$$

in which we have extracted geometry parameters from I_L and R, assuming $R_o = \frac{ab}{l^2}R$. For this assumed surface, all geometry terms cancel and (8.5) produces a direct relationship between areal loss density and I_{Lmaxo}:

$$I_{Lmaxo}^H = \sqrt{\frac{2}{R_o}H_{max}} \tag{8.6}$$

We note that the H_{max} in (8.6) refers to loss density with respect to the input port's electrode surface area. Loss density with respect to the output port must be scaled by α to create an effective H_{max} for use in the analysis above.

8.4 Piezoelectric Transformer Geometry Conditions

Similar to PRs in Chapter 6, we derive the maximum efficiency and power density for a PT and leverage their corresponding geometry conditions for PT design.

8.4.1 Condition for Maximum Efficiency

The efficiency of a PT can be expressed as

$$\eta = \frac{1}{1 + \frac{P_{loss}}{P_{out}}} \tag{8.7}$$

We can therefore maximize PT efficiency by minimizing loss ratio $\frac{P_{loss}}{P_{out}}$ as conducted for PRs in Chapter 6. Assuming the V_{in}, -V_{in} | V_{out}, -V_{out}, *Zero+* switching sequence described in Section 8.3.1, the loss ratio of a PT can be expressed as follows from the perspective of the input port:

$$\frac{P_{loss}}{P_{out}} = \frac{\frac{1}{2} I_L^2 R}{P_{out}} = \frac{\pi^2}{2}\Big(\frac{P_{out}}{4V_{in}^2} R + 2BR + \frac{4V_{in}^2 B^2}{P_{out}} R\Big) \tag{8.8}$$

in which we have substituted frequency-capacitance product B:

$$B := fC_{pA} \tag{8.9}$$

In (8.8), B and R consist of material properties and the same geometry term G, which we define as

$$G := \frac{ab}{l^2} = \frac{B}{B_o} = \frac{R_o}{R} \tag{8.10}$$

in which B_o and R_o are

$$B_o = \frac{v_a \varepsilon_{33}^S}{2} \tag{8.11}$$

$$R_o = \frac{\pi(1+\alpha)}{8 Q_m \varepsilon_{33}^S k_{33}^2 v_a} \tag{8.12}$$

assuming the geometry-normalized wave number within the PT is π.

(8.8) can be re-written with these terms explicit as follows:

$$\frac{P_{loss}}{P_{out}} = \frac{\pi^2}{2}\left(\frac{P_{out}}{4V_{in}^2}\frac{R_o}{G} + 2B_o R_o + \frac{4V_{in}^2}{P_{out}} G B_o^2 R_o\right) \tag{8.13}$$

This loss ratio expression is a second-order equation with respect to its only PT geometry term: G. Minimizing (8.13) with respect to G reveals the following condition (denoted by $\hat{G}$) and minimum loss ratio:

$$\widehat{G} = \frac{P_{out}}{4V_{in}^2 B_o} \tag{8.14}$$

$$\Rightarrow \quad \left(\frac{P_{loss}}{P_{out}}\right)_{min} = 2\pi^2 B_o R_o \tag{8.15}$$

This minimum loss ratio and geometry condition are similar in form to those of PRs derived in Chapter 6 in that they contain no operating point information or explicit geometric dimensions. However, the dependence of R_o on α causes the minimum loss ratio of (8.15) to increase for high α, negatively impacting the PT's achievable efficiency.

8.4.2 Condition for ZVS

In the experimental prototype of Section 3.6, the operating points corresponding to peak efficiency cannot be reached within the PT's ZVS region for a certain range of voltage conversion ratios. As a result, this prototype is confined to lower efficiencies than predicted to be possible for part of its operating region.

We therefore derive a geometry condition for which the minimum loss ratio (8.15) occurs within the PT's ZVS region for a nominal operating point. The ZVS condition (8.1) may be re-written as follows with geometry terms extracted and approximating $P_{in} \approx P_{out}$:

$$\frac{P_{out}}{V_{in}} + 4GB_oV_{in} = \frac{P_{out}}{\alpha K_B V_{out}} + 4GB_oV_{out} \tag{8.16}$$

This condition has two terms related to the PT's geometry: G and α. Since G is constrained for maximum efficiency in Section 8.4.1, we solve for α to be the following if (8.16) is true:

$$\alpha = \frac{P_{out}V_{in}}{K_B V_{out}(4B_oGV_{in}(V_{in} - V_{out}) + P_{out})} \tag{8.17}$$

Assuming the designer adheres to geometry condition $\hat{G}$, we set $G = \hat{G}$ in (8.17) to arrive at the following geometry condition for α (denoted with $\widehat{\alpha}$):

$$\widehat{\alpha} = \frac{1}{K_B \frac{V_{out}}{V_{in}}(2 - \frac{V_{out}}{V_{in}})} \tag{8.18}$$

Thus, as the voltage conversion ratio decreases below 1, α must increase to maintain ZVS. We note that $\frac{1}{2} < K_B < 1$ for the V_{in}, -V_{in} | V_{out}, -V_{out}, *Zero+* sequence, so the designer should select α to be in the following range to ensure the desired operating point with maximum efficiency is obtainable with ZVS:

$$\frac{1}{\frac{V_{out}}{V_{in}}(2 - \frac{V_{out}}{V_{in}})} < \widehat{\alpha} < \frac{2}{\frac{V_{out}}{V_{in}}(2 - \frac{V_{out}}{V_{in}})} \tag{8.19}$$

We further note that α must be positive to be valid, so (8.19) can be satisfied only for $0 < \frac{V_{out}}{V_{in}} < 2$ with this switching sequence.

Finally, the ZVS capability of other operating points (besides the maximum efficiency point) can be evaluated using (8.17). A designer may choose to select α such that ZVS is achieved at a certain minimum power level P_{min}. Assuming a scaling factor of $\chi = \frac{P_{min}}{P_{out}}$, in which P_{out} is the maximum-efficiency power level used to compute $\widehat{G}$, α has the following condition in this case:

$$\widehat{\alpha} = \frac{\chi}{K_B \frac{V_{out}}{V_{in}}(1 + \chi - \frac{V_{out}}{V_{in}})} \tag{8.20}$$

We caution the designer that the ranges for $\widehat{\alpha}$ in (8.18) and (8.20) may not necessarily overlap depending on the desired operation region. In this case, the designer may elect to

use different switching sequences for different regions of operation as illustrated in Section 3.5.3.

8.4.3 Condition for Maximum Power Density

We adopt a similar approach to that of Chapter 6 to derive a PT geometry condition for maximum power density. In particular, we focus on maximizing energy handling density ($\frac{P_{out}}{\text{vol}\cdot f}$), which quantifies the power density capability of the component for a given frequency. The PT in Fig. 8-1 has the following volume:

$$\text{vol} = abl \cdot (1+\alpha) \tag{8.21}$$

Thus, the volumetric energy handling density can be expressed as follows, assuming P_{out} calculated in (8.3) with geometry components of I_L and B extracted:

$$\frac{E_{out}}{\text{vol}} = \frac{P_{out}}{\text{vol}\cdot f} = \frac{4}{v_a(1+\alpha)}\Big(\frac{I_{Lmaxo}V_{in}}{\pi l} - \frac{2B_oV_{in}^2}{l^2}\Big) \tag{8.22}$$

We maximize this expression with respect to l to arrive at the following geometry condition $\widehat{l}$ and maximum volumetric energy handling density:

$$\widehat{l} = 4\pi\frac{B_oV_{in}}{I_{Lmaxo}} \tag{8.23}$$

$$\Rightarrow \quad \Big(\frac{E_{out}}{\text{vol}}\Big)_{max} = \frac{I_{Lmaxo}^2}{2\pi^2 v_a(1+\alpha)B_o} \tag{8.24}$$

The forms of this geometry condition and resulting energy handling density are similar to those for PRs in Chapter 6 except for the α term in (8.24). In the context of PTs, we constrain I_{Lmaxo} based on an acceptable loss density and set $I_{Lmaxo} = I_{Lmaxo}^H$ as calculated in (8.6).

The α term in (8.24) suggests that the energy handling density for a given I_{Lmaxo} decreases as α increases, but this is without considering potential dependence of I_{Lmaxo} on α. I_{Lmaxo}^H depends on α when the loss density limit of interest is referenced from the secondary side; this limit must be scaled by α to serve as H_{max} when calculating I_{Lmaxo}^H.

8.5 Piezoelectric Transformer Design

The geometry conditions outlined in Section 8.4 each constrain different dimensions, suggesting that a PT may be designed to reach both its maximum efficiency and maximum power density at a nominal operating point within its ZVS region. Here we detail the design process for achieving this and validate it via simulation.

8.5.1 Design Process

Designing a PT according to the geometry conditions described in Section 8.4 begins with selection of α. The geometry condition in (8.19) constitutes a range for α based on the boundaries of K_B, so selecting α from this condition requires an assumption for K_B. To design for ZVS at a single operating point, we suggest assuming K_B to be near the center of its range in (8.19). However, the designer may also choose α such that ZVS is achieved at multiple operating points or power levels as considered in (8.20). In this case, the designer may also elect to use different switching sequences for different parts of the operating region as visualized in Fig. 3-8, for which other α conditions may be similarly derived.

With the selected α, the designer may then calculate the component's dimensions a, b, and l using (8.14) and (8.23). The scaling between a and b is a final degree of freedom that may be used to constrain the PT's form factor.

8.5.2 Validation via Simulation

We illustrate this process with an example PT design for V_{in} = 100 V, V_{out} = 20 V, and P_{out} = 100 W assuming the V_{in}, -V_{in} | V_{out}, -V_{out}, *Zero+* switching sequence described in Section 8.3.1. We design the PT based on APC 841 material (with properties summarized in Table 8.2) and a maximum loss density of 1 W/cm^2 for the output port, which translates to $H_{max} = \alpha \cdot 1$ W/cm^2. Following the procedure of Section 8.5.1, we calculate the PT's dimensions assuming $K_B = 0.8$ at the specified operating point and $a = b$. The resulting PT design and its model parameters are summarized in Table 8.3. We note that such planar

Table 8.2: Assumed PT Material Properties (APC 841)

Parameter	Value
ρ	7600 kg/m^3
ϵ_{33}^S	6.545 nF/m
s_{33}^D	8.533 μm^2/N
v_a	3.927 km/s
k_{33}	0.68
Q_M	1400

Table 8.3: PT Dimensions and Model Parameters

Parameter	Value
α	3.47
a, b	8.78 mm
l	630 μm
C_{pA}	802 pF
C_{pB}	2.78 nF
L	53.3 μH
C	67.2 pF
R	543 mΩ
N	0.288

dimensions are more accurately represented by the k_t coupling coefficient rather than k_{33}, but we continue to assume k_{33} in this analysis to serve as an upper bound for performance since $k_t < k_{33}$.

Fig. 8-5 plots the ZVS region for this PT design according to the condition in (8.1). The nominal operating point lies within this ZVS region as intended, and ZVS may be achieved with this switching sequence across a wide range of surrounding operating points. We evaluate the PT's expected efficiency by numerically solving for the "exact" periodic steady-state solution of its state trajectories throughout the switching sequence as described in Section 3.4, using the script in Appendix A.1.2. This solution reveals the PT's expected efficiency to be 97.6%, which is higher than the 97.4% efficiency capability predicted by the minimum loss ratio in (8.15). This discrepancy can be attributed to the dependence of (8.15) on the PT's geometry-normalized wave number, which is assumed to be π to simplify the model derivation but is actually lower at the maximum-efficiency operating point.

We likewise extract switching times from the exact periodic steady-state solution, which we then use to simulate the complete converter design in LTspice with the topology of Fig. 8-3 and the LTspice schematic of Appendix A.2.2. The resulting waveforms are displayed in Fig. 8-6 and exhibit the switching sequence's desired high-efficiency behaviors (including ZVS) as described in Section 8.3.1. Table 8.4 compares the PT's simulated performance with

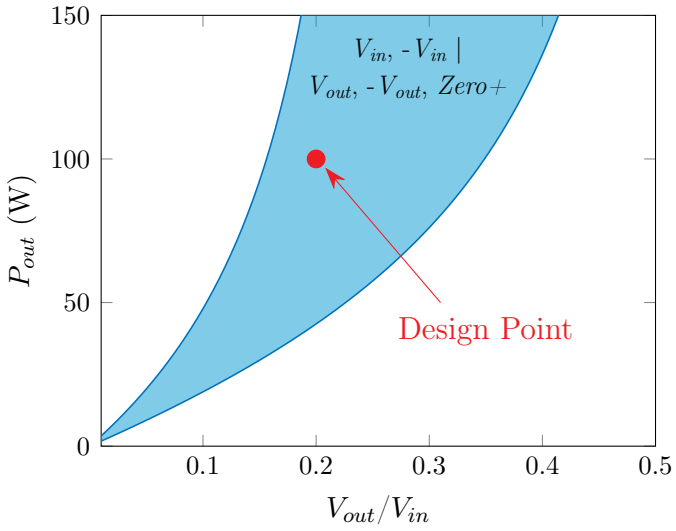

Figure 8-5: ZVS region defined by (8.1) for the PT design summarized in Table 8.3, assuming the V_{in}, -V_{in} | V_{out}, -V_{out}, *Zero+* switching sequence and $V_{in} = 100$ V. The nominal operating point for this PT design is marked with a red dot.

Table 8.4: Designed and Simulated PT Performance

Parameter	Design	Simulation
P_{out}	100 W	100 W
$\frac{P_{out}}{\text{vol}}$	461 W/cm^3	461 W/cm^3
f	3.12 MHz	2.73 MHz
η	97.4 %	97.6 %
I_L	3.14 A	2.99 A
H_{max}	3.47 W/cm^2	3.24 W/cm^2

its design values. Deviations in frequency, I_L, and efficiency may be similarly attributed to the geometry-normalized wave number assumption of π; for a more accurate prediction, the analysis herein may be re-derived based on the maximum-efficiency geometry-normalized wave number as conducted for PRs in Chapters 6 and 7. The simulated converter's efficiency is 97.6% with ideal switches, which aligns with the PSSS calculation. Moreover, this PT design has a power handling density of 461 W/cm^3, validating the design strategy in Section 8.5.1 for achieving both maximum efficiency and maximum power density in a single PT design.

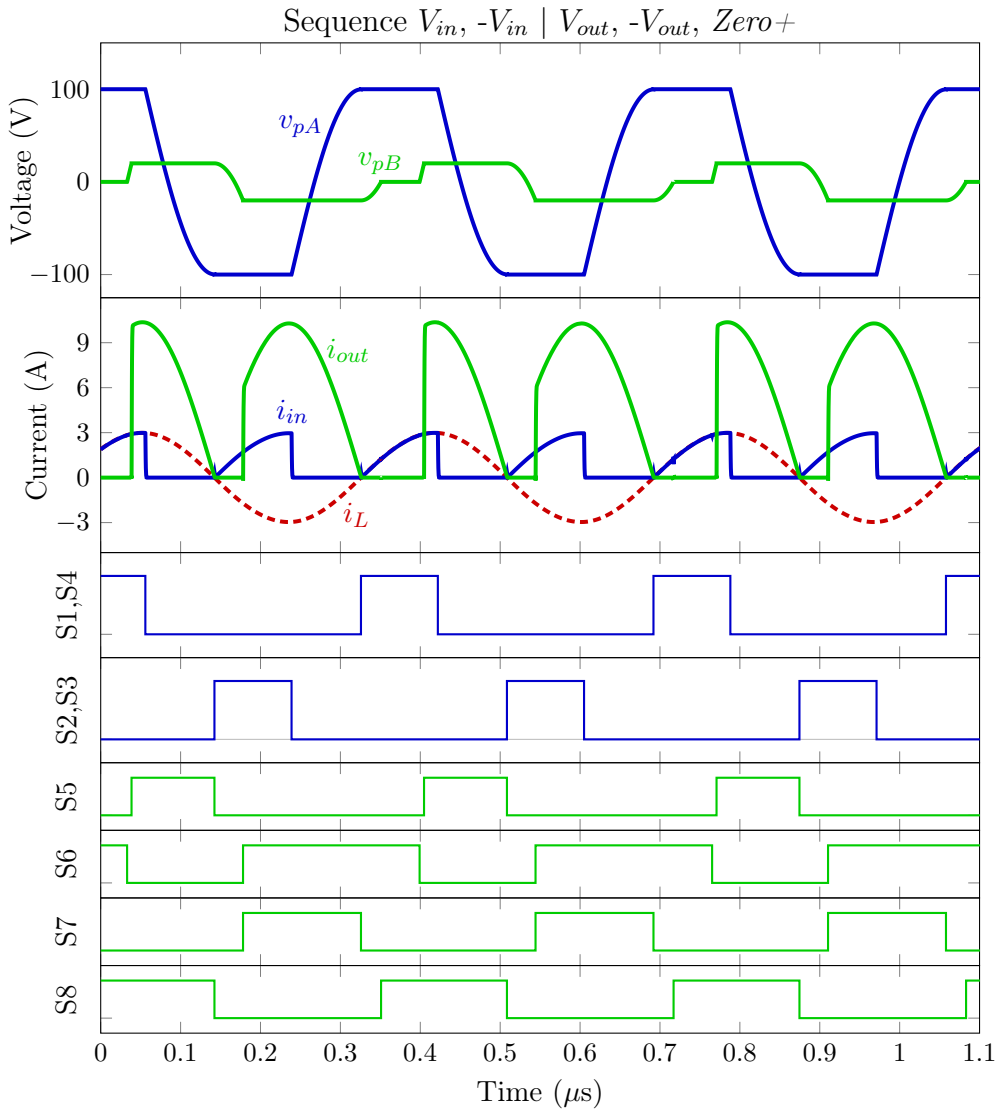

Figure 8-6: Simulated waveforms for switching sequence V_{in}, -V_{in} | V_{out}, -V_{out}, *Zero+* with the topology of Fig. 8-3 and the PT design of Table 8.3. V_{in} = 100 V, V_{out} = 20 V, P_{out} = 100 W.

8.6 Conclusion

To aid high-performance PT design, we have established geometry conditions for maximum efficiency, maximum power density, and the ability to achieve these within a PT's ZVS region. We validate these geometry conditions with an example PT design, which we verify in simulation to have a PT power handling density of 461 W/cm^3 with a realistic thermal limit. This PT design validates not only the utility of the proposed design process but

also that PTs are capable of significantly greater performance than is presently achievable in magnetic-less PT-based converters. However, we note that several aspects of the PT's construction and fabrication have assumed to be ideal in this analysis and will likewise require development to realize these theoretical advantages. This especially includes the effects of the electrode and insulation layers in the mechanical transfer path, and the means for building the proposed structure.

The work of this chapter has been published in [82].

Part III

Miniaturization

Chapter 9

Miniaturization of Piezoelectric-Based DC-DC Converters

9.1 Introduction

Magnetic-less dc-dc converters based on piezoelectric resonators (PRs) have been demonstrated with high efficiency in [58, 67, 69–71, 74]. These designs are based on recently-developed operated sequences and associated circuit topologies that maximize the PR's utilization across wide operating ranges; several of these are enumerated in Chapter 2. Reciprocally, design tools including figures of merit for selecting material and vibration modes and guidelines for optimizing PR geometry for power conversion are established in Chapter 6.

In this chapter, we combine these recent developments in topologies, operating sequences, material selection, and PR design criteria to experimentally demonstrate the power density promise of piezoelectrics. To the authors' knowledge, the resulting prototype achieves the highest PR power-handling density of any PR-based dc-dc converter reported to date, and demonstrates the value of the aforementioned developments in enabling high power density. We also draw on the framework of Chapter 6 to analyze the fundamental scaling properties of piezoelectrics, which reveals that the power handling densities of PRs fundamentally increase

at small scales.

9.2 Design Principles

To demonstrate the power density capability of piezoelectrics, we design a prototype converter with the objective of maximizing the PR's volumetric power handling density. This is achieved by combining (a) a maximum-efficiency circuit topology and switching sequence proposed in Chapter 2, with (b) a maximum-power-density PR design based on criteria for piezoelectric materials, vibration modes, and geometric dimensions developed in Chapter 6.

9.2.1 Topology and Operating Mode

Switching sequences for magnetic-less PR-based converters have been enumerated and down-selected in Chapter 2 based on high-efficiency behaviors and practical characteristics. One of the highest-efficiency step-down switching sequences in this set is the V_{in}-V_{out}, *Zero*, V_{out} sequence, named for the consecutive voltages v_p of its energy transfer stages. This six-stage switching sequence can be realized with the topology of Fig. 9-1 and the waveforms of Fig. 9-2.

This switching sequence maintains high-efficiency behaviors such as soft charging of the PR's capacitance C_p, zero-voltage switching (ZVS), all-positive instantaneous power transfer, and minimum charge circulation across wide operating ranges. This switching sequence likewise maintains constant theoretical efficiency for a given V_{in} and P_{out} in the $\frac{1}{2} < \frac{V_{out}}{V_{in}} < 1$ voltage conversion range, allowing for high-efficiency regulation of V_{out}. As derived in Chapter 2, the PR's amplitude of resonance (i.e., the amplitude I_L of its assumed-sinusoidal i_L in Fig. 9-1) for this sequence and operating region can be modeled as:

$$I_L = \pi \left(\frac{P_{out}}{V_{in}} + f C_p V_{in} \right) \tag{9.1}$$

for which P_{out} is the power delivered to the load, f is the switching frequency, and V_{in} and C_p are as defined in Fig. 9-1. More information about the amplitude of resonance model

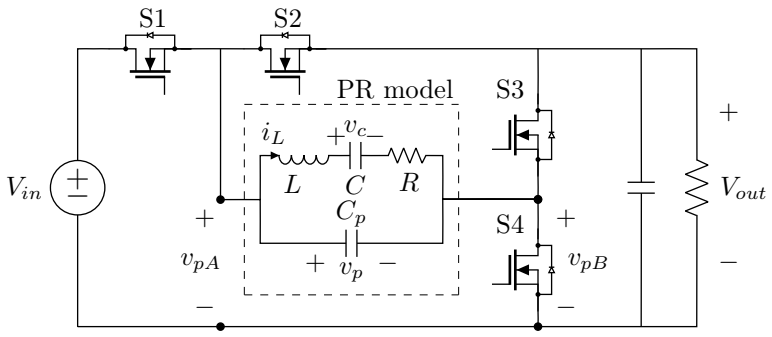

Figure 9-1: Topology corresponding to the V_{in}-V_{out}, *Zero*, V_{out} switching sequence proposed in Chapter 2.

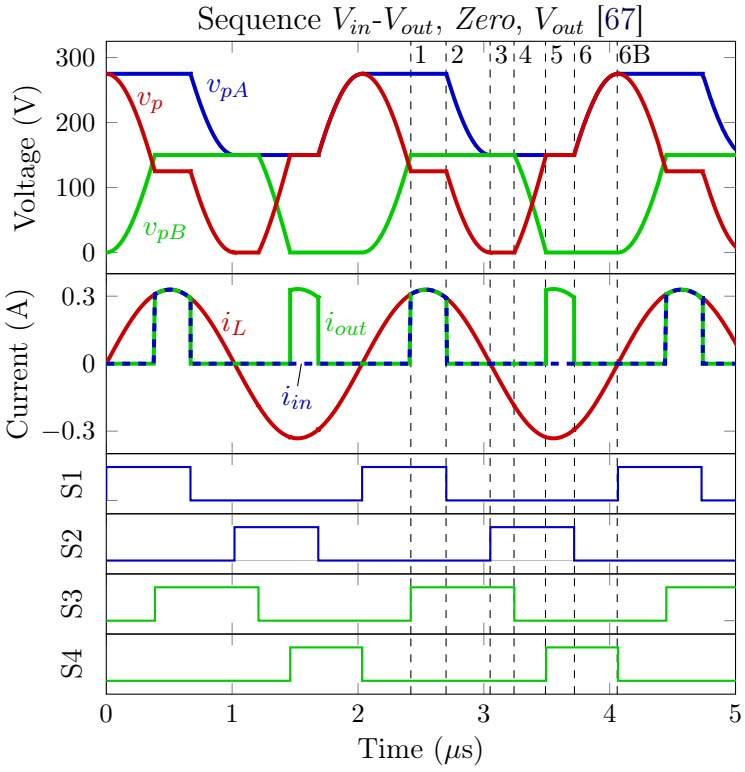

Figure 9-2: Simulated waveforms for switching sequence V_{in}-V_{out}, *Zero*, V_{out} with PR parameters in Table 9.2. $V_{in} = 275$ V, $V_{out} = 150$ V, $P_{out} = 12$ W.

and limits for I_L can be found in Chapter 6.

We adopt the V_{in}-V_{out}, *Zero*, V_{out} switching sequence and its corresponding topology in Fig. 9-1 for this prototype.

9.2.2 Piezoelectric Resonator

The performance of a PR can vary widely based on its material, vibration mode, geometric dimensions, electrode pattern, mechanical mounting structure, and electrical contacts. A typical first step in the PR design process is co-selection of a material and intended vibration mode. Figures of merit (FOMs) for piezoelectric materials and vibration modes have been derived in Chapter 6 based on the highest-efficiency switching sequence described in Section 9.2.1. One promising material and mode combination for high volumetric power density is hard PZT in its radial vibration mode, which has an exceptionally high FOM for volumetric energy handling density (i.e., power density normalized to frequency) and an acceptably high FOM for mechanical efficiency. The radial vibration mode is visualized in Fig. 9-3, and its mechanical efficiency FOM (FOM_M) is

$$\text{FOM}_M = \left(\frac{P_{out}}{P_{loss}}\right)_{max} = \frac{1}{2\pi^2 B_o R_o} \tag{9.2}$$

where

$$B_o = \varepsilon_{33}^T (1 - k_p^2) \frac{\bar{\kappa}_o v_a}{4\pi} \tag{9.3}$$

$$R_o = \frac{\kappa_{o,r}^2 - (1 - \sigma^2)}{Q_m k_p^2 \varepsilon_{33}^T v_a \kappa_{o,r} (1 + \sigma)} \tag{9.4}$$

for which material properties are defined in Table 9.1. We note that this FOM and theoretical minimum loss ratio are independent of operating point, frequency, and amplitude of resonance as long as their parameters are also independent.

Besides its FOMs, the radial vibration mode is also advantageous in that (a) it is the

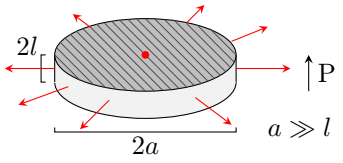

$$C_p = \varepsilon_{33}^T (1 - k_p^2) \frac{\pi a^2}{2l}$$
$$C = C_p \frac{k_p^2}{1-k_p^2} \frac{2(1+\sigma)}{\kappa_{o,r}^2 - (1-\sigma^2)}$$
$$L = \frac{a^2}{2 v_a^2 C_p} \frac{1-k_p^2}{k_p^2} \frac{\kappa_{o,r}^2 - (1-\sigma^2)}{\kappa_{o,r}^2 (1+\sigma)}$$
$$R = \frac{1}{Q_m} \sqrt{\frac{L}{C}}$$

Figure 9-3: Example illustration of the radial vibration mode with electrodes denoted by shaded areas, displacement directions marked with red arrows, and the material's polarization direction shown with 'P'. Circuit model parameters are provided in terms of material properties defined in Table 9.1 [2].

Table 9.1: Piezoelectric Material Properties and Typical PZT Values

Symbol	Name	APC 841 Value*
Q_m	Mechanical Quality Factor	1400
k_p	Electromechanical Coupling Factor	0.6
ε_{33}^T	Permittivity at Constant Stress	12.2 nF/m
v_a	Acoustic Velocity	3.07 km/s
σ	Poisson's Ratio	0.395
$\kappa_{o,r}$	Geometry-Normalized Wave Number at f_r	2.11
$\bar{\kappa}_o$	Geometry-Normalized Wave Number at Maximum Efficiency	2.28

*Q_m, k_p, and ε_{33}^T are provided by [99]. Others are calculated as in [2, 112].

lowest-frequency mode for a circular disc, which minimizes the presence of spurious modes[1] in the PR's inductive region, and (b) its necessary shape for maximum efficiency is more planar than that of other modes[2], providing more surface area for heat extraction. Discrete radial-mode PZT components are also widely available and have been demonstrated with high efficiency in multiple experimental power converter prototypes to date [58, 67, 74, 112]. We therefore adopt hard PZT in its radial vibration mode for this prototype.

The FOMs proposed in Chapter 6 correspond to PR geometry design conditions for achieving both maximum efficiency and maximum energy handling density at a desired converter operating point. These geometry conditions may also be applied to find the converter

[1]Spurious modes (i.e., minor resonant modes that increase loss) are often higher-order harmonics of a component's lower-frequency vibration modes.

[2]The radial vibration mode is one of several "perpendicular" vibration modes as defined in Chapter 6, which tend to require more planar shapes than "parallel" vibration modes for maximum efficiency.

operating points that maximally utilize a given PR. For a PR operating in the radial mode, the V_{in} and P_{out} corresponding to maximum efficiency and loss-limited volumetric energy handling density are:

$$V_{in} = \sqrt{\frac{al \cdot H \cdot \mathrm{FOM}_M}{B_o}} \tag{9.5}$$

$$P_{out} = \pi a^2 \cdot H \cdot \mathrm{FOM}_M \tag{9.6}$$

where H is the PR's areal loss density (i.e., $\frac{P_{loss}}{\pi a^2}$) and describes the PR's thermal management requirement assuming most heat extraction occurs through its electrode surface(s). Thus, maximum loss-limited energy handling density is set by the maximum H that a PR's thermal design can accommodate. For any V_{in} corresponding to lower values of H, maximum efficiency can still be achieved at the P_{out} specified in (9.5)-(9.6). We note that these relationships for other vibration modes, stress-limited density, or electric-field-limited density can also be derived from the framework of Chapter 6.

These analyses assume ideal switching devices, but the presence of significant switch capacitance can be detrimental to a PR's efficiency and power density capability. Switch capacitance also requires resonance between energy transfer stages for ZVS, necessitating more PR charge displacement for the same P_{out}. Switch capacitance may be integrated into (9.2)-(9.6) above by substituting B_o for B_{o+sw}, where

$$B_{o+sw} = (1 + \frac{2C_{oss}}{C_p})B_o \tag{9.7}$$

and C_{oss} equals the effective switch capacitance across relevant bias levels. Thus, the impact of switch capacitance on achievable efficiency and power density is minimized as $\frac{2C_{oss}}{C_p} \to 0$.

9.3 Experimental Demonstration

We utilize the principles of Section 9.2 to design an experimental prototype rated for $V_{in} = 275$ V, $V_{out} = 150$ V, and $P_{out} = 12$ W. Here we detail the prototype's construction, operation, and performance.

9.3.1 Converter Prototype

As a case study, we confine this prototype to off-the-shelf piezoelectric components and evaluate candidates according to their power densities at their maximum-utilization operating points in (9.5) and (9.6). This calculation assumes $H = 1$ W/cm^2 and considers suitable switch capacitance, requiring co-selection of a switching device capable of supporting the PR's suggested V_{in} with minimal capacitance compared to C_p. We select the APC International part 186 (APC 841 disc, $2a = 4.75$ mm, $2l = 0.67$ mm) with EPC2012C FETs for this prototype; the analysis of Section 9.2.2 suggests this combination to be capable of 1 kW/cm^3 PR power handling density with $H < 1$ W/cm^2 at $V_{in} = 275$ V and $P_{out} \approx 12$ W. More details about this prototype, including its PCB layout, are provided in Appendix A.3.3.

As pictured in Fig. 9-4, we implement this design on a two-layer 1-oz copper printed circuit board with the parts listed in Fig. 9-4's caption. For this size PR, traditional mounting structures present considerable challenges and trade-offs: solder joints provide a reliable electrical connection but degrade Q_m if too large and break if too small, and spring mounts provide high Q_m but scratch the electrode if too tight and lose electrical connection if too loose. For demonstration purposes, the PR in this prototype is mounted with a modified coin battery holder (Keystone Electronics part 500), which provides a reliable electrical connection with a wide contact point and an acceptable degradation of Q_m. We note that this structure permits lateral PR movement, and the PR settles to the position shown in Fig. 9-4 upon initial converter operation.

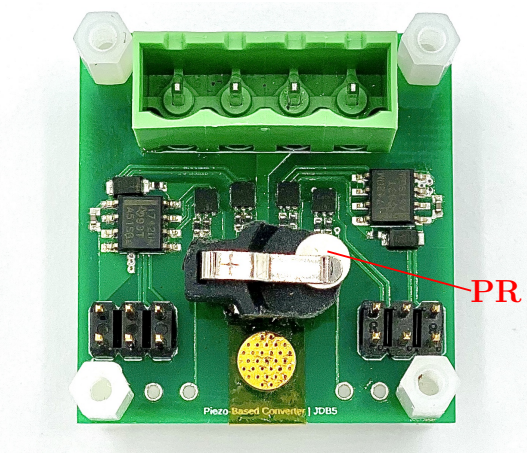

Figure 9-4: Experimental prototype based on the topology of Fig. 9-1 with an APC International PR (part 186: APC 841 material, $2a = 4.75$ mm, $2l = 0.67$ mm) mounted with a Keystone Electronics coin battery holder (part 500). All switches are EPC2012C GaN FETs, located under the PR mount on the board. Drive circuitry includes Texas Instruments UCC27611 gate drivers and ISO7420MD digital isolators.

Table 9.2: Characterized Prototype Model Parameters

C_{p+par}	L	C	R	Q_m	k_p	$\kappa_{o,r}$	$\bar{\kappa}_o$
457 pF	1.51 mH	75.2 pF	4.45 Ω	1030	0.424	2.05	2.13

9.3.2 Small-Signal Characterization

To contextualize this prototype's performance, we conduct a small-signal characterization of the PR mounted in this fully-assembled converter prototype using an impedance analyzer with no bias voltage. A frequency sweep throughout the PR's inductive region is shown in Fig. 9-5, revealing near-ideal smoothness except for one discontinuity at 495 kHz. This discontinuity causes the equivalent series resistance and phase to locally increase and decrease, respectively. Fitting the Butterworth-Van Dyke equivalent circuit to this impedance curve yields the parameters shown in Table 9.2, though we note that C_{p+par} is an overestimate since switch capacitance decreases with respect to bias voltage. The PR's Q_m, k_p, $\kappa_{o,r}$, and $\bar{\kappa}_o$ are characterized as described in [2] (provided in Chapter 6) and translate to an expected maximum PR efficiency of 98.2% at 491 kHz ignoring the effect of the impedance discontinuity.

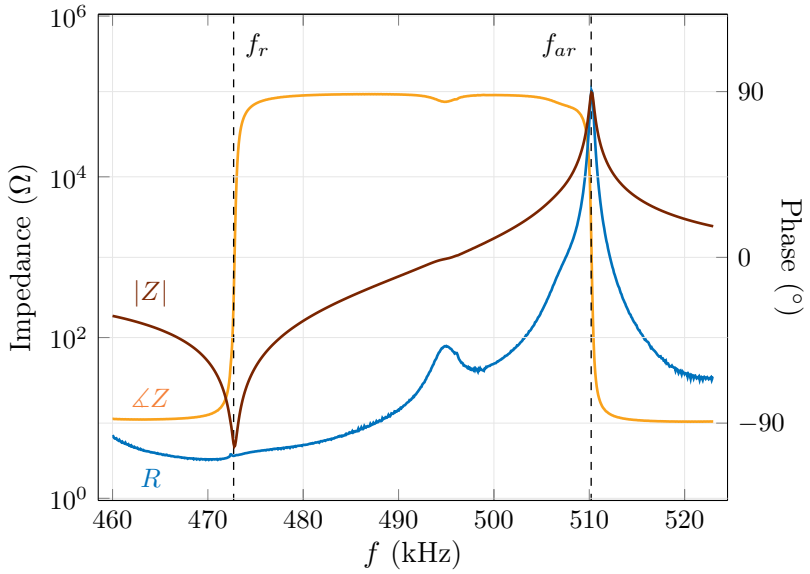

Figure 9-5: Small-signal impedance characteristic of the PR in the fully-assembled prototype pictured in Fig. 9-4, obtained after experiments to capture the PR's steady-state position in the mounting structure. Corresponding circuit model parameters are provided in Table 9.2.

9.3.3 Converter Operation

For all experiments, we operate this converter with a constant-voltage load and forced convection of approximately 300 LFM for thermal management. We control the converter with open-loop switching times, which we manually tune at each operating point for the switching sequence's high-efficiency behaviors discussed in Section 9.2.1. Control handles for tuning include frequency, duty cycle of each half bridge, phase shift between the half bridges, and dead time, and there is one unique tuning point at which all of the switching sequence's high-efficiency behaviors are achieved for a given V_{in}, V_{out}, and P_{out}. The result is the experimental waveforms shown in Fig. 9-6, which compare closely in form with those in Fig. 9-2.

9.3.4 Experimental Results

We test this converter's power stage efficiency vs. P_{out} for three different input/output voltage levels, each with the same conversion ratio, and Fig. 9-7a displays the results. This converter achieves competitive efficiency across a wide operating range and a full load

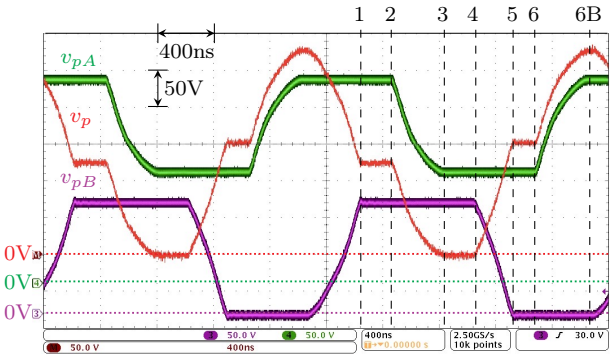

Figure 9-6: Experimental waveforms at V_{in} = 275 V, V_{out} = 150 V, P_{out} = 12 W, and f = 493 kHz with the prototype pictured in Fig. 9-4.

efficiency of 93.3%. The maximum observed efficiency for the lowest voltage level (V_{in} = 55 V) approaches the theoretical maximum PR efficiency of 98.2%. However, maximum efficiency is observed to be lower for higher voltage levels, which correspond to greater I_L. This dependence on excitation level is a departure from the framework described in Section 9.2, in which maximum efficiency is a function of only Q_m and material properties. This suggests the piezoelectric component's material properties and/or loss characteristics to be nonlinear with respect to excitation level.

Fig. 9-7b plots these efficiency curves with respect to frequency, further highlighting the aforementioned discrepancies between voltage levels. The downward efficiency spikes between 491 kHz and 495 kHz may be attributed to the impedance discontinuity shown in Fig. 9-5. The V_{in} = 55 V efficiency characteristic rebounds from this spike at lower frequencies, suggesting that the V_{in} = 165 V and V_{in} = 275 V efficiencies may do the same if operated at lower frequency (and therefore higher power).

Previous reports for PR power handling density in [69, 70, 74] have considered only the component's "active" volume between its electrodes, in which most energy is assumed to be stored. This does not consider the component's mounting structure (including "inactive" material used for anchoring) or electrical connections, as these aspects of PR design are yet to be optimized for power conversion. Adopting this convention, this prototype achieves a piezoelectric component power handling density of 1.01 kW/cm^3 at V_{in} = 275 V, V_{out} = 150 V, and P_{out} = 12 W. We validate the stability of this operating point with ten

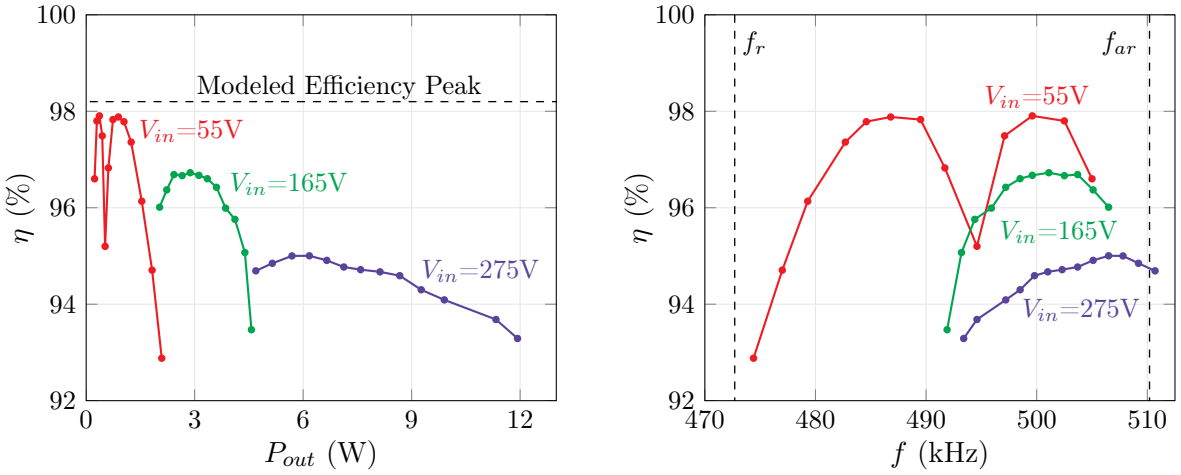

Figure 9-7: (a) Experimental power-stage efficiency vs. P_{out} for various V_{in} (marked) each with $V_{out} = \frac{6}{11}V_{in}$. (b) Experimental power-stage efficiency vs. f for various V_{in} (marked) each with $V_{out} = \frac{6}{11}V_{in}$. Efficiencies do not consider auxiliary power. Plots are based on the same data points.

minutes of continuous operation, during which the prototype maintains the same waveforms without need to adjust its open-loop switching times. After this ten-minute period, the PR is thermally stable at <36 °C with forced convection.

The observed piezoelectric component power handling density of 1.01 kW/cm^3 represents a substantial increase over other recent piezoelectric-based dc-dc converter prototypes, which report 148 W/cm^3 [69], 176.8 W/cm^3 [74], and 128 W/cm^3 [70]. All four prototypes are based on the same family of high-efficiency six-stage switching sequences, so the difference in density may be attributed to this prototype's high-energy-handling-density PR design according to the FOMs and geometry conditions in Chapter 6.

9.4 Broader Context

Finally, we contextualize the results of Section 9.3 with a competing magnetic design and the fundamental scaling properties of piezoelectric components.

Table 9.3: Assumed Inductor Design Parameters and Material Properties

Symbol	Name	Value
K_u	Window Utilization Factor	0.35
ρ	Copper Resistivity	1.724 $\mu\Omega$-cm
K_{fe}	Core Loss Coefficient	7024 W/cm^{3}T$^\beta$
β	Core Loss Exponent	3.59
B_{max}	Maximum Flux Density	0.42 T

9.4.1 Magnetic Design Comparison

To provide context for the PR power handling density achieved in Section 9.3, we design a magnetic component to serve as a comparison. There are many potential approaches for such a design; we elect to constrain it for the same operating point and frequency (V_{in} = 275 V, V_{out} = 150 V, P_{out} = 12 W, f = 493 kHz), with a maximum temperature rise of 50 °C.

Given these specifications, we focus on the inductor of a resonant-transition buck converter, which we select for its high utilization of the magnetic component. We design this inductor using the iterative design algorithm in [123]. We assume a Ferroxcube 3F36 core material with properties shown in Table 9.3; this material is widely utilized for magnetics in the frequency range of interest. We likewise assume a pot core shape for its compactness and enclosure of most magnetic flux.

Design parameters pertaining to the desired operating point are summarized in Table 9.4. For a given core size, we optimize this inductor's number of turns with respect to total power loss, assuming only core loss and dc copper loss. We then estimate the core's thermal resistance using Fig. 20.3 of [123], calculate its expected temperature rise, and repeat this process to identify to smallest core size capable of <50 °C temperature rise. This results in the design summarized in Table 9.5, which is based on the P5.8/3.3 core and bobbin dimensions detailed in [124].

For the same operating point and frequency, this inductor design has a volume of 87.2 mm^3 and a power handling density of 138 W/cm^3. This result is more than 7x lower than

Table 9.4: Inductor Design Operating Point Parameters

Symbol	Name	Value
L	Inductance	864 μH
λ	Flux Linkage	138 μV-s
I_{pk}	Peak Current	160 mA
I_{rms}	RMS Current	92.4 mA

Table 9.5: Inductor Design Summary

Symbol	Name	Value
-	Core Size	P5.8/3.3
-	Material	3F36
-	Wire Size	AWG 44
N	Number of Turns	162
l_g	Gap Length	179 μm
P_{core}	Core Loss	47.4 mW
P_{cu}	Copper Loss	137 mW
η	Efficiency	98.5%
ΔT	Temperature Rise	44 °C
-	Volume	87.2 mm^3

the 1 kW/cm^3 power handling density of the PR in Section 9.3, highlighting the significance of this experimental demonstration. We note several caveats to this comparison:

- The PR in Section 9.3 is an off-the-shelf part, while the core of this inductor design is not readily available in its exact size and material combination. Constraining for an off-the-shelf magnetic core would likely result in an inductor design with greater volume.

- This inductor design ignores winding capacitance, which would favor a lower number of turns in the inductor and therefore greater total loss. This may necessitate a design with greater volume.

- The expected efficiency of the inductor design is close to that of the PR based on

its small-signal characterization in Section 9.3, but the PR's experimental efficiency is lower. An inductor design that compares to the PR's experimental efficiency would likely have lower volume but would require more aggressive thermal management.

- This inductor is designed with standard techniques, and use of more sophisticated methods would likely yield an inductor design with lower volume.

In summary, this magnetic design comparison suggests the experimental demonstration in Section 9.3 to be a major milestone in realizing the miniaturization potential of piezoelectrics.

9.4.2 Fundamental Scaling Properties

We now examine the scaling properties of piezoelectrics through the lens of a PR operating in a highest-efficiency switching sequence described in Section 9.2.1. To do so, we assume that a PR design of any vibration mode follows the geometry conditions in Chapter 6 for maximum efficiency and power density, respectively:

$$\widehat{G} = G_f \frac{A}{l} = \frac{P_{out}}{V_{in}^2 B_o} \tag{9.8}$$

$$\widehat{l} = 2\pi \frac{B_o V_{in}}{I_{Lmaxo}} \tag{9.9}$$

We also assume power density to be constrained by a fixed geometry-normalized amplitude of resonance (I_{Lmaxo}) based on an electric field, stress, or loss density limit as described in Chapter 6. The geometry conditions then constrain all dimensions of the component, and therefore its resonant frequency, based on a nominal operating point (i.e., P_{out} and V_{in}, assuming the V_{in}-V_{out}, *Zero*, V_{out} sequence). For perpendicular modes, we note that I_{Lmaxo} is not independent of operating point for the loss-density-limited case, so this analysis only applies for stress or electric field limits.

With these constraints, a component design always achieves both the minimum loss ratio and the maximum power density quantities derived in Chapter 6. The minimum loss ratio has no dependence on geometry, which implies that the achievable efficiency of a piezoelectric

Table 9.6: Piezoelectric Resonator Scaling Properties for Fixed I_{Lmaxo}

Case Study	Mode Type	vol	A	l	f	V_{in}	P_{out}	η
Scale all dimensions by α	Any	α^3	α^2	α	α^{-1}	α	α^2	1
Scale l by α	Parallel	α	1	α	α^{-1}	α	1	1
	Perpendicular	α	1	α	1	α	α	1
Scale a by α	Parallel ($a \neq b$)	α	α	1	1	1	α	1
	Parallel ($a = b$)	α^2	α^2	1	1	1	α^2	1
	Perpen. ($a = b$)*	α^2	α^2	1	α^{-1}	1	α	1
Scale a by α, and l by α^{-1}	Perpen. ($a = b$)*	α	α^2	α^{-1}	α^{-1}	α^{-1}	1	1

*The 'Perpendicular ($a = b$)' mode type is inclusive of perpendicular modes for which both planar dimensions are a.

component is irrespective of size to the extent that Q_m and k also remain the same. Further, the maximum volumetric energy handling density also has no dependence on geometry, which suggests that maximum volumetric power density rises linearly with operating frequency as long as the piezoelectric material properties are independent of frequency. Thus, achievable volumetric power density at a fixed I_{Lmaxo} rises linearly as the component's frequency-setting dimension scales down in size.

The effects of this scaling can be illuminated through case studies in which certain PR dimensions are scaled by factor α. We begin by scaling all three dimensions of a PR by α, which corresponds to a volume change of α^3. The resulting frequency, and therefore the achievable volumetric power density given I_{Lmaxo}, scales by α^{-1}, so both quantities rise as a component is scaled down in size (α<1). To satisfy the maximum power density geometry condition in (9.9), V_{in} must also scale by α, which then requires P_{out} to scale by α^2 to satisfy the maximum efficiency geometry condition in (9.8). This suggests that the greatest power density potential for piezoelectric components occurs as $\alpha \to 0$, which corresponds to low voltage, very low power, and high frequency components. These scaling characteristics are displayed in Table 9.6 and illustrated in Fig. 9-8.

Realistically, manufacturing or application constraints may allow only partial scaling of a PR, so we next examine the independent scalability of PR dimensions l and a. The result is different between parallel and perpendicular vibration modes in part due to different

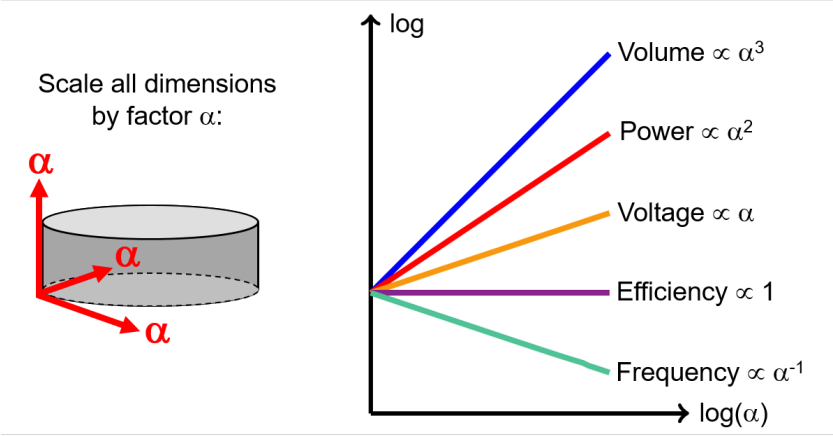

Figure 9-8: PR scaling characteristics constrained for fixed I_{Lmaxo}, maintaining (9.8) and (9.9) for maximum efficiency and power density.

frequency-setting dimensions but also due to different geometry conditions for maximum efficiency. Independently scaling l and a by α results in the effects summarized in Table 9.6; this includes scaling of the PR's form factor and frequency along with the required scaling of P_{out} and V_{in} to uphold the geometry conditions for maximum efficiency and power density.

Several conclusions can be drawn from Table 9.6. For parallel modes, V_{in} and P_{out} can be manipulated independently through l and a, respectively. However, decreasing l for lower V_{in} also corresponds to an increase in frequency and achievable power density given I_{Lmaxo}. The highest density therefore occurs as $V_{in} \to 0$; varying a for P_{out} has no effect on frequency or density. For perpendicular modes, P_{out} can be manipulated independently from V_{in} through a, though decreasing a results in higher frequency and power density. V_{in} can only be manipulated independently of P_{out} if a and l are scaled inversely, which directly manipulates the component's form factor. However, decreasing l (for lower V_{in}) and increasing a results in decreases for frequency and power density. Thus, for the same P_{out}, highest achievable density is achieved at higher V_{in} for perpendicular modes.

The general conclusion to be drawn from Table 9.6 and Fig. 9-8 is that piezoelectric components have highly favorable scaling characteristics for miniaturization, especially compared to their magnetic counterparts. Although promising, this analysis stems from a simple theoretical framework that does not consider potential high-frequency losses or nonlinear

piezoelectric material properties, and miniaturization will require a thorough understanding of these factors.

9.5 Conclusion

To illustrate the power density promise of piezoelectrics, we have designed and experimentally demonstrated a dc-dc converter prototype capable of 1 kW/cm^3 PR power handing density at $V_{in} = 275$ V, $V_{out} = 150$ V, and $P_{out} = 12$ W; this power handling density is more than an order of magnitude greater than a competing magnetic design. This case study validates not only the power density capabilities of piezoelectrics but also the recent developments in circuit topologies, operating sequences, material selection, and PR design as means for realizing this power density. Further, we show through theoretical case studies that the achievable power densities of piezoelectric components fundamentally increase at small scales and therefore scale favorably for miniaturization.

We note that there are several opportunities and challenges to be addressed for piezoelectric-based power conversion in the future [125,126], including the material property nonlinearities observed in this prototype at high levels of excitation. Nonetheless, this chapter marks a significant milestone in demonstrating the power density capabilities of piezoelectrics and their promise for miniaturized power conversion.

The work of this chapter has been partially published in [112].

Chapter 10

Conclusion

This thesis explores how we can leverage the advantages of piezoelectrics to substantially miniaturize power electronics. Piezoelectric components offer numerous potential advantages to power electronics, but realizing these advantages requires specific design approaches for both power electronic circuits and piezoelectrics themselves. Here we summarize the findings of this thesis in regards to dc-dc converter implementations, piezoelectric components, and miniaturization prospects.

10.1 DC-DC Converter Implementations

While traditional dc-dc converter implementations yield limited efficiencies with piezoelectrics, efficient utilization of piezoelectrics is possible through specific converter implementations tailored to such. At the foundation of these implementations are six- and eight-stage switching sequences capable of specific high-efficiency behaviors such as soft charging of the piezoelectric component's terminal capacitances, ZVS of all switches, all-positive instantaneous power transfer, and minimal charge circulation. The switching sequences maintain these high-efficiency behaviors across wide voltage conversion and power ranges, the boundaries of which vary. Realizing these switching sequences requires practical circuit topologies of only four unidirectional-blocking switches, some of which may be implemented passively.

For a given input voltage, output voltage, and load, piezoelectric component state trajectories throughout a six-stage switching sequence are fully constrained for its high-efficiency behaviors. These state trajectories may be visualized using state planes and analytically computed using conservation equations for the ideal case, which is useful for estimating switching times. An exact periodic steady-state solution considering loss must be obtained numerically but provides additional information on power transfer and efficiency.

The amplitude of resonance model is a valuable tool for quantifying a piezoelectric component's resonant current amplitude I_L, power handling, mechanical energy storage, and mechanical loss characteristics with a given switching sequence. Because the piezoelectric component's state trajectories are fully constrained, its amplitude of resonance may be calculated based on known charge displacement quantities during each stage of the switching sequence. How effectively a switching sequence utilizes a piezoelectric component is quantified with charge transfer utilization factor K; switching sequences with higher K require lower I_L for the same power throughput.

Piezoelectric component efficiency with a given switching sequence can be calculated using an exact periodic steady-state solution or estimated using the amplitude of resonance model. The proposed high-efficiency switching sequences have highly varying efficiency capabilities, with highest efficiency associated with less charge displacement during non-energy-transfer stages. The highest-efficiency PR-based switching sequences for the step-down case are: V_{in}-V_{out}, *Zero*, V_{out} ; V_{in}, V_{in}-V_{out}, V_{out} ; and V_{in}, V_{in}-V_{out}, *Zero*, V_{out}. The highest-efficiency sequences for the step-up case are: V_{in}, *Zero*, V_{out}-V_{in}; V_{in}, V_{out}-V_{in}, V_{out}; and V_{in}, *Zero*, V_{out}-V_{in}, V_{out}.

These highest-efficiency PR-based switching sequences have been validated for the step-down case in an experimental prototype based on an off-the-shelf PR. This prototype demonstrates high experimental efficiencies across wide operating ranges, with peak efficiencies of >99%. Further, all three switching sequences are observed to have near-identical efficiencies for the $\frac{1}{2} < \frac{V_{out}}{V_{in}} < 1$ operating region. Ignoring downward efficiency spikes due to spurious modes, the amplitude of resonance model predicts these observed efficiency trends. These efficiencies greatly exceed those of previous PR-based converter designs, owing to the switching

sequence's efficient utilization of the PR.

High-efficiency PT-based converter implementations may be realized with a six-stage switching "sub-sequence" at one port and a four-stage switching sub-sequence at the other port. This combination harnesses the wide conversion ratio advantage the six-stage sub-sequence and the high K advantage (and therefore high efficiency advantage) of the four-stage sub-sequence. Switching sequences for isolated PTs can be realized with combinations of full-bridges and half-brides at each port. Non-isolated PTs allow for a wider variety of high-efficiency switching sequences and topologies, with several topologies consisting of only four unidirectional-voltage-blocking switches.

PT-based switching sequences may be analyzed with the same techniques as PRs but necessitate consideration of both ports. Periodic steady-state analysis requires first dividing the PT's resonant cycle into segments based on the temporal order of stage transitions at each port. The total charge displacement and amplitude of resonance may be calculated from the perspective of either port, though the four-stage sub-sequence port is more straightforward. One distinct characteristic of PT-based switching sequences is that their compatible voltage conversion regions (i.e., ZVS regions) deviate from their ideal regions at low power due to differences between the two ports' necessary charge displacement for ZVS. This region may be modeled based on total charge displacement. Depending on a PT's model parameters, its peak mechanical efficiency operating point with a given switching sequence may or may not occur within this ZVS region.

In contrast to PR-based switching sequences, which PT-based switching sequence produces highest efficiency depends on the PT's model parameters and intended operating point. For high power applications, efficiency tends to be higher for sequences requiring full-bridges at their four-stage sub-sequence ports. The same applies vice versa; for low power applications, sequences requiring half-bridges at their four-stage sub-sequence ports dominate in terms of efficiency. In general, non-isolated switching sequences provide opportunity for greater efficiency than isolated switching sequences, especially if one PT port contributes to both extracting energy from the source and delivering energy to the load.

The V_{in}, *Zero+*, *Zero-* | V_{out}, V_{in} non-isolated switching sequence has been experimentally

demonstrated using an off-the-shelf PT. This prototype exhibits near-constant efficiency across wide operating ranges, but its efficiency is limited to approximately 90% in part due to its ZVS region boundary. The observed efficiency trend and ZVS region boundaries are reflected in the amplitude of resonance and ZVS region models, respectively. This efficiency result is significantly higher than those of PT-based converter designs based on traditional resonant converter implementations but marks a distinct difference in achievable efficiency between commercially available PRs and PTs.

Closed-loop control of six-stage switching sequences requires elements of frequency modulation, pulse-width modulation, and dead time control, with additional feedback loop(s) needed for active rectification. Output voltage is regulated primarily with the duty cycle of one half-bridge (i.e., the regulating half-bridge), though all other switching times must be simultaneously adjusted to maintain the sequence's high-efficiency behaviors. Frequency is not an independent control variable; switching times must be synchronized to the piezoelectric component's resonant cycle via i_L zero crossings. The output voltage dynamics associated with a six-stage switching sequence can be described with only two states: the output voltage and amplitude of resonance.

One straightforward closed-loop control method is "sensed" control, in which the regulating half-bridges are triggered on based on sensed voltage measurements and the i_L zero crossing is detected based on a diode's blocking voltage. This strategy requires only two control loops assuming passive rectification, but hardware limitations may constrain its upper bound for frequency. A second closed-loop control method is "static" control, in which all four switching times for the regulating half-bride are actively controlled and the i_L zero crossing is detected geometrically based on waveform symmetry. Static control is more robust to high frequency noise and comparator delays, and with it, synchronous control of the non-regulating half-bridge requires only one additional control loop. This static control strategy has been experimentally validated using a digital micro-controller.

As an alternative to PTs, PR-based and SC-based power conversion may be hybridized to serve high voltage conversion ratios with high efficiency and high power density across wide voltage conversion ranges. One example of such hybridization is a two-stage cascaded

converter architecture with a PR-based regulation stage and a SC-based transformation stage. PRs tend to have very high characteristic impedances, so the PR-based regulation stage is a natural fit for the higher-voltage side of this conversion architecture.

The control of a PR-based regulation stage in the $\frac{1}{2} < \frac{V_{out}}{V_{in}} < 1$ operating region may be simplified through use of eight-stage switching sequence V_{in}, V_{in}-V_{out}, *Zero*, V_{out}. Eight stage switching sequences have one additional degree of freedom in their periodic steady-state trajectories that may be constrained so that both sides of the resonant cycle are nearly symmetric with approximately 50% duty cycles. The primary control handle for voltage regulation in this sequence is the phase shift between the half-bridge switch signals, reducing the number of necessary control loops by one. This eight-stage sequence has the same K, I_L, and efficiency as both highest-efficiency six-stage sequences in this operating region.

This two-stage hybrid PR/SC-based dc-dc converter architecture, along with use of the eight-stage sequence in the PR stage, has been experimentally demonstrated with an efficiency of 96% at a voltage conversion ratio of 0.128 and high efficiency across a continuous 2:1 input voltage range. This greatly exceeds the efficiency capabilities of present PR-based and PT-based converter designs at similar conversion ratios.

10.2 Piezoelectric Component Design

The piezoelectric component design process begins with co-selection of a piezoelectric material and vibration mode, followed by selection of its geometric dimensions. Vibration modes can be broadly categorized as parallel and perpendicular modes depending on whether their applied and induced electric fields are parallel or perpendicular, respectively. Design tools for piezoelectric components can be derived based on the amplitude of resonance model, which provides a direct relationship between a component's material properties, geometric dimensions, and amplitude of resonance I_L for a given converter operating point and switching sequence. I_L can be constrained for a maximum allowable stress, strain, electric field strength, or loss density, and the geometry-normalized amplitude of resonance I_{Lmaxo} quantifies this limit in terms of only material properties (akin to a magnetic flux density limit for

magnetics) and thermal limits if considered. Presently available piezoelectric materials are typically constrained by stress and loss density limits.

Assuming a highest-efficiency switching sequence, the minimum loss ratio, maximum areal power density, and maximum volumetric energy handling density (i.e., volumetric power density normalized to frequency) of a PR are functions of only material properties and I_{Lmaxo}. These extrema therefore respectively serve as figures of merit FOM_M, FOM_{APD}, and FOM_{VED} for piezoelectric materials and vibration modes. FOM_M is an important consideration for any design, and whether to weigh FOM_{APD} or FOM_{VED} more heavily depends on whether the design is most constrained by footprint area, volume, and/or frequency. These FOMs assume the maximum-efficiency operating frequency, which occurs at the harmonic mean of a PR's resonant and anti-resonant frequencies.

The FOMs correspond to PR geometry conditions for maximum efficiency, maximum areal power density, and maximum volumetric energy handling density. These geometry conditions are orthogonal and therefore enable PR designs capable of meeting both maximum efficiency and maximum power density at a nominal operating point. Satisfying the maximum-efficiency geometry condition $\widehat{G}$ generally requires a planar PR design, so non-planar vibration modes have limited utility in power conversion. $\widehat{G}$ scales proportionally with power and inversely with voltage squared, so reaching maximum efficiency at higher power translates to a higher $\widehat{G}$ and therefore more extreme planar dimensions. Parallel modes tend to have less-extreme planar shapes than perpendicular modes and are particularly advantageous for satisfying large $\widehat{G}$.

Two promising piezoelectric materials are PZT and lithium niobate. Four high-performing vibration modes for PZT are thickness shear (with side electrodes), thickness extensional, contour extensional, and radial. The thickness shear mode is likewise an auspicious vibration mode for lithium niobate, and other modes such as the quasi-thickness extensional mode are also possible with different crystal cuts. Lithium niobate has a higher characteristic impedance than PZT and therefore requires an order of magnitude higher $\widehat{G}$ for the same operating point, requiring more extreme planar PR dimensions. Both materials have high FOM_M, with lithium niobate having a higher efficiency capability if its theoretical me-

chanical quality factor can be realized. PZT perpendicular modes offer particularly high FOM_{VED}, while lithium niobate parallel modes have higher FOM_{APD}.

These FOMs, geometry conditions, and operating frequency have been validated using exact periodic steady-state solutions for >500 commercially available PRs of different materials, sizes, shapes, and vibration modes. This study also validates the FOMs' independence from PR geometry and operating point information, as well as the role of I_{Lmaxo} in constraining power density. FOM_M has been validated experimentally with PRs of different materials, sizes, and vibration modes, for which the observed minimum loss ratio tracks the values predicted by $\frac{1}{\text{FOM}_M}$. These FOMs are concluded to be highly representative metrics for the capabilities of piezoelectric materials and vibration modes, and their corresponding geometry conditions facilitate achievement of both maximum efficiency and maximum power density in a single PR design.

There is opportunity to further build on the capabilities of PRs with augmentation, defined as the addition of non-piezoelectric material layers to the surfaces of a PR to create a composite electromechanical energy storage component. Augmenting the dynamic surfaces of a PR with thin layers of mass adds inertial energy storage, which can be modeled as an additional inductance in the PR circuit model's LCR branch. Assuming the mass layers to be rigid bodies and the original PR resistance to remain the same, this augmentation decreases the component's resonant frequency, decreases its minimum loss ratio, and increases its power density capability.

Design of mass-augmented PRs begins with selecting a mass ratio to be as high as beneficial, after which the component's dimensions may be designed based on bare PR geometry conditions. A larger mass ratio tends to result in a thinner, more planar component shape. This analysis has been validated through simulation of an augmented PR design intended to serve as a drag-and-drop replacement for a bare PR. The augmented PR design has an identical resonant frequency but significantly lower footprint area, volume, and loss than the bare PR. Thus, this study suggests that PR augmentation may open doors to greater power densities and greater efficiencies at lower operating frequencies.

Although presently available PTs exhibit limited efficiencies without magnetics, greater

efficiencies are possible through specific geometry design criteria. Drawing on the design strategy for PRs, these PT design criteria contain geometry conditions for maximum efficiency and maximum power density. In the case of PTs, one additional geometry condition is necessary to ensure that the operating region of interest occurs within the PT's ZVS region. This geometry condition constrains the PT's transformation ratio.

This design process has been validated via simulation for a PT structure with both halves operating in the length extensional mode (with end electrodes). The resulting PT design operates at its maximum efficiency and maximum volumetric energy handling density at its nominal operating point, which occurs within the ZVS region as designed. The PT's simulated efficiency and power density are significantly greater than those of presently available PTs, highlighting the value of such criteria for high performance PT design.

10.3 Miniaturization

Realizing the exceptional power density capabilities of piezoelectrics requires the combination of a high-efficiency converter implementation and a high-performance piezoelectric component design, which are respectively explored in Parts I and II of this thesis. PZT perpendicular modes are advantageous for PR power handling density in that they have the highest FOM_{VED}, high FOM_{M}, minimal spurious modes, and high surface area for heat extraction. Pursuit of high power handling density motivates use of higher-frequency PRs, which tend to be smaller in size and more sensitive to their mounting structures. Soldering and spring mounts present considerable trade-offs between Q_m degradation and reliability of the mechanical and electrical connections.

High PR power handling density has been experimentally demonstrated with the V_{in}-V_{out}, *Zero*, V_{out} switching sequence and an off-the-shelf PZT radial mode PR mounted in a modified coin battery holder. In contrast to magnetics, a small-signal characterization of this PR closely predicts its large-signal operation and performance. The prototype's maximum efficiency aligns with the expectation, though efficiency slightly wanes for higher voltage levels; this suggests the component's material and/or loss characteristics to be mildly non-

linear with respect to excitation level at high power density. This prototype exhibits a power handling density of >1 kW/cm^3 at a switching frequency of 500 kHz, representing a substantial increase over other piezoelectric-based dc-dc converter prototypes. This power handling density is 7x greater than that of a competing magnetic design for the same operating point.

Unlike magnetics, piezoelectric components exhibit increasing power handling densities at small scales. Maximum efficiency, volumetric energy handling, and areal power density are each independent of geometry and therefore independent of scale to the extent that the PR's material properties remain constant. Assuming a PR design adheres to the geometry conditions for maximum efficiency and power density (with fixed I_{Lmaxo}), volumetric power density rises linearly with frequency, and therefore rises linearly as a PR's frequency-setting dimension scales down in size. Thus, the greatest power density potential for piezoelectrics occurs at small scales, which is highly favorable for miniaturization.

In summary, this thesis has found piezoelectric passive components to be promising alternatives to magnetics for future miniaturized power conversion. We argue that progress up to this point has merely scratched the surface of possibilities for piezoelectric-based power conversion, for which there are several opportunities and challenges to still address [125,126]. With further development, piezoelectrics are positioned to open new opportunities for power electronic systems in computing, wireless communication, robotics, biomedical devices, renewable energy, and beyond.

Appendix A

Supplementary Materials

A.1 Periodic Steady-State Solution Scripts

A.1.1 Piezoelectric-Resonator-Based Switching Sequence

This appendix contains a MATLAB script that solves for the periodic steady-state solution of a six-stage PR-based switching sequence. The script is currently configured for the V_{in}-V_{out}, *Zero*, V_{out} switching sequence in the $\frac{1}{2} \leq \frac{V_{out}}{V_{in}} \leq 1$ operating region but may be configured for other six-stage switching sequences. The solver requires an initial condition for the PR's resonant capacitor voltage, which may be estimated using the amplitude of resonance model (currently commented out) or hard-coded. This script first solves for the ideal periodic steady-state solution (detailed in Section 2.4.2), and then uses the solution as a starting point for solving the exact solution (detailed in Section 2.4.4). In addition to the PR's states, this script computes the switching times, output power, and efficiency associated with the exact periodic steady-state solution. To obtain the desired output power, the script sweeps initial conditions until it achieves this output power within a certain error margin.

This script is utilized as-is to compute switching times for the simulation in Section A.2.1.

```
1 %% Periodic Steady State Solution Script for Six-stage PR-based Switching
     Sequence
```

```
%% Authors: Joshua Piel and Jessica Boles
% Current switching sequence configuration: Vin-Vout, Zero, Vout
% Note: This script assumes the two-part open stage occurs in stage 6. To
% use this script for any six-stage sequence, the sequence must be ordered
% such that its two-part open stage occurs in stage 6.


% PR Parameters

Cp = 457e-12;           % F
L = 1.51e-3;            % H
C = 75.2e-12;           % F
R = 4.45;               % ohm


% Operating Point Specification and Initial Condition

Vin = 275;              % V
power = 12;             % W (This script will sweep initial conditions
    until this power is achieved, within 0.5%)
Vout = 150;             % V
Vs7_n = -1350;          % V (Corresponds to the negative peak for vc)


% Optional Initial Condition Estimate

% effexp = .98;         % (Expected efficiency - only used to calculate
    initial condition)
% Pout = power/effexp;  % W (Desired power - only used to calculate
    initial condition)
% f = 491926;           % Hz (Expected frequency - only used to calculate
    initial condition)
% K = Vin/(2*Vout);     % (UPDATE based on switching sequence)
% IL = pi*(Pout/(2*Vout*K) + f*Cp*Vin);
```

```
% Vs7_n = Vin - IL*sqrt(L/C);


% Switching Sequence

% 2x6 matrix:
%
% 1st row - specify switching sequence in terms of Vin and Vout
% Voltage of stage is linear combination of Vin and Vout based on
    multiplier in matrix
%
% 1st stage | 3rd stage | 5th stage | SS stage (voltage between open
    stages)
% Vin  Vout | Vin  Vout | Vin  Vout | Vin Vout
%
% Example: Vin, Vin-Vout, Zero, Vss=Vout
% [1 0 1 -1 0 0 0 1]
%
% 2nd Row - specify current polariy constraints
% kth column is -1 if iLk <= 0, 1 if iLk >= 0, 0 if iLk == 0
% then add a 0 in the 8th column
%
% Example: iL1, iL4 == 0; iL2, iL3 >= 0; iL5, iL6a, iL6b <= 0
% [0 1 1 0 -1 -1 -1 0]

top = [1 -1 0 0 0 1 1 0 ;  1 1 0 -1 -1 -1 0 0];     % Current
    configuration corresponds to Vin-Vout, Zero, Vout



% NO NEED TO EDIT BELOW THIS LINE
%-------------------------------------


```

```
% Equivalent Resonant Circuit Setup

Ceff = C*Cp/(C+Cp);
V = [Vin, Vout];

Va = dot(V,top(1,1:2));
Vz = dot(V,top(1,3:4));
Vb = dot(V,top(1,5:6));
Vss = dot(V,top(1,7:8));


% Sweep for Solution with Desired Power

sol = false;

while(sol==false)

Vs = Vs7_n;

fprintf("---------- NEW RUN ---------- \n\n")


% Variables and Assumptions

syms  iL1 iL2 iL3 iL4 iL5 iL6a iL6b vr1 vr2 vr3 vr4 vr5 vr6a vr6b a b

vr = [vr1 vr2 vr3 vr4 vr5 vr6a vr6b];
iL = [iL1 iL2 iL3 iL4 iL5 iL6a iL6b];
assume(vr1,'real');
assume(iL.*top(2,1:7) > 0);

fixed_i = iL(top(2,1:7)==0);
free_i = iL(top(2,1:7)~=0);
free_v = vr(1:6);
```

```
fixed_v = vr(7);
fixed_sv = [fixed_i fixed_v];


% Equations Setup

eqns = [

            (vr1-Va)^2 + (L/C)*iL1^2 == (vr2 - Va)^2 + (L/C)*iL2^2,... % 1
            ...
            Cp*(Va)^2 + C*vr2^2 + L*iL2^2 == Cp*Vz^2 + C*vr3^2 + L*iL3^2,
   ... % 2
            Cp*(Vz-Va) ==  -C*(vr3 - vr2), ...
            ...
            (vr3-Vz)^2 + (L/C)*iL3^2 == (vr4 - Vz)^2 + (L/C)*iL4^2, ... %
   3
            ...
            Cp*(Vz)^2 + C*vr4^2 + L*iL4^2 == Cp*Vb^2 + C*vr5^2 + L*iL5^2,
   ...  % 4
            Cp*(Vb-Vz) ==  -C*(vr5 - vr4), ...
            ...
            (vr5-Vb)^2 + (L/C)*iL5^2 == (vr6a - Vb)^2 + (L/C)*iL6a^2, ...
   % 5
            ...
            Cp*Vb^2 + C*vr6a^2 + L*iL6a^2 == Cp*(Vss)^2 + C*vr6b^2 + L*
   iL6b^2, ... % 6a
            Cp*(Vss-Vb) == -C*(vr6b - vr6a), ...
            ...
            Cp*Vss^2 + C*vr6b^2 + L*iL6b^2 == Cp*(Va)^2 + C*vr1^2 + L*iL1
   ^2, ... % 6b
            Cp*(Va-Vss) == -C*(vr1 - vr6b), ...
            ...
            ...
            ...% Initial conditions and constraints
```

```
            ...
            vr6b == Vs, ...
            ...%-Eout/Ts == power,...
            fixed_i == 0 ...
            ];


% Solve System of Equations

fprintf("\nStarting ideal solver\n\n")

vars = [vr1 vr2 vr3 vr4 vr5 vr6a vr6b iL1 iL2 iL3 iL4 iL5 iL6a iL6b];
[svr1, svr2, svr3, svr4, svr5, svr6a, svr6b, siL1, siL2, siL3, siL4, siL5,
    siL6a, siL6b] = solve(eqns,vars);


% Load Output Variables

svr = [svr1,svr2,svr3,svr4,svr5,svr6a,svr6b];
siL = [siL1, siL2, siL3, siL4, siL5, siL6a, siL6b];


% Resonant Angles

theta1 = atan2(norm(cross([(svr(1)-Va),siL(1)*sqrt(L/C),0],[(svr(2)-Va),
   siL(2)*sqrt(L/C),0])),dot([(svr(1)-Va),siL(1)*sqrt(L/C),0],[(svr(2)-Va)
   ,siL(2)*sqrt(L/C),0]));
theta2 = atan2(norm(cross([(Va-svr(2)),siL(2)*sqrt(L/Ceff),0],[(Vz-svr(3))
   ,siL(3)*sqrt(L/Ceff),0])),dot([(Va-svr(2)),siL(2)*sqrt(L/Ceff),0],[(Vz-
   svr(3)),siL(3)*sqrt(L/Ceff),0]));
theta3 = atan2(norm(cross([(svr(3)-Vz),siL(3)*sqrt(L/C),0],[(svr(4)-Vz),
   siL(4)*sqrt(L/C),0])),dot([(svr(3)-Vz),siL(3)*sqrt(L/C),0],[(svr(4)-Vz)
   ,siL(4)*sqrt(L/C),0]));
theta4 = atan2(norm(cross([(Vz-svr(4)),siL(4)*sqrt(L/Ceff),0],[(Vb-svr(5))
```

```
    ,siL(5)*sqrt(L/Ceff),0])),dot([(Vz-svr(4)),siL(4)*sqrt(L/Ceff),0],[(Vb-
    svr(5)),siL(5)*sqrt(L/Ceff),0]));
theta5 = atan2(norm(cross([(svr(5)-Vb),siL(5)*sqrt(L/C),0],[(svr(6)-Vb),
    siL(6)*sqrt(L/C),0])),dot([(svr(5)-Vb),siL(5)*sqrt(L/C),0],[(svr(6)-Vb)
    ,siL(6)*sqrt(L/C),0]));
theta6a = atan2(norm(cross([(Vb-svr(6)),siL(6)*sqrt(L/Ceff),0],[(Vss-svr
    (7)),siL(7)*sqrt(L/Ceff),0])),dot([(Vb-svr(6)),siL(6)*sqrt(L/Ceff)
    ,0],[(Vss-svr(7)),siL(7)*sqrt(L/Ceff),0]));
theta6b = atan2(norm(cross([(Vss-svr(7)),siL(7)*sqrt(L/Ceff),0],[(Va-svr
    (1)),siL(1)*sqrt(L/Ceff),0])),dot([(Vss-svr(7)),siL(7)*sqrt(L/Ceff)
    ,0],[(Va-svr(1)),siL(1)*sqrt(L/Ceff),0]));

theta = [theta1,theta2,theta3,theta4,theta5,theta6a,theta6b];


% Switching Times

t1 = theta1*sqrt(L*C);
t2 = theta2*sqrt(L*Ceff);
t3 = theta3*sqrt(L*C);
t4 = theta4*sqrt(L*Ceff);
t5 = theta5*sqrt(L*C);
t6a = theta6a*sqrt(L*Ceff);
t6b = theta6b*sqrt(L*Ceff);

fnew = 1./(t1+t2+t3+t4+t5+t6a+t6b);
T = [t1, t2, t3, t4, t5, t6a, t6b];


% Display

% vpa(svr)
% vpa(siL)
% vpa(T)
```

```
178
179 fprintf('Ideal switching times:\n')
180 fprintf('.param t1 = %e\n',double(t1))
181 fprintf('.param t2 = %e\n',double(t2))
182 fprintf('.param t3 = %e\n',double(t3))
183 fprintf('.param t4 = %e\n',double(t4))
184 fprintf('.param t5 = %e\n',double(t5))
185 fprintf('.param t6 = %e\n',double(t6a))
186 fprintf('.param t7 = %e\n\n',double(t6b))
187
188
189
190  %% LOSSY SOLVER
191
192 fprintf("Starting exact solver\n\n")
193
194
195 % Variables and Assumptions
196
197 syms Vp(t) Vs(t) iL(t) VinS1 Vs0S1 iL0S1 VinS2 Vs0S2 iL0S2 CpS CsS LSS VS
       RS VaS VbS VzS VssS;
198 assume([CpS, CsS, LSS, RS] > 0);
199 assumeAlso([VinS1 Vs0S1 iL0S1 VinS2 Vs0S2 iL0S2 CpS CsS LSS VS RS], 'real'
       );
200
201 sfixed_i = siL(top(2,1:7)==0);
202 sfixed_v = svr(7);
203 sfixed_sv = [sfixed_i sfixed_v];
204
205 sfree_i = vpa(siL(top(2,1:7)~=0));
206 sfree_v = vpa(svr(1:6));
207
208 VsS = [vr1 vr2 vr3 vr4 vr5 vr6a vr6b];
209 iLS = [iL1 iL2 iL3 iL4 iL5 iL6a iL6b];
```

```
tS = sym('t',[1,7]);


% Solve Differential Equations for Connected Stages

eqns1 = [diff(Vp,t) == 0, diff(Vs,t) == iL/CsS, diff(iL, t) == Vp/LSS - Vs
    /LSS - RS/LSS*iL];
cond1 = [Vp(0) == VinS1, Vs(0) == Vs0S1, iL(0) == iL0S1];
stage1d = dsolve(eqns1, cond1);


% Solve Differential Equations for Open Stages

eqns2 = [diff(Vp,t) == -iL/CpS, diff(Vs,t) == iL/CsS, diff(iL,t) == Vp/LSS
    -Vs/LSS-RS/LSS*iL];
cond2 = [Vp(0) == VinS2, Vs(0) == Vs0S2, iL(0) == iL0S2];
stage2d = dsolve(eqns2, cond2);


% Equations Setup

eqns = zeros(1,15,'sym');

eqns(1) = VsS(2) - subs(stage1d.Vs,[Vs0S1, iL0S1, VinS1,t],[VsS(1), iLS(1)
    , VaS, tS(1)]);
eqns(2) = iLS(2) - subs(stage1d.iL,[Vs0S1, iL0S1, VinS1,t],[VsS(1), iLS(1)
    , VaS, tS(1)]);

eqns(3) = VsS(3) - subs(stage2d.Vs,[Vs0S2, iL0S2, VinS2,t],[VsS(2), iLS(2)
    , VaS, tS(2)]);
eqns(4) = iLS(3) - subs(stage2d.iL,[Vs0S2, iL0S2, VinS2,t],[VsS(2), iLS(2)
    , VaS, tS(2)]);
eqns(5) = VzS - subs(stage2d.Vp,[Vs0S2, iL0S2, VinS2,t],[VsS(2), iLS(2),
    VaS, tS(2)]);
```

```
237
238 eqns(6) = VsS(4) - subs(stage1d.Vs,[Vs0S1, iL0S1, VinS1,t],[VsS(3), iLS(3)
        , VzS, tS(3)]);
239 eqns(7) = iLS(4) - subs(stage1d.iL,[Vs0S1, iL0S1, VinS1,t],[VsS(3), iLS(3)
        , VzS, tS(3)]);
240
241 eqns(8) = VsS(5) - subs(stage2d.Vs,[Vs0S2, iL0S2, VinS2,t],[VsS(4), iLS(4)
        , VzS, tS(4)]);
242 eqns(9) = iLS(5) - subs(stage2d.iL,[Vs0S2, iL0S2, VinS2,t],[VsS(4), iLS(4)
        , VzS, tS(4)]);
243 eqns(10) = VbS - subs(stage2d.Vp,[Vs0S2, iL0S2, VinS2,t],[VsS(4), iLS(4),
        VzS, tS(4)]);
244
245 eqns(11) = VsS(6) - subs(stage1d.Vs,[Vs0S1, iL0S1, VinS1,t],[VsS(5), iLS
        (5), VbS, tS(5)]);
246 eqns(12) = iLS(6) - subs(stage1d.iL,[Vs0S1, iL0S1, VinS1,t],[VsS(5), iLS
        (5), VbS, tS(5)]);
247
248 eqns(13) = VsS(7) - subs(stage2d.Vs,[Vs0S2, iL0S2, VinS2,t],[VsS(6), iLS
        (6), VbS, tS(6)]);
249 eqns(14) = iLS(7) - subs(stage2d.iL,[Vs0S2, iL0S2, VinS2,t],[VsS(6), iLS
        (6), VbS, tS(6)]);
250 eqns(15) = VssS - subs(stage2d.Vp,[Vs0S2, iL0S2, VinS2,t],[VsS(6), iLS(6),
         VbS, tS(6)]);
251
252 eqns(16) = VsS(1) - subs(stage2d.Vs,[Vs0S2, iL0S2, VinS2,t],[VsS(7), iLS
        (7), VssS, tS(7)]);
253 eqns(17) = iLS(1) - subs(stage2d.iL,[Vs0S2, iL0S2, VinS2,t],[VsS(7), iLS
        (7), VssS, tS(7)]);
254 eqns(18) = VaS - subs(stage2d.Vp,[Vs0S2, iL0S2, VinS2,t],[VsS(7), iLS(7),
        VssS, tS(7)]);
255
256 eqns_n = subs(eqns,[CpS CsS LSS RS VaS VzS VbS VssS fixed_sv],[Cp C L R Va
         Vz Vb Vss sfixed_sv]);
```

```
257
258
259 % Variables and Guess Setup
260
261 guess = [sfree_v sfree_i T];
262 solve_vars = [free_v free_i tS];
263
264
265 % Numerically Solve System of Equations
266
267 out = vpasolve(eqns_n,solve_vars,guess);
268
269
270 % Load Output Variables
271
272 if in(vr1,fixed_sv)
273     Vs0 = svr(1);
274 else
275     Vs0 = out.vr1;
276 end
277
278 if in(vr2,fixed_sv)
279     Vs1 = svr(2);
280 else
281     Vs1 = out.vr2;
282 end
283
284 if in(vr3,fixed_sv)
285     Vs2 = svr(3);
286 else
287     Vs2 = out.vr3;
288 end
289
290 if in(vr4,fixed_sv)
```

```
    Vs3 = svr(4);
else
    Vs3 = out.vr4;
end

if in(vr5,fixed_sv)
    Vs4 = svr(5);
else
    Vs4 = out.vr5;
end

if in(vr6a,fixed_sv)
    Vs5 = svr(6);
else
    Vs5 = out.vr6a;
end

if in(vr6b,fixed_sv)
    Vs5b = svr(7);
else
    Vs5b = out.vr6b;
end

if in(iL1,fixed_sv)
    iL0 = siL(1);
else
    iL0 = out.iL1;
end

if in(iL2,fixed_sv)
    iL1 = siL(2);
else
    iL1 = out.iL2;
end
```

```
325
326 if in(iL3,fixed_sv)
327     iL2 = siL(3);
328 else
329     iL2 = out.iL3;
330 end
331
332 if in(iL4,fixed_sv)
333     iL3 = siL(4);
334 else
335     iL3 = out.iL4;
336 end
337
338 if in(iL5,fixed_sv)
339     iL4 = siL(5);
340 else
341     iL4 = out.iL5;
342 end
343
344 if in(iL6a,fixed_sv)
345     iL5 = siL(6);
346 else
347     iL5 = out.iL6a;
348 end
349
350 if in(iL6b,fixed_sv)
351     iL5b = siL(7);
352 else
353     iL5b = out.iL6b;
354 end
355
356 t1 = out.t1;
357 t2 = out.t2;
358 t3 = out.t3;
```

```
t4 = out.t4;
t5 = out.t5;
t6a = out.t6;
t6b = out.t7;

Vs_n = [Vs0, Vs1, Vs2, Vs3, Vs4, Vs5, Vs5b];
iL_n = [iL0, iL1, iL2, iL3, iL4, iL5, iL5b];
t_n = [t1, t2, t3 , t4, t5, t6a, t6b];


% Current Integration

i_int = int(stage1d.iL,t,0,t);
I1 = subs(i_int,[VinS1, Vs0S1, iL0S1, CpS, CsS, LSS, RS, t], [Va, Vs0, iL0
    , Cp, C, L, R, t1]);
I3 = subs(i_int,[VinS1, Vs0S1, iL0S1, CpS, CsS, LSS, RS, t], [Vz, Vs2, iL2
    , Cp, C, L, R, t3]);
I5 = subs(i_int,[VinS1, Vs0S1, iL0S1, CpS, CsS, LSS, RS, t], [Vb, Vs4, iL4
    , Cp, C, L, R, t5]);


% Display Operating Point

fprintf("Solution @ Vin = %d, Vout = %d, initial condition vc1 = %d:\n",
    Vin,Vout,Vs_n(7))

Eout = -Vout*dot(top(1,:),[0 I1 0 I3 0 I5 0 0]);
Ein = Vin*dot(top(1,:),[I1 0 I3 0 I5 0 0 0]);
pd = t1+t2+t3+t4+t5+t6a+t6b;
pwr = double(Eout/pd);
eff = Eout/Ein;
lossratio = 1/eff-1;

fprintf('Power = %e W\n', pwr)
```

```
fprintf('Frequency = %e Hz\n', 1/pd)
fprintf('Efficiency = %e\n', eff)
fprintf('Loss Ratio = %e\n\n', lossratio)


% Display Switching Times

fprintf('Exact switching times:\n')
fprintf('.param t1 = %e\n',double(t1))
fprintf('.param t2 = %e\n',double(t2))
fprintf('.param t3 = %e\n',double(t3))
fprintf('.param t4 = %e\n',double(t4))
fprintf('.param t5 = %e\n',double(t5))
fprintf('.param t6 = %e\n',double(t6a))
fprintf('.param t7 = %e\n\n',double(t6b))


% Sweep IC for Correct Power

fprintf('Power compare: %e\n', pwr/power);

if pwr > 1.005*power
    Vs7_n = .9925*Vs7_n;
elseif pwr < .995*power
    Vs7_n = 1.0031*Vs7_n;
else
    sol = true;
end



end

```

```
423
424
425 function b = in(v,a)
426 b = any(v==a);
427 end
```

A.1.2 Piezoelectric-Transformer-Based Switching Sequence

This appendix contains a MATLAB script that solves for the periodic steady-state solution of a PT-based switching sequence. The script assumes one of eight possible segment orders (described in Section 3.4.1) for the V_{in}, -V_{in} | V_{out}, -V_{out}, *Zero+* switching sequence. No solution is returned outside of this segment order's operating region even if a solution for the switching sequence exists, so the script must be reconfigured for different segment orders. This solver requires an initial condition for the PR's resonant capacitor voltage, which may be estimated using the amplitude of resonance model. Like the solver for PR-based switching sequences in Section A.1.1, this script first solves for the ideal periodic steady-state solution (detailed in Section 3.4.3) and then uses the solution as a starting point for solving the exact solution (detailed in Section 3.4.5). Further, this script computes switching times, output power, and efficiency in addition to the PR's states for the exact periodic steady-state solution.

This script is utilized as-is to compute switching times for the simulation in Section A.2.2.

```
1 %% Periodic Steady State Solution Script for PT-based Switching Sequence
2 %% Authors: Jessica Boles and Joshua Piel
3 % Assumed switching sequence: Vin, -Vin, | Vout, -Vout, Zero+
4 % Note: This script assumes one of eight potential segment orderings for
5 % this switching sequence. If this script fails to find a solution, a
6 % solution may still exist with a different segment order.
7
8
9 % PT Parameters
```

```
10
11 CpA = 8.02e-10;          % F
12 CpBo = 2.78e-9;          % F (enter the CpB as modeled)
13 L = 5.33e-5;             % H
14 C = 6.72e-11;            % F
15 R = .543;                % ohm
16 N = .288;
17
18
19 % Operating Point Specification
20
21 Vin = 100;               % V
22 Vout = 20;               % V
23 Pout = 100;              % W (Desired power - only used to calculate
       initial condition)
24 effexp = .9739;          % (Expected efficiency - only used to calculate
       initial condition)
25 f = 2.77e6;              % (Expected frequency - only used to calculate
       initial condition)
26
27
28
29 % NO NEED TO EDIT BELOW THIS LINE
30 %-----------------------------------
31
32
33 % Initial Condition
34
35 Pin = Pout/effexp;
36 IL = pi*(Pin/(2*Vin) + 2*f*CpA*Vin);
37 Vc1_n = Vin - sqrt(L/C)*IL;
38
39
40 % Equivalent Resonant Circuit Setup
```

```
41
42 CpB = CpBo*N^2;
43 CeffA = C*CpA/(C+CpA);
44 CeffB = C*CpB/(C+CpB);
45 %Ceff3 = C*Cp1*Cp2*N^2/(C+Cp1+Cp2*N^2);
46
47 Vpin1 = Vin;
48 Vpin2 = Vin;
49 Vpin3 = Vin;
50 Vpin4 = Vin;
51 Vpin5 = Vin;
52 Vpin6 = -Vin;
53 Vpin7 = -Vin;
54 Vpin8 = -Vin;
55
56 Vpout1 = -Vout/N;
57 Vpout2 = 0;
58 Vpout3 = 0;
59 Vpout4 = Vout/N;
60 Vpout5 = Vout/N;
61 Vpout6 = Vout/N;
62 Vpout7 = -Vout/N;
63 Vpout8 = -Vout/N;
64
65 V1 = Vpin1;
66 V2 = Vpin2-Vpout2;
67 V3 = Vpin3;
68 V4 = Vpin4-Vpout4;
69 V5 = -Vpout5;
70 V6 = Vpin6;
71 V7 = Vpin7-Vpout7;
72 V8 = -Vpout8;
73
74
```

```
% Variables and Assumptions

syms  iL1 iL2 iL3 iL4 iL5 iL6 iL7 iL8  vc1 vc2 vc3 vc4 vc5 vc6 vc7 vc8

assume(iL1 == 0);
assume(iL2 >= 0);
assume(iL3 >= 0);
assume(iL4 >= 0);
assume(iL5 >= 0);
assume(iL6 == 0);
assume(iL7 <= 0);
assume(iL8 <= 0);
assume(vc1 == Vc1_n);
assumeAlso(vc2>vc1);
assumeAlso(vc3>vc2);
assumeAlso(vc4>vc3);
assumeAlso(vc5>vc4);
assumeAlso(vc6>vc5);
assumeAlso(vc7<vc6);
assumeAlso(vc8<vc7);


% Equations Setup

eqns = [

          ((vc1+Vpout1) - V1)^2 + (L/CeffB)*iL1^2 == ((vc2 +Vpout2) - V1)
   ^2 + (L/CeffB)*iL2^2, % 1
          CpB*(Vpout2-Vpout1) ==  C*(vc2 - vc1),

          (vc2-V2)^2 + (L/C)*iL2^2 == (vc3 - V2)^2 + (L/C)*iL3^2, % 2

          ((vc3+Vpout3) - V3)^2 + (L/CeffB)*iL3^2 == ((vc4 +Vpout4) - V3)
   ^2 + (L/CeffB)*iL4^2, % 3
```

```
107             CpB*(Vpout4-Vpout3) ==  C*(vc4 - vc3),
108
109             (vc4-V4)^2 + (L/C)*iL4^2 == (vc5 - V4)^2 + (L/C)*iL5^2, % 4
110
111             ((vc5-Vpin5)- V5)^2 + (L/CeffA)*iL5^2 == ((vc6-Vpin6) - V5)^2 +
    (L/CeffA)*iL6^2, % 5
112             CpA*(Vpin6-Vpin5) ==  -C*(vc6 - vc5),
113
114             ((vc6+Vpout6) - V6)^2 + (L/CeffB)*iL6^2 == ((vc7 +Vpout7) - V6)
   ^2 + (L/CeffB)*iL7^2, % 6
115             CpB*(Vpout7-Vpout6) ==  C*(vc7 - vc6),
116
117             (vc7-V7)^2 + (L/C)*iL7^2 == (vc8 - V7)^2 + (L/C)*iL8^2, % 7
118
119             ((vc8-Vpin8)- V8)^2 + (L/CeffA)*iL8^2 == ((vc1-Vpin1) - V8)^2 +
    (L/CeffA)*iL1^2, % 8
120             CpA*(Vpin1-Vpin8) ==  -C*(vc1 - vc8),
121
122              ];
123
124
125 % Solve System of Equations
126
127 fprintf("\nStarting ideal solver\n\n")
128
129 vars = [vc1 vc2 vc3 vc4 vc5 vc6 vc7 vc8 iL1 iL2 iL3 iL4 iL5 iL6 iL7 iL8];
130 [svc1, svc2, svc3, svc4, svc5, svc6, svc7, svc8, siL1, siL2, siL3, siL4,
    siL5, siL6, siL7, siL8] = solve(eqns,vars,'Real',true) ;
131
132
133 % Load Output Variables
134
135 svc = double([svc1, svc2, svc3, svc4, svc5, svc6, svc7, svc8]);
136 siL = double([siL1, siL2, siL3, siL4, siL5, siL6, siL7, siL8]);
```

```
137
138 %scatter (svc, siL)
139
140
141 % Resonant Angles
142
143 U2 = [svc(2)-V2, siL(2)*sqrt(L/C), 0 ];
144 U3 = [svc(3)-V2, siL(3)*sqrt(L/C), 0 ];
145 U4 = [svc(4)-V4, siL(4)*sqrt(L/C), 0 ];
146 U5 = [svc(5)-V4, siL(5)*sqrt(L/C), 0 ];
147 U7 = [svc(7)-V7, siL(7)*sqrt(L/C), 0 ];
148 U8 = [svc(8)-V7, siL(8)*sqrt(L/C), 0 ];
149
150 U5A = [svc(5)+Vpout5-Vpin5, siL(5)*sqrt(L/CeffA), 0 ];
151 U6A = [svc(6)+Vpout6-Vpin6, siL(6)*sqrt(L/CeffA), 0 ];
152 U8A = [svc(8)+Vpout8-Vpin8, siL(8)*sqrt(L/CeffA), 0 ];
153 U1A = [svc(1)+Vpout1-Vpin1, siL(1)*sqrt(L/CeffA), 0 ];
154
155 U1B = [svc(1)+Vpout1-Vpin1, siL(1)*sqrt(L/CeffB), 0 ];
156 U2B = [svc(2)+Vpout2-Vpin2, siL(2)*sqrt(L/CeffB), 0 ];
157 U3B = [svc(3)+Vpout3-Vpin3, siL(3)*sqrt(L/CeffB), 0 ];
158 U4B = [svc(4)+Vpout4-Vpin4, siL(4)*sqrt(L/CeffB), 0 ];
159 U6B = [svc(6)+Vpout6-Vpin6, siL(6)*sqrt(L/CeffB), 0 ];
160 U7B = [svc(7)+Vpout7-Vpin7, siL(7)*sqrt(L/CeffB), 0 ];
161
162 theta1 = atan2(norm(cross(U1B,U2B)),dot(U1B,U2B));
163 theta2 = atan2(norm(cross(U2,U3)),dot(U2,U3));
164 theta3 = atan2(norm(cross(U3B,U4B)),dot(U3B,U4B));
165 theta4 = atan2(norm(cross(U4,U5)),dot(U4,U5));
166 theta5 = atan2(norm(cross(U5A,U6A)),dot(U5A,U6A));
167 theta6 = atan2(norm(cross(U6B,U7B)),dot(U6B,U7B));
168 theta7 = atan2(norm(cross(U7,U8)),dot(U7,U8));
169 theta8 = atan2(norm(cross(U8A,U1A)),dot(U8A,U1A));
170
```

```
theta = [theta1,theta2,theta3,theta4,theta5,theta6,theta7,theta8];


% Switching Times

t1 = theta1*sqrt(L*CeffB);
t2 = theta2*sqrt(L*C);
t3 = theta3*sqrt(L*CeffB);
t4 = theta4*sqrt(L*C);
t5 = theta5*sqrt(L*CeffA);
t6 = theta6*sqrt(L*CeffB);
t7 = theta7*sqrt(L*C);
t8 = theta8*sqrt(L*CeffA);

fnew = 1./(t1+t2+t3+t4+t5+t6+t7+t8);
T = [t1, t2, t3, t4, t5, t6, t7, t8];


% Display

%vpa(svc)
%vpa(siL)
%vpa(T)

fprintf('Ideal switching times:\n')
fprintf('.param t1 = %e\n',double(t1))
fprintf('.param t2 = %e\n',double(t2))
fprintf('.param t3 = %e\n',double(t3))
fprintf('.param t4 = %e\n',double(t4))
fprintf('.param t5 = %e\n',double(t5))
fprintf('.param t6 = %e\n',double(t6))
fprintf('.param t7 = %e\n',double(t7))
fprintf('.param t8 = %e\n\n',double(t8))

```

```
205
206 %% EXACT SOLVER
207
208 fprintf("Starting exact solver\n\n")
209
210
211 % Variables and Assumptions
212
213 syms VpA(t) VpB(t) Vc(t) iL(t)     VpAS1 VpBS1 VcS1 iLS1     VpAS2 VpBS2
    VcS2 iLS2     VpAS3 VpBS3 VcS3 iLS3      VpAS4 VpBS4 VcS4 iLS4      VS
    VaS VbS VzS VssS;
214 assumeAlso([VpAS1 VpBS1 VcS1 iLS1     VpAS2 VpBS2 VcS2 iLS2     VpAS3
    VpBS3 VcS3 iLS3      VpAS4 VpBS4 VcS4 iLS4     VS], 'real');
215
216 vcS = [Vc1_n vc2 vc3 vc4 vc5 vc6 vc7 vc8];
217 iLS = [0 iL2 iL3 iL4 iL5 0 iL7 iL8];
218 tS = sym('t',[1,8]);
219
220
221 % Solve Differential Equations for Connected CpA and Open CpB
222
223 eqns1 = [diff(VpA,t) == 0, diff(VpB,t) == iL/CpB, diff(Vc,t) == iL/C, diff
    (iL, t) == VpA/L - VpB/L - Vc/L - R/L*iL];
224 cond1 = [VpA(0) == VpAS1, VpB(0) == VpBS1, Vc(0) == VcS1, iL(0) == iLS1];
225 stage1d = dsolve(eqns1, cond1);
226
227
228 % Solve Differential Equations for Open CpA and Connected CpB
229
230 eqns2 = [diff(VpA,t) == -iL/CpA, diff(VpB,t) == 0, diff(Vc,t) == iL/C,
    diff(iL, t) == VpA/L - VpB/L - Vc/L - R/L*iL];
231 cond2 = [VpA(0) == VpAS2, VpB(0) == VpBS2, Vc(0) == VcS2, iL(0) == iLS2];
232 stage2d = dsolve(eqns2, cond2);
233
```

```
234
235 % Solve Differential Equations for Connected CpA and Connected CpB
236
237 eqns3 = [diff(VpA,t) == 0, diff(VpB,t) == 0, diff(Vc,t) == iL/C, diff(iL,
       t) == VpA/L - VpB/L - Vc/L - R/L*iL];
238 cond3 = [VpA(0) == VpAS3, VpB(0) == VpBS3, Vc(0) == VcS3, iL(0) == iLS3];
239 stage3d = dsolve(eqns3, cond3);
240
241
242 % Equation Setup
243
244 eqns = zeros(1,18,'sym');
245
246 eqns(1) = vcS(2) - subs(stage1d.Vc,[VpAS1 VpBS1 VcS1 iLS1 t],[Vpin1,
       Vpout1, vcS(1), iLS(1), tS(1)]);
247 eqns(2)= iLS(2) - subs(stage1d.iL,[VpAS1 VpBS1 VcS1 iLS1 t],[Vpin1, Vpout1
       , vcS(1), iLS(1), tS(1)]);
248 eqns(3) = Vpout2 - subs(stage1d.VpB,[VpAS1 VpBS1 VcS1 iLS1 t],[Vpin1,
       Vpout1, vcS(1), iLS(1), tS(1)]);
249
250 eqns(4) = vcS(3) - subs(stage3d.Vc,[VpAS3 VpBS3 VcS3 iLS3 t],[Vpin2,
       Vpout2, vcS(2), iLS(2), tS(2)]);
251 eqns(5)= iLS(3) - subs(stage3d.iL,[VpAS3 VpBS3 VcS3 iLS3 t],[Vpin2, Vpout2
       , vcS(2), iLS(2), tS(2)]);
252
253 eqns(6) = vcS(4) - subs(stage1d.Vc,[VpAS1 VpBS1 VcS1 iLS1 t],[Vpin3,
       Vpout3, vcS(3), iLS(3), tS(3)]);
254 eqns(7)= iLS(4) - subs(stage1d.iL,[VpAS1 VpBS1 VcS1 iLS1 t],[Vpin3, Vpout3
       , vcS(3), iLS(3), tS(3)]);
255 eqns(8) = Vpout4 - subs(stage1d.VpB,[VpAS1 VpBS1 VcS1 iLS1 t],[Vpin3,
       Vpout3, vcS(3), iLS(3), tS(3)]);
256
257 eqns(9) = vcS(5) - subs(stage3d.Vc,[VpAS3 VpBS3 VcS3 iLS3 t],[Vpin4,
       Vpout4, vcS(4), iLS(4), tS(4)]);
```

```
eqns(10)= iLS(5) - subs(stage3d.iL,[VpAS3 VpBS3 VcS3 iLS3 t],[Vpin4,
    Vpout4, vcS(4), iLS(4), tS(4)]);

eqns(11)= vcS(6) - subs(stage2d.Vc,[VpAS2 VpBS2 VcS2 iLS2 t],[Vpin5,
    Vpout5, vcS(5), iLS(5), tS(5)]);
eqns(12)= iLS(6) - subs(stage2d.iL,[VpAS2 VpBS2 VcS2 iLS2 t],[Vpin5,
    Vpout5, vcS(5), iLS(5), tS(5)]);
eqns(13)= Vpin6 - subs(stage2d.VpA,[VpAS2 VpBS2 VcS2 iLS2 t],[Vpin5,
    Vpout5, vcS(5), iLS(5), tS(5)]);

eqns(14) = vcS(7) - subs(stage1d.Vc,[VpAS1 VpBS1 VcS1 iLS1 t],[Vpin6,
    Vpout6, vcS(6), iLS(6), tS(6)]);
eqns(15)= iLS(7) - subs(stage1d.iL,[VpAS1 VpBS1 VcS1 iLS1 t],[Vpin6,
    Vpout6, vcS(6), iLS(6), tS(6)]);
eqns(16) = Vpout7 - subs(stage1d.VpB,[VpAS1 VpBS1 VcS1 iLS1 t],[Vpin6,
    Vpout6, vcS(6), iLS(6), tS(6)]);

eqns(17) = vcS(8) - subs(stage3d.Vc,[VpAS3 VpBS3 VcS3 iLS3 t],[Vpin7,
    Vpout7, vcS(7), iLS(7), tS(7)]);
eqns(18)= iLS(8) - subs(stage3d.iL,[VpAS3 VpBS3 VcS3 iLS3 t],[Vpin7,
    Vpout7, vcS(7), iLS(7), tS(7)]);

eqns(19)= vcS(1) - subs(stage2d.Vc,[VpAS2 VpBS2 VcS2 iLS2 t],[Vpin8,
    Vpout8, vcS(8), iLS(8), tS(8)]);
eqns(20)= iLS(1) - subs(stage2d.iL,[VpAS2 VpBS2 VcS2 iLS2 t],[Vpin8,
    Vpout8, vcS(8), iLS(8), tS(8)]);
eqns(21)= Vpin1 - subs(stage2d.VpA,[VpAS2 VpBS2 VcS2 iLS2 t],[Vpin8,
    Vpout8, vcS(8), iLS(8), tS(8)]);


% Variables and Guess Setup

guess = [vpa(svc(2:8)) vpa(siL(siL(1:8)~=0)) T];
solve_vars = [vcS(2:8) [iL2 iL3 iL4 iL5 iL7 iL8] tS];
```

```
280
281
282 % Numerically Solve System of Equations
283
284 out = vpasolve(eqns,solve_vars,guess);
285
286
287 % Load Output Variables
288
289 Vc0 = svc(1);
290 Vc1 = out.vc2;
291 Vc2 = out.vc3;
292 Vc3 = out.vc4;
293 Vc4 = out.vc5;
294 Vc5 = out.vc6;
295 Vc6 = out.vc7;
296 Vc7 = out.vc8;
297
298 iL0 = siL(1);
299 iL1 = out.iL2;
300 iL2 = out.iL3;
301 iL3 = out.iL4;
302 iL4 = out.iL5;
303 iL5 = siL(6);
304 iL6 = out.iL7;
305 iL7 = out.iL8;
306
307 t1 = out.t1;
308 t2 = out.t2;
309 t3 = out.t3;
310 t4 = out.t4;
311 t5 = out.t5;
312 t6 = out.t6;
313 t7 = out.t7;
```

```
t8 = out.t8;

Vs_n = [Vc0, Vc1, Vc2, Vc3, Vc4, Vc5, Vc6, Vc7];
iL_n = [iL0, iL1, iL2, iL3, iL4, iL5, iL6, iL7];
t_n = [t1, t2, t3 , t4, t5, t6, t7, t8];


% Current Integration

i_int1 = int(stage1d.iL,t,0,t);
i_int2 = int(stage2d.iL,t,0,t);
i_int3 = int(stage3d.iL,t,0,t);

I1 = subs(i_int1,[VpAS1 VpBS1 VcS1 iLS1 t],[Vpin1, Vpout1, Vc0, iL0, t1]);
I2 = subs(i_int3,[VpAS3 VpBS3 VcS3 iLS3 t],[Vpin2, Vpout2, Vc1, iL1, t2]);
I3 = subs(i_int1,[VpAS1 VpBS1 VcS1 iLS1 t],[Vpin3, Vpout3, Vc2, iL2, t3]);
I4 = subs(i_int3,[VpAS3 VpBS3 VcS3 iLS3 t],[Vpin4, Vpout4, Vc3, iL3, t4]);
I5 = subs(i_int2,[VpAS2 VpBS2 VcS2 iLS2 t],[Vpin5, Vpout5, Vc4, iL4, t5]);
I6 = subs(i_int1,[VpAS1 VpBS1 VcS1 iLS1 t],[Vpin6, Vpout6, Vc5, iL5, t6]);
I7 = subs(i_int3,[VpAS3 VpBS3 VcS3 iLS3 t],[Vpin7, Vpout7, Vc6, iL6, t7]);
I8 = subs(i_int2,[VpAS2 VpBS2 VcS2 iLS2 t],[Vpin8, Vpout8, Vc7, iL7, t8]);


% Display Operating Point

fprintf("Solution @ Vin = %d, Vout = %d, initial condition vc1 = %d:\n",
    Vin,Vout,Vc1_n)

Eout = Vout*(I4+I5)/N-Vout*(I7+I8)/N;
Ein = Vin*(I1+I2+I3+I4)-Vin*(I6+I7);
pd = t1+t2+t3+t4+t5+t6+t7+t8;
pwr = Eout/pd;
eff = Eout/Ein;

```

```
347 fprintf('Power = %e W\n', pwr)
348 fprintf('Frequency = %e Hz\n', 1/pd)
349 fprintf('Efficiency = %e\n\n', eff)
350
351
352 % Display Switching Times
353
354 fprintf('Exact switching times:\n')
355 fprintf('.param t1 = %e\n',double(t1))
356 fprintf('.param t2 = %e\n',double(t2))
357 fprintf('.param t3 = %e\n',double(t3))
358 fprintf('.param t4 = %e\n',double(t4))
359 fprintf('.param t5 = %e\n',double(t5))
360 fprintf('.param t6 = %e\n',double(t6))
361 fprintf('.param t7 = %e\n',double(t7))
362 fprintf('.param t8 = %e\n\n',double(t8))
```

A.2 Simulation Schematics

A.2.1 Piezoelectric-Resonator-Based Converter

This Appendix contains an example LTspice schematic for a PR-based dc-dc converter, shown in Fig. A-1. The schematic's switching times are configured for the V_{in}-V_{out}, *Zero*, V_{out}, intended to accompany the periodic steady-state solution script of Section A.1.1. When simulated, this schematic produces the waveforms of Fig. 9-2. If needed, the user may add a small quantity of inductance and resistance in series with the voltage source and load to minimize input/output current spikes.

A.2.2 Piezoelectric-Transformer-Based Converter

This Appendix contains an example LTspice schematic for a PT-based dc-dc converter, shown in Fig. A-2. The schematic's switching times are configured for the V_{in}, -V_{in} | V_{out}, -V_{out}, *Zero+*, intended to accompany the periodic steady-state solution script of Section A.1.2. We implement the PT model's ideal transformer with a pair of behavioral voltage sources rather than coupled inductors, which introduce additional dynamics. When simulated, this schematic produces the waveforms of Fig. 8-6. If needed, the user may add a small quantity of inductance and resistance in series with the voltage source and load to minimize input/output current spikes.

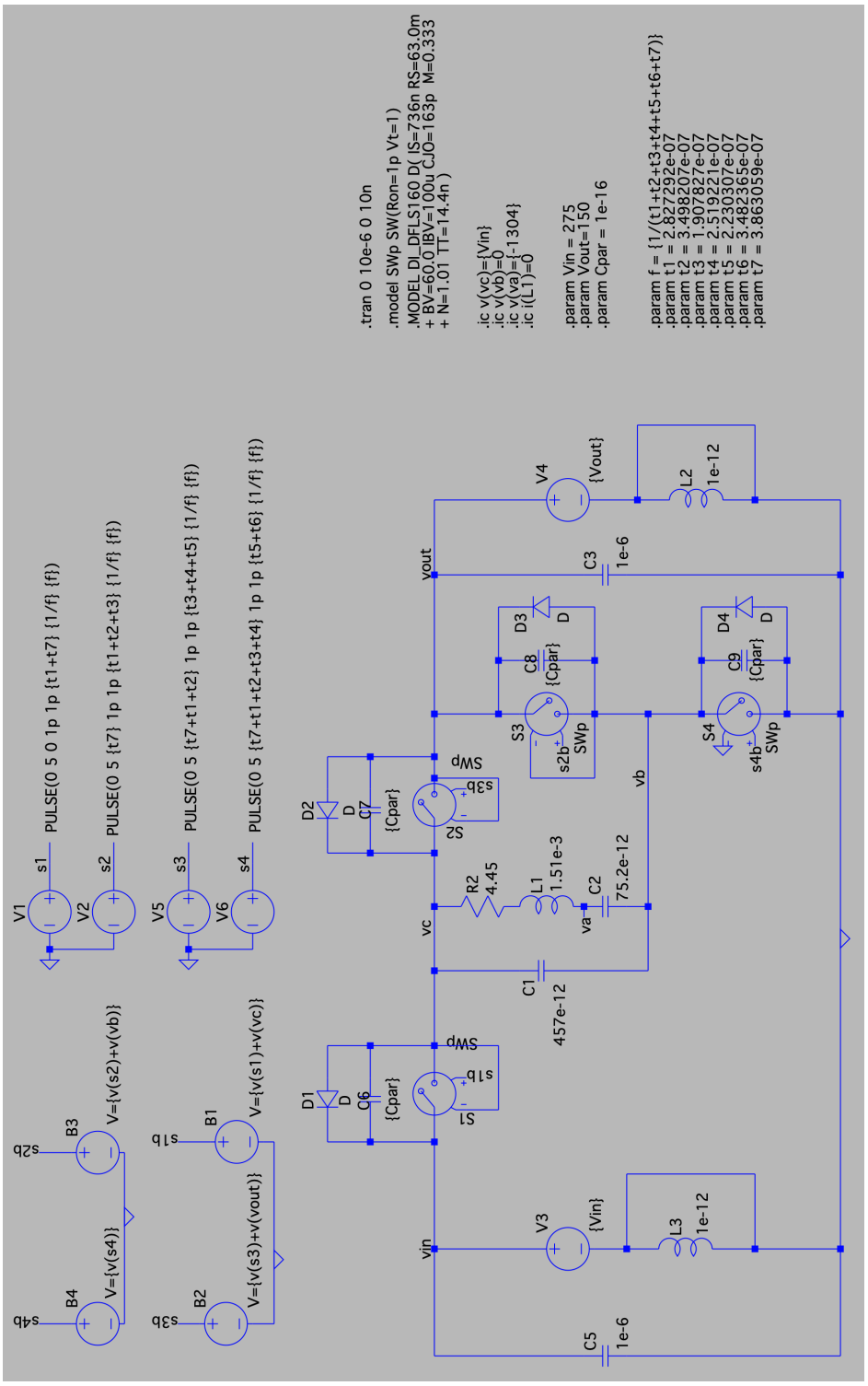

Figure A-1: PR-based converter simulation schematic.

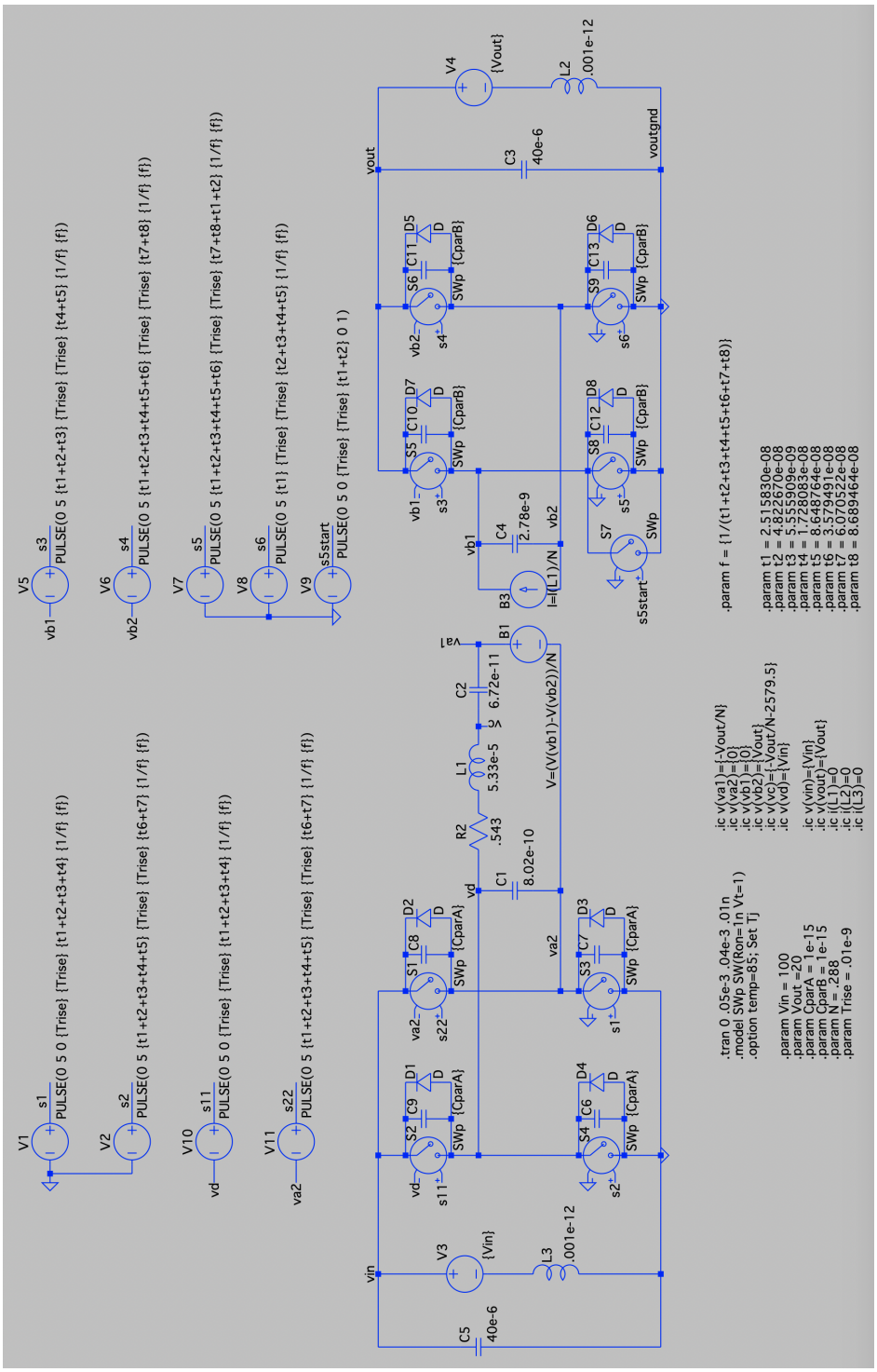

Figure A-2: PT-based converter simulation schematic.

A.3 Prototype Details

A.3.1 High-Efficiency PR-based DC-DC Converter

This appendix contains the parts list, schematic, and PCB layout for the PR-based dc-dc converter prototype utilized in Chapters 2 and 6. This prototype implements the topology of Fig. 2-17 with footprints for both switches and diodes for S3 and S4. Its layout is designed for low-frequency operation with space to test different PR sizes and mounting structures.

Table A.1: Parts List for High-Efficiency PR-Based Converter Prototype

Description	Part	Details	Quantity
PR	APC International 790	PZT, APC 844, disc, 19.8x0.8mm	1
FET	EPC2019	GaN, 200V, 8.5A	4
Diode	ON Semiconductor NRVTSA4100T3G	Schottky, 100V, 4A, SMA-2	2
Gate Driver	Texas Instruments UCC27611DRVT	6SON	4
Isolator	Silicon Labs SI8620BB-B-ISR	2.5kVrms, 2ch, 8SOIC	4
Bus Capacitor (Input)	TDK CGA9P4X7T2W105K250KA	Ceramic, 1μF, 450V, X7T, 2220	3
Bus Capacitor (Output)	TDK C5750X7S2A156M250KB	Ceramic, 15μF, 100V, X7S, 2220	1
Decoupling Capacitor (Switch Loops)	TDK C2012C0G2E102J085AA	Ceramic, 1nF, 250V, C0G, 0805	2
Decoupling Capacitor (Gate Circuitry)	Murata GRM21BR61E226ME44L	Ceramic, 22μF, 25V, X5R, 0805	16
Bootstrap Diode	ST Microelectronics STPS2200U	Schottky, 200V, 2A, SMB	2
Bootstrap Resistor	Vishay CRCW04021R00FKEDHP	1Ω, 1%, 1/5W, 0402	2
Gate Resistor	Panasonic ERJ-2GEJ4R7X	4.7Ω, 5% 1/10W, 0402	8
Power Terminal Socket	Phoenix Contact 1755752	4pos, vertical, 5.08mm	3
Control Terminal Header Pins	Amphenol 67997-208HLF	8pos, vertical, 2.54mm	2

The PCB layout files are displayed at 3x the prototype's scale, assuming a page size of 8.5x11 inches. This prototype was designed by Joshua Piel, and more information about it can be found in [93].

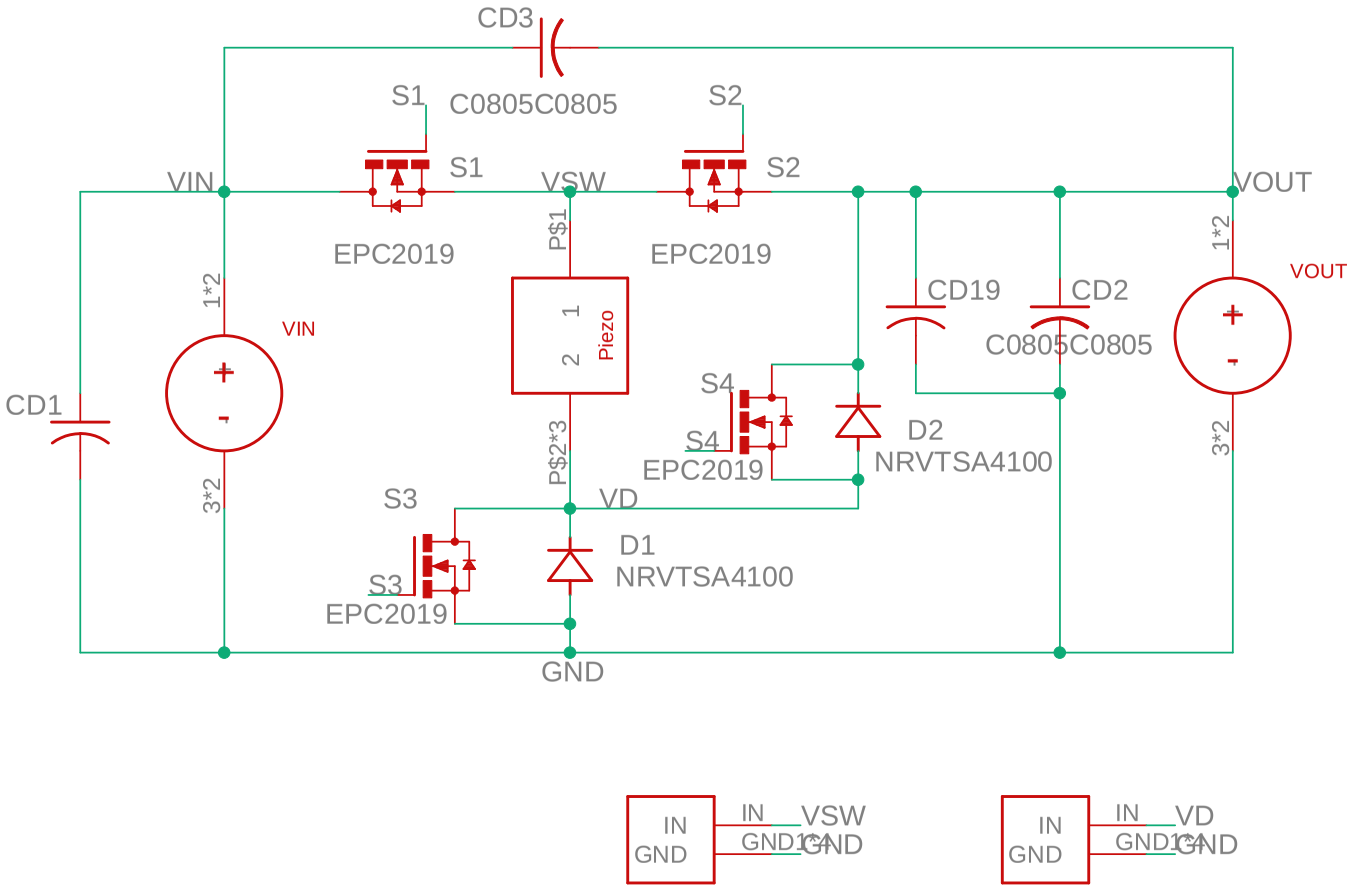
CD3
S1
C0805C0805
S2
VIN
S1
VSW
S2
VOUT
EPC2019
P$1
EPC2019
1*2
VIN
CD19
CD2
C0805C0805
1*2
VOUT
Piezo
2
1
CD1
S4
S4
EPC2019
D2
NRVTSA4100
P$2*3
3*2
3*2
S3
VD
D1
NRVTSA4100
S3
EPC2019
GND
IN
GND
IN
GND1
VSW
GND
IN
GND
IN
GND1
VD
GND

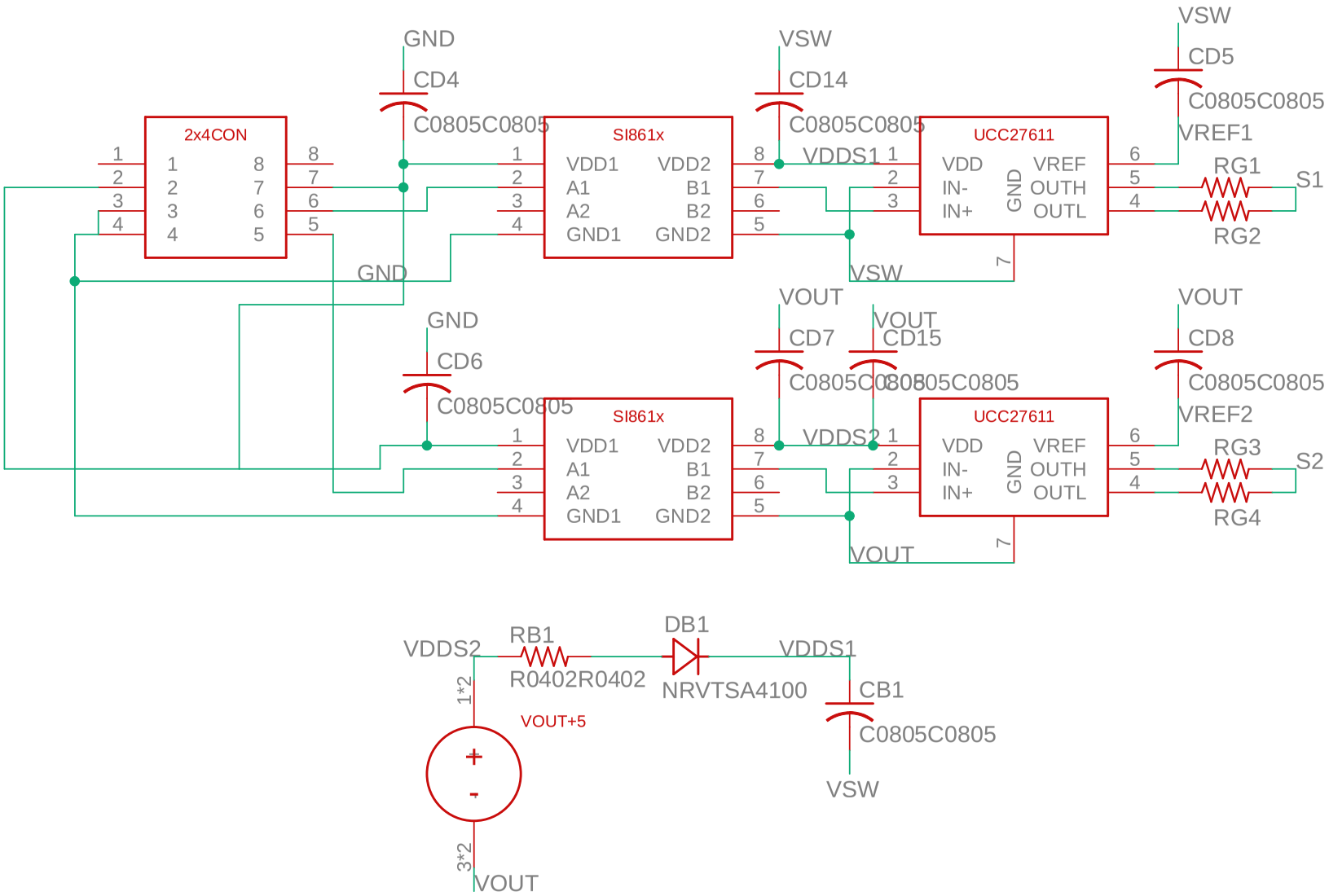
2x4CON
SI861x
UCC27611
GND
CD4
C0805C0805
VSW
CD14
VDDS1
CD5
VREF1
RG1
RG2
S1
VDD1
VDD2
A1
B1
A2
B2
GND1
GND2
VDD
IN-
IN+
VREF
OUTH
OUTL
CD6
CD7
CD15
VDDS2
CD8
VREF2
RG3
RG4
S2
VOUT
RB1
R0402R0402
DB1
NRVTSA4100
CB1
VOUT+5
1*2
3*2

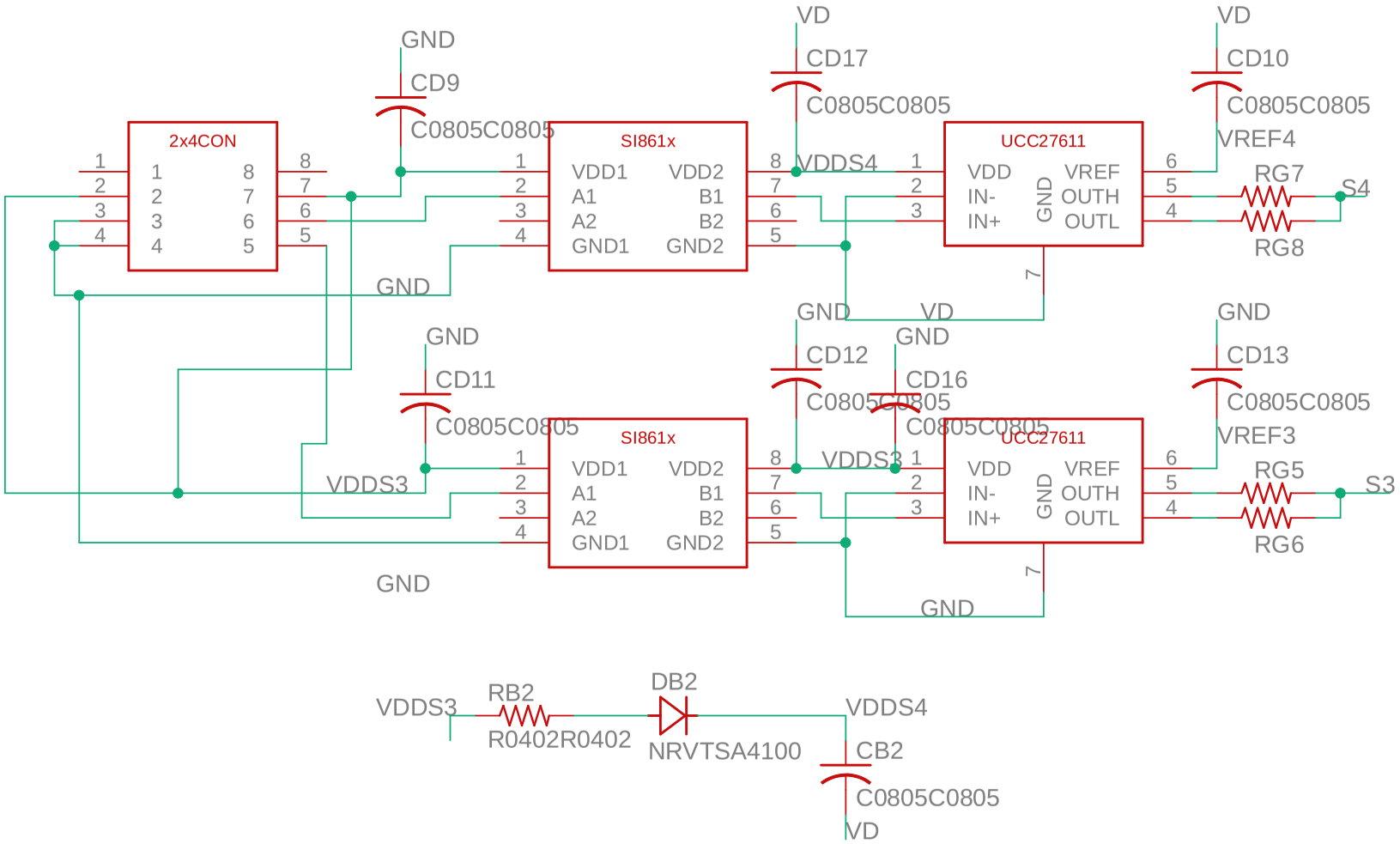
2x4CON
SI861x
SI861x
UCC27611
UCC27611
GND
CD9
C0805C0805
VD
CD17
C0805C0805
VD
CD10
C0805C0805
VREF4
RG7
RG8
S4
VDDS4
GND
VD
GND
CD11
C0805C0805
GND
CD12
C0805C0805
GND
CD16
C0805C0805
GND
CD13
C0805C0805
VREF3
RG5
RG6
S3
VDDS3
VDDS3
GND
RB2
R0402R0402
DB2
NRVTSA4100
VDDS4
CB2
C0805C0805
VD

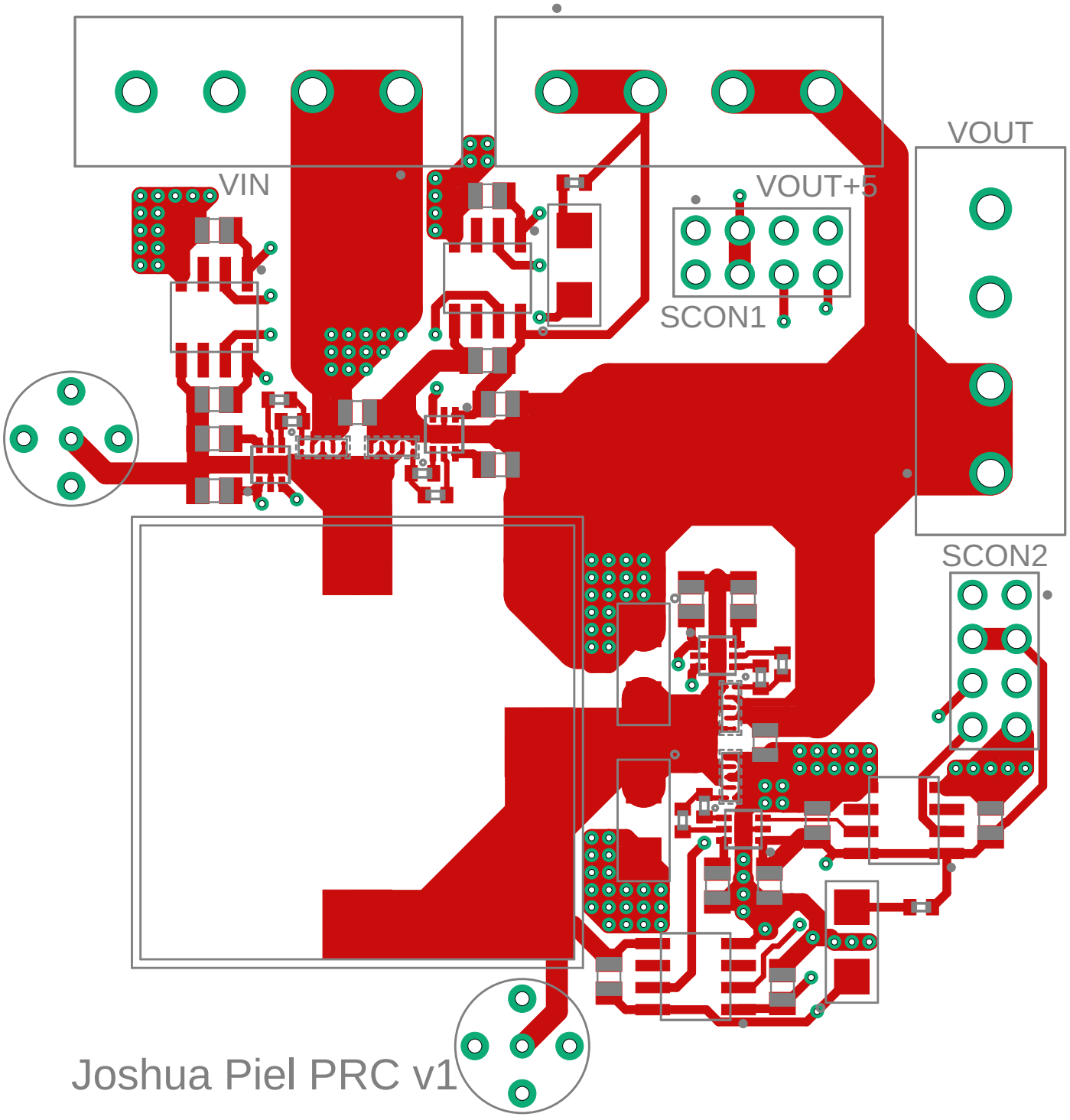
VOUT
VIN
VOUT+5
SCON1
SCON2
Joshua Piel PRC v1

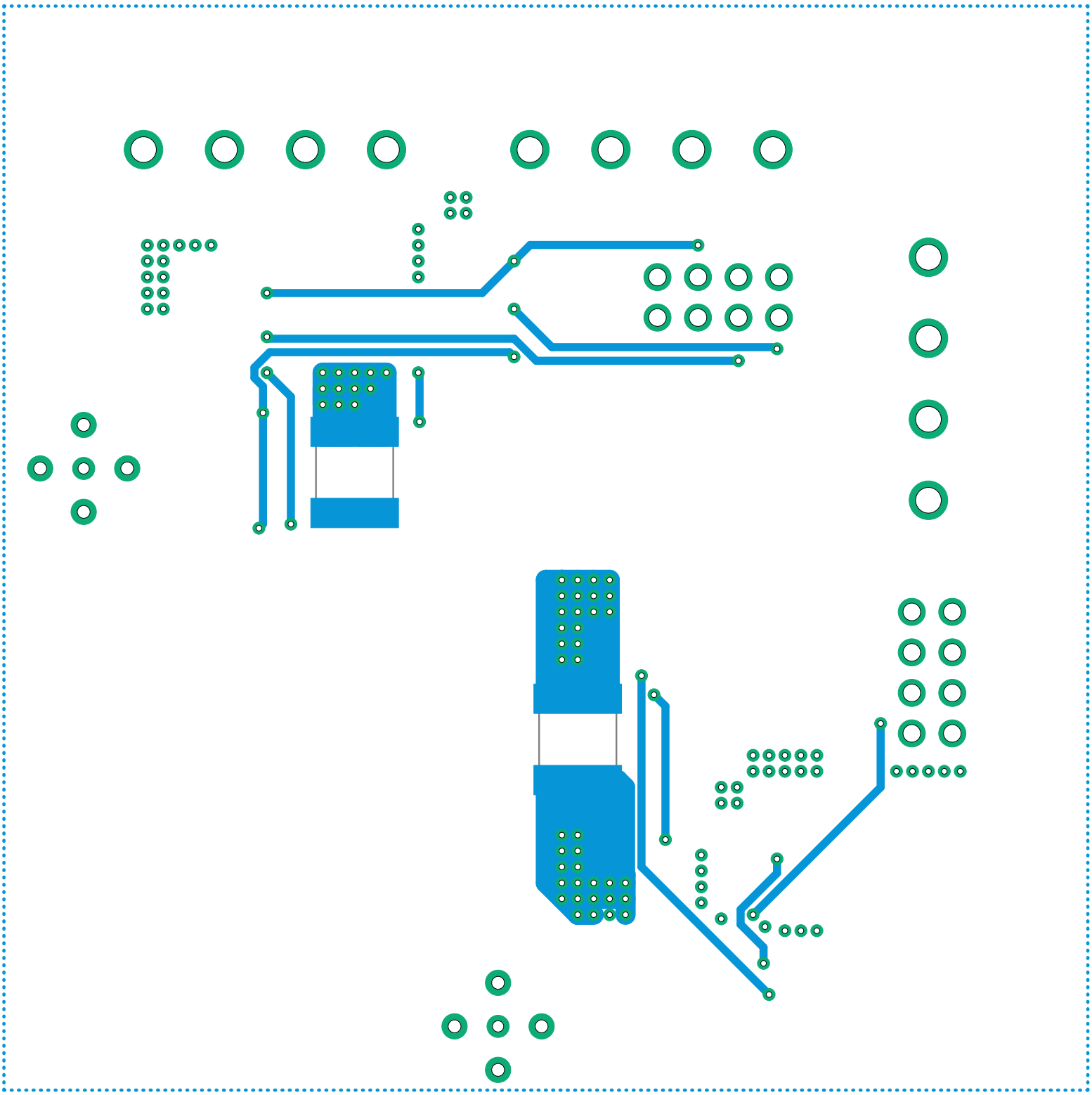

A.3.2 PT-based DC-DC Converter

This appendix contains the parts list, schematic, and PCB layout for the PT-based dc-dc converter prototype utilized in Chapter 3. This prototype implements the topology of Fig. 3-11 with pads to mount the PT on either side of the board to allow testing of different switching sequences. Its layout is designed for low-frequency operation with minimal parasitic capacitance around the PT's high-voltage node. The PCB layout files are displayed at 2x the prototype's scale, assuming a page size of 8.5x11 inches.

Table A.2: Parts List for PT-Based Converter Prototype

Description	Part	Details	Quantity
PT	STEMiNC SMSTF50P2S6	PZT, Rosen-type, 35x6x1.2mm	1
FET	EPC2012C	GaN, 200V, 5A	2
Diode	GeneSiC Semiconductor GB01SLT06-214	Schottky, 650V, 1A, DO214AA	2
Gate Driver	Texas Instruments UCC27611DRVT	6SON	2
Isolator	Silicon Labs SI8620BB-B-ISR	2.5kVrms, 2ch, 8SOIC	1
Bus Capacitor (Input)	TDK C5750X7T2E225K250KA	Ceramic, 2.2μF, 250V, X7T, 2220	4
Bus Capacitor (Output)	TDK C5750X7T2J474M250KC	Ceramic, 0.47μF, 630V, X7T, 2220	4
Decoupling Capacitor (Switch Loops)	Wurth Elektronik 885342206006	Ceramic, 10nF, 250V, X7R, 0603	1
Decoupling Capacitor (Gate Circuitry)	TDK C1005X5R1E104K050BC	Ceramic, 0.1μF, 25V, X5R, 0402	6
Bootstrap Diode	Comchip Technology ACDBA1200-HF	Schottky, 200V, 1A, DO-214AC	1
Bootstrap Resistor	Panasonic ERJ-2GEJ4R7X	4.7Ω, 5%, 1/10W, 0402	1
Gate Resistors	Panasonic ERJ-2GEJ4R7X	4.7Ω, 5%, 1/10W, 0402	4
Power Terminal Socket	Phoenix Contact 1755752	4pos, vertical, 5.08mm	2
Control Terminal Header Pins	Amphenol 67997-208HLF	8pos, vertical, 2.54mm	1

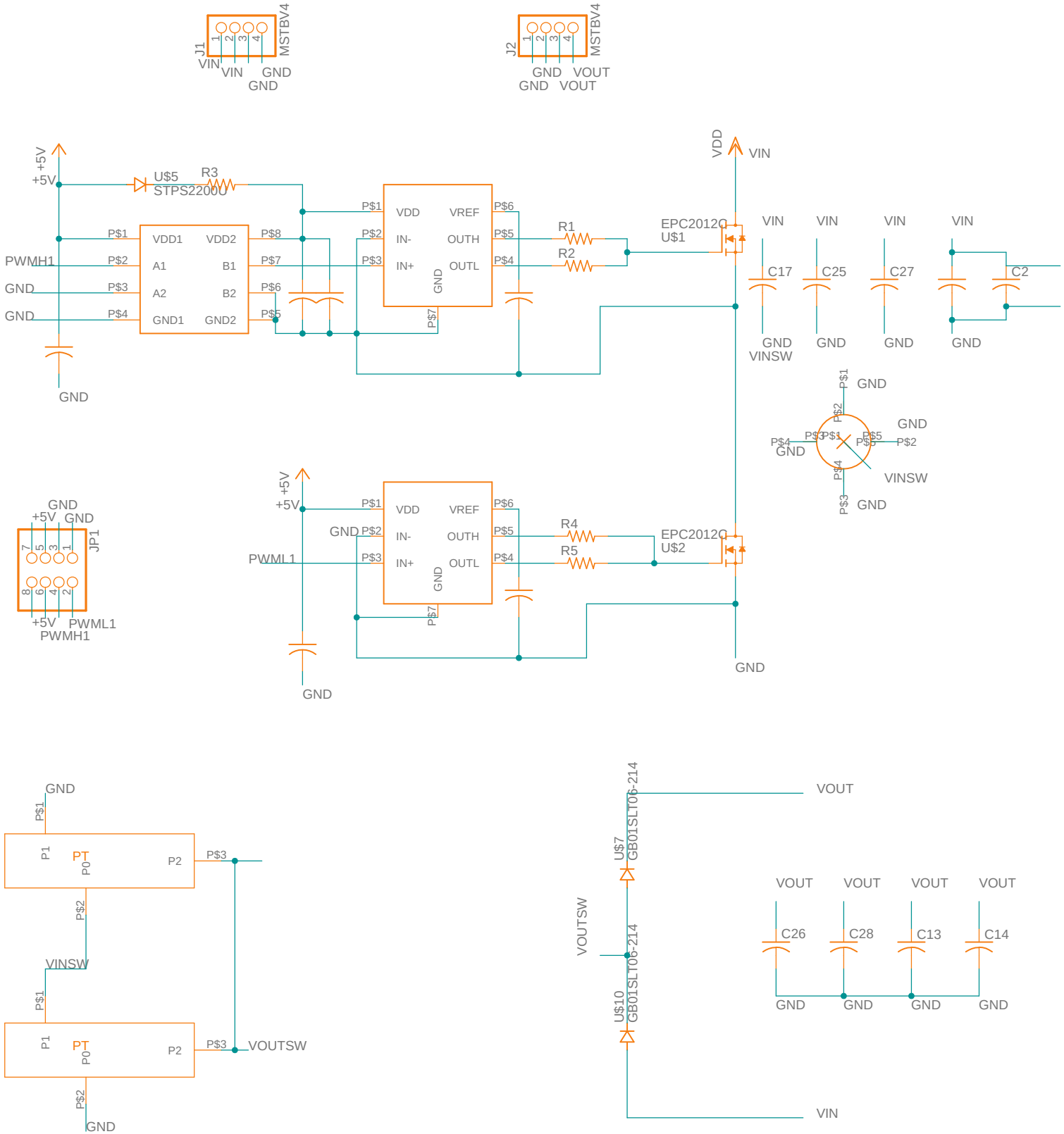
J1
MSTBV4
VIN
VIN GND
GND
J2
MSTBV4
GND VOUT
GND VOUT
+5V
+5V
U$5
STPS2200U
R3
PWMH1
GND
GND
VDD1
VDD2
A1
B1
A2
B2
GND1
GND2
P$1
P$2
P$3
P$4
P$8
P$7
P$6
P$5
VDD
VREF
IN-
OUTH
IN+
OUTL
GND
P$7
R1
R2
EPC2012C
U$1
VDD
VIN
C17
C25
C27
C2
GND
VINSW
GND
+5V
GND
+5V
PWML1
PWMH1
JP1
+5V
+5V
PWML1
GND P$2
R4
R5
EPC2012C
U$2
GND
GND
VOUT
VOUT
VOUTSW
U$7
GB01SLT06-214
U$10
GB01SLT06-214
VOUT
VOUT
VOUT
VOUT
C26
C28
C13
C14
GND
GND
GND
GND
VIN
GND
P$1
P1
PT
P0
P2
P$3
P$2
VINSW
P$1
P1
PT
P0
P2
P$3
VOUTSW
P$2
GND

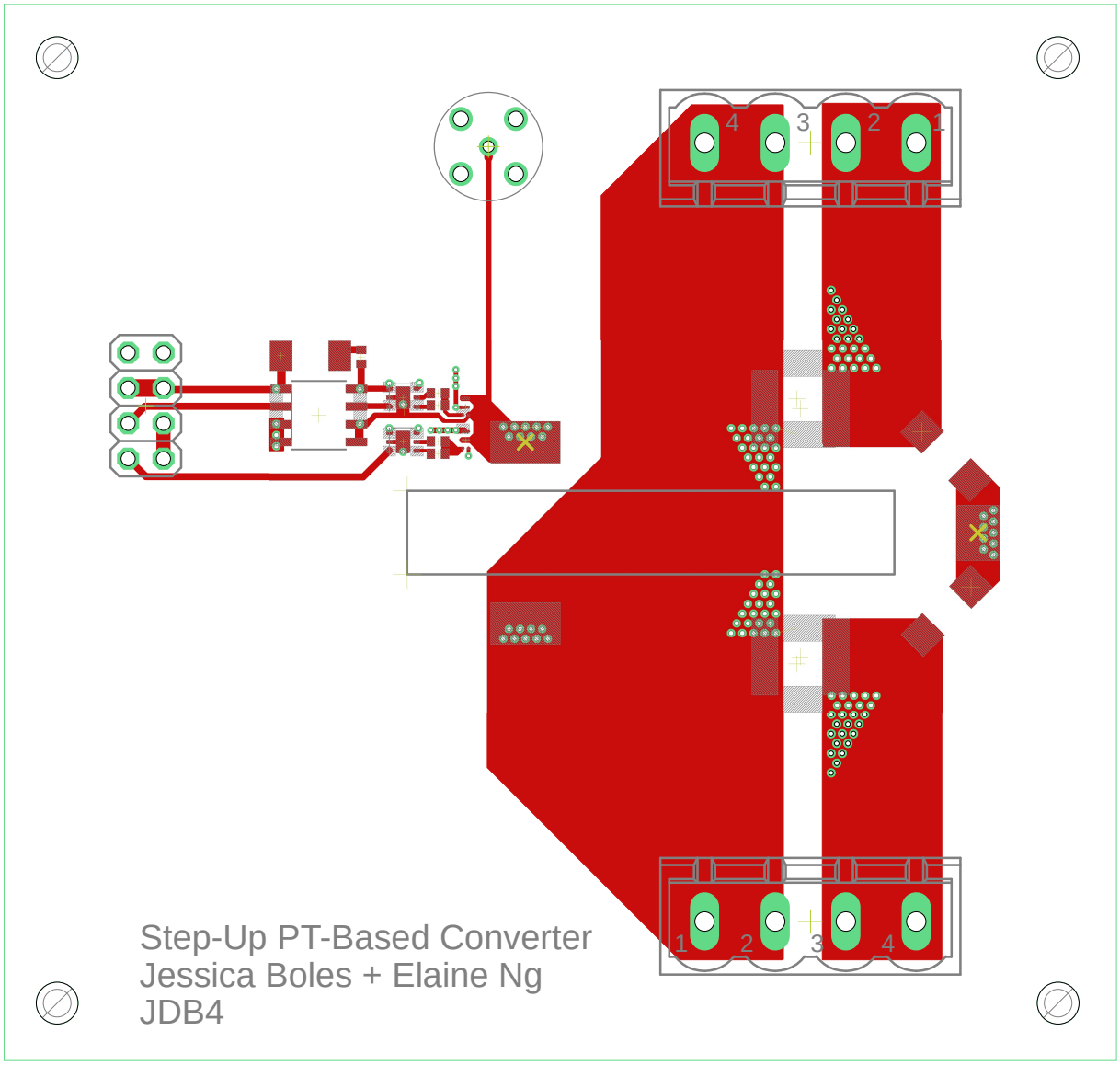
4
3
2
1
1
2
3
4
Step-Up PT-Based Converter
Jessica Boles + Elaine Ng
JDB4

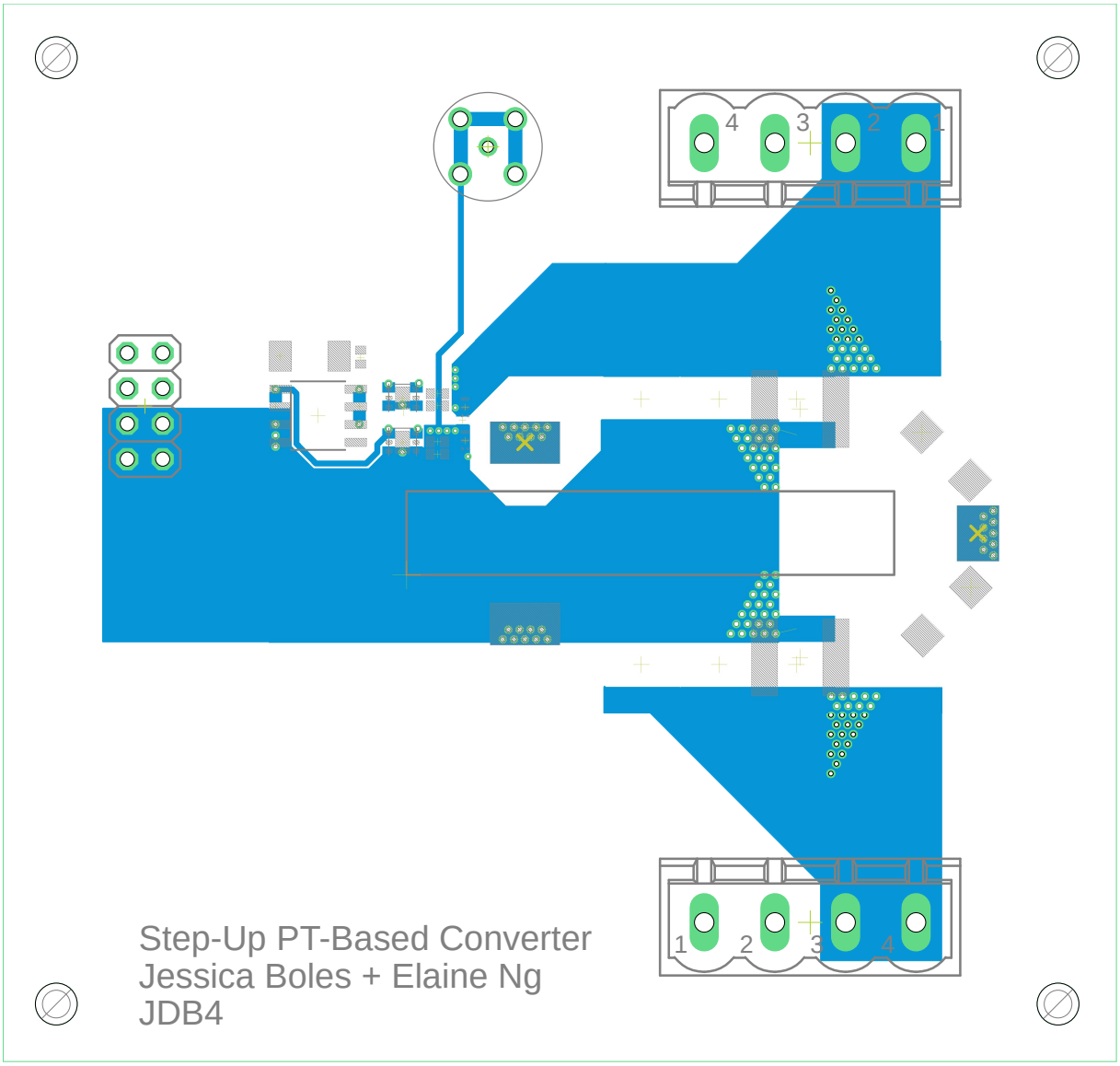
4
3
2
1
1
2
3
4
Step-Up PT-Based Converter
Jessica Boles + Elaine Ng
JDB4

A.3.3 Miniaturized PR-based DC-DC Converter

This appendix contains the parts list, schematic, and PCB layout for the PR-based dc-dc converter prototype utilized in Chapter 9. This prototype implements the topology of Fig. 9-1. Its layout is designed with ample room to test different PR mounting structures, including a pad to mount the PR directly onto the board (though this is unused in the experiments of Chapter 9). The PCB layout files are displayed at 5x the prototype's scale, assuming a page size of 8.5x11 inches.

Table A.3: Parts List for Miniaturized PR-Based Converter Prototype

Description	Part	Details	Quantity
PR	APC International 186	PZT, APC 841, disc, 4.75x0.67mm	1
Coin Battery Holder	Keystone Electronics 500	22mm	1
FET	EPC2012C	GaN, 200V, 5A	2
Gate Driver	Texas Instruments UCC27611DRVT	6SON	4
Isolator	Texas Instruments ISO7420MD	2.5kVrms, 2ch, 8SOIC	2
Bus Capacitor (Input)	TDK CGA9P4X7T2W105M250K	Ceramic, 1μF, 450V, X7T, 2220	2
Bus Capacitor (Output)	TDK C5750X7T2E225M250KA	Ceramic, 2.2μF, 250V, X7T, 2220	2
Decoupling Capacitor (Switch Loops)	TDK CGA5L3X7T2E224M160AE	Ceramic, 0.22μF, 250V, X7T, 1206	2
Decoupling Capacitor (Gate Circuitry)	TDK C1005X5R1E104K050BC	Ceramic, 0.1μF, 25V, X5R, 0402	10
Bootstrap Diode	Micro Commercial Co SMD1200-PL-TP	Schottky, 200V, 1A, SOD123FL	2
Bootstrap Resistor	Stackpole Electronics CSR0402FKR500	0.5Ω, 1%, 1/8W, 0402	2
Gate Resistor	Panasonic ERJ-2GEJ4R7X	4.7Ω, 5% 1/10W, 0402	8
Power Terminal Socket	Phoenix Contact 1755752	4pos, vertical, 5.08mm	3
Control Terminal Header Pins	Amphenol 67997-208HLF	8pos, vertical, 2.54mm	2

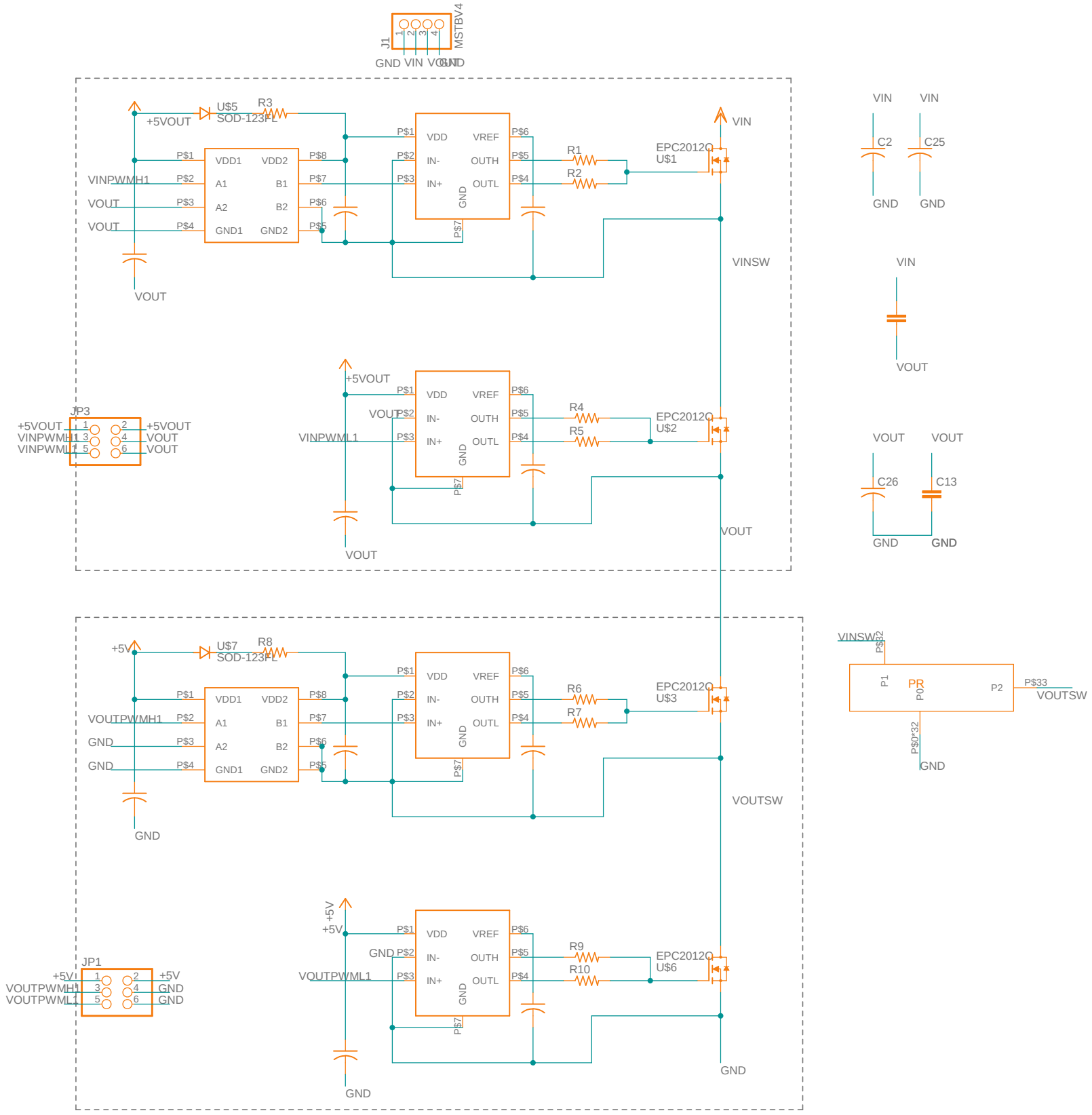
J1
MSTBV4
GND VIN VOUT GND
U$5
SOD-123FL
R3
+5VOUT
VINPWMH1
VOUT
VOUT
VDD1
VDD2
A1
B1
A2
B2
GND1
GND2
VDD
VREF
IN-
OUTH
IN+
OUTL
GND
R1
R2
EPC2012C
U$1
VIN
VINSW
VOUT
C2
C25
GND
GND
VIN
VIN
VOUT
JP3
+5VOUT
VINPWMH1
VINPWML1
+5VOUT
VOUT
VOUT
+5VOUT
VOUT
VINPWML1
R4
R5
EPC2012C
U$2
VOUT
VOUT
C26
C13
GND
GND
VOUT
VOUTSW
U$7
SOD-123FL
R8
+5V
VOUTPWMH1
GND
GND
R6
R7
EPC2012C
U$3
VOUTSW
VINSW
P$32
P1
PR
P0R
P2
P$33
VOUTSW
P$0*32
GND
JP1
+5V
VOUTPWMH1
VOUTPWML1
+5V
GND
GND
+5V
+5V
GND
VOUTPWML1
R9
R10
EPC2012C
U$6
GND
GND

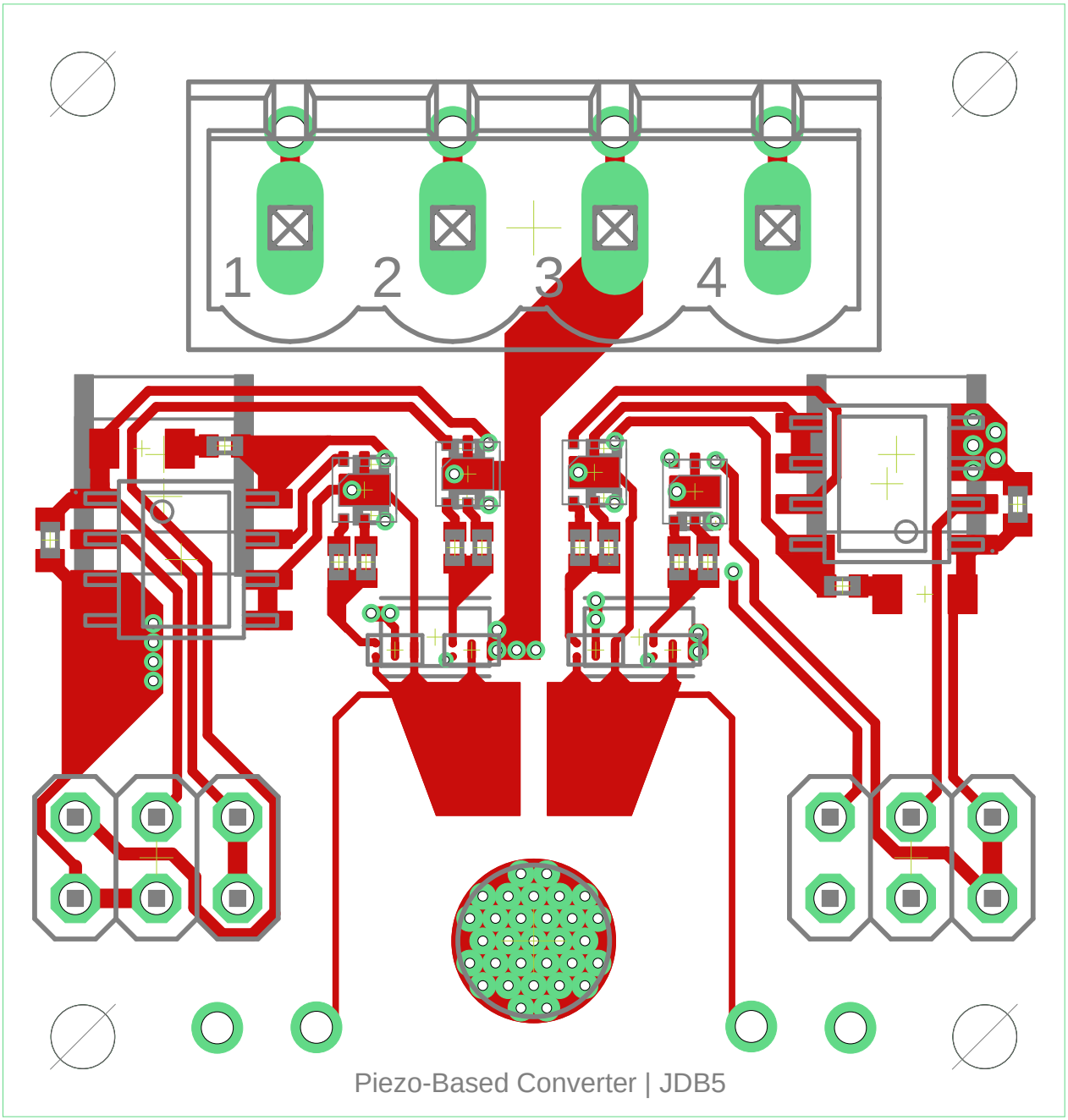
1
2
3
4
Piezo-Based Converter | JDB5

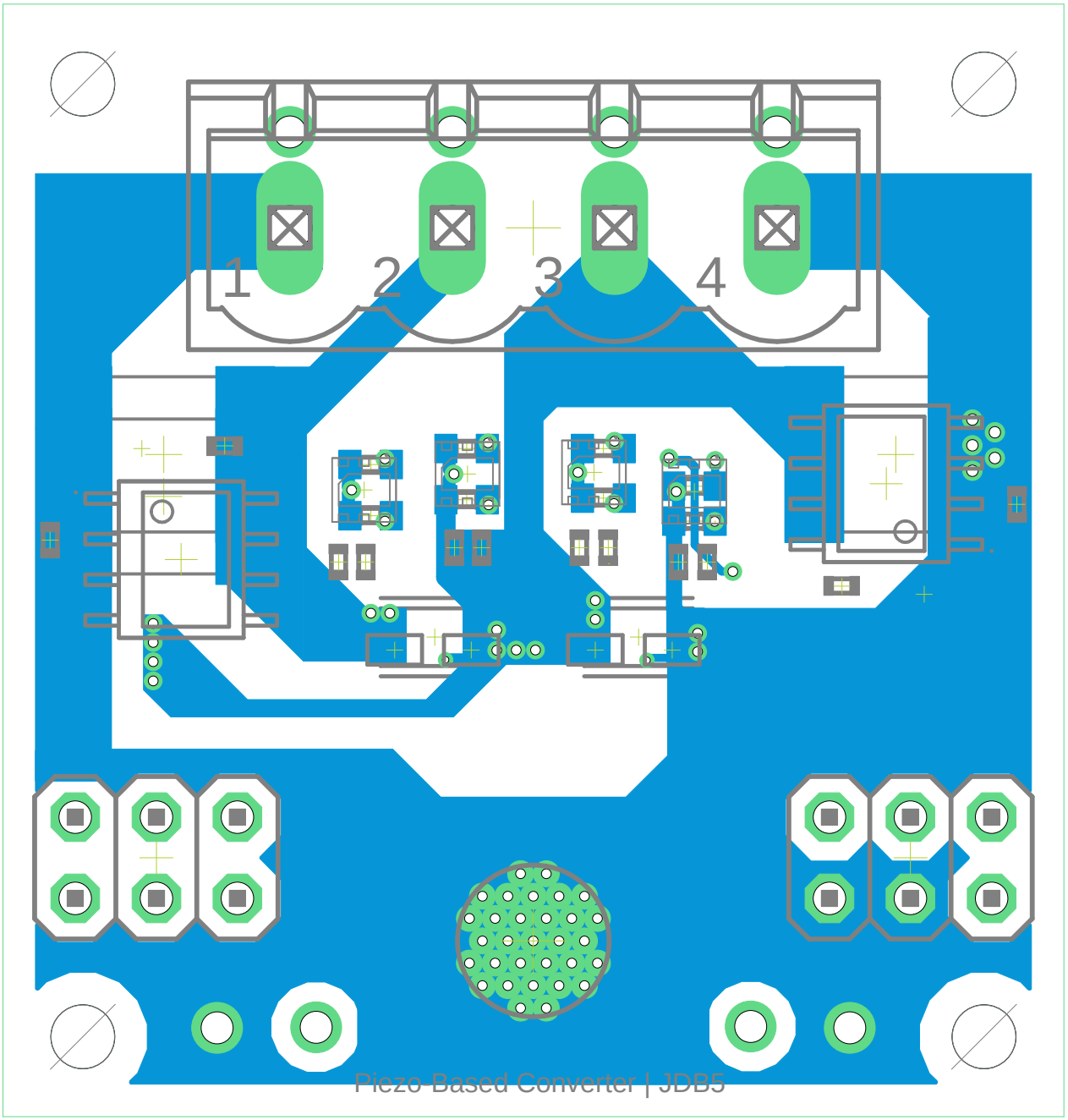
1
2
3
4
Piezo-Based Converter | JDB5

Bibliography

[1] K. S. Van Dyke, "The piezo-electric resonator and its equivalent network," *Proceedings of the Institute of Radio Engineers*, vol. 16, no. 6, pp. 742–764, 1928.

[2] J. Erhart, P. Půlpán, and M. Pustka, *Piezoelectric Ceramic Resonators*. Springer, 2017.

[3] W. P. Mason, *Electromechanical Transducers and Wave Filters*. D. Van Nostrand Co., 1948.

[4] C.-y. Lin, "Design and analysis of piezoelectric transformer converters," Ph.D. dissertation, Virginia Tech, 1997.

[5] C. R. Sullivan, B. A. Reese, A. L. Stein, and P. A. Kyaw, "On size and magnetics: Why small efficient power inductors are rare," in *Proc. IEEE Intl. Symposium on 3D Power Electronics Integration and Manufacturing*, Raleigh, NC, USA, Jun. 2016, pp. 1–23.

[6] D. J. Perreault, J. Hu, J. M. Rivas, Y. Han, O. Leitermann, R. C. Pilawa-Podgurski, A. Sagneri, and C. R. Sullivan, "Opportunities and challenges in very high frequency power conversion," in *Proc. IEEE Applied Power Electronics Conference and Exposition*, Washington, DC, USA, Feb. 2009, pp. 1–14.

[7] A. J. Hanson, J. A. Belk, S. Lim, C. R. Sullivan, and D. J. Perreault, "Measurements and performance factor comparisons of magnetic materials at high frequency," *IEEE Transactions on Power Electronics*, vol. 31, no. 11, pp. 7909–7925, 2016.

[8] Y. Li, J. Chen, M. John, R. Liou, and S. R. Sanders, "Resonant switched capacitor stacked topology enabling high dc-dc voltage conversion ratios and efficient wide range regulation," in *Proc. IEEE Energy Conversion Congress and Exposition*, Milwaukee, WI, USA, Sep. 2016, pp. 1–7.

[9] R. C. Pilawa-Podgurski and D. J. Perreault, "Merged two-stage power converter with soft charging switched-capacitor stage in 180 nm CMOS," *IEEE Journal of Solid-State Circuits*, vol. 47, no. 7, pp. 1557–1567, 2012.

[10] D. M. Giuliano, M. E. D'Asaro, J. Zwart, and D. J. Perreault, "Miniaturized low-voltage power converters with fast dynamic response," *IEEE Journal of Emerging and Selected Topics in Power Electronics*, vol. 2, no. 3, pp. 395–405, 2014.

[11] C. Schaef and J. T. Stauth, "A highly integrated series–parallel switched-capacitor converter with 12 V input and quasi-resonant voltage-mode regulation," *IEEE Journal of Emerging and Selected Topics in Power Electronics*, vol. 6, no. 2, pp. 456–464, 2018.

[12] K. Kesarwani, R. Sangwan, and J. T. Stauth, "Resonant-switched capacitor converters for chip-scale power delivery: Design and implementation," *IEEE Transactions on Power Electronics*, vol. 30, no. 12, pp. 6966–6977, 2014.

[13] Y. Lei and R. C. N. Pilawa-Podgurski, "A general method for analyzing resonant and soft-charging operation of switched-capacitor converters," *IEEE Transactions on Power Electronics*, vol. 30, no. 10, pp. 5650–5664, 2015.

[14] M. D. Seeman and S. R. Sanders, "Analysis and optimization of switched-capacitor dc–dc converters," *IEEE Transactions on Power Electronics*, vol. 23, no. 2, pp. 841–851, 2008.

[15] P. A. Kyaw, A. L. Stein, and C. R. Sullivan, "Fundamental examination of multiple potential passive component technologies for future power electronics," *IEEE Transactions on Power Electronics*, vol. 33, no. 12, pp. 10,708–10,722, 2018.

[16] S. Sherrit, S. P. Leary, B. P. Dolgin, and Y. Bar-Cohen, "Comparison of the Mason and KLM equivalent circuits for piezoelectric resonators in the thickness mode," in *Proc. IEEE Ultrasonics International Symposium*, vol. 2, Tahoe, NV, USA, Oct. 1999, pp. 921–926.

[17] L. Wang and R. P. Burgos, "Comprehensive analysis of models and operational characteristics of piezoelectric transformers," in *Proc. IEEE Applied Power Electronics Conference and Exposition*, New Orleans, LA, USA, Mar. 2020, pp. 1422–1429.

[18] A. Vazquez Carazo, "Piezoelectric transformers: An historical review," in *Actuators*, vol. 5, no. 2. MDPI, 2016, p. 12.

[19] F. E. Bisogno, M. Radecker, A. Knoll, A. V. Carazo, A. Riedlhammer, G. Deboy, N. Norvez, and J. Pacas, "Comparison of resonant topologies for step-down applications using piezoelectric transformers," in *Proc. IEEE Power Electronics Specialists Conference*, vol. 4, Aachen, Germany, Jun. 2004, pp. 2662–2667.

[20] S. Nittayarumphong, F. Bisogno, M. Radecker, A. Knoll, A. V. Carazo, and A. Riedlhammer, "Dynamic behaviour of PI controlled class-E resonant converter for step-down applications using piezoelectric transformers," in *Proc. IEEE European Conference on Power Electronics and Applications*, Dresden, Germany, Sep. 2005, pp. 1–10.

[21] Y. Yang, F. E. Bisogno, A. Schittler, S. Nittayarumphong, M. Radecker, W.-J. Fischer, and M. Fahlenkamp, "Comparison of inductor-half-bridge and class-E resonant topologies for piezoelectric transformer applications," in *Proc. IEEE Energy Conversion Congress and Exposition*, San Jose, CA, USA, Sep. 2009, pp. 776–782.

[22] W. Zhang, D. Zhang, Y. Wang, Y. Chen, Y. Liu, and J. Cao, "A low-cost-ZVS-class-E converter using pt," in *Proc. IEEE Power Electronics Specialists Conference*, vol. 3, Aachen, Germany, Jun. 2004, pp. 1803–1807.

[23] M. Ryu, S. Choi, S. Lee, and B. H. Cho, "A new piezoelectric transformer driving topology for universal input ac/dc adapter using a constant frequency pwm control,"

in *Proc. IEEE Applied Power Electronics Conference and Exposition*, Dallas, TX, USA, Mar. 2006, pp. 1–4.

[24] J.-h. Park, S. Choi, S. Lee, and B. H. Cho, "Gain-adjustment technique for resonant power converters with piezoelectric transformer," in *Proc. IEEE Power Electronics Specialists Conference*, Orlando, FL, USA, Jun. 2007, pp. 2549–2553.

[25] J. Navas, T. Bove, J. Cobos, F. Nuno, and K. Brebol, "Miniaturised battery charger using piezoelectric transformers," in *Proc. IEEE Applied Power Electronics Conference and Exposition*, vol. 1, Anaheim, CA, USA, Mar. 2001, pp. 492–496.

[26] Y.-P. Liu, D. Vasic, F. Costa, W.-J. Wu, and D. Schwander, "Fixed frequency controlled piezoelectric 10W DC/DC converter," in *Proc. IEEE Energy Conversion Congress and Exposition*, Atlanta, GA, USA, Sep. 2010, pp. 3030–3037.

[27] C. Lin and F. Lee, "Design of a piezoelectric transformer converter and its matching networks," in *Proc. IEEE Power Electronics Specialist Conference*, vol. 1, Taipei, Taiwan, Jun. 1994, pp. 607–612.

[28] W. Zhang, X. Zhang, Y. Lei, and Y. Liu, "Narrow-control-bandwidth operation of piezoelectric-transformer converter," in *Proc. IEEE International Conference on Power Electronics and Drive Systems*, Bangkok, Thailand, Nov. 2007, pp. 1628–1632.

[29] J. Díaz, F. Nuño, J. M. Lopera, and J. A. Martín-Ramos, "A new control strategy for an ac/dc converter based on a piezoelectric transformer," *IEEE Transactions on Industrial Electronics*, vol. 51, no. 4, pp. 850–856, 2004.

[30] Y. Li and W. Chen, "Ac-dc converter with worldwide range input voltage by series and parallel piezoelectric transformer connection," in *Proc. IEEE Power Electronics Specialists Conference*, vol. 4, Aachen, Germany, Jun. 2004, pp. 2668–2671.

[31] O. Ohnishi, H. Kishie, A. Iwamoto, Y. Sasaki, T. Zaitsu, and T. Inoue, "Piezoelectric ceramic transformer operating in thickness extensional vibration mode for power supply," in *Proc. IEEE Ultrasonics Symposium*, Tucson, AZ, USA, Oct. 1992, pp. 483–488.

[32] T. Zaitsu, O. Ohnishi, T. Inoue, M. Shoyama, T. Ninomiya, F. Lee, and G. Hua, "Piezoelectric transformer operating in thickness extensional vibration and its application to switching converter," in *Proc. IEEE Power Electronics Specialist Conference*, vol. 1, Taipei, Taiwan, Jun. 1994, pp. 585–589.

[33] T. Yamane, S. Hamamura, T. Zaitsu, T. Minomiya, M. Shoyama, and Y. Fuda, "Efficiency improvement of piezoelectric-transformer dc-dc converter," in *Proc. IEEE Power Electronics Specialists Conference*, vol. 2, Fukuoka, Japan, May 1998, pp. 1255–1261.

[34] L. Wang, Q. Wang, M. Khanna, R. P. Burgos, K. D. Ngo, and A. VazquezCarazo, "Design and control of tunable piezoelectric transformer based dc/dc converter," in *Proc. IEEE Energy Conversion Congress and Exposition (ECCE)*, Portland, OR, USA, Sep. 2018, pp. 5987–5993.

[35] L. Wang, Q. Wang, R. P. Burgos, K. D. T. Ngo, and A. Carazo Vazquez, "A comparison of dc and ac output inductors in tunable piezoelectric transformer based dc/dc converters," in *Proc. IEEE Energy Conversion Congress and Exposition*, Baltimore, MD, USA, Sep. 2019.

[36] L. Wang, K. Sun, and R. Burgos, "Planar piezoelectric transformer-based high step-down voltage-ratio dc-dc converter," *IEEE Transactions on Power Electronics*, 2022.

[37] M. Ekhtiari, Z. Zhang, and M. A. Andersen, "State-of-the-art piezoelectric transformer-based switch mode power supplies," in *IECON 2014-40th Annual Conference of the IEEE Industrial Electronics Society*. IEEE, 2014, pp. 5072–5078.

[38] G. Ivensky, S. Bronstein, and S. Ben-Yaakov, "A comparison of piezoelectric transformer ac/dc converters with current doubler and voltage doubler rectifiers," *IEEE Transactions on Power Electronics*, vol. 19, no. 6, pp. 1446–1453, 2004.

[39] A. M. Flynn and S. R. Sanders, "Fundamental limits on energy transfer and circuit considerations for piezoelectric transformers," *IEEE Transactions on Power Electronics*, vol. 17, no. 1, pp. 8–14, 2002.

[40] S. Bronstein and S. Ben-Yaakov, "Design considerations for achieving ZVS in a half bridge inverter that drives a piezoelectric transformer with no series inductor," in *Proc. IEEE Power Electronics Specialists Conference*, vol. 2, Cairns, Queensland, Australia, Jun. 2002, pp. 585–590.

[41] J. M. Alonso, C. Ordiz, and M. A. Dalla Costa, "A novel control method for piezoelectric-transformer based power supplies assuring zero-voltage-switching operation," *IEEE Transactions on Industrial Electronics*, vol. 55, no. 3, pp. 1085–1089, 2008.

[42] S.-Y. Chen and C.-L. Chen, "ZVS considerations for a phase-lock control dc/dc converter with piezoelectric transformer," in *Proc. Annual Conference of the IEEE Industrial Electronics Society*, Paris, France, Nov. 2006, pp. 2244–2248.

[43] M. Rodgaard, T. Andersen, and M. A. Andersen, "Empiric analysis of zero voltage switching in piezoelectric transformer based resonant converters," in *Proc. IET International Conference on Power Electronics, Machines and Drives*, Bristol, UK, Mar. 2012.

[44] M. Ekhtiari, Z. Zhang, and M. A. Andersen, "Analysis of bidirectional piezoelectric-based converters for zero-voltage switching operation," *IEEE Transactions on Power Electronics*, vol. 32, no. 1, pp. 866–877, 2017.

[45] M. Ekhtiari, T. Andersen, M. A. Andersen, and Z. Zhang, "Dynamic optimum dead time in piezoelectric transformer-based switch-mode power supplies," *IEEE Transactions on Power Electronics*, vol. 32, no. 1, pp. 783–793, 2017.

[46] M. S. Rødgaard, "Bi-directional piezoelectric transformer based converter for high-voltage capacitive applications," in *Proc. IEEE Applied Power Electronics Conference and Exposition*, Charlotte, NC, USA, Mar. 2015, pp. 1993–1998.

[47] M. S. Rødgaard, M. Weirich, and M. A. Andersen, "Forward conduction mode controlled piezoelectric transformer-based PFC LED drive," *IEEE Transactions on Power Electronics*, vol. 28, no. 10, pp. 4841–4849, 2012.

[48] E. L. Horsley, A. V. Carazo, N. Nguyen-Quang, M. P. Foster, and D. A. Stone, "Analysis of inductorless zero-voltage-switching piezoelectric transformer-based converters," *IEEE Transactions on Power Electronics*, vol. 27, no. 5, pp. 2471–2483, 2012.

[49] M. Sanz, P. Alou, A. Soto, R. Prieto, J. Cobos, and J. Uceda, "Magnetic-less converter based on piezoelectric transformers for step-down dc/dc and low power application," in *Proc. IEEE Applied Power Electronics Conference and Exposition*, Miami Beach, FL, USA, Feb. 2003, pp. 615–621.

[50] D. Vasic, Y.-P. Liu, F. Costa, and D. Schwander, "Piezoelectric transformer-based dc/dc converter with improved burst-mode control," in *2013 IEEE Energy Conversion Congress and Exposition*. IEEE, 2013, pp. 140–146.

[51] B. Ju, W. Shao, L. Zhang, H. Wang, and Z. Feng, "Piezoelectric ceramic acting as inductor for capacitive compensation in piezoelectric transformer," *IET Power Electronics*, vol. 8, no. 10, pp. 2009–2015, 2015.

[52] M. P. Foster, J. N. Davidson, E. L. Horsley, and D. A. Stone, "Critical design criterion for achieving zero voltage switching in inductorless half-bridge-driven piezoelectric-transformer-based power supplies," *IEEE Transactions on Power Electronics*, vol. 31, no. 7, pp. 5057–5066, 2015.

[53] S. Moon and J.-H. Park, "High power dc–dc conversion applications of disk-type radial mode Pb (Zr, Ti) O3 ceramic transducer," *Japanese Journal of Applied Physics*, vol. 50, no. 9S2, p. 09ND20, 2011.

[54] G.-S. Seo, J.-W. Shin, and B.-H. Cho, "A magnetic component-less series resonant converter using a piezoelectric transducer for low profile application," in *Proc. IEEE*

International Power Electronics Conference - ECCE Asia, Sapporo, Japan, Jun. 2010, pp. 2810–2814.

[55] G.-S. Seo and B.-H. Cho, "Multilayer piezoelectric transducer design guidelines for low profile magnetic-less dc/dc converter," in *Proc. IEEE International Conference on Power Electronics - ECCE Asia*, Jeju, South Korea, May 2011, pp. 972–976.

[56] A. M. Imtiaz, F. H. Khan, and J. S. Walling, "Contour-mode ring-shaped AlN microresonator on Si and feasibility of its application in series-resonant converter," *IEEE Transactions on Power Electronics*, vol. 30, no. 8, pp. 4437–4454, 2015.

[57] D. C. Hamill, "Time reversal duality in dc-dc converters," in *Proc. IEEE Power Electronics Specialists Conference*, vol. 1, St. Louis, MO, USA, Jun. 1997, pp. 789–795.

[58] B. Pollet, G. Despesse, and F. Costa, "A new non-isolated low power inductorless piezoelectric dc-dc converter," *IEEE Transactions on Power Electronics*, vol. 34, no. 11, pp. 11 002–11 013, 2019.

[59] Y. Li, M. John, J. Poon, J. Chen, and S. R. Sanders, "Lossless voltage regulation and control of the resonant switched-capacitor dc-dc converter," in *Proc. IEEE Workshop on Control and Modeling for Power Electronics*, Vancouver, BC, Canada, Jul. 2015, pp. 1–7.

[60] R. Oruganti and F. C. Lee, "Resonant power processors, part I — State plane analysis," *IEEE Transactions on Industry Applications*, no. 6, pp. 1453–1460, 1985.

[61] R. Oruganti, "State-plane analysis of resonant converters," Ph.D. dissertation, Virginia Polytechnic Institute and State University, 1987.

[62] M. K. Kazimierczuk and W. D. Morse, "State-plane analysis of zero-voltage-switching resonant dc/dc converters," *IEEE Transactions on Aerospace and Electronic Systems*, vol. 25, no. 2, pp. 232–240, 1989.

[63] C. Lee and K. Siri, "Analysis and design of series resonant converter by state-plane diagram," *IEEE Transactions on Aerospace and Electronic Systems*, no. 6, pp. 757–763, 1986.

[64] "State plane analysis, averaging, and other analytical tools". University of Colorado, Boulder. [Online]. Available: http://ecee.colorado.edu/~ecen5817/notes/ch3.pdf

[65] J. D. Boles, J. J. Piel, and D. J. Perreault, "Enumeration and analysis of dc-dc converter implementations based on piezoelectric resonators," in *Proc. IEEE Workshop on Control and Modeling for Power Electronics*, Toronto, Canada, Jun. 2019, pp. 1–8.

[66] J. D. Boles, J. J. Piel, and D. J. Perreault, "Analysis of high-efficiency operating modes for piezoelectric resonator-based dc-dc converters," in *Proc. IEEE Applied Power Electronics Conference and Exposition*, New Orleans, LA, USA, Mar. 2020, pp. 1–8.

[67] J. D. Boles, J. J. Piel, and D. J. Perreault, "Enumeration and analysis of dc-dc converter implementations based on piezoelectric resonators," *IEEE Transactions on Power Electronics*, vol. 36, no. 1, pp. 129–145, 2021.

[68] W. Braun, Z. Tong, and J. Rivas-Davila, "Inductorless soft switching dc-dc converter with an optimized piezoelectric resonator," in *Proc. IEEE Applied Power Electronics Conference and Exposition*, New Orleans, LA, USA, Mar. 2020, pp. 2272–2278.

[69] W. D. Braun, E. A. Stolt, L. Gu, J. Segovia-Fernandez, S. Chakraborty, R. Lu, and J. M. Rivas-Davila, "Optimized resonators for piezoelectric power conversion," *IEEE Open Journal of Power Electronics*, vol. 2, pp. 212–224, 2021.

[70] M. Touhami, G. Despesse, T. Hilt, M. Bousquet, A. Reinhardt, E. Borel, V. Breton, K.-F. Gneza, and F. Costa, "Piezoelectric materials for the dc-dc converters based on piezoelectric resonators," in *Proc. IEEE Workshop on Control and Modelling of Power Electronics (COMPEL)*. Cartagena de Indias, Columbia: IEEE, Nov. 2021, pp. 1–8.

[71] E. Stolt, W. D. Braun, L. Gu, J. Segovia-Fernandez, S. Chakraborty, R. Lu, and J. Rivas-Davila, "Fixed-frequency control of piezoelectric resonator dc-dc converters

for spurious mode avoidance," *IEEE Open Journal of Power Electronics*, vol. 2, pp. 582–590, 2021.

[72] B. Pollet, F. Costa, and G. Despesse, "A new inductorless dc-dc piezoelectric flyback converter," in *Proc. IEEE International Conference on Industrial Technology (ICIT)*, Lyon, France, Feb. 2018, pp. 585–590.

[73] M. Touhami, G. Despesse, and F. Costa, "A new topology of dc-dc converter based on piezoelectric resonator," in *2020 IEEE 21st Workshop on Control and Modeling for Power Electronics (COMPEL)*. IEEE, 2020, pp. 1–7.

[74] ——, "A new topology of dc–dc converter based on piezoelectric resonator," *IEEE Transactions on Power Electronics*, vol. 37, no. 6, pp. 6986–7000, 2022.

[75] Z. Yang, J. Forrester, J. N. Davidson, M. P. Foster, and D. A. Stone, "Resonant current estimation and phase-locked loop feedback design for piezoelectric transformer-based power supplies," *IEEE Transactions on Power Electronics*, vol. 35, no. 10, pp. 10 466–10 476, 2020.

[76] J. Forrester, J. N. Davidson, M. P. Foster, and D. A. Stone, "Influence of spurious modes on the efficiency of piezoelectric transformers: A sensitivity analysis," *IEEE Transactions on Power Electronics*, vol. 36, no. 1, pp. 617–629, 2020.

[77] J. D. Boles, E. Ng, J. H. Lang, and D. J. Perreault, "High-efficiency operating modes for isolated piezoelectric-transformer-based dc-dc converters," in *Proc. IEEE Workshop on Control and Modeling for Power Electronics*, Aalborg, Denmark, Nov. 2020, pp. 1–8.

[78] "Equivalent circuit parameters for piezo transformers". Steiner & Martins, Inc. [Online]. Available: http://www.steminc.com/piezo/EquivCircuitPT.asp

[79] K. Uchino and S. Hirose, "Loss mechanisms in piezoelectrics: how to measure different losses separately," *IEEE Transactions on Ultrasonics, ferroelectrics, and frequency control*, vol. 48, no. 1, pp. 307–321, 2001.

[80] E. Ng, J. D. Boles, J. H. Lang, and D. J. Perreault, "Non-isolated dc-dc converter implementations based on piezoelectric transformers," in *Proc. IEEE Energy Conversion Congress and Exposition*, Vancouver, Canada, Oct. 2021, pp. 1–8.

[81] J. D. Boles, E. Ng, J. H. Lang, and D. J. Perreault, "Dc-dc converter implementations based on piezoelectric transformers," *IEEE Journal of Emerging and Selected Topics in Power Electronics*, 2022.

[82] E. Ng, "Design of high-performance piezoelectric transformer-based DC-DC converters," Master's thesis, Massachusetts Institute of Technology, 2022.

[83] M. Ekhtiari, T.-G. Zsurzsan, M. A. Andersen, and Z. Zhang, "Optimum phase shift in the self-oscillating loop for piezoelectric-transformer-based power converters," *IEEE Transactions on Power Electronics*, vol. 33, no. 9, pp. 8101–8109, 2017.

[84] E. Dallago, A. Danioni, M. Passoni, and G. Venchi, "Modelling of DC-DC converter based on a piezoelectric transformer and its control loop," in *Proc. IEEE Power Electronics Specialists Conference*, vol. 2, Cairns, QLD, Australia, Jun. 2002, pp. 927–931.

[85] S. Ben-Yaakov and S. Lineykin, "Maximum power tracking of piezoelectric transformer hv converters under load variations," *IEEE Transactions on power electronics*, vol. 21, no. 1, pp. 73–78, 2006.

[86] S. Yun, J. Sim, J. Park, S. Choi, and B. Cho, "Adaptive phase control method for load variation of resonant converter with piezoelectric transformer," in *2007 7th International Conference on Power Electronics and Drive Systems*, Bangkok, Thailand, Nov. 2007, pp. 164–168.

[87] S. Hamamura, D. Kurose, T. Ninomiya, and M. Yamamoto, "New control method of piezoelectric transformer converter by PWM and PFM for wide range of input voltage," in *Proc. IEEE International Power Electronics Congress.* Acapulco, Mexico: IEEE, Oct. 2000, pp. 3–8.

[88] J. A. Martin-Ramos, M. A. J. Prieto, F. N. García, J. D. González, and F. F. Linera, "A new full-protected control mode to drive piezoelectric transformers in dc-dc converters," *IEEE Transactions on Power Electronics*, vol. 17, no. 6, pp. 1096–1103, 2002.

[89] J. Diaz, F. Nuno, M. J. Prieto, J. A. Martin-Ramos, and P. J. V. Saiz, "Closing a second feedback loop in a dc–dc converter based on a piezoelectric transformer," *IEEE Transactions on Power Electronics*, vol. 22, no. 6, pp. 2195–2201, 2007.

[90] M. Touhami, G. Despesse, F. Costa, and B. Pollet, "Implementation of control strategy for step-down DC-DC converter based on piezoelectric resonator," in *Proc. IEEE European Conference on Power Electronics and Applications*, Lyon, France, Sep. 2020, pp. 1–9.

[91] A. J. Hanson and D. J. Perreault, "A high-frequency power factor correction stage with low output voltage," *IEEE Journal of Emerging and Selected Topics in Power Electronics*, vol. 8, no. 3, pp. 2143–2155, 2019.

[92] S. Lim, J. Ranson, D. M. Otten, and D. J. Perreault, "Two-stage power conversion architecture suitable for wide range input voltage," *IEEE Transactions on Power Electronics*, vol. 30, no. 2, pp. 805–816, 2014.

[93] J. J. Piel, "Closed loop control for a piezoelectric-resonator-based DC-DC power converter," Master's thesis, Massachusetts Institute of Technology, 2022.

[94] J. J. Piel, J. D. Boles, and D. J. Perreault, "Feedback control for a piezoelectric-resonator-based DC-DC power converter," in *IEEE Workshop on Control and Modeling for Power Electronics (COMPEL)*, Cartagena de Indias, Columbia, Nov. 2021, pp. 1–8.

[95] B. Wanyeki, "A two-stage piezoelectric resonator and switched capacitor DC-DC converter," Master's thesis, Massachusetts Institute of Technology, 2022.

[96] H. H. Woodson and J. R. Melcher, *Electromechanical Dynamics Part III: Elastic and Fluid Media*. Wiley, 1968.

[97] A. Ballato, "Modeling piezoelectric and piezomagnetic devices and structures via equivalent networks," *IEEE Transactions on Ultrasonics, Ferroelectrics, and Frequency Control*, vol. 48, no. 5, pp. 1189–1240, 2001.

[98] L. de Araujo Pereira, A. Morel, M. Touhami, T. Lamorelle, G. Despesse, and G. Pillonnet, "Operating frequency prediction of piezoelectric dc–dc converters," *IEEE Transactions on Power Electronics*, vol. 37, no. 3, pp. 2508–2512, 2021.

[99] "Physical and piezoelectric properties of APC materials". APC International, Ltd. [Online]. Available: https://www.americanpiezo.com/apc-materials/physical-piezoelectric-properties.html

[100] "Ceramic materials". Boston Piezo Optics Inc. [Online]. Available: https://www.bostonpiezooptics.com/ceramic-materials-pzt

[101] "Material properties". Piezo Technologies. [Online]. Available: https://piezotechnologies.com/materials-chart/

[102] "Physical and piezoelectric properties of T&P materials". T&Partners Praha. [Online]. Available: https://www.tpartnerspraha.com/maretials-type-1.html

[103] "Material data". PI Ceramic GmbH. [Online]. Available: https://static.piceramic.com/fileadmin/user_upload/physik_instrumente/files/datasheets/PI_Ceramic_Material_Data.pdf

[104] "PZT materials complete properties". CTS Corporation. [Online]. Available: https://www.ctscorp.com/wp-content/uploads/CTS_-PZT-Materials_Complete-Properties_20180829.pdf

[105] "Piezo ceramics". Fuji Ceramics Corporation. [Online]. Available: http://www.fujicera.co.jp/managed/wp-content/themes/fujicera/digitalbook/en/elements/index_h5.html#1

[106] "Piezoceramic hard materials material data". CeramTec. [Online]. Available: https://www.ceramtec.com/files/ms_piezoceramic-hard-materials_en_de.pdf

[107] "Material coefficients PIC181". PI Ceramic.

[108] "Lithium niobate". Boston Piezo Optics Inc. [Online]. Available: https://www.bostonpiezooptics.com/lithium-niobate

[109] "Ready to deliver piezoelectric ceramics". APC International. [Online]. Available: https://www.americanpiezo.com/piezo-sale/piezoelectric-ceramics.html

[110] D. Costinett, D. Maksimovic, and R. Zane, "Circuit-oriented treatment of nonlinear capacitances in switched-mode power supplies," *IEEE Transactions on Power Electronics*, vol. 30, no. 2, pp. 985–995, 2014.

[111] J. D. Boles, P. L. Acosta, Y. K. Ramadass, J. H. Lang, and D. J. Perreault, "Evaluating piezoelectric materials for power conversion," in *Proc. IEEE Workshop on Control and Modeling for Power Electronics*, Aalborg, Denmark, Nov. 2020, pp. 1–8.

[112] J. D. Boles, J. E. Bonavia, P. L. Acosta, Y. K. Ramadass, J. H. Lang, and D. J. Perreault, "Evaluating piezoelectric materials and vibration modes for power conversion," *IEEE Transactions on Power Electronics*, 2022.

[113] S. J. Martin, V. E. Granstaff, and G. C. Frye, "Characterization of a quartz crystal microbalance with simultaneous mass and liquid loading," *Analytical chemistry*, vol. 63, no. 20, pp. 2272–2281, 1991.

[114] A. Fort, E. Panzardi, V. Vignoli, M. Tani, E. Landi, M. Mugnaini, and P. Vaccarella, "An adaptive measurement system for the simultaneous evaluation of frequency shift and series resistance of QCM in liquid," *Sensors*, vol. 21, no. 3, p. 678, 2021.

[115] J. E. Bonavia, J. D. Boles, J. H. Lang, and D. J. Perreault, "Augmented piezoelectric resonators for power conversion," in *Proc. IEEE Workshop on Modeling and Control in Power Electronics*, Cartagena de Indias, Columbia, Nov. 2021, pp. 1–8.

[116] S. Dong, A. V. Carazo, and S. H. Park, "Equivalent circuit and optimum design of a multilayer laminated piezoelectric transformer," *IEEE Transactions on Ultrasonics, Ferroelectrics, and Frequency Control*, vol. 58, no. 12, pp. 2504–2515, 2011.

[117] M. Khanna, R. Burgos, Q. Wang, K. D. Ngo, and A. V. Carazo, "New tunable piezoelectric transformers and their application in dc–dc converters," *IEEE Transactions on Power Electronics*, vol. 32, no. 12, pp. 8974–8978, 2017.

[118] K. S. Meyer, M. A. Andersen, and F. Jensen, "Parameterized analysis of zero voltage switching in resonant converters for optimal electrode layout of piezoelectric transformers," in *Proc. IEEE Power Electronics Specialists Conference*, Rhodes, Greece, Jun. 2008, pp. 2543–2548.

[119] E. Horsley, M. Foster, and D. Stone, "State-of-the-art piezoelectric transformer technology," in *Proc. IEEE European Conference on Power Electronics and Applications*, Aalborg, Denmark, Sep. 2007, pp. 1–10.

[120] A. M. Sánchez, M. Sanz, R. Prieto, J. A. Oliver, P. Alou, and J. A. Cobos, "Design of piezoelectric transformers for power converters by means of analytical and numerical methods," *IEEE transactions on industrial electronics*, vol. 55, no. 1, pp. 79–88, 2008.

[121] G. Ivensky, I. Zafrany, and S. Ben-Yaakov, "Generic operational characteristics of piezoelectric transformers," *IEEE Transactions on Power Electronics*, vol. 17, no. 6, pp. 1049–1057, 2002.

[122] Y.-P. Liu, D. Vasic, F. Costa, W.-J. Wu, and C.-K. Lee, "Design of fixed frequency controlled radial-mode stacked disk-type piezoelectric transformers for dc/dc converter applications," *Smart Materials and Structures*, vol. 18, no. 8, p. 085025, 2009.

[123] J. G. Kassakian, D. J. Perreault, G. C. Verghese, and M. F. Schlecht, "Introduction to magnetics design," in *Principles of Power Electronics*. Cambridge University Press, 2023, ch. 20.

[124] "Ferrite for telecommunication miniature pot cores p series". TDK Corporation. [Online]. Available: https://www.dextermag.com/wp-content/uploads/2017/03/TDK_Dexter_Ferrites_Telecommunication_Miniature_Pot_Cores.pdf

[125] J. D. Boles, J. J. Piel, E. Ng, J. E. Bonavia, J. H. Lang, and D. J. Perreault, "Piezoelectric-based power conversion: Recent progress, opportunities, and challenges," in *Proc. IEEE Custom Integrated Circuits Conference*, Newport Beach, CA, Apr. 2022, pp. 1–8.

[126] J. D. Boles, J. J. Piel, E. Ng, J. E. Bonavia, B. M. Wanyeki, J. H. Lang, and D. J. Perreault, "Opportunities, progress and challenges in piezoelectric-based power electronics," in *Proc. IEEE International Power Electronics Conference*, Himeji, Japan, May 2022, pp. 1–8.